Evolution of High Arctic Ocean Basins and Continental Margins

Øyvind Engen

Dissertation for the Degree Doctor Scientiarum

Department of Geosciences
Faculty of Mathematics and Natural Sciences
University of Oslo
Norway

Submitted: 30 June 2005
Date of Defence: 22 August 2005

Series of dissertations submitted to the
Faculty of Mathematics and Natural Sciences, University of Oslo.
No. 450

ISSN 1501-7710

The Idea of North

Preface

The present dissertation consists of four scientific papers resulting from my employment as a research assistant and later as a Dr. Scient. candidate at the Department of Geosciences, University of Oslo, during 2001–2005. The advisory committee has been Prof. Jan Inge Faleide (University of Oslo), Prof. Olav Eldholm (formerly at the University of Oslo; now at the University of Bergen), and Prof. Hilmar Bungum (University of Oslo and NORSAR). Paper 1 is an extension of my Cand. Scient. thesis [*Engen*, 2001] and was in part developed during two visits to NORSAR, Kjeller, in 2000 and 2001. The basis for Paper 3 was set in Honolulu during the spring semester 2004 in collaboration with Prof. Pål Wessel, Prof. Neil Frazer, and Dr. Fernando Martinez at the Department of Geology and Geophysics, School of Ocean and Earth Science and Technology (SOEST), University of Hawai'i at Manoa. Paper 2 benefited from an exchange visit to the All-Russia Research Institute for Geology and Mineral Resources of the World Ocean (VNIIOkeangeologia) in St. Petersburg in October, 2002, supervised by Dr. Vladimir Glebovsky and Dr. Andrey Zayonchek. The study was supported by a 3-year doctoral fellowship for basic scientific research from the Norwegian Research Council, grant no. 147541/432, and funding from the Norwegian Petroleum Directorate.

Acknowledgments

I thank my advisors, Prof. Jan Inge Faleide, Prof. Olav Eldholm, and Prof. Hilmar Bungum, for valuable comments, discussions and support during the study. I am also grateful to my co-authors Jakob Andreas Gjengedal, Prof. Yngve Kristoffersen, Prof. Neil Frazer, and Prof. Pål Wessel for spending time and effort on improving the manuscripts. Dr. Vladimir Glebovsky and Dr. Andrey Zayonchek are kindly recognised for advice and support during my stay at VNIIOkeangeologia. Special thanks go to Dr. Asbjørn Breivik, Dr. Oliver Ritzmann, and Dr. Fernando Martinez for stimulating exchange of ideas and technical support. Likewise, my best regards go to Dr. Filippos Tsikalas, Dr. Conrad Lindholm, Anton Likhachev, Seung-Sep Kim, and Michael Chandler for kind assistance and support. Prof. Annik M. Myhre kindly took care of preparations for the defence.

I acknowledge the institutions involved in the study: NORSAR; SOEST; and VNIIOkeangeologia, for making their research facilities and teaching resources available to me free of charge. I am grateful to the Norwegian Research Council for providing three years of funding, a travel grant to Hawai'i, and ample funds for conference participation. Gro Corell was instrumental in transforming the funds from budgetary numbers to useful money. The Norwegian Petroleum Directorate kindly provided financial support for me as a research assistant in 2001, my participation in the Norwegian Arctic expedition of 2001, my stay at VNIIOkeangeologia, and two scientific conferences in St. Petersburg. I commend Harald Brekke for making these funds available and Elena Miloradovskaya for carefully arranging my visits to Russia. I send my sincere thanks to Evelyn Norris who took care of the paperwork necessary for my stay at SOEST.

I thank the crew of *MV Oden* during the 2001 expedition for their around-the-hour commitment to seismic data acquisition under challenging Arctic conditions. Paper 2 would not have been possible without the combined efforts of everyone aboard.

I am indebted to Olvar Løvås for data processing and Dr. Tormod Kværna for providing software. Andrey Chernykh, Prof. Brian Taylor, Dr. Berit Kuvaas, Dr. Jonathan Snow, Dr. Bernard Coakley, Dr. Walter H. F. Smith, Prof. Knut Bjørlykke, and many more gave helpful hints, comments, and technical support. Thanks to my colleagues at the University of Oslo, SOEST, NORSAR, and VNIIOkeangeologia for creating a nice scientific and social environment.

Personal thanks go to Chris Chambers and Geoff Ashton for teaching me how to live in a Hawaiian student flat community. I am, as always, grateful to André Nilsen, Lars Ove Hagset, Håvard Austvik, and Kjetil Larsen for reminding me about sublime ideals and friendship. Sincere appreciation goes to my family for life-long personal support. And of course, my deepest gratitude is for my dear Kristine and our daughter Stella who never doubted neither me nor this thesis.

Oslo, 22 August 2005

Øyvind Engen

Contents

Introduction

The Arctic Ocean comprises two main ocean basins, the Amerasia and Eurasia basins, separated by the elongate Lomonosov Ridge (Figure I-1). In a plate tectonic framework the Eurasia Basin is linked to the Norwegian–Greenland Sea and the Atlantic by the northernmost part of the Eurasia–North America plate boundary. The plate boundary comprises two mid-ocean ridges, the Knipovich Ridge in the Norwegian–Greenland Sea and the Gakkel Ridge in the Eurasia Basin, linked by transform faults and oblique spreading segments in the Fram Strait. The passive margins flanking the plate boundary feature two marginal plateaus, the Morris Jesup Rise and the Yermak Plateau.

The Norwegian–Greenland Sea and the Eurasia Basin developed in a three-plate setting as Cretaceous–Paleocene rifts propagated north on either side of Greenland [*Pitman and Talwani*, 1972]. By the earliest Eocene, seafloor spreading was established in both basins [*Karasik*, 1968; *Talwani and Eldholm*, 1977; *Vogt et al.*, 1979] while relative motions between the Eurasia and Greenland plates were accommodated by a megashear region, the De Geer Zone, in the emergent ocean basin between Svalbard and Greenland [*Harland*, 1969]. At the Eocene–Oligocene transition, Greenland became part of the North American plate and transform faulting in the Greenland Sea was replaced by oblique rifting and seafloor spreading [*Talwani and Eldholm*, 1977].

The opening of the Eurasia Basin split off a fragment of the Eurasian continental margin that subsequently became the Lomonosov Ridge continental sliver [*Jokat et al.*, 1992; *Grantz et al.*, 2001]. The inner part of the Yermak Plateau is continental while its outer part and the Morris Jesup Rise have been attributed to voluminous volcanism at the Eurasia–Greenland–North America extinct triple junction [*Feden et al.*, 1979; *Jackson et al.*, 1984]. Continental remnants in the Norwegian–Greenland Sea include the Hovgård Ridge microcontinent [*Myhre et al.*, 1982] and possibly the Greenland Ridge [*Tsikalas et al.*, 2002].

In terms of plate tectonics and geodynamics the Arctic Ocean region poses some challenging questions. Among these are:

1. At half-spreading rates of 0.3–0.7 cm yr^{-1}, the Gakkel Ridge is the slowest-spreading ridge in the global mid-ocean ridge system [*Dick et al.*, 2003]. How does the exceptionally slow seafloor spreading affect earthquake occurrence and ridge structure?
2. The plate boundary continues into continental lithosphere on the Laptev Sea continental margin [*Drachev et al.*, 1998; *Franke et al.*, 2000] and the present plate rotation pole is located in northern Siberia about 500 km farther south (Figure I-1) [*DeMets et al.*, 1990]. How does the transition from a narrow zone of seafloor spreading to a broad continental rift system take place?

3. Because of the plate geometry, seafloor spreading in the northern Norwegian–Greenland Sea was delayed with respect to the adjacent ocean basins [*Talwani and Eldholm*, 1977], but the space–time relationship of rifting and seafloor spreading in the region is poorly understood. This relationship is crucial for dating the deep

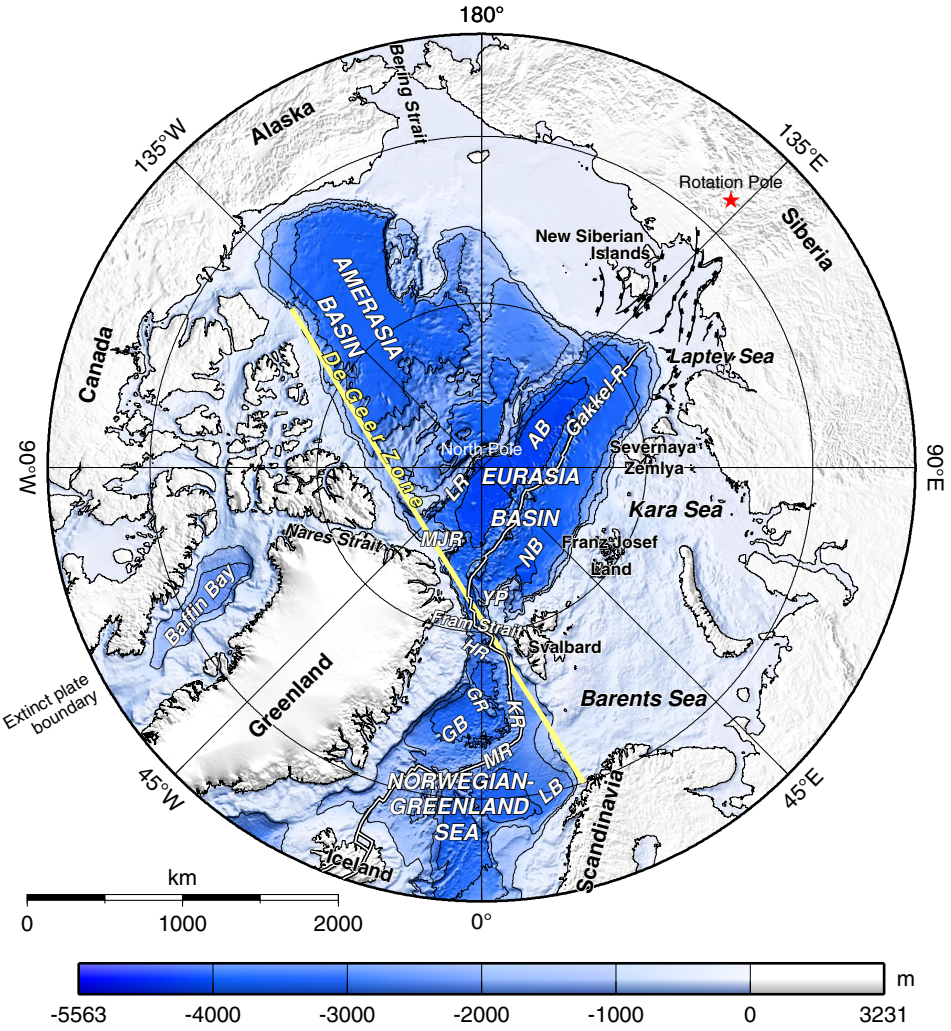

Figure I-1. High Arctic ocean basins and continental margins. The Arctic Ocean comprises the Amerasia Basin and the Eurasia Basin. The Gakkel Ridge subdivides the Eurasia Basin into the Nansen Basin (*NB*) on the Eurasian plate and the Amundsen Basin (*AB*) on the North American plate. IBCAO bathymetry and land elevations from *Jakobsson et al.* [2000]; Laptev Sea structures from *Drachev et al.* [1998]. *GB*, Greenland Basin; *GR*, Greenland Ridge; *HR*, Hovgård Ridge; *KR*, Knipovich Ridge; *LB*, Lofoten Basin; *LR*, Lomonosov Ridge; *MJR*, Morris Jesup Rise; *MR*, Mohn Ridge; *YP*, Yermak Plateau. Polar stereographic projection with true scale at the North Pole.

water passage through the Fram Strait, a main boundary condition for Late Cenozoic environmental change [*Eldholm et al.*, 1994].

4. Rifting and seafloor spreading on the northern and western Barents Sea margins initiated uplift and erosion of the Barents Sea shelf [e.g., *Vågnes and Amundsen*, 1993]. The uplift was progressively larger to the northwest and was amplified by glacial erosion [*Dimakis et al.*, 1998]. How were the erosional products transported into the adjacent ocean basins and deposited?

During the 1990s, technological advances and the end of the Cold War led to increased peaceful research activities in the Arctic Ocean, and significant geophysical data sets were published to the global research community. In particular, the 1998–99 SCICEX submarine cruises [*Edwards et al.*, 2001; *Tolstoy et al.*, 2001; *Cochran et al.*, 2003] and the AMORE tandem icebreaker expedition in 2001 [*Jokat et al.*, 2003; *Michael et al.*, 2003; *Jokat and Micksch*, 2004] have made the western two thirds of the Gakkel Ridge one of the best studied mid-ocean ridge segments in the world. The governments of countries around the Arctic Ocean are engaging in geoscientific research because of promising hydrocarbon potentials and the delineation of legal outer shelf limits set forth by the United Nations Convention on the Law of the Sea. Multilateral research efforts are being planned in preparation for the International Polar Year 2007–2008, with the aim of understanding the key role of the Arctic Ocean region in past and present global cycles.

Taking advantage of the much increased detail offered by new data, the dissertation attempts to answer some of the remaining questions about the ocean basins and continental margins flanking the Eurasia–North America plate boundary. Its four constituent papers result from integrated geophysical analysis of gravity and magnetic anomalies, bathymetry, seismic reflection and refraction profiles, earthquake locations and focal mechanisms, and onshore and offshore geological data. The overall objectives are to:

- ***Elucidate aspects of the structure, composition and evolution of the Eurasia Basin and Norwegian–Greenland Sea and their passive continental margins; and***
- ***Relate the findings to fundamental Earth processes, specifically associated with lithospheric break-up and seafloor spreading.***

The Norwegian Arctic Expedition, 2001

In the autumn of 2001, the Norwegian Petroleum Directorate and the universities of Bergen and Oslo acquired multi-channel and wide-angle seismic data from the icebreaker *MV Oden* in ice-covered waters north of Svalbard. The purpose of the expedition was to map sediment thickness and the foot of the continental slope in the Nansen Basin, and to gain new insight into processes forming the Yermak Plateau and the Gakkel Ridge.

Seismic surveying during icebreaking is challenging due to (1) limited direct line of sight in ice-covered waters; (2) the noise of icebreaking; and (3) thick ice pressure ridges. Limited direct line of sight inhibits the radio transmission range of sonobuoys used for wide-angle velocity measurements. After the receiver antenna

was elevated to the *Oden*'s chimney ~30 m above sea level, the ranges improved and several sonobuoys transmitted for >20 km.

Icebreaking introduces an additional noise component relative to open-water conditions because of the ship's ramming and splintering of the ice; collisions between ice fragments and the seismic equipment; and complex acoustic scatter from the bottom of the ice. Fragments of drifting and bouncing ice in the ship's wake closed the trail of open water a few hundred meters behind the ship. Damage to the seismic equipment was minimized by robust towing arrangements keeping a short, 400 m long streamer without depth-controlling birds as close to the stern as possible. However, in the turbulent zone just behind the vessel, the airguns were easily damaged or entangled with the hydrophone cable. To avoid these problems one may

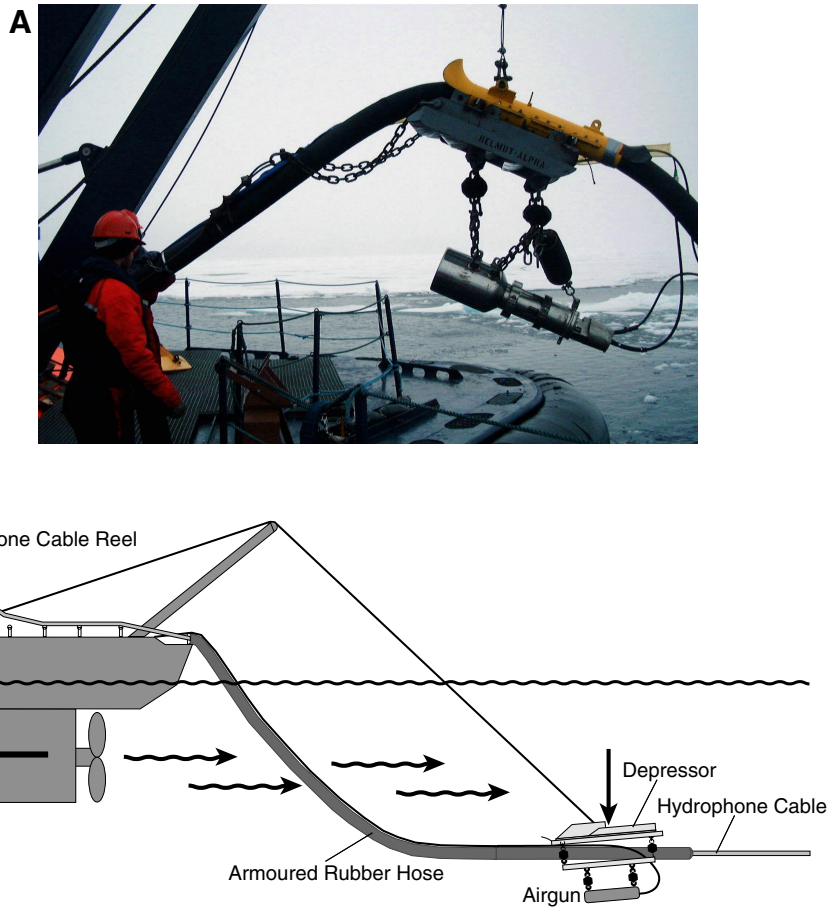

Figure I-2. 20 l airgun mounted on depressor with armoured hose for hydrophone cable. **(A)** Launch from the stern of *MV Oden*. Note ice conditions which were typical during surveying in the Nansen Basin. **(B)** Equipment in towing position, i.e. depressed 0–7 m below sea level by the ship's thrust [modified from *Gjengedal*, 2004].

tow the equipment beneath the turbulent zone, applying heavy weights [*Grantz et al.*, 2004], but this configuration introduces unwanted bubble pulse signals. A more flexible and acoustically more appropriate arrangement is to mount the airguns on a depressor bird also carrying an armoured rubber hose funnelling the hydrophone cable (Figure I-2) [*Kristoffersen*, 1997]. The bird kept the seismic equipment depressed and allowed it to slide past bouncing ice fragments.

The sea ice was ~2.5 m thick on average; however, ice pressure ridges 3–4 times as thick intercepted the planned seismic lines and could not be handled while surveying. In response, the vessel had to manoeuvre along a crooked path. Because shots were fired at constant time intervals while the speed and heading of the ship varied, the original shotpoint distances were not constant and false geometries would result if seismic traces were plotted at constant spacing. Evenly spaced traces for interpretation and analysis were achieved by a special binning procedure where the hydrophone cable was assumed to follow the shiptrack and traces were stacked at 25 m intervals along track [*Gjengedal*, 2004].

The expedition resulted in ~1100 km of good-quality multi-channel seismic lines and 50 wide-angle velocity profiles imaging sedimentary and basement rocks at previously unsurveyed locations. The new data are presented and interpreted in Paper 2 where they are discussed in the context of recent airborne gravity and magnetic data [*Brozena et al.*, 2003] and results from the AMORE expedition [*Jokat et al.*, 2003; *Michael et al.*, 2003; *Jokat and Micksch*, 2004].

Summary of Papers

The present-day global seismograph network is capable of detecting earthquakes with nearly uniform magnitude threshold throughout the Eurasia Basin region. Given that the location of each earthquake is constrained by at least 12 recording stations, global earthquake catalogues confidently show that (1) earthquakes along the oceanic part of the plate boundary occur in swarms; (2) plate boundary stress decreases eastwards, in accordance with decreasing spreading rates; and (3) deformation takes place in a narrow zone in the oceanic domain but is abruptly defocused at the transition to the Laptev Sea continental rift system.

When integrated with bathymetry and potential field data, the earthquake distribution indicates four distinct plate boundary provinces. The *Spitsbergen Transform System* is a series of oblique ridges and transform faults where the seismicity becomes increasingly diffuse to the north. The *western Gakkel Ridge* (west of 60°E) has clustered and focused seismicity, accentuated topography and high-amplitude magnetic anomalies, whereas the *eastern Gakkel Ridge* has smoother topographic relief, lower magnetic amplitudes, and slightly more focused seismicity. At the *Laptev Sea* continental slope, the change from ultra-slow seafloor spreading to active continental rifting takes place over a less than 60-km-wide continent–ocean transition featuring a 150–200-km-long sheared margin segment.

The western Gakkel Ridge province is magmatically segmented. The central, sparsely magmatic segment [*Michael et al.*, 2003] is characterised by discrete magmatic centres that have been stationary with respect to the spreading axis since

at least Chron 6 times (~19.6 Ma) and possibly since before Chron 18 times (~39.9 Ma). The westernmost, volcanic segment may have been amagmatic during Chron 13–5 times (~33.3–9.8 Ma).

Sedimentary rocks in the Nansen Basin comprise four turbidite units with typical seismic velocities of 2.3, 2.2, 1.9 and 1.8 km s^{-1}. The upper unit is associated with glaciomarine deposition in the Franz-Victoria Fan system and dates accordingly to ~2.3 Ma. The deeper, regional velocity contrast from 2.2 to 1.9 km s^{-1} probably represents a late Miocene (~10 Ma) response to major paleoceanographic changes during the opening of the Fram Strait gateway.

A location of the continent–ocean transition (COT) on conjugate margins of the western Eurasia Basin and the northern Norwegian–Greenland Sea is proposed from the relation between seismically observed crustal thinning and seaward increasing mantle Bouguer anomalies. A refined location of the COT around the Hovgård and Greenland ridges is also provided. The new COT location indicates that the distinct segmentation of the western Barents Sea margin is mirrored on the conjugate northeast Greenland margin. The Hinlopen margin north of Svalbard is characterised by a steep boundary fault on the COT and may be a sheared margin segment. The present geological and geophysical data base favours a continental origin of the Yermak Plateau and the Morris Jesup Rise, but a firm conclusion on their crustal structure cannot yet be drawn.

A continuous oceanic corridor formed through shear-rifted continental crust in the Fram Strait between Chron 5B (14.8 Ma) and Chron 5 times (9.8 Ma). This is consistent with the deep-sea sedimentary record of emerging deep-water exchange between the Arctic and North Atlantic oceans at ~10 Ma. Coeval thinning and uplift of the NW Barents Sea shelf, and formation of the Yermak H-Zone [*Feden et al.*, 1979] in the western Eurasia Basin, may point to the Fram Strait as a gateway also for northward asthenospheric flow.

Previously unsurveyed sediment depocentres in the Norwegian–Greenland Sea are predicted from inversion of gravity supported by bathymetry, oceanic basement age, and seismic calibration points. The locations of depocentres are reliable down to spatial scales of 20–25 km, while predicted sediment thicknesses are ~1 km uncertain. The predicted sediment thickness map maintains previous findings of thick sediments on the Eurasian side relative to the Greenland side of the mid-ocean ridge because of different Late Cenozoic glaciomarine input. Other predictions include an anomalous, high-standing basement province in the central Greenland Basin; V-shaped abyssal hills on the Mohn Ridge; and an extinct fracture zone on the younger side of the Greenland Ridge.

Outlook

The COT and oceanic isochrons identified in Papers 2 and 4 should be tested in a series of plate tectonic reconstructions of the Eurasia Basin and the North Atlantic. Refined rotation poles should be calculated for the relative motions of Eurasia, Greenland, North America and various continental fragments, and their implications for continental break-up and early margin development should be

investigated. The Eocene triple junction between Eurasia, Greenland and North America is only approximately located within the Yermak Plateau province [*Jackson et al.*, 1984] and its influence on Arctic regional geodynamics is still poorly understood.

Correlation of sedimentary units between the Eurasia Basin, its continental margins and the western Barents Sea margin is hampered by the lack of age control (Paper 2); in fact, the only drill hole on the northern Eurasian continental margin penetrates Pliocene sedimentary strata on the inner Yermak Plateau [*Thiede et al.*, 1995]. Deep sea drilling and coring of the Eurasia Basin would facilitate insight into the mass balance between shelf erosion and basin deposition. In particular, the possible links between plate tectonics, marginal uplift, paleoceanographic changes and the onset of glaciations might be deciphered with more confidence than at present. However, drilling in these areas is technically complex and would require additional site surveying which is still some years ahead. Drilling of the outer Yermak Plateau is within reach and may answer questions on basement structure and origin, as well as depositional ages.

The prediction of sediment thickness from gravity (Paper 3) may be refined in order to predict absolute thickness values more accurately. Nonetheless, the method may be easily applied to the Arctic Ocean. Preliminary tests in the Eurasia Basin were unsuccessful because of limited resolution of airborne gravity data. However, the Amerasia Basin south of 81.5°N is covered by gravity derived from satellite altimetry [*Laxon and McAdoo*, 1994] and sediment thickness may be predicted at approximately the same resolution as in the Norwegian–Greenland Sea.

References

Brozena, J.M., V.A. Childers, L.A. Lawver, L.M. Gahagan, R. Forsberg, J.I. Faleide, and O. Eldholm (2003), New aerogeophysical study of the Eurasia Basin and Lomonosov Ridge: Implications for basin development, *Geology, 31* (9), 825–828.

Cochran, J.R., G.J. Kurras, M.H. Edwards, and B.J. Coakley (2003), The Gakkel Ridge: Bathymetry, gravity anomalies, and crustal accretion at extremely slow spreading rates, *Journal of Geophysical Research*, *108* (B2), 2116, doi:10.1029/2002JB001830.

DeMets, C., R.G. Gordon, D.F. Argus, and S. Stein (1990), Current plate motions, *Geophysical Journal International*, *101* (2), 425–478.

Dick, H.J.B., J. Lin, and H. Schouten (2003), An ultraslow-spreading class of ocean ridge, *Nature*, *426* (6965), 405–412.

Dimakis, P., B.I. Braathen, J.I. Faleide, A. Elverhøi, and S.T. Gudlaugsson (1998), Cenozoic erosion and the preglacial uplift of the Svalbard–Barents Sea region, *Tectonophysics*, *300* (1–4), 311–327.

Drachev, S.S., L.A. Savostin, V.G. Groshev, and I.E. Bruni (1998), Structure and geology of the continental shelf of the Laptev sea, eastern Russian Arctic, *Tectonophysics*, *298* (4), 357–393.

Edwards, M.H., G.J. Kurras, M. Tolstoy, D.R. Bohnenstiehl, B.J. Coakley, and J.R. Cochran (2001), Evidence of recent volcanic activity on the ultraslow-spreading Gakkel ridge, *Nature*, *409* (6822), 808–812.

Eldholm, O., A.M. Myhre, and J. Thiede (1994), Cenozoic tectono-magmatic events in the Northern Atlantic: Potential paleoenvironmental implications, in *Cenozoic Plants and Climates of the Arctic*, *NATO ASI Series*, vol. I 27, edited by M.C. Boulter and H.C. Fischer, pp. 35–55, Springer-Verlag, Berlin.

Engen, Ø. (2001), The Arctic Plate Boundary, Cand. Scient. thesis, 116 pp., University of Oslo, Norway.

Feden, R.H., P.R. Vogt, and H.S. Fleming (1979), Magnetic and bathymetric evidence for the Yermak Hot Spot northwest of Svalbard in the Arctic Basin, *Earth and Planetary Science Letters*, *44* (1), 18–38.

Franke, D., F. Kruger, and K. Klinge (2000), Tectonics of the Laptev Sea – Moma 'Rift' region: Investigation with seismologic broadband data, *Journal of Seismology*, *4* (2), 99–116.

Gjengedal, J.A. (2004), Prosessering og tolkning av seismiske data frå Nansenbassenget og Yermakplatået, Cand. scient. thesis, University of Bergen, Norway (in Norwegian).

Grantz, A., V.L. Pease, D.A. Willard, R.L. Phillips, and D.L. Clark (2001), Bedrock cores from 89°N: Implications for the geologic framework and Neogene paleoceanography of Lomonosov Ridge and a tie to the Barents shelf, *Geological Society of America Bulletin*, *113* (10), 1272–1281.

Grantz, A., P.E. Hart, and S.D. May (2004), Seismic Reflection and Refraction Data Acquired in the Canada Basin, Northwind Ridge and Northwind Basin, Arctic Ocean in 1988, 1992 and 1993, Open-File Report 2004-1243, 34 pp., U.S. Geological Survey, Menlo Park, CA.

Harland, W.B. (1969), Contribution of Spitsbergen to understanding of tectonic evolution of the North Atlantic region, in *North Atlantic geology and continental drift*, *Memoir*, vol. 12, edited by M. Kay, pp. 817–851, American Association of Petroleum Geologists, Tulsa, OK.

Jackson, H.R., G.L. Johnson, E. Sundvor, and A.M. Myhre (1984), The Yermak Plateau – formed at a triple junction, *Journal of Geophysical Research*, *89* (B5), 3223–3232.

Jakobsson, M., N. Cherkis, J. Woodward, R. Macnab, and B. Coakley (2000), New grid of Arctic bathymetry aids scientists and mapmakers, *Eos, Transactions, American Geophysical Union*, *81* (9), 89, 93, 96.

Jokat, W., and U. Micksch (2004), Sedimentary structure of the Nansen and Amundsen basins, Arctic Ocean, *Geophysical Research Letters*, *31*, L02603, doi:10.1029/2003GL018352.

Jokat, W., G. Ünzelmann-Neben, Y. Kristoffersen, and T.M. Rasmussen (1992), Lomonosov Ridge – A double-sided continental margin, *Geology*, *20* (10), 887–890.

Jokat, W., O. Ritzmann, M.C. Schmidt-Aursch, S. Drachev, S. Gauger, and J. Snow (2003), Geophysical evidence for reduced melt production on the Arctic ultraslow Gakkel mid-ocean ridge, *Nature*, *423* (6943), 962–965.

Karasik, A.M. (1968), Magnetic anomalies of the Gakkel Ridge and origin of the Eurasian subbasin of the Arctic Ocean, English Translation, in *Geophysical Methods of Prospecting in the Arctic*, vol. 5, pp. 8–19, Nauchno-Issled. Inst. Geologii Arktiki, Leningrad.

Kristoffersen, Y. (1997), Seismic reflection surveys during Arctic Ocean-96, in *Yearbook 1995/96*, pp. 75–77, Swedish Polar Research Secretariat, Stockholm.

Laxon, S., and D. McAdoo (1994), Arctic Ocean gravity field derived from ERS-1 satellite altimetry, *Science*, *265* (5172), 621–624.

Michael, P.J., C.H. Langmuir, H.J.B. Dick, J.E. Snow, S.L. Goldstein, D.W. Graham, K. Lehnert, G. Kurras, W. Jokat, R. Mühe, and H.N. Edmonds (2003), Magmatic and amagmatic seafloor generation at the ultraslow-spreading Gakkel ridge, Arctic Ocean, *Nature*, *423* (6943), 956–961.

Myhre, A.M., O. Eldholm, and E. Sundvor (1982), The margin between Senja and Spitsbergen fracture zones: Implications from plate tectonics, *Tectonophysics*, *89* (1–3), 33–50.

Pitman, W.C., III, and M. Talwani (1972), Sea-floor spreading in the North Atlantic, *Geological Society of America Bulletin*, *83* (3), 619–645.

Talwani, M., and O. Eldholm (1977), Evolution of the Norwegian–Greenland Sea, *Geological Society of America Bulletin*, *88* (7), 969–999.

Thiede, J., A.M. Myhre, J.V. Firth, and the Shipboard Scientific Party (1995), Cenozoic Northern Hemisphere polar and subpolar ocean paleoenvironments (summary of ODP Leg 151 drilling results), in *North Atlantic–Arctic Gateways I*, *Proceedings of the Ocean Drilling*

Program, Initial Reports, vol. 151, edited by A.M. Myhre et al., pp. 397–420, Texas A & M University, Ocean Drilling Program, College Station, TX.

Tolstoy, M., D.R. Bohnenstiehl, M.H. Edwards, and G.J. Kurras (2001), Seismic character of volcanic activity at the ultraslow-spreading Gakkel Ridge, *Geology*, *29* (12), 1139–1142.

Tsikalas, F., O. Eldholm, and J.I. Faleide (2002), Early Eocene sea floor spreading and continent–ocean boundary between Jan Mayen and Senja fracture zones in the Norwegian–Greenland Sea, *Marine Geophysical Researches*, *23* (3), 247–270.

Vågnes, E., and H.E.F. Amundsen (1993), Late Cenozoic uplift and volcanism on Spitsbergen: Caused by mantle convection?, *Geology*, *21*, 251–254.

Vogt, P.R., P.T. Taylor, L.C. Kovacs, and G.L. Johnson (1979), Detailed aeromagnetic investigation of the Arctic Basin, *Journal of Geophysical Research*, *84* (B3), 1071–1089.

Conference and Popular Scientific Contributions

International Conference Presentations

1. Engen, Ø. (2001), The Arctic plate boundary: Talk, International Conference: Polar Regions of the Earth: Geology, Tectonics, Resource Significance, Natural Environment, St. Petersburg, Russia, 1–3 Nov.
2. Engen, Ø., O. Eldholm, and H. Bungum (2002), The Arctic plate boundary: seismotectonics at ultra-slow spreading: Poster, 4th European Ocean Drilling Program (ODP) Forum, Tromsø, Norway, 10–12 Apr. *Abstracts and Proceedings of the Norwegian Geological Society*, no. 3, p. 40, 2002.
3. Engen, Ø., O. Eldholm, and H. Bungum (2002), The Arctic plate boundary: seismotectonics at ultra-slow spreading: Poster, American Geophysical Union Fall Meeting, San Francisco, USA, 6–10 Dec. *Eos, Transactions, AGU*, v. 83, no. 47, Fall Meeting Supplement, Abstract T11A-1238, 2002.
4. Engen, Ø., J.A. Gjengedal, O. Eldholm, and Y. Kristoffersen (2003), The Nansen Basin, Arctic Ocean: Seismic data acquisition and geological results: Talk, 4th International Conference on Arctic Margins (ICAM IV), Dartmouth, Nova Scotia, Canada, 30 Sept–3 Oct.
5. Engen, Ø., J.I. Faleide, A.J. Breivik, F. Tsikalas, A.M. Myhre, and O. Eldholm (2003), Structure of the West and North Svalbard Margins in a plate tectonic setting: Poster, 4th International Conference on Arctic Margins (ICAM IV), Dartmouth, Nova Scotia, Canada, 30 Sept–3 Oct.
6. Brekke, H., V. Glebovsky, J.I. Faleide, Ø. Engen, E. Astafurova, A. Zayonchek, and A. Likhachev (2003), Sediment distribution in the Nansen Basin from an integrated analysis of seismic, bathymetry, and potential field data: Talk, 4th International Conference on Arctic Margins (ICAM IV), Dartmouth, Nova Scotia, Canada, 30 Sept–3 Oct.
7. Faleide, J.I., F. Tsikalas, A.J. Breivik, Ø. Engen, O. Eldholm, and S. Ren (2003), Late Mesozoic–Cenozoic evolution of the NE Atlantic region and links to the Arctic: Talk, 4th International Conference on Arctic Margins (ICAM IV), Dartmouth, Nova Scotia, Canada, 30 Sept–3 Oct.
8. Engen, Ø., J.I. Faleide, O. Eldholm, and A.J. Breivik (2003), Opening of the Arctic–North Atlantic gateway: Poster, American Geophysical Union Fall Meeting, San Francisco, USA, 8–12 Dec. *Eos Transactions AGU*, v. 84, no. 46, Fall Meeting Supplement, Abstract T12A-0498, 2003. Awarded.
9. Faleide, J.I., F. Tsikalas, A.J. Breivik, Ø. Engen, O. Eldholm, and S. Ren (2003), Late Mesozoic–Cenozoic evolution of the NE Atlantic Region and links to the Arctic: Poster, American Geophysical Union Fall Meeting, San Francisco, USA, 8–12 Dec. *Eos Transactions AGU*, v. 84, no. 46, Fall Meeting Supplement, Abstract T12A-0495, 2003.
10. Engen, Ø., J.I. Faleide, O. Eldholm, and A.J. Breivik (2004), Opening of the Arctic–North Atlantic gateway: Poster, International Conference: Arctic Geology, Hydrocarbon Resources and Environmental Challenges, Tromsø, Norway, 24–26 May. *Abstracts and Proceedings of the Norwegian Geological Society*, no. 2, p. 43, 2004.
11. Engen, Ø., J.A. Gjengedal, Y. Kristoffersen, and O. Eldholm (2004), Results of the Norwegian seismic expedition to the Yermak Plateau and Nansen Basin in 2001: Talk, International Conference: Arctic Geology, Hydrocarbon Resources and Environmental Challenges, Tromsø, Norway, 24–26 May. *Abstracts and Proceedings of the Norwegian Geological Society*, no. 2, p. 44, 2004.
12. Faleide, J.I., F. Tsikalas, A.J. Breivik, Ø. Engen, J.D. Wilson, O. Eldholm, and S. Ren (2004), Late Mesozoic–Cenozoic evolution of the NE Atlantic Region and links to the Arctic: Talk, 32nd International Geological Congress (IGC), Florence, Italy, 20–28 Aug.
13. Engen, Ø., P. Wessel, J.I. Faleide, and L.N. Frazer (2004), Gravity inversion predicts sediment thickness in the Norwegian–Greenland Sea: Poster, American Geophysical Union

Fall Meeting, San Francisco, USA, 13–17 Dec. *Eos, Transactions, AGU*, v. 85, no. 47, Fall Meeting Supplement, Abstract G51C-0098, 2004.

Domestic Conference Presentations

1. Engen, Ø., O. Eldholm, H. Bungum, and J.I. Faleide (2001), Plategrensen i Arktis: Talk, Norsk geologisk forenings vinterkonferanse, Oslo, Norway, 8-10 Jan. Awarded (in Norwegian).
2. Engen, Ø. (2001), Plategrensen i Arktis: Talk, Norsk geologisk forening avd. Stavanger, Stavanger, Norway, 27 Mar (in Norwegian).
3. Gjengedal, J.A., Ø. Engen, O. Løvås, Y. Kristoffersen, and O. Eldholm (2003), Polhavet: Seismikk i grenseland: Poster, Norsk geologisk forenings vinterkonferanse, Oslo, Norway, 6–8 Jan. *Abstracts and Proceedings of the Norwegian Geological Society*, no. 1, p. 31, 2003 (in Norwegian).
4. Engen, Ø., J.A. Gjengedal, Y. Kristoffersen, and O. Eldholm (2003), Polhavet: Ny seismikk avdekker geologiske særpreg: Talk and poster, Norsk geologisk forenings vinterkonferanse, Oslo, Norway, 6–8 Jan. *Abstracts and Proceedings of the Norwegian Geological Society*, no. 1, p. 25, 2003 (in Norwegian).
5. Engen, Ø. (2003), Fast fjell – et flytende grunnlag: Talk, Geodesi- og hydrografidagene, Hønefoss, Norway, 7 Nov. Invited (in Norwegian).
6. Engen, Ø., and J.I. Faleide (2005), Begrenset åpningstid – En platetektonisk historie om havstrømmer i Framstredet: Talk, Norsk geologisk forenings vinterkonferanse, Røros, Norway, 9–12 Jan. *Abstracts and Proceedings of the Norwegian Geological Society*, no. 1, pp. 31–32, 2005 (in Norwegian).
7. Engen, Ø., P. Wessel, J.I. Faleide, and L.N. Frazer (2005), Gravity inversion predicts sediment thickness in the Norwegian–Greenland Sea: Poster, Norsk geologisk forenings vinterkonferanse, Røros, Norway, 9–12 Jan. *Abstracts and Proceedings of the Norwegian Geological Society*, no. 1, p. 32, 2005.

Non-refereed Publications (in Norwegian)

1. Engen, Ø. (2002), Polhavet sprekker: Popular scientific article, http://www.viten.com/nyviten/engen.htm.
2. Engen, Ø. (2004), Fast fjell – et flytende grunnlag: Kart og Plan, v. 97(64), no. 1, p. 6–9, ISSN 0047-3278.

Paper 1

Paper 1

The Arctic plate boundary

Øyvind Engen[1], Olav Eldholm[1,2], and Hilmar Bungum[1,3]

1) Department of Geology, University of Oslo, Norway
2) *Now at* Department of Earth Science, University of Bergen, Norway
3) Norwegian Seismic Array (NORSAR), Kjeller, Norway

Published in *Journal of Geophysical Research, 108* (B2), 2075, 2003, doi: 10.1029/2002JB001809.

Abstract. Earthquakes provide information on the regional segmentation and seismotectonics of the poorly known boundary between the Eurasian and North American plates from the Knipovich Ridge to the Laptev Sea continental margin. To this end, we have sorted earthquake epicentre locations and focal mechanism solutions from global and regional catalogues, assessed location errors and network detectabilities, and compiled a well-constrained Arctic Catalogue of events north of 72°N for the period 1955–99. The seismological data are integrated with bathymetry and potential field data to locate ridge and transform segments along the Arctic mid-oceanic ridge, and we suggest that the plate boundary is divided into four regional provinces. The *Spitsbergen Transform System* comprises a series of short ridge and transform segments. The seismicity is constrained to the plate boundary in the south but is diffuse in the north. Gakkel Ridge has clustered and focused seismicity and relatively elongated ridge segments cut by small-offset transforms. A first-order change in axis trend at 60°E divides the ridge into two areas of different morphology and geophysical character. The *West Gakkel Ridge* has an accentuated relief and high-amplitude magnetic anomalies, whereas the *East Gakkel Ridge* has a smoother relief and lower magnetic amplitudes. At the *Laptev Sea* continental slope the seismicity indicates that the change from ultra-slow sea floor spreading to active continental rifting occurs over a less than 60-km-wide continent–ocean transition with a 150–200-km-long sheared-margin segment.

Keywords: Plate tectonics; Seafloor morphology; Seismicity and seismotectonics; Stresses – crust and lithosphere; Arctic region

Introduction

The Arctic part of the Eurasia–North America plate boundary comprises the Knipovich Ridge in the Greenland Sea and the Gakkel Ridge in the Eurasia Basin, connected by the complex Spitsbergen Transform System of short ridges and transform faults (Figure 1.1). The ultra-slow Gakkel Ridge sea floor spreading, at 0.3–0.7 cm yr^{-1} [*Eldholm et al.*, 1990], is the slowest of the global mid-oceanic ridge (MOR) system. In the Laptev Sea the plate boundary continues into continental lithosphere, and the present rotation pole is located in northern Siberia ~500 km farther south [e.g., *Talwani and Eldholm*, 1977; *Franke et al.*, 2000]. Thus, the outer Laptev Sea margin marks the transition from a narrow zone of slowly accreting oceanic crust to a broad continental rift system [*Fujita et al.*, 1990a; *Drachev et al.*, 1998].

Because of the ice conditions, the plate boundary north of the Knipovich Ridge has commonly been defined from regional bathymetry and seismicity [*Perry et al.*, 1985; *Eldholm et al.*, 1990; *Fujita et al.*, 1990b]. More recently, however, new geophysical data sets have become available. These include bathymetric maps [*HDNO-VNIIOkeangeologia*, 1999; *Jakobsson et al.*, 2000] and an improved earthquake data base [*Engen*, 2001]. Moreover, the U.S. Naval Research Laboratory (NRL) conducted airborne gravity and magnetic surveys in a wide corridor between Svalbard and the Lomonosov Ridge in 1998 and 1999 [*Childers et al.*, 2001; *Brozena et al.*, 2003] (Figure 1.1).

Here, we focus on the regional character of the plate boundary north of the Knipovich Ridge, denoted the Arctic plate boundary. We integrate seismicity, inferred primarily from teleseismic earthquakes, bathymetry and potential field data to study its location, segmentation and geodynamic characteristics. To this end, we divide the area into four plate boundary provinces (Figure 1.1).

Bathymetry and Potential Field Data

The regional bathymetry data includes the GEBCO [*Johnson et al.*, 1979; *Jones et al.*, 1994] and *Perry et al.* [1985] maps, portraying the Arctic ocean floor with >10 km resolution. However, the new HDNO [*HDNO-VNIIOkeangeologia*, 1999] and IBCAO [*Jakobsson et al.*, 2000] maps provide a much improved regional plate boundary resolution, as the former is contoured from 5–15-km-spaced depth soundings and the latter from 2.5×2.5 km gridded values. In the eastern Eurasia Basin the IBCAO consists entirely of HDNO contours. We ascribe minor discrepancies between the maps to differences in coverage and navigation and consider both maps adequate for regional studies. In addition to the principal data base (Table 1.1), published bathymetric and gravity profiles have contributed locally [*Thiede et al.*, 1990; *Jokat et al.*, 1995; *Coakley and Cochran*, 1998; *Weigelt*, 1998].

No complete circum-Arctic gravity map is yet available because of inadequate satellite orbits and the ice cover which inhibits surface ship operations and standard satellite altimetry. Nonetheless, *Laxon and McAdoo* [1994; 1998] constructed a gravity grid covering the plate boundary south of 82°N. Our main data source, however, has

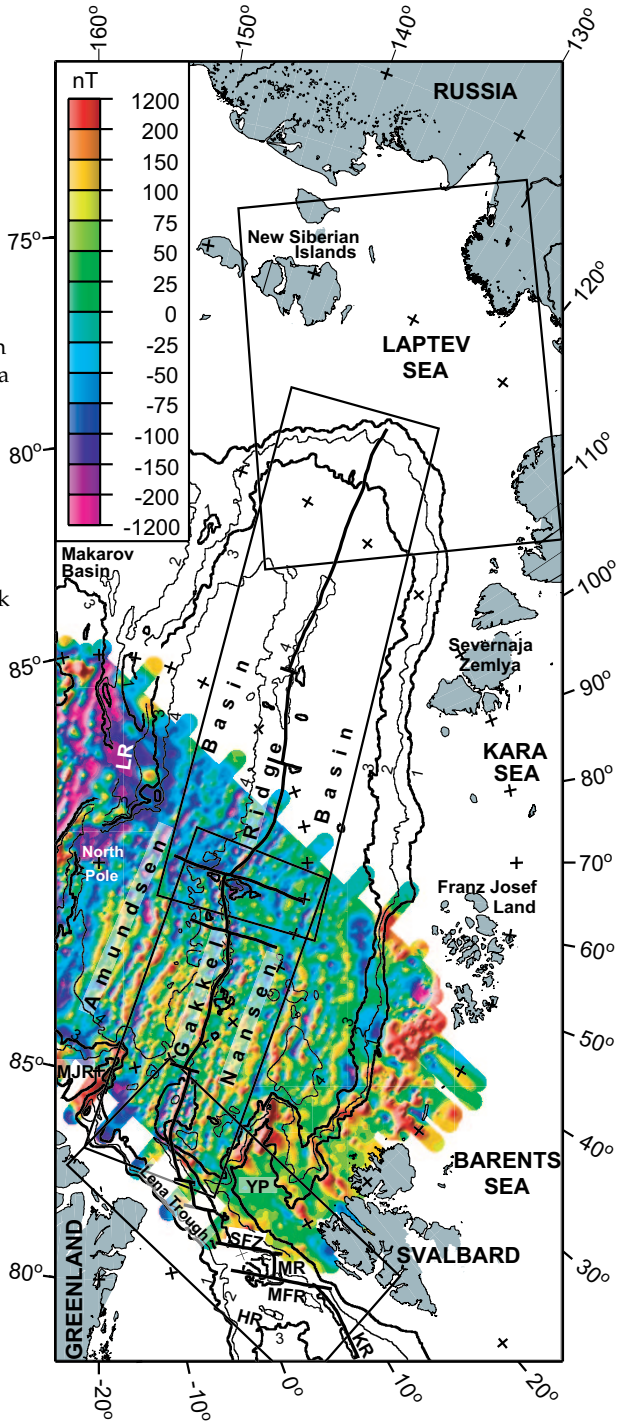

Figure 1.1. Main physiographic and structural elements in the eastern Arctic. Bathymetry from *Jakobsson et al.* [2000], contour interval 1 km. The magnetic anomalies show the coverage of the NRL surveys [*Brozena et al.*, 2003]. The four plate boundary provinces are shown within boxes. The plate boundary segments between the Knipovich Ridge (*KR*) and the northern Lena Trough are termed the Spitsbergen Transform System [*Crane et al.*, 1982]. *GS*, Greenland Sea; *LR*, Lomonosov Ridge; *MFZ*, Molloy Fracture Zone; *MJR*, Morris Jesup Rise; *MR*, Molloy Ridge; *SFZ*, Spitsbergen Fracture Zone; *YP*, Yermak Plateau.

been a gridded version of the NRL aerogravity data set [*Brozena et al.*, 2003], supplemented by the most recent satellite gravity grid, KMS99 [*Andersen and Knudsen*, 1998]. The NRL data cover ~1000 km of the plate boundary north of the Spitsbergen Transform System (Figure 1.1). KMS99, incorporating both Geosat and ERS-1 data, covers the same area as *Laxon and McAdoo* [1998], but with improved resolution. The two data sets will be part of the uniformly gridded Arctic Gravity Project (ArcGP) map of which a preliminary version has been consulted on regional trends in the eastern plate boundary provinces (ArcGP data are available from the National Imagery and Mapping Agency World Wide Web server at http://www.nima.mil/GandG/agp).

A summary of older Arctic magnetic profiles [*Kovacs et al.*, 1990] shows that the coverage of magnetic survey lines is relatively good in the western Eurasia Basin but poorer farther east. These and other profiles have been incorporated in the GSC

Table 1.1. Regional Geophysical Data Sets Used to Delineate the Arctic Plate Boundary[a]

Data	Map Scale Cont. Interval	Digital Version	Data Acquisition				Reference
			Surface	Submarine	Aero	Satellite	
Bathymetry							
IBCAO	1:8,795,800 500 m	Grid 2.5×2.5 km	x	x			*Jakobsson et al.* [2000]; *Jakobsson* [2000]
HDNO	1:5,000,000 200 m		x	x			*HDNO-VNIIOkeangeologia* [1999]
NRL	1:4,704,075 500 m		x	x			*Perry et al.* [1985]
GEBCO	1:6,000,000 500 m	500 m contours	x				*Johnson et al.* [1979]; *Jones et al.* [1994]
Free-air gravity							
NRL 98/99	1:1,200,000 2 mGal	Track values Grid 2.5×2.5 km			x		*Brozena et al.* [2003]; This study
KMS99		Grid 2×2′				x	*Andersen and Knudsen* [1998]
Laxon/McAdoo		Grid 4×4′				x	*Laxon and McAdoo* [1998]
ArcGP	– 10 mGal	Grid 5×5′	x	x	x	x	http://www.nima.mil/GandG/agp
Magnetics							
NRL 98/99	1:1,200,000 25 nT	Track values Grid 2.5×2.5 km			x		*Brozena et al.* [2003]; This study
GSC		Grid 5×5 km	x		x		*Verhoef et al.* [1996]
DNAG	1:6,000,000 Track values		x		x		*Kovacs et al.* [1990]

[a]Contour intervals refer to the plate boundary province. *AGP*, Arctic Gravity Project; *DNAG*, Decade of North American Geology; *GEBCO*, General Bathymetric Chart of the Oceans; *GSC*, Geological Survey of Canada; *HDNO*, Head Department of Navigation and Oceanography (Russia); *IBCAO*, International Bathymetric Chart of the Arctic Ocean; *KMS*, Kort- og Matrikelstyrelsen (Denmark); *NRL*, U.S. Naval Research Laboratory.

regional grid [*Verhoef et al.*, 1996], which covers the entire Arctic plate boundary province. However, its resolution is poor east of 80˚E. We use the GSC and NRL gridded data sets [*Brozena et al.*, 2003] as our primary data sources, noting that the latter offers improved resolution due to its GPS navigation.

Seismicity

The dynamics and spatial distribution of Arctic earthquakes are less well determined than in most ocean basins due to magnitudes close to the detection limit and a poor circum-Arctic seismograph network [*Fujita et al.*, 1990b]. However, the World-Wide Standardized Seismograph Network (WWSSN) allowed *Sykes* [1965] and *Hodgson et al.* [1965] to publish significantly improved Arctic relocations, with error estimates, outlining ridge and transform plate boundary segments. Subsequently, the Arctic seismicity has been updated by *Barazangi and Dorman* [1970], *Wetmiller and Forsyth* [1978], and *Fujita et al.* [1990b], in addition to the routine global epicentre locations from the International Seismological Centre (ISC) and the National Earthquake Information Center of the U.S. Geological Survey (NEIC). Many new seismograph stations, including broadband and arrays, have also improved the data base.

Data Sources

We have examined earthquake epicentre locations north of 72˚N from January 1955 to December 1999 (Figure 1.2). These locations, mostly contributed from the ISC, *Engdahl et al.* [1998] and *Sykes* [1965], are sorted to minimise location errors while still maintaining a reasonable coverage (Table 1.2). The result is an updated and improved seismicity data base, the Arctic Catalogue [*Engen*, 2001].

To supplement the Arctic Catalogue we compiled focal mechanism solutions from mostly large, M_S>5.5, earthquakes and grouped them according to predominant mode of faulting. We gathered solutions both from regional compilations [*Savostin and Karasik*, 1981; *Jemsek et al.*, 1986; *Fujita et al.*, 1990a, b; *Franke et al.*, 2000; *Hicks et al.*, 2000] and from the routinely computed solutions of the NEIC [*Sipkin et al.*, 2000] and the Harvard University centroid–moment tensor project [*Dziewonski et al.*, 2000] (NEIC solutions are available from the World Wide Web at http://wwwneic.cr.usgs.gov/ and Harvard solutions at http://www.seismology.harvard.edu/projects/CMT/). The composite focal mechanism catalogue has a few overlapping sources, yielding up to seven quite different solutions for each event. In such cases we selected the presumably best-determined solution (Table 1.2) by assessing the data quality, inversion procedure, constraints on the nodal planes, and information on hypocentral depth. The NEIC, Harvard and *Jemsek et al.* [1986] solutions are thereby ranked before the others. Noting the small temporal overlap and that the highest ranked solution usually varies both with time and epicentral region, we prefer not to rank the remaining solutions formally.

Elimination of Redundancy

The raw epicentre catalogue contains 12,382 reports, but the many reporting agencies cause a large redundancy. To ensure that each report represents only one event, and that location errors are sufficiently small for a seismological plate boundary analysis, we group multiple reports from the same event and evaluate their constraints (Figure 1.3). The grouping procedure was developed at NORSAR [e.g., *Lindholm and Bungum*, 2000] to account for empirical location uncertainties for each recording year (Table 1.3). Because locations separated by <100 km in location and <20 s

Table 1.2 (below). The Arctic Catalogue of Earthquakes North of 72°N from January 1955 to December 1999[a]

Agency/reference	Events	Period
Arctic Catalogue	**1189**	**1955–99**
1 *Engdahl et al.* [1998]	511	1964–95
Sykes [1965]	42	1955–62
2 ISC	621	1964–99
3 NEIC	6	1962–63
4 Misc.	9	1980–99
Focal mechanism solutions	**137**	**1959–99**
NEIC	9	1988–99
Harvard	91	1977–99
Jemsek et al. [1986]	5	1964–76
Chung and Gao [1997]	1	1987
Franke et al. [2000]	7	1984–94
Avetisov [1993]	1	1987
Stein et al. [1979]	1	1976
Bungum [1977]	1	1976
Savostin and Karasik [1981]	12	1964–75
Cook [1988]	4	1960–73
Sykes and Sbar [1974]	1	1971
Horsfield and Maton [1970]	2	1967
Lazareva and Misharina [1965]	2	1959

[a]Agencies are ranked by number. Focal mechanism solutions include published studies and routinely computed solutions. *ISC*, International Seismological Centre; *NEIC*, National Earthquake Information Center, U.S. Geological Survey.

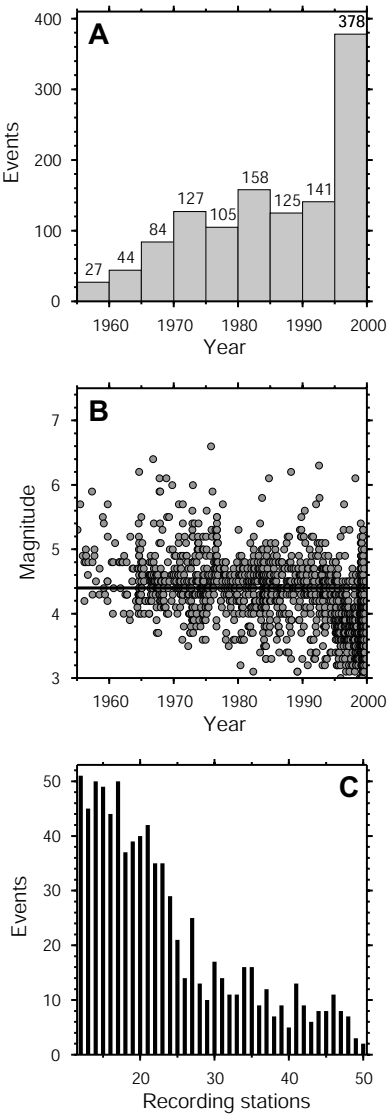

Figure 1.2 (above). Arctic Catalogue statistics. **(A)** Time distribution. **(B)** M_S for the same events. The increased number of events during the 1990s and the stepwise decrease in lower magnitudes reflect the improved coverage and recording performance of the Arctic seismograph network. Horizontal line shows the M_S 4.4 completeness threshold. **(C)** Number of events as a function of number of stations.

in origin time are treated as the same event, even when reported by the same agency, we cannot exclude that some events may have been grouped together. The reports in each group are then sorted qualitatively and the presumed best-constrained location is selected. The ranking favours locations with listed magnitudes; focal depths; location errors; and large numbers of recording stations, so the grouping reduces location errors in the catalogue. The grouping extracted 4551 events, i.e., the average reporting redundancy is 2.72.

Of the catalogues in Table 1.2, *Engdahl et al.* [1998] is given priority because it consists of ISC locations, refined by (1) involving only the ~100,000 best constrained teleseismic records, i.e. locations where stations at epicentral distances >30° have azimuthal coverages >180°; (2) by using the *ak135* radial Earth velocity model [*Kennett et al.*, 1995] which is closer to the true globally averaged Earth structure than is the standard *Jeffreys and Bullen* [1940] model, and; (3) by including later-arriving phases in addition to the first P arrivals used by the ISC. In sum, this treatment yields fewer but less biased locations than the corresponding ISC catalogue [*Engdahl et al.*, 1998]. The *Sykes* [1965] locations, listing location errors and number of recording stations, were assigned the same priority as *Engdahl et al.* [1998] because there is no temporal overlap. The global ISC and NEIC locations further take precedence over regional locations.

Quality Sorting

To obtain a common magnitude reference we convert all local (M_L), body-wave (m_b), and moment (M_W) magnitudes into surface-wave magnitude (M_S) using a simple linear regression [*Lindholm and Bungum*, 2000]. M_S yields the largest proportion of unconverted magnitudes in the catalogue (53%) while being an appropriate magnitude scale for the shallow and moderately large Arctic earthquakes. However, surface waves travelling across the continent–ocean transition (COT) may be considerably affected, both by *Lg* blockage [*Kennett et al.*, 1985; *Mendi et al.*, 1997; *Baumgardt*, 2001] and surface-wave reflections and refractions [*Bungum and Capon*, 1974]. Also, network magnitudes (m_b) may suffer a considerable bias when the number of stations is reduced [*Ringdal*, 1976] and consequently, magnitudes may be both under- and over-estimated for many Arctic events. In this study, however, we consider reliable epicentre locations more important than accurate magnitudes.

Table 1.3. Empirical Grouping Parameters for Processing Arctic Catalogue Epicentre Locations[a]

Period	Same agency		Different agency	
	Time (s)	Distance (km)	Time (s)	Distance (km)
1955–1969	130	200	4000	400
1970–1979	70	150	700	400
1980–1998	40	100	80	300
1999	20	100	40	200

[a]If two locations are within the same time and distance window, they are grouped under the same event. Even locations from the same agency may be grouped (Figure 1.3).

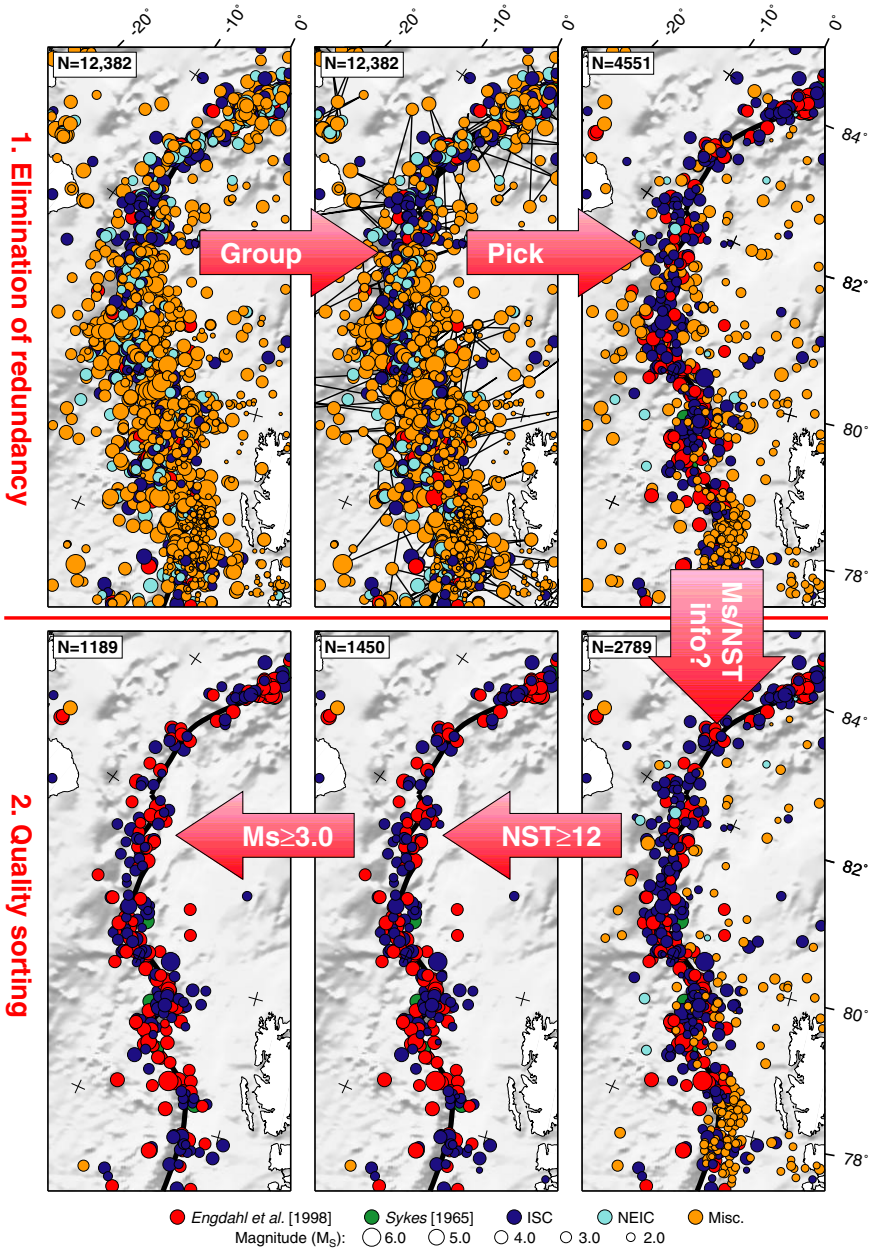

Figure 1.3. The epicentre processing sequence, illustrated in the Spitsbergen Transform System. It includes: (1) grouping of locations according to the criteria in Table 1.3; (2) selection of the presumed best-constrained location in each group (Table 1.2); (3) keeping locations that can be quality evaluated; (4) filtering by number of stations to reduce mean location error (Figure 1.5); and (5) magnitude cut-off to discriminate against artificial sources. Numbers refer to the entire region north of 72°N.

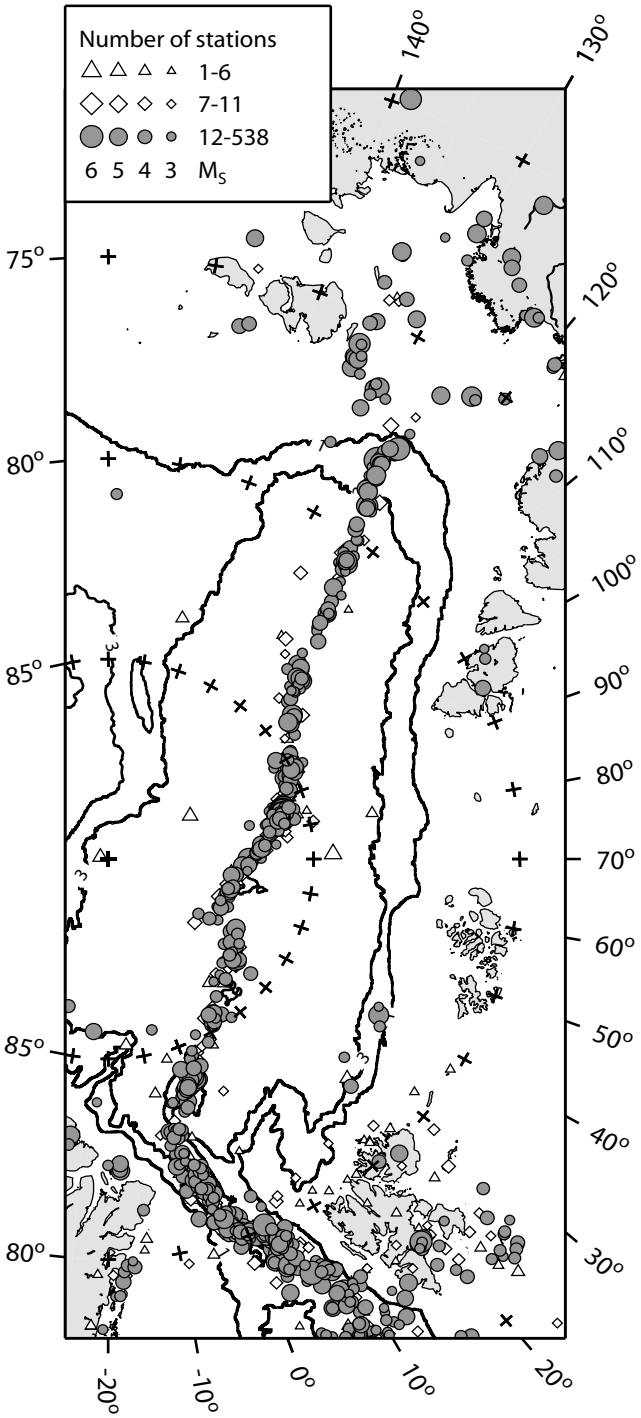

Figure 1.4. Events recorded between 1955 and 1999 by at least one station. For clarity, only $M_S \geq 3.0$ events are shown. The epicentre locations become better confined to the plate boundary as the number of stations increases. Note the defocusing of seismicity at the Eurasia Basin–Laptev Sea transition. Bathymetry, in km, from *Jakobsson et al.* [2000].

A common quality reference is established by keeping only locations with information on both magnitude and number of stations. The remaining 2789 locations are grouped by number of stations in Figure 1.4, which clearly shows that including a larger number of stations decreases the location error. Much of the adjacent and apparently intra-plate seismicity may result from inaccurate location by few stations. Thus, the number of stations is probably the best diagnostic criterion for location accuracy.

Figure 1.4 shows that a regional analysis of the plate boundary requires a better resolution than offered by the grouping procedure alone. We therefore quality evaluate the events further, keeping only events with <15 km location error, comparable to the width of the Gakkel Ridge axial valley [*Jokat et al.*, 1995]. The *Engdahl et al.* [1998] locations indicate that only the 567 locations recorded by >30 stations satisfy this threshold level (Figure 1.5). However, even fewer locations should be kept because the lower-ranked locations (Table 1.2) have greater error estimates, if any.

With these considerations we attempt to balance the trade-off between location errors and number of events in the final catalogue by: retaining events recorded by 12stations, i.e., a mean location error of 10 km for the *Engdahl et al.* [1998] locations (Figure 1.5); and removing M_S<3.0 events to discriminate against artificial sources. The 12-station threshold for well-constrained epicentres compares with the 10-station levels of *Sykes* [1965] and *Engdahl et al.* [1998]. The resulting Arctic Catalogue contains 1189 events (Table 1.2).

Station Distribution and Detectability

The term 'location error' only implies the statistical deviations derived from the differences between observed and modelled travel times [e.g., *Lindholm and Bungum*, 2000]. As such, *Sykes* [1965] and *Engdahl et al.* [1998] reported location uncertainties of about 10 km and 6.0 km, respectively. The *real* errors in earthquake location commonly exceed 15 km in the Arctic region and depend on statistical as well as possible biased errors, which in particular may occur when the station distribution is azimuthally uneven [*Engdahl et al.*, 1998]. For example, Figure 1.6 shows the ISC station distribution for the M_S 4.6 Gakkel Ridge earthquake of 8 June 1968, 00:41:28 GMT, recorded by 73 stations. The distribution is highly biased, and we notice an azimuthal gap of ~150° in Asia.

However, from the station distribution we may also assess the possible temporal and regional detectability variations, using a continuous seismic threshold monitoring technique [*Ringdal and Kværna,* 1989; *Kværna and Ringdal*, 1999]. The method uses the location and instantaneous noise level of each network station and calculates for each point in a geographical grid the three-station network detectability estimate at the 90% confidence level. Figure 1.7 shows results in terms of contoured detectability estimates for the network of the 1968 event (Figure 1.6) compared with similar estimates for the International Data Centre (IDC) network during a quiet period in 2001. For the 1968 event we approximate the station noise levels by subtracting the P-phase magnitude correction factor [*Veith and Clawson*, 1972], at a reference distance of 60°, from the station capability estimates of *Ringdal et al.* [1977]. Note that in 1968 most of the ISC phase readings were from analog data, commonly using different reading procedures for different stations. The 2001 IDC

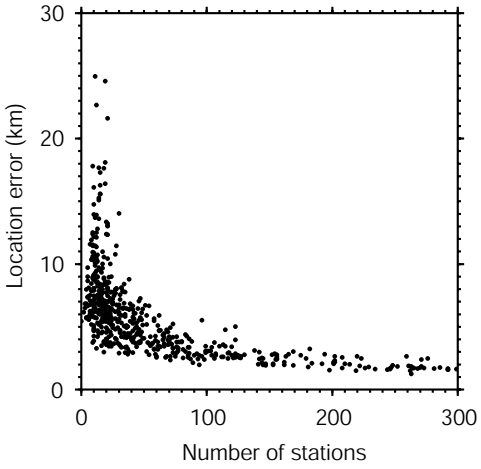

Figure 1.5 (right). Standard error of epicentre locations as a function of number of stations for *Engdahl et al.* [1998] locations north of 72°N. 12 locations plot outside the diagram.

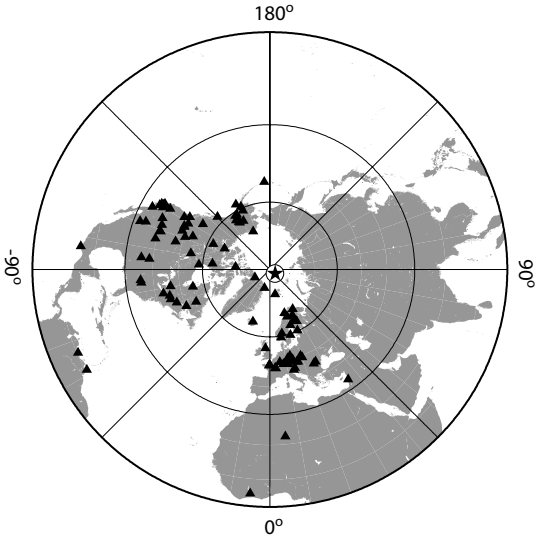

Figure 1.6 (left). Distribution of ISC stations (triangles) recording the M_S 4.6 Gakkel Ridge earthquake (star) of 8 June 1968, 00:41:28 GMT.

network, which also reports to the ISC, uses the most modern array recording technology, including digital signal processing with beam-forming, filtering and signal detection, phase association, and event location. The Arctic plate boundary region is covered by the most sensitive array stations of the IDC network, and therefore in practice determine the capability of the ISC network.

Because recent epicentre locations form the bulk of the Arctic Catalogue (Figure 1.2a), the above results suggest only a small geographical bias. Nonetheless, the high detectability thresholds in the 1968 case contribute to the high, M_S 4.4, completeness threshold of our catalogue. This implies that events of magnitude M_S 3.0–4.4 are under-represented, particularly pre-1970 seismicity in the east. Thus, we expect the western plate boundary provinces to be best constrained by the seismicity. For M_S>4.4 events, however, the observed regional differences in earthquake occurrence are real.

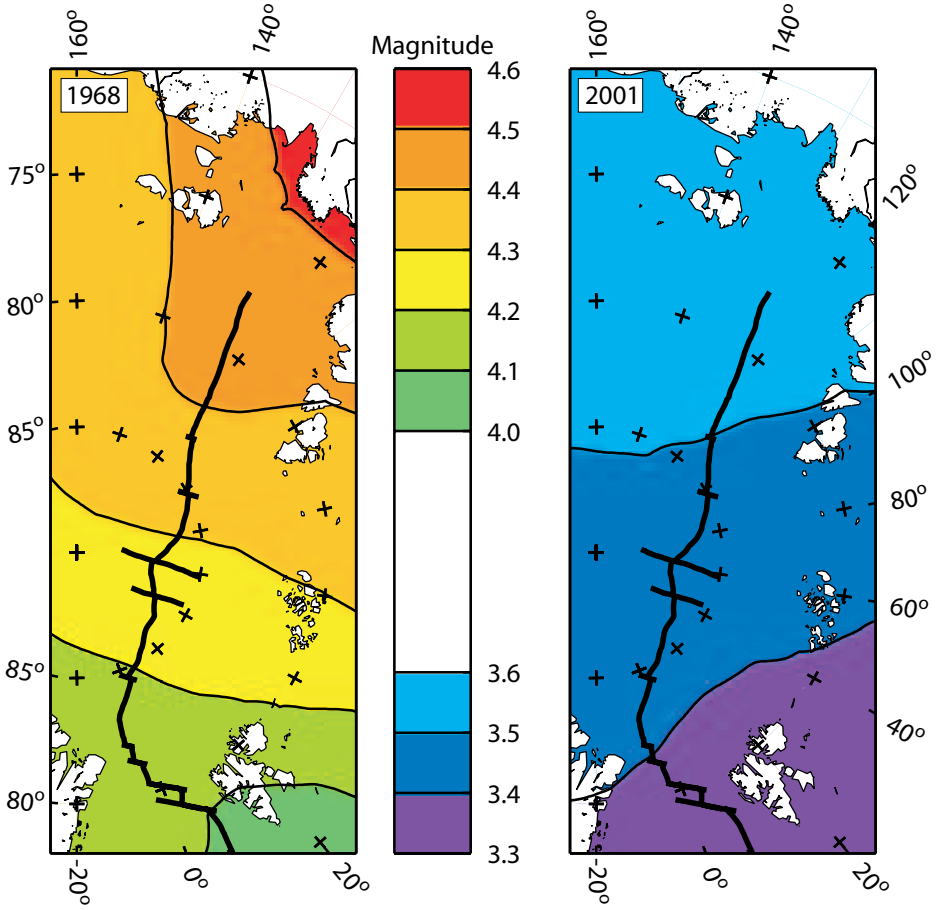

Figure 1.7. Representative detectability thresholds along the Arctic plate boundary for the 8 June 1968, 00:41:28 GMT, event on the Gakkel Ridge, and for a quiet period, 7 July 2001, 09:00–09:10 GMT.

Arctic Mid-Oceanic Ridge

In terms of seismicity and ridge segmentation we divide the Arctic MOR system into four regional plate boundary provinces: the Spitsbergen Transform System; the West and East Gakkel Ridge; and the Laptev Sea (Figures 1.8–1.11). To locate the plate boundary, i.e., the ridge segments and transform faults, we perform an integrated analysis of the seismological and geophysical data within each province. The analysis takes into account that: 1) the largest earthquakes occur at transform faults [*Rundquist and Sobolev*, 2002], while swarms of smaller earthquakes commonly reflect extensional tectonics [*Bergman and Solomon*, 1990]; 2) the axial bathymetry

reflects the rift valley and characteristic transform features such as transform valleys, nodal basins and high inside corners [*Fox and Gallo*, 1984]; 3) free-air gravity anomalies which originate mainly from the sea floor and basement topographies, may be considered as low-pass filtered bathymetry [e.g., *Smith and Sandwell*, 1994], thus enhancing regional features; and 4) the pattern of near-axis magnetic lineations is offset across fracture zones (FZ). In addition, we have constructed synthetic flowlines from the Norwegian–Greenland Sea rotation poles of *Talwani and Eldholm* [1977] to examine the regional consistency of the inferred transform trends and whether they may extend as fracture zones into the adjacent basins.

Snow et al. [2001] interpreted the Eurasia Basin to be composed of ultramafic oceanic crust accreted by very low-degree partial melting. The ultra-slow spreading of the Arctic MOR may increase the role of conductive cooling relative to that of faster-spreading ridges, concentrating magmatism in discrete axial spreading centres which create rough topography [*Cannat et al.*, 1999; *White et al.*, 2001]. In fact, the crust along the Arctic plate boundary is thin, in the range of 1–4 km [*Jackson et al.*, 1982; *Coakley and Cochran*, 1998]. Flowline-striking basement highs may thus represent cooling-induced mantle diapirs or local melting cells near transforms; similarly, seismicity gaps either represent the weak rheology of serpentinised mantle rocks [*Escartín et al.*, 2001] or the absence of transforms. Nevertheless, by applying the above procedure we confidently propose nine transform faults. These continue as fracture zones characterised by offset magnetic lineations and flowline-striking topography (FZ 1–5, 9–12; Figures 1.8–1.10). Hence, the present transforms reflect persistent areas of plate boundary offsets. In the Spitsbergen Transform System, the fracture zones can be traced from the ridge to the continental margins. We also indicate three features which are candidate fracture zones (fz 6–8; Figure 1.9) satisfying some of the selection criteria but having offsets less than the data resolution.

Spitsbergen Transform System (Figure 1.8)

The plate boundary, consisting of short ridge and dextral transform segments with narrow ocean basins between the ridge province and the continental margins, is subdivided into four main structural segments: the Molloy Fracture Zone; the Molloy Ridge; the Spitsbergen FZ; and the Lena Trough. A complex plate boundary has been inferred in this region [*Husebye et al.*, 1975; *Savostin and Karasik*, 1981; *Vogt et al.*, 1981]. However, the *Perry et al.* [1985] bathymetry outlined the two southern transforms and a largely continuous Lena Trough depression farther north, interpreted as the axial valley of a curved and obliquely spreading ridge axis [*Eldholm et al.*, 1990]. We maintain their model except in the Lena Trough where we introduce two, 40- and 32-km-offset, transforms. The location and morphology of the present Spitsbergen Transform System may suggest relatively young features, and we note that:

- The complex ridge and basin morphologies may reflect short-lived changes in plate boundary geometry;
- The system is an area of oblique sea floor spreading between the azimuthally different Knipovich and Gakkel ridges; a similar, but continuous change in azimuth occurs at the Mohn–Knipovich ridge transition farther south [*Eldholm et al.*, 1990];

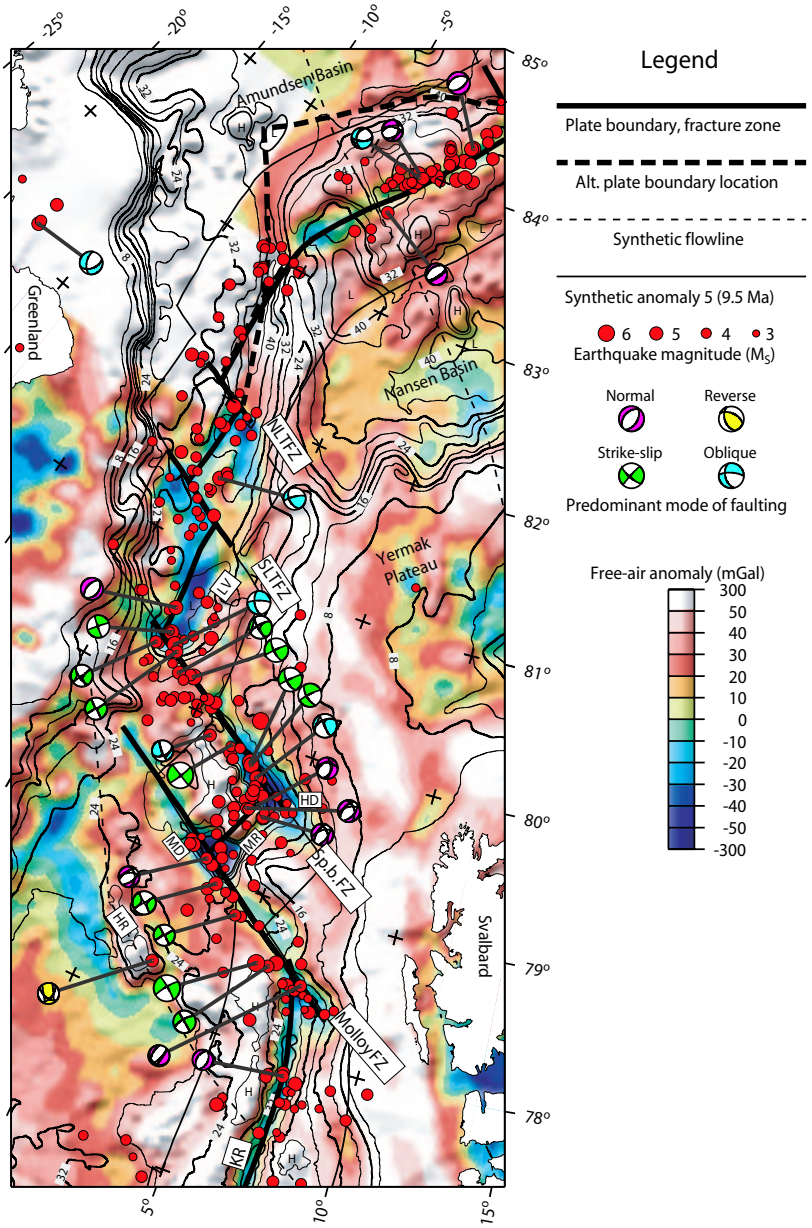

Figure 1.8. Spitsbergen Transform System. IBCAO bathymetry in hundreds of meters from *Jakobsson et al.* [2000], contour interval 0.4 km. Free-air gravity anomalies from *Andersen and Knudsen* [1998] and *Brozena et al.* [2003]. Epicentres from the Arctic Catalogue (Table 1.2). The synthetic fracture zone trends and anomaly 5 position assume symmetric spreading and the Chron 1–5 rotation parameters of *Talwani and Eldholm* [1977]. *HD*, Hayes Deep; *HR*, Hovgård Ridge; *KR*, Knipovich Ridge; *LV*, Lena Valley; *MD*, Molloy Deep; *NLTFZ*, North Lena Trough Fracture Zone; *SLTFZ*, South Lena Trough Fracture Zone.

- Sea floor spreading was delayed with respect to the Eurasia and southern Greenland Sea basins. In fact, extension between Svalbard and NE Greenland was initiated after the change in relative motion between Eurasia and Greenland near the Eocene–Oligocene transition, whereas the onset of sea floor spreading may have occurred as late as in the Middle or Late Miocene [*Kristoffersen*, 1990b; *Eldholm et al.*, 1994].

The northern Knipovich Ridge is spreading obliquely at 0.8–0.9 cm yr^{-1} without large-offset transforms [*Eldholm et al.*, 1990]. The prominent 3.0–3.7-km-deep and ~10-km-wide axial valley approaches the Svalbard continental margin at a low angle, becoming entirely buried by lower slope sediments near the Molloy FZ [*Eldholm and Windisch*, 1974; *Sundvor and Eldholm*, 1979]. By acting as a depositional barrier, the ridge mountains cause a considerable sediment load on the eastern ridge flank and a greater relief west of the axis [*Desimon and Karasik*, 1979; *Vogt*, 1986].

The Molloy FZ is a north-deepening trough that strikes along the present flowline. *Thiede et al.* [1990] interpreted the topography in this area as a ridge–transform intersection (RTI) with a nodal basin, a mantle protrusion and probably a high inside corner. Moreover, they found that the bathymetric trend continues into a depression that may be a relict nodal basin. A flowline-trending, negative free-air anomaly continues onto the Svalbard and Greenland continental margins, terminating at distinct offsets in the margin morphology. The seismicity is focused and most intense near the Molloy Deep, and four NEIC and Harvard focal mechanism solutions show nearly uniform, dextral strike-slip motion.

The 70-km-long Molloy Ridge rises >3.6 km from the adjacent Molloy Deep. It has a clear axial magnetic anomaly and some symmetric lineations that are difficult to date [*Vogt*, 1986]. Four almost identical Harvard focal mechanism solutions show normal faulting with an oblique component. The earthquake activity is high compared to the other plate boundary segments in this province.

The Spitsbergen FZ is in a regional sense similar to the Molloy FZ, although its southern RTI nodal basin, the Hayes Deep [*Thiede et al.*, 1990], is ~1.1 km shallower than the Molloy Deep. The fracture zone bathymetry is well defined, but changes into a 2.5-km-deep saddle to the northwest where the plate boundary continues into the Lena Trough. Therefore we have considered alternative plate boundary geometries, noting that the HDNO bathymetry indicates a trough connecting the Molloy FZ and the Lena Trough parallel to the Spitsbergen FZ. This feature is, however, not evident in the IBCAO bathymetry. We attribute the difference to the choice in contouring rather than inconsistent data bases. The free-air gravity forms a linear low along the fracture zone, most consistent with the IBCAO bathymetry. This trend is also sustained by the earthquake distribution, which is linear and node-concentrated like that of the Molloy FZ. The mode of faulting is transform [*Horsfield and Maton*, 1970; *Savostin and Karasik*, 1981]. Hence, we place the Spitsbergen FZ along the IBCAO bathymetric trend.

We define the Lena Trough as the ~100-km-wide and ~400-km-long deep-water province in the Fram Strait between the Greenland margin and the Yermak Plateau. It comprises several high-relief basement peaks penetrating a variable sediment cover. The ridge province separates the trough into two elongate sub-basins most evident in the HDNO bathymetry, where the southern one is denoted the Lena Valley. We interpret the basins to be underlain by oceanic crust accreted along an

oblique-spreading rift segment. The segment is cut by the South and North Lena Trough FZs, which connect ~4.0-km-deep RTI nodal basins and are associated with flowline-trending basement highs of up to 1 km relief. Despite their small offsets, the bathymetry and gravity signature resembles that of the longer Molloy and Spitsbergen transforms. Farther north the connection to the Gakkel Ridge is problematic due to sparse bathymetric and gravity coverage [*Jakobsson et al.*, 2000; *Brozena et al.*, 2003]. Nonetheless, we infer a curved extension of the northern Lena Trough ridge segment. On the other hand, we cannot rule out another small-offset transform in this area. Parallel magnetic anomalies, though of lower amplitude than on the Gakkel Ridge, are present north of the fracture zone but absent in the south [*Feden et al.*, 1979]. However, the magnetic and bathymetric trends of the rift segment differ, suggesting that the inferred axial valley may be a recent feature which has reduced the offset across the North Lena Trough FZ.

The sea floor spreading becomes more oblique northward in the Lena Trough. The only available focal mechanism solution indicates oblique, transform faulting [*Savostin and Karasik*, 1981]. However, the correlation between the plate boundary location and seismicity is diffuse, with epicentres distributed over the full width of the Lena Trough.

At 83°N the Lena Trough broadens into the Eurasia Basin and the ridge province changes direction to that of the Gakkel Ridge. There is a continuous basin passage into the Amundsen Basin, whereas the entrance to the Nansen Basin is barred by a 20–30-km-wide, spine-shaped high between the Yermak Plateau and the Gakkel Ridge, rising >1.2 km above the basin floor.

Gakkel Ridge

The 1800-km-long Gakkel Ridge divides the Eurasia Basin asymmetrically into two basins: The 350-km-wide and 4.3-km-deep Amundsen Basin is dominated by steep, local basement highs, whereas the 400-km-wide and 3.7-km-deep Nansen Basin shoals gently towards the continental margin (Figure 1.1). In a regional sense the Gakkel Ridge appears continuous, but it may be cut by a number of small-offset transforms [*Karasik*, 1974; *Vogt et al.*, 1979], most of which must have formed post-Chron 13n (33 Ma). The spreading is generally orthogonal, but locally up to 20° oblique, at rates decreasing from 0.7 cm yr^{-1} in the west to 0.3 cm yr^{-1} in the east [*Eldholm et al.*, 1990]. A characteristic kink in ridge trend near 60°E marks a change in geophysical characteristics and the transition from an accentuated to a smoother ridge morphology. The change corresponds to the transform region around FZ 10 (Figures 1.9 and 1.10), which divides the ridge province into two parts.

West Gakkel Ridge (Figure 1.9)

Morphologically, the ~150-km-wide axial province can be divided into three parts by the small-offset, dextral FZ 5 and fz 8. The wide, wedge-shaped ridge province between the northern Lena Trough and FZ 5 was described by *Feden et al.* [1979] as the 'Yermak H-zone'. It comprises elongate troughs comparable in depth to the ~4.0-km-deep rift valley, and its average ~2.8 km depth and a seamount reaching 0.8 km make it shallower than the ridge segments farther east. The IBCAO bathymetry suggests that the plate boundary must either be located in the central ridge province, i.e., >1.5 km shallower than the rift valley in the northern Lena

Trough, or turn around the northern ridge flank (Figures 1.8 and 1.9). On the other hand, the HDNO bathymetry favours the former location, which is also compatible with the potential field data. The relatively high earthquake activity with normal and oblique focal mechanisms also favours a plate boundary within the main ridge province.

In a Chron 13 plate reconstruction, FZ 5 aligns along the eastern flanks of the Yermak Plateau and Morris Jesup Rise, but the signature of the fracture zone beyond magnetic anomaly 5 is weak. Furthermore, the bathymetry may imply overlapping spreading centres, but the seismicity only correlates with that on the northern side. The 16-km, dextral offset is also reflected in the –50 mGal axial free-air anomaly. The axial magnetic anomaly decreases eastward from >1000 nT to ~700 nT across FZ 5.

Between FZ 5 and fz 8 the ridge curves gently and the deep and continuous axial valley consists of 12–15-km-wide [*Jokat et al.*, 1995] and 20–130-km-long troughs, in some places 5 km deep. The axial mountains commonly rise to 1.6–2.8 km, i.e., 1–2 km above the ocean floor and 2–3 km above the axial valley. The axial troughs are separated by sills, clearly imaged as gravity highs, where the valley floor shoals by >1.0 km and flowline-trending highs continue basinward. We base the candidate fzs 6 and 7 mainly on a seismicity cluster that continues off-axis, and a basin-wide magnetic gradient, respectively. The overall earthquake activity along the segment is remarkably low.

At the candidate fz 8 the turn of the axis is similar to that of FZ 5, but the earthquake activity is greater. The normal faulting indicated by a *Jemsek et al.* [1986] focal mechanism solution weakens the argument for a fracture zone, but may in fact be ascribed to complex faulting in the transform zone [*Fox and Gallo*, 1984; *Wolfe et al.*, 1993].

East of fz 8 the plate boundary turns slightly north. From somewhat offset magnetic anomalies, one normal to strike slip focal mechanism solution [*Savostin and Karasik*, 1981] and earthquakes along the flowline we suggest FZ 9. Elsewhere, we are not able to determine whether the axial valley is continuous or composed of ~20-km-long, orthogonally spreading segments. The epicentre distribution does not resolve this question, as the majority of the events are located outside the axial valley. Actually, the seismicity shows a 40-km, left-lateral seismicity offset east of FZ 9 (Figure 1.4), where the axial valley appears continuous.

The 12-km-offset, sinistral FZ 10 marks the transition to the eastern Gakkel Ridge and is associated with a pronounced bathymetric relief of ~4.5 km and flowline-trending highs extending >150 km into the Nansen and Amundsen Basins. The potential field data correlate well with the bathymetry, outlining both the axial offsets and its basinward extension, and one Harvard focal mechanism solution indicates oblique faulting.

East Gakkel Ridge (Figure 1.10)

The sea floor spreading is largely orthogonal along the eastern ~1100 km of the Gakkel Ridge. There is a minor trend change at 115°E, a region in which we infer one transform, FZ 12. The amount of potential field data are poorer than farther west, hence, the plate boundary location is mainly based on seismicity and bathymetry.

The ridge segment between FZs 10 and 12 is gently curved, but with ~10 km dextral offset at FZ 11. In the west, the transition into the East Gakkel Ridge is asso-

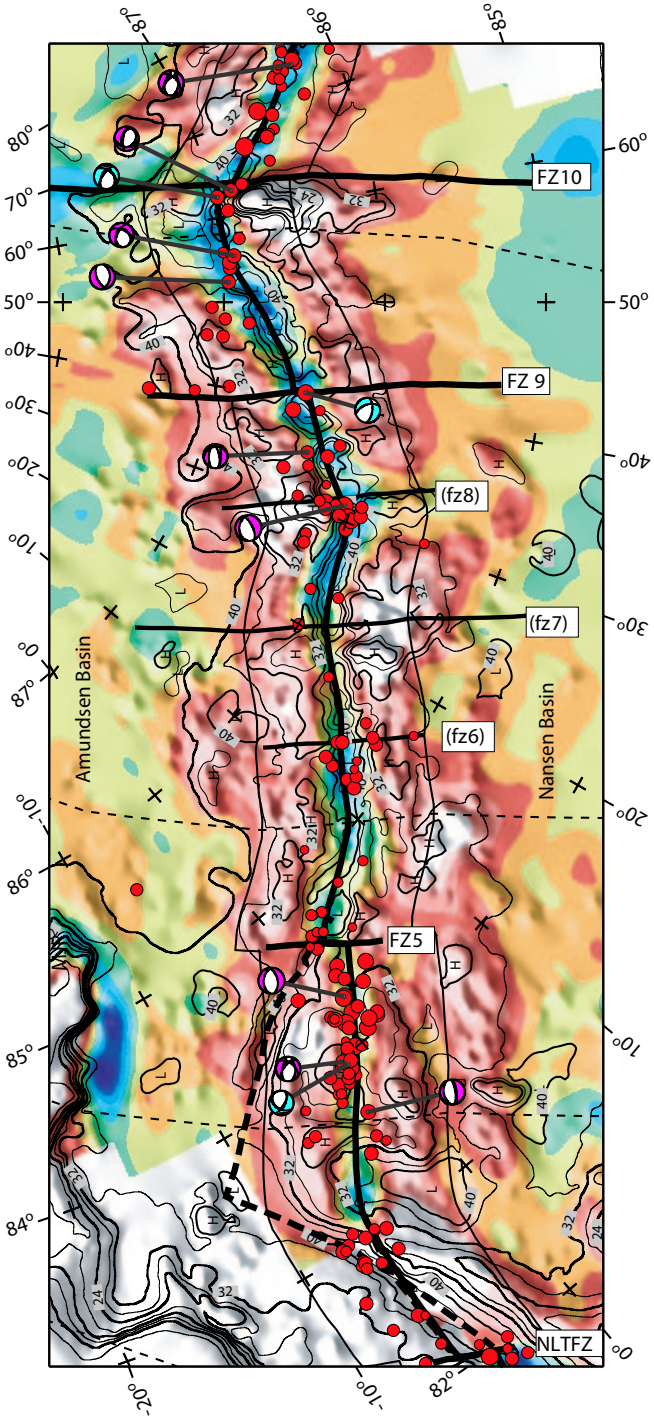

Figure 1.9. West Gakkel Ridge. Legend in Figure 1.8. Candidate fracture zones are annotated in parentheses.

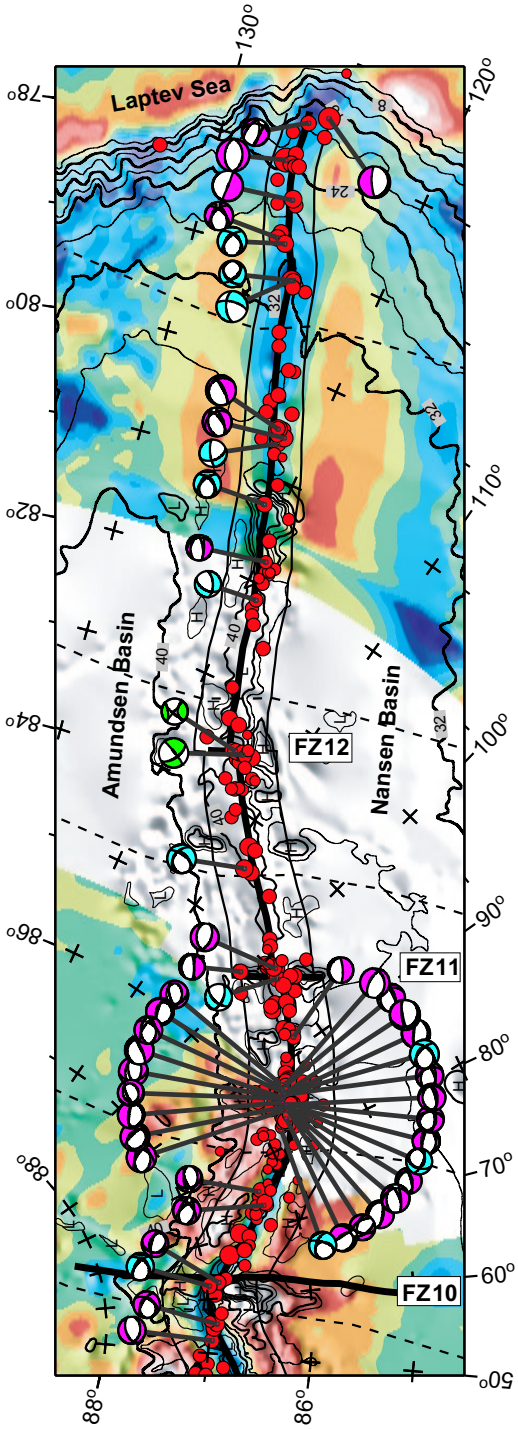

Figure 1.10. East Gakkel Ridge. Legend in Figure 1.8.

ciated with lower ridge mountains, decrease in bathymetric relief, change from an axis-parallel ridge complex to more discrete ridge mountains, low magnetic amplitudes, and a slight focusing of seismicity. The 15–20-km-wide axial valley, at 4.2–4.4 km depth, is fairly continuous with a gentle valley floor. The Nansen Basin ridge flank is covered with sediments forming a 4.0-km-deep basin floor, which is penetrated by 2.3–3.2-km-deep axial peaks. The sediment thickness in the rift valley is 0.1–1.3 km [*Grachev and Karasik*, 1974], compatible with gravity modelling which indicates a crustal thickness of only 1–4 km [*Coakley and Cochran*, 1998]. Although well-developed linear magnetic anomalies exist along the entire ridge province, the axial and Nansen Basin ridge flank anomalies have lower amplitudes than those in the western province.

Local side-scan sonar and gravity surveying during the submarine SCICEX program [*Coakley and Cochran*, 1998] covers the area of a 209-event earthquake swarm, from January to August, 1999, near 85°E. Recent lava flows suggest a relationship between volcanic activity and the swarm [*Müller and Jokat*, 2000; *Edwards et al.*, 2001; *Tolstoy et al.*, 2001], and crustal accretion in the ultra-slow spreading environment is also indicated by 22 Harvard solutions showing predominantly rift focal mechanisms with variably reduced double-couple components [cf. *Julian et al.*, 1998].

FZ 12 is part of a ~150-km-long, high-relief zone with one axial mountain rising to ~1.8 km depth. Magnetic anomalies indicate a ~12-km, dextral offset. Two similar focal mechanism solutions, from Harvard and *Lazareva and Misharina* [1965], show strike-slip motion contrasting with the largely normal mode of faulting on the adjacent ridge segments.

The axial province becomes still narrower and smoother east of FZ 12, and the sediments on the Nansen Basin ridge flank increase to as much as 4–6.5 km thickness near the Laptev Sea margin [*Kristoffersen*, 1990a; *Kim and Verba*, 1995]. An anomalous, 5260-m-deep basin at 81°N is superimposed on the regional ridge bathymetry [*Karasik and Pozdnyakova*, 1979; *HDNO-VNIIOkeangeologia*, 1999]. Landward of the basin, the morphology of the oceanic plate boundary can be traced to ~60 km from the Laptev Sea shelf edge (Figure 1.11). Earthquakes, well confined to the axial region, are relatively abundant along the entire ridge province. The focal mechanism solutions reveal zones of either pure normal or oblique modes of faulting, of which the latter may be attributed to small transforms.

Laptev Sea Continental Margin (Figure 1.11)

The accreting plate boundary terminates at the Laptev Sea continental margin where its prolongation lies within the continental Laptev Rift System. Onshore geological studies and seismic profiles from the shelf show a >500-km-wide zone of horst and graben structures, formed by rift activity from at least the Maastrichtian to present [*Roeser et al.*, 1995; *Drachev et al.*, 1998; *Franke et al.*, 2001]. Some low-angle faults, of which the MV Lazarev Fault appears to be a major detachment zone, continues through the entire 22–30-km-thick crust [*Franke et al.*, 2001]. The maximum thickness of syn- and post-rift sediments is ~13 km in the Ust' Lena Rift in the west,

decreasing to 6–10 km in the eastern grabens [*Drachev et al.*, 1998; *Franke et al.*, 2001]. The main rift structures are clearly imaged by the gravity anomalies.

The earthquake distribution in Figure 1.11 and previous studies [*Chapman and Solomon*, 1976; *Fujita et al.*, 1990a,b; *Franke et al.*, 2000] shows an abrupt change from focused to defocused seismicity where the ridge terminates below the slope sediments. Also, the focal mechanism solutions show that the interchanging normal and oblique faulting along the ridge is replaced by predominantly extensional deformation on the shelf. We propose that these changes reflect the shift from sea floor spreading to continental rifting, possibly related to the transcurrent Khatanga–Lomonosov Fracture [*Drachev et al.*, 1998]. From the seismicity, we conservatively estimate the COT as a <60-km-wide zone near the shelf edge.

The continental seismicity is dominated by normal faulting events with variable strike-slip components. The N–S trend just west of the New Siberian Islands supports the suggestion of *Drachev et al.* [1998] that the Bel'kov–Svyatoi Nos Rift is currently the most active rift segment, but a cluster of events within the East Laptev Horst also corresponds to the Neogene crustal partitioning zone of *Franke et al.* [2001]. Thus, a total offset of 150–200 km between the Gakkel Ridge and the seaward prolongation of the Bel'kov Svyatoi Nos Rift may be accommodated by rift transfer via the NW flank of the East Laptev Horst. We also notice a more diffuse NE–SW trend of predominantly strike-slip events on the western outer shelf, and some earthquake activity east of the New Siberian Islands (Figure 1.4).

Structurally, the present offset along the COT constitutes a sheared margin segment. This setting is in some respects similar to that of the Senja sheared margin off the SW Barents Sea. In particular, both margins were formed along pre-existing mega-lineaments, the Khatanga–Lomonosov Fracture [*Fujita et al., 1990a*] and the De Geer Zone [*Faleide et al.*, 1993], respectively. Long sheared margin segments commonly have a sharp, narrow COT [*Scrutton*, 1982]. Hence, from the analogy with the Senja margin we predict an even narrower COT than indicated by the seismicity. A sharp COT was also indicated by *Franke et al.* [2000], who found increased focal depths and decreased anelastic shear-wave attenuation landward of the continental slope.

The width of the Eurasia Basin decreases only slightly to the east (Figure 1.1), reflecting the decreasing distance to the rotation pole since opening, and linear magnetic anomalies continue to the Laptev Sea continental slope [*Karasik*, 1974]. Structural and seismic data suggest that the ridge axis has migrated relative to the continental rift since the opening of the Eurasia Basin [*Drachev et al.*, 1998]. This may imply that: 1) most of the Eurasia Basin opened almost simultaneously, splitting the narrow Lomonosov Ridge continental block off Eurasia at ~55 Ma [e.g., *Lawver et al.*, 1990]; and 2) a persistent nature, although its length and actual location may have varied, of the Laptev Sea sheared margin segment during this period. In fact, the wide, wedge-shaped margin bathymetry may suggest limited, stepwise landward propagation of the Gakkel Ridge. Relative to the ~55 Ma history of the Eurasia Basin, however, this process appears less efficient than on other active ridge–rift transitions. In the Red Sea, for example, the spreading axis has propagated by steps across closely spaced, pre-rift structures since 4–5 Ma [*Cochran and Martinez*, 1988]. Similarly, the 6 m.y. old Woodlark back-arc basin off Papua New Guinea is wedge-shaped, composed of progressively younger and narrower oceanic segments

towards the COT [*Taylor et al.*, 1999].

A main question is why this ocean–continent setting has persisted for >50 m.y., i.e., why the Eurasia Basin has not propagated farther east. One explanation may relate to anomalous elastic properties of the Laptev Sea crust [*Avetisov*, 1993] where several onshore foldbelts continue offshore [*Drachev et al.*, 1998]. Thus, the continental extension of the plate boundary propagates through heterogeneous lithosphere. In fact, the region may be considered a "locked" zone of initially thickened crust that requires increased extension prior to break-up, hence delaying further opening [*Courtillot*, 1982]. Such settings are described in the North Atlantic, where the total extension of neighbouring passive margin segments and their conjugates may differ by >500 km [*Dunbar and Sawyer*, 1996]. Observed Moho depths and the >10-km-deep Laptev Sea grabens [*Franke et al.*, 2001] indicate that the crust is greatly thinned and near break-up. On the other hand, *Levshin et al.* [2001] found a

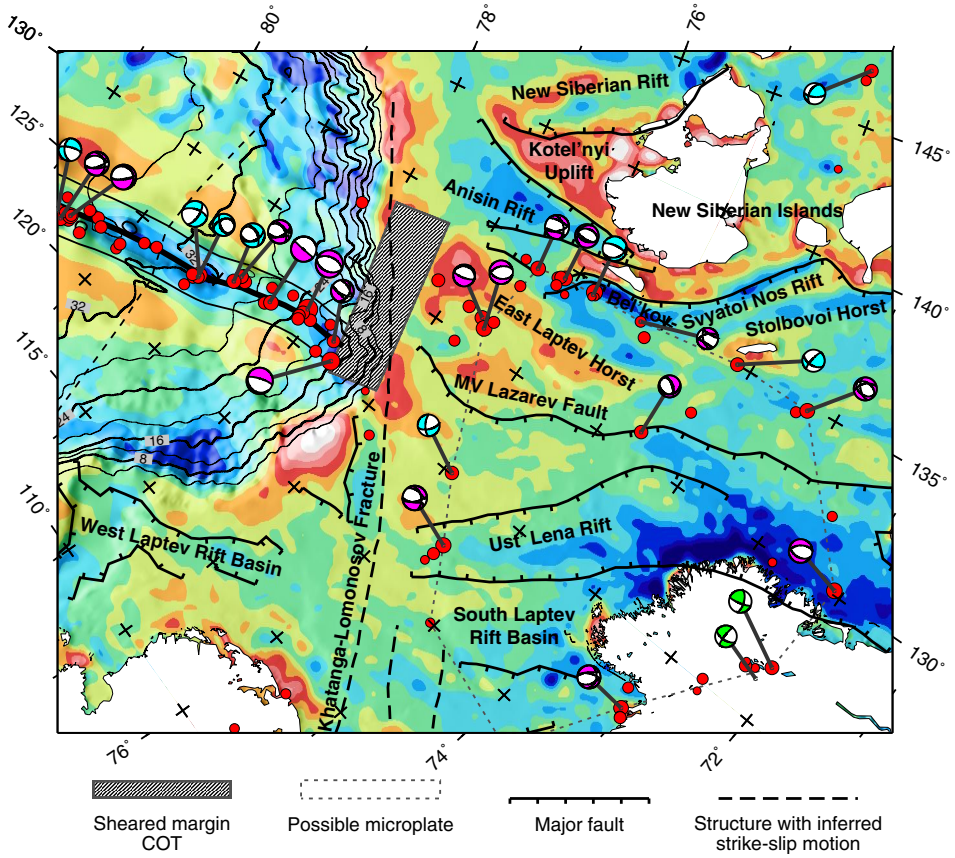

Figure 1.11. East Gakkel Ridge (Figure 1.10) and Laptev Sea margin seismicity. The transition from focused to defocused seismicity occurs within a <60-km-wide COT, and a 150–200-km-long transform is inferred between the ridge axis and the Bel'kov–Svyatoi Nos Rift. The outline of the Laptev Rift System and strike-slip related structures are based on *Drachev et al.* [1998]. The 'Laptev Sea microplate' is proposed by *Avetisov* [1993] and *Franke et al.* [2000].

low-velocity anomaly in the upper mantle beneath the Laptev and East Siberian seas, not coincident with the earthquake activity. Hence, there may be elevated lithospheric temperatures which favour an aseismic deformation component over a much wider zone than the Laptev Rift System proper.

Avetisov [1993] proposed the formation of a future Laptev Sea microplate if the present tectonic setting is maintained, and *Franke et al.* [2000] interpreted the seismicity consistent with a present microplate whose geometry is indicated in Figure 1.11. However, the Laptev Sea crust is extensively faulted both on and off the inferred microplate boundaries. Neotectonism is shown by faults continuing to the sea floor, primarily in the Bel'kov–Svyatoi Nos Rift but also in the Ust' Lena Rift and on the MV Lazarev Fault [*Franke et al.*, 2001]. This is expected from the earthquake distribution and is difficult to reconcile with the proposed microplate geometry. Furthermore, there is little evidence in the seismic profiles of significant crustal thinning along microplate boundaries. We therefore prefer to interpret the observed seismicity trends as reflecting tectonism within a system of migrating rift and transfer zones throughout the Cenozoic.

Inferences from Interplate Seismicity

High oceanic b-values [e.g., *Francis and Porter*, 1971] in the *Gutenberg and Richter* [1949] relationship $\log N = a - bM$ of cumulative number of events N and magnitude M, have been related to low stress in the source region [*Wyss*, 1973]. Using Figure 1.2b and magnitude scaling relations obtained from the Arctic Catalogue, we calculate the Gutenberg–Richter relationship for $M_S \geq 4.0$ in each plate boundary province, except for the sparse events on the Laptev Sea margin where a low b-value is expected [*Scholz*, 1990]. The three oceanic provinces have approximately log-linear distributions above the M_S 4.4 Arctic Catalogue completeness threshold (Figure 1.12). The Spitsbergen Transform System has the lowest b-value, and hence appears to be in a slightly higher state of stress. We ascribe the difference in b-values to the proportion of transforms in each province, noting that magnitude conversion from m_b to M_S yields b-values of ~0.8 for transforms and ~1.5 for ridge segments of the Mid-Atlantic Ridge [*Einarsson*, 1986].

Although the seismicity and bathymetry expressions of the Arctic plate boundary generally agree, there are two significant deviations. One occurs in the Lena Trough where the epicentre distribution is defocused over an area three-to-four times the width of the axial valley (Figure 1.8). The other includes several events north of the central Gakkel Ridge and east of FZ 9 (Figure 1.9), not associated with systematic location errors. We note that slow-spreading ridges, such as the Kolbeinsey Ridge north of Iceland, may respond to small rotation-pole perturbations by propagation, asymmetric spreading and lateral migration [*Appelgate*, 1997]. Thus, an initially continuous axial valley may develop a segmented geometry which is first recorded by the seismicity and later by the bathymetry and potential field anomalies. In fact, the off-axis seismicity near FZ 9 may indicate a recent episode of northward

ridge migration [cf. *Stein et al.*, 1977], a mechanism that must be considered when comparing the wider Nansen Basin with the narrower Amundsen Basin.

In the Lena Trough, the up to 45-year-old locations of the shallow earthquakes may be biased due to the poorly constrained reference Earth models. On the other hand, the defocused seismicity is common to both the Lena Trough and the exceptionally well-defined Knipovich Ridge valley [*Eldholm et al.*, 1990]. The abundant off-axis seismicity along the Knipovich Ridge, in particular, suggests stress release over a wide region. Possibly, this is related to: (1) Migration of the spreading axis [*Sundvor and Eldholm*, 1979; *Vogt*, 1986]; (2) recent construction of glacial fans that have rapidly loaded the adjacent, post-Eocene downfaulted continental margin, enhancing the local stress field [*Byrkjeland et al.*, 2000]; and (3) incipient plate boundary formation east of the ridge [*Savostin and Karasik*, 1981; *Høgden*, 1999]. The first two factors may also contribute in the Lena Trough.

We evaluate the temporal earthquake distribution by calculating the median occurrence time from Figure 1.13 and performing a median test for temporal randomness along the plate boundary [*Lindholm et al.*, 1990]. Under the assumption of a normal distribution, the hypothesis of a random plate boundary seismicity is rejected at 85% level of significance. Hence, the seismicity has a swarm nature, which on other slow-spreading ridges has been related to extension and magmatic intrusion [*Sykes*, 1970; *Bergman and Solomon*, 1990].

The first known Arctic plate boundary swarm, recorded by *Kristoffersen et al.* [1982] on 11–13 May 1979, is not shown in Figure 1.13 because it consisted of micro-earthquakes not reported by the catalogues in Table 1.2. However, the 1999 swarm west of FZ 11 [*Müller and Jokat*, 2000; *Tolstoy et al.*, 2001] is clearly imaged as the single largest cluster of plate boundary earthquakes. The large number of events occurring on a previously almost quiet ridge segment could imply a region of untypical crustal properties and stress build-up. On the other hand, the magnitude–frequency distribution of the swarm has approximately the same b-value as the total Gakkel

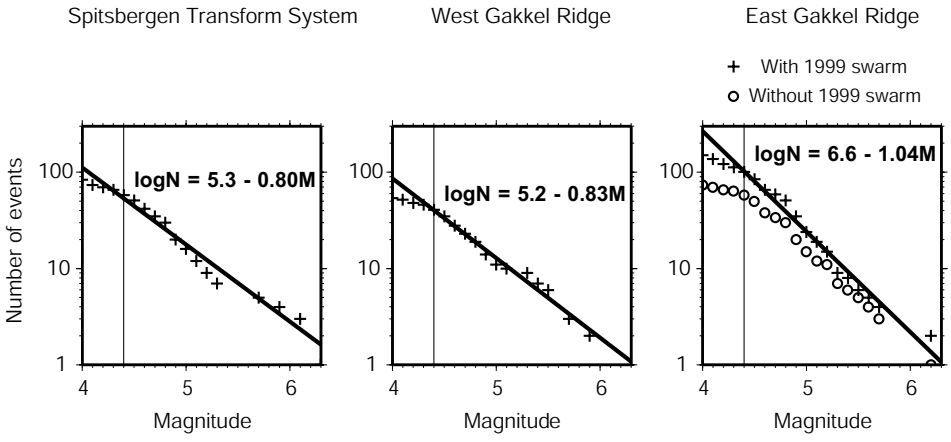

Figure 1.12. Gutenberg–Richter relationship of earthquakes along the Arctic MOR. The 1999 swarm scales with the background distribution, thus it does not appear to reflect anomalous stress release.

Ridge seismicity (Figure 1.12). Hence, the region does not appear to be under anomalous stress but rather reflects a pre-1999 seismicity gap.

All Arctic plate boundary segments are seismically active (Figure 1.13), and the large transforms in the southern Spitsbergen Transform System has the greatest number of events. In this region the seismicity may have a characteristic ~12-year cycle of interchanging high and moderate earthquake activity, the peak activity occurring around 1973, 1985 and 1996. A similar cyclicity is reported for Mohn Ridge earthquakes [*Lindholm et al.*, 1990]. In contrast, the Gakkel Ridge does not exhibit any consistent recurrence pattern. However, an uncommonly long interseismic period is found between FZs 9 and 10, where no large earthquakes have occurred since 1987. The off-axis seismicity in this area (Figure 1.9) may indicate that the ridge segment is an anomalous part of the plate boundary.

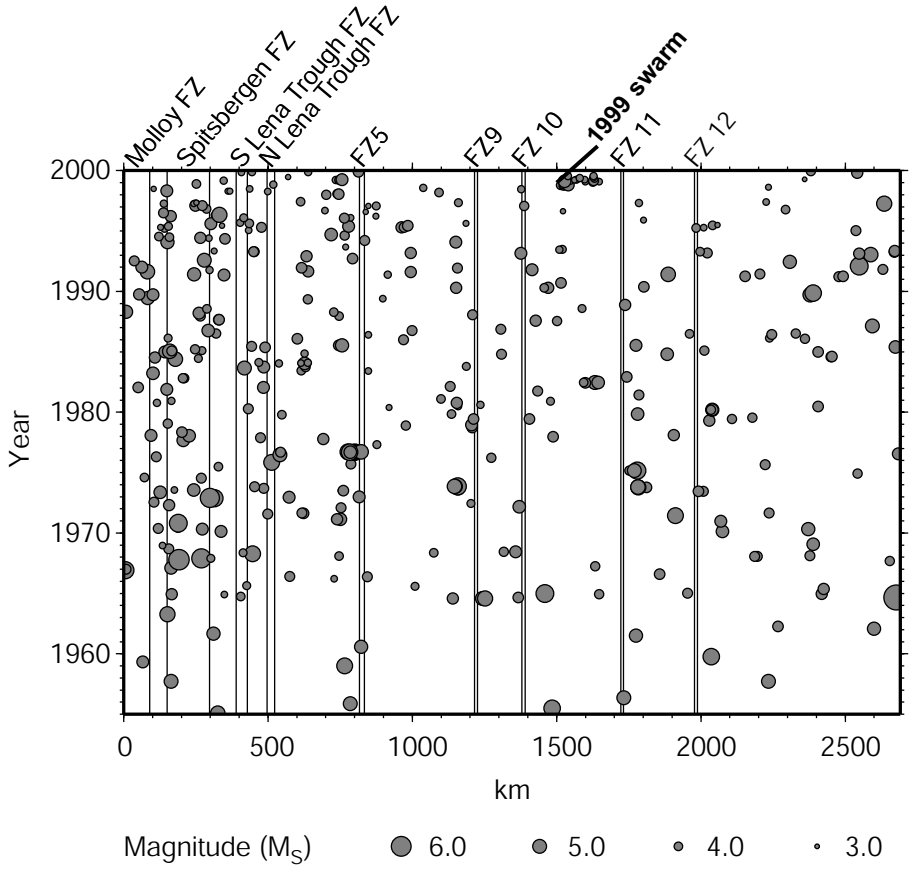

Figure 1.13. Temporal earthquake distribution along the Arctic MOR. Swarms are common along the entire plate boundary. The seismicity is most abundant in the Spitsbergen Transform System where it may indicate earthquake periodicity.

Conclusions

By careful sorting and error evaluation we have compiled an Arctic Catalogue of well-constrained teleseismic epicentre locations, supplemented by focal mechanism solutions. The catalogue is complete for events greater than magnitude M_S 4.4, has only a small geographical bias and a mean location uncertainty of about 10 km. Sorting epicentre locations by number of recording stations proved to be the most efficient and reliable way of reducing location errors.

We have integrated the Arctic Catalogue with available regional bathymetry and potential field data and obtained a model of the seismicity and segmentation of the Arctic plate boundary. Based on the structural setting and geophysical character we suggest a division into four provinces, the Spitsbergen Transform System; the West and East Gakkel Ridge; and the Laptev Sea. The Spitsbergen Transform System is subdivided into (1) the Molloy–Spitsbergen fracture zone and ridge system, where the earthquakes are focused and have uniform focal mechanisms; and (2) the Lena Trough where we infer two small-offset fracture zones. Here the earthquakes are scattered, which we by analogy with the Knipovich Ridge ascribe to an unstable plate boundary and rapid sediment loading.

The linear, 1800-km-long Gakkel Ridge has a very deep, almost continuous axial valley with offsets less than 12 km. The transition between its western and eastern province is marked by FZ 10, where a change in axial trend occurs. The transition is also associated with an eastward decrease of bathymetric and magnetic relief, increased sediment cover, and a slight focusing of the low-level earthquake activity.

At the Laptev Sea continental margin oblique focal mechanisms and a change from focused to defocused seismicity indicates a less than 60-km-wide COT with a left-lateral, 150–200-km-long offset along the Laptev Sea continental margin. The ridge-rift transition may be a persistent feature during the opening of the Eurasia Basin. The longevity of continental rifting landward of the COT may be related to a "locked" zone of initially thickened crust, examples of which are known from the North Atlantic [*Dunbar and Sawyer*, 1996]. The continental seismicity shows two trends reflecting the current activity of a dynamic rift system rather than an incipient microplate.

The Arctic Catalogue and the plate boundary location allow for a seismotectonic analysis of Arctic plate boundary earthquakes. Their magnitude–event distribution indicate high stress in the western plate boundary provinces relative to the East Gakkel Ridge, with b-values typical for oceanic transform faults. The earthquakes are spatially clustered along the plate boundary, and statistical analysis also indicates temporal clustering in swarms. A 209-event swarm near 85°E in 1999 [*Müller and Jokat*, 2000; *Tolstoy et al.*, 2001] is the largest recorded, but is not a special case in terms of stress release. There may be a ~12-year seismicity cycle in the Spitsbergen Transform System, whereas seismicity gaps along the Gakkel Ridge may be of variable duration.

Acknowledgments. The new potential field data were acquired by the U.S. Naval Research Laboratory during the U.S.–Norway Arctic Aerogeophysics Program in 1998–99. We are particularly grateful for having been invited to participate in this project. We thank NORSAR for providing facilities for the senior author, Conrad Lindholm for the raw epicentre data and

processing software, Tormod Kværna for assistance and making available the continuous seismic threshold monitoring software, Filippos Tsikalas for regridding of data and technical support, and Harald Brekke for assistance and support. All figures were generated with the Generic Mapping Tools [*Wessel and Smith*, 1991]. This project was partially funded by the Norwegian Petroleum Directorate.

References

Andersen, O.B., and P. Knudsen (1998), Global marine gravity field from the ERS-1 and Geosat geodetic mission altimetry, *Journal of Geophysical Research, 103*, 8129–8138.

Appelgate, B. (1997), Modes of axial reorganization on a slow-spreading ridge: the structural evolution of Kolbeinsey Ridge since 10 Ma, *Geology, 25*, 431–434.

Avetisov, G.P. (1993), Some aspects of lithospheric dynamics of Laptev Sea, *Physics of the Solid Earth, 29*, 402–412.

Barazangi, M., and J. Dorman (1970), Seismicity map of the Arctic compiled from ESSA, Coast and Geodetic Survey, epicenter data January 1961 through September 1969, *Bulletin of the Seismological Society of America, 60*, 1741–1743.

Baumgardt, D.R. (2001), Sedimentary basins and the blockage of Lg propagation in the continents, *Pure and Applied Geophysics, 158*, 1207–1250.

Bergman, E.A., and S.C. Solomon (1990), Earthquake swarms on the Mid-Atlantic Ridge: products of magmatism or extensional tectonics?, *Journal of Geophysical Research, 95*, 4943–4965.

Brozena, J.M., V.A. Childers, L.A. Lawver, and L.M. Gahagan (2003), New aerogeophysical study of the Eurasia Basin and Lomonosov Ridge: implications for basin development, *Geology, 31*(9), 825–828.

Bungum, H. (1977), Two focal-mechanism solutions for earthquakes from Iceland and Svalbard, *Tectonophysics, 41*, T15–T18.

Bungum, H., and J. Capon (1974), Coda pattern and multipath propagation of surface waves at NORSAR, *Physics of the Earth and Planetary Interiors, 9*, 111–127.

Byrkjeland, U., H. Bungum, and O. Eldholm (2000), Seismotectonics of the Norwegian continental margin, *Journal of Geophysical Research, 105*, 6221–6236.

Cannat, M., C. Rommevaux-Jestin, D. Sauter, C. Deplus, and V. Mendel (1999), Formation of the axial relief at the very slow spreading Southwest Indian Ridge (49° to 69°E), *Journal of Geophysical Research, 104*, 22,825–22,843.

Chapman, M.E., and S.C. Solomon (1976), North American–Eurasian plate boundary in northeast Asia, *Journal of Geophysical Research, 81*, 921–930.

Childers, V.A., D.C. McAdoo, J.M. Brozena, and S.W. Laxon (2001), New gravity data in the Arctic Ocean: comparison of airborne and ERS gravity, *Journal of Geophysical Research, 106*, 8871–8886.

Chung, W.-Y., and H. Gao (1997), The Greenland earthquake of 11 July 1987 and postglacial fault reactivation along a passive margin, *Bulletin of the Seismological Society of America, 87*, 1058–1068.

Coakley, B.J., and J.R. Cochran (1998), Gravity evidence of very thin crust at the Gakkel Ridge (Arctic Ocean), *Earth and Planetary Science Letters, 162*, 81–95.

Cochran, J.R., and F. Martinez (1988), Evidence from the northern Red Sea on the transition from continental to oceanic rifting, *Tectonophysics, 153*, 25–53.

Cook, D.B. (1988), Seismology and tectonics of the North American plate in the Arctic: Northeast Siberia and Alaska, Ph. D. thesis, 250 pp., Michigan State University, East Lansing, Michigan.

Courtillot, V. (1982), Propagating rifts and continental breakup, *Tectonics, 1*, 239–250.

Crane, K., O. Eldholm, A.M. Myhre, and E. Sundvor (1982), Thermal implications for the evolution of the Spitsbergen Transform Fault, *Tectonophysics, 89*, 1–32.

Desimon, A.I., and A.M. Karasik (1979), Some features of bottom relief and sea-floor spreading on the Knipovich Ridge, Arctic Ocean, *Academy of Science of the USSR, Earth Science Section*, English Translation, no. 247, 73–77.

Drachev, S.S., L.A. Savostin, V.G. Groshev, and I.E. Bruni (1998), Structure and geology of the continental shelf of the Laptev Sea, eastern Russian Arctic, *Tectonophysics, 298*, 357– 393.

Dunbar, J.A., and D.S. Sawyer (1996), Three-dimensional dynamical model of continental rift propagation and margin plateau formation, *Journal of Geophysical Research, 101*, 27,845–27,863.

Dziewonski, A.M., G. Ekström, and N.N. Maternovskaya (2000), Centroid–moment tensor solutions for October–December 1999, *Physics of the Earth and Planetary Interiors, 121*, 205–221.

Edwards, M.H., G.J. Kurras, M. Tolstoy, D.R. Bohnenstiehl, B.J. Coakley, and J.R. Cochran (2001), Evidence of recent volcanic activity on the ultraslow-spreading Gakkel Ridge, *Nature, 409*, 808–812.

Einarsson, P. (1986), Seismicity along the eastern margin of the North American Plate, in *The Geology of North America*, vol. M, *The Western North Atlantic Region*, edited by P.R. Vogt and B.E. Tucholke, pp. 99–116, Geological Society of America, Boulder, CO.

Eldholm, O., and C.C. Windisch (1974), Sediment distribution in the Norwegian–Greenland Sea, *Geological Society of America Bulletin, 85*, 1661–1676.

Eldholm, O., A.M. Karasik, and P.A. Reksnes (1990), The North American plate boundary, in *The Arctic Ocean Region*, *The Geology of North America*, vol. L, edited by A. Grantz et al., pp. 171–182, Geological Society of America, Boulder, CO.

Eldholm, O., A.M. Myhre, and J. Thiede (1994), Cenozoic tectono-magmatic events in the Northern Atlantic, potential paleoenvironmental implications, in *Cenozoic Plants and Climates of the Arctic*, *NATO ASI Series,* vol. I 27, edited by M.C. Boulter and H.C. Fischer, pp. 35–55, Springer-Verlag, New York.

Engdahl, E.R., R. van der Hilst, and R. Buland (1998), Global teleseismic earthquake relocation with improved travel times and procedures for depth determination, *Bulletin of the Seismological Society of America, 88*, 722–743.

Engen, Ø. (2001), The Arctic plate boundary, Cand. Scient. thesis, 116 pp., Department of Geology, University of Oslo.

Escartín, J., G. Hirth, and B. Evans (2001), Strength of slightly serpentinized peridotites; implications for the tectonics of oceanic lithosphere, *Geology, 29*, 1023–1026.

Faleide, J.I., E. Vågnes, and S.T. Gudlaugsson (1993), Late Mesozoic–Cenozoic evolution of the south-western Barents Sea in a regional rift–shear tectonic setting, *Marine and Petroleum Geology, 10*, 186–214.

Feden, R.H., P.R. Vogt, and H.S. Fleming (1979), Magnetic and bathymetric evidence for the "Yermak Hot Spot" northwest of Svalbard in the Arctic Basin, *Earth and Planetary Science Letters, 44*, 18–38.

Fox, P.J., and D.G. Gallo (1984), A tectonic model for ridge–transform–ridge plate boundaries, *Tectonics, 104*, 205–242.

Francis, T.J.G., and I.T. Porter (1971), A statistical study of mid-Atlantic Ridge earthquakes, *Geophysical Journal of the Royal astronomical Society, 24*, 31–50.

Franke, D., F. Kruger, and K. Klinge (2000), Tectonics of the Laptev Sea – Moma 'Rift' Region: investigation with seismologic broadband data, *Journal of Seismology, 4*, 99–116.

Franke, D., K. Hinz, and O. Oncken (2001), The Laptev Sea rift, *Marine and Petroleum Geology, 18*, 1083–1187.

Fujita, K., F.W. Cambray, and M.A. Velbel (1990a), Tectonics of the Laptev Sea and Moma rift systems, northeastern USSR, *Marine Geology, 93*, 95–118.

Fujita, K., D.B. Cook, H. Hasegawa, D. Forsyth, and R. Wetmiller (1990b), Seismicity and focal mechanisms of the Arctic region and the North American plate boundary in Asia, in *The Arctic Ocean Region, The Geology of North America*, vol. L, edited by A. Grantz et al., pp. 79–100, Geological Society of America, Boulder, CO.

Grachev, A.F. and A.M. Karasik (1974), *Sea-floor Spreading and Tectonics of the Eurasia Basin: Geotectonic Implications to the Prospects of Mineral Resources on the Arctic Shelf* (in Russian), pp. 19–33, Nauchno-Issledovatel'skiy Inst. Geol. Arktiki, Leningrad.

Gutenberg, B., and C.F. Richter (1949), *Seismicity of the Earth and Associated Phenomena*, 273 pp., Princeton University Press, Princeton.

HDNO-VNIIOkeangeologia (1999), Bottom relief of the Arctic Ocean, scale 1:5,000,000, St. Petersburg.

Hicks, E.C., H. Bungum, and C.D. Lindholm (2000), Stress inversion of earthquake focal mechanism solutions from onshore and offshore Norway, *Norsk Geologisk Tidsskrift, 80*, 235–250.

Hodgson, J.H., M. Båth, H. Jensen, A. Kvale, N.A. Linden, L.M. Murphy, N.V. Shebalin, E. Tryggvason, and E. Vesanen (1965), Seismicity of the Arctic, *Annals of the International Geophysical Year, 30*, 33–65.

Høgden, S. (1999), Seismotectonics and crustal structure of the Svalbard region, Cand. Scient. thesis, 142 pp., Department of Geology, University of Oslo.

Horsfield, W.T., and P.I. Maton (1970), Transform faulting along the De Geer Line, *Nature, 226*, 256– 257.

Husebye, E.S., H. Gjøystdal, H. Bungum, and O. Eldholm (1975), The seismicity of the Norwegian and Greenland Seas and adjacent continental shelf areas, *Tectonophysics, 26*, 55–70.

Jackson, H.R., I. Reid, and R.K.H. Falconer (1982), Crustal structure near the Arctic mid-ocean ridge, *Journal of Geophysical Research, 87*, 1773–1783.

Jakobsson, M. (2000), Mapping of the Arctic Ocean: Bathymetry and Pleistocene paleoceanography, Ph. D. thesis, 94 pp., Department of Geology and Geochemistry, Stockholm University.

Jakobsson, M., N.Z. Cherkis, J. Woodward, R. Macnab, and B.J. Coakley (2000), New grid of Arctic bathymetry aids scientists and mapmakers, *Eos, Transactions, AGU, 81*, 89–96.

Jeffreys, H., and Bullen, K.E. (1940), *Seismological Tables*, 50 pp., British Association for the Advancement of Science, London.

Jemsek, J.P., E.A. Bergman, J.L. Nabelek, and S.C. Solomon (1986), Focal depths and mechanisms of large earthquakes on the Mid-Arctic Ridge system, *Journal of Geophysical Research, 91*, 13,993–14,005.

Johnson, G.L., D. Monahan, G. Grønlie, and L. Sobczak (1979), General Bathymetric Chart of the Oceans (GEBCO), Sheet 5.17, scale 1:6,000,000, Canadian Hydrographic Service, Ottawa.

Jokat, W., E. Weigelt, Y. Kristoffersen, T. Rasmussen, and T. Schöne (1995), New geophysical results from the south-western Eurasian Basin (Morris Jesup Rise, Gakkel Ridge, Yermak Plateau) and the Fram Strait, *Geophysical Journal International, 123*, 601–610.

Jones, M.T., A.R. Tabor, and P. Weatheral (1994), GEBCO Digital Atlas [CD-ROM], British Oceanographic Data Centre, Birkenhead, UK.

Julian, B.R., A.D. Miller, and G.R. Foulger (1998), Non-double-couple earthquakes: 1. Theory, *Reviews of Geophysics, 36*, 525–549.

Karasik, A.M. (1974), The Eurasia Basin of the Arctic Ocean in terms of plate tectonics (in Russian), in *Problems in Geology of the Polar Regions of the World*, edited by V.M. Lazurkin et al., pp. 23–31, NIRDA, Leningrad.

Karasik, A.M., and R.A. Pozdnyakova (1979), Basement depth versus its age in Eurasian Basin, Arctic Ocean, *Doklady Akad. Nauk SSSR, 248*, 169–174.

Kennett, B.L.N., S. Gregersen, S. Mykkeltveit, and R. Newmark (1985), Mapping of crustal heterogeneity in the North Sea basin via the propagation of Lg-waves, *Geophysical Journal of the Royal astronomical Society, 83*, 299–306.

Kennett, B.L.N., E.R. Engdahl, and R. Buland (1995), Constraints on seismic velocities in the Earth from traveltimes, *Geophysical Journal International, 122*, 108–124.

Kim, V.I., and V.V. Verba (1995), The geological structure of the Laptev Shelf and adjacent parts of the Eurasian Subbasin (in the context of planned drilling), in *Russian–German Cooperation: the Laptev Sea System*, edited by H. Kassens et al., *AWI Reports on Polar Research, 176*, 383–387.

Kovacs, L.C., G.L. Johnson, S.P. Srivastava, P.T. Taylor, and P.R. Vogt (1990), Residual magnetic anomaly chart of the Arctic Ocean region, in *The Arctic Ocean Region*, *The Geology of North America*, vol. L, edited by A. Grantz et al., Plate 4, Geological Society of America, Boulder, CO.

Kristoffersen, Y. (1990a), Eurasia Basin, in *The Arctic Ocean Region*, *The Geology of North America*, vol. L, edited by A. Grantz et al., pp. 365–378, Geological Society of America, Boulder, CO.

Kristoffersen, Y. (1990b), On the tectonic evolution and paleoceanographic significance of the Fram Strait gateway, in *Geological History of the Polar Oceans: Arctic versus Antarctic*, *NATO ASI Series*, vol. C 308, edited by U. Bleil and J. Thiede, pp. 63–76, Kluwer Academic Publishers, Dordrecht, Netherlands.

Kristoffersen, Y., E.S. Husebye, H. Bungum, and S. Gregersen (1982), Seismic investigations of the Nansen Ridge during the FRAM I experiment, *Tectonophysics, 82*, 57–68.

Kværna, T. and F. Ringdal (1999), Seismic threshold monitoring for continuous assessment of global detection capability, *Bulletin of the Seismological Society of America, 89*, 946–959.

Lawver, L.A., R.D. Müller, S.P. Srivastava, and W. Roest (1990), The opening of the Arctic Ocean, in *Geological History of the Polar Oceans: Arctic versus Antarctic*, *NATO ASI Series*, vol. C 308, edited by U. Bleil and J. Thiede, pp. 29–62, Kluwer Academic Publishers, Dordrecht, Netherlands.

Laxon, S., and D. McAdoo (1994), Arctic Ocean gravity derived from ERS-1 satellite altimetry, *Science, 265*, 621–624.

Laxon, S., and D. McAdoo (1998), Satellites provide new insights into polar geophysics, *Eos, Transactions, AGU, 79*, 69–74.

Lazareva, A.P., and L.A. Misharina (1965), Stresses in earthquake foci in the Arctic seismic belt, *Izvestiya, Academy of Science of the USSR, Physics of the Solid Earth*, English Translation, *1*, 84–87.

Levshin, A.L., M.H. Ritzwoller, M.P. Barmin, A. Villaseñor, and C.A. Padgett (2001), New constraints on the arctic crust and uppermost mantle: surface wave group velocities, Pn, and Sn, *Physics of the Earth and Planetary Interiors, 123*, 185–204.

Lindholm, C.D., and H. Bungum (2000), Probabilistic seismic hazard: a review of the seismological frame of reference with examples from Norway, *Soil Mechanics and Earthquake Engineering, 20*, 27–38.

Lindholm, C.D., J. Havskov, and M.A. Sellevoll (1990), Periodicity in seismicity: examination of four catalogs, *Tectonophysics, 191*, 155–164.

Mendi, C.D., B.O. Ruud, and E.S. Husebye (1997), The North Sea Lg-blockage puzzle, *Geophysical Journal International, 130*, 669–680.

Müller, C., and W. Jokat (2000), Seismic evidence for volcanic activity discovered in Central Arctic, *Eos, Transactions, AGU, 81*, 265.

Perry, R.K., H.S. Fleming, J.R. Weber, Y. Kristoffersen, J.K. Hall, A. Grantz, G.L. Johnson, N.Z. Cherkis, and B. Larsen (1985), Bathymetry of the Arctic Ocean, map scale 1:4,704,075, *Map and Chart Series, MC-56*, Geological Society of America, Boulder, CO.

Ringdal, F. (1976), Maximum-likelihood estimation of earthquake magnitude, *Bulletin of the Seismological Society of America, 66*, 789–802.

Ringdal, F., E.S. Husebye, and J. Fyen (1977), Earthquake detectability estimates for 478 globally distributed seismograph stations, *Physics of the Earth and Planetary Interiors, 15*, P24–P32.

Ringdal, F., and T. Kværna (1989), A multichannel processing approach to real time network detection, phase association and threshold monitoring, *Bulletin of the Seismological Society of America, 79*, 1927–1940.

Roeser, H.A., M. Block, K. Hinz, and C. Reichert (1995), Marine geophysical investigations in the Laptev Sea and the western part of the East Siberian Sea, in *Russian–German Cooperation: the Laptev Sea System*, edited by H. Kassens et al., *AWI Reports on Polar Research, 176*, 367–377.

Rundquist, D.V., and P.O. Sobolev (2002), Seismicity of mid-oceanic ridges and its geodynamic implications: a review, *Earth Science Reviews, 58*, 143–161.

Savostin, L.A., and A.M. Karasik (1981), Recent plate tectonics of the Arctic Basin and of northeastern Asia, *Tectonophysics, 74*, 111–145.

Scholz, C.H. (1990), *The Mechanics of Earthquakes and Faulting*, 439 pp., Cambridge University Press, Cambridge.

Scrutton, R.A. (1982), Crustal structure and development of sheared passive continental margins, in *Dynamics of Passive Margins, Geodynamics Series*, vol. 6, edited by R.A. Scrutton, pp. 133–140, American Geophysical Union, Washington D.C.

Sipkin, S.A., C.G. Bufe, and M.D. Zirbes (2000), Moment tensor solutions estimated using optimal filter theory: global seismicity, 2000, *Physics of the Earth and Planetary Interiors, 122*, 147–159.

Smith, W.H.F., and D.T. Sandwell (1994), Bathymetric prediction from dense satellite altimetry and sparse shipboard bathymetry, *Journal of Geophysical Research, 99*, 21,803–21,824.

Snow, J., E. Hellebrand, W. Jokat, and R. Mühe (2001), Magmatic and hydrothermal activity in Lena Trough, Arctic Ocean, *Eos, Transactions, AGU, 82*, 193–198.

Stein, S., H.J. Melosh, and J.B. Minster (1977), Ridge migration and asymmetric sea-floor spreading, *Earth and Planetary Science Letters, 36*, 51–62.

Stein, S., N.H. Sleep, R.J. Geller, S.-C. Wang, and G.C. Kroeger (1979), Earthquakes along the passive margin of eastern Canada, *Geophysical Research Letters, 6*, 537–540.

Sundvor, E., and O. Eldholm (1979), The western and northern margin off Svalbard, *Tectonophysics, 59*, 239–250.

Sykes, L.R. (1965), The seismicity of the Arctic, *Bulletin of the Seismological Society of America, 55*, 519–536.

Sykes, L.R. (1970), Earthquake swarms and sea-floor spreading, *Journal of Geophysical Research, 75*, 6598–6611.

Sykes, L.R., and M.L. Sbar (1974), Focal mechanism solutions of intraplate earthquakes and stresses in the lithosphere, in *Geodynamics of Iceland and the North Atlantic Area*, edited by L. Kristjansson, pp. 207–224, D. Reidel, Boston.

Talwani, M., and O. Eldholm (1977), Evolution of the Norwegian–Greenland Sea, *Geological Society of America Bulletin, 88*, 969–999.

Taylor, B., A.M. Goodliffe, and F. Martinez (1999), How continents break up: insights from Papua New Guinea, *Journal of Geophysical Research, 104*, 7497–7512.

Thiede, J., S. Pfirman, H.-W. Schenke, and W. Reil (1990), Bathymetry of Molloy Deep: Fram Strait between Svalbard and Greenland, *Marine Geophysical Researches, 12*, 197–214.

Tolstoy, M., D.R. Bohnenstiehl, M.H. Edwards, and G.J. Kurras (2001), Seismic character of volcanic activity at the ultraslow-spreading Gakkel Ridge, *Geology, 29*, 1139–1142.

Veith, K.F., and G.E. Clawson (1972), Magnitude from short-period P-wave data, *Bulletin of the Seismological Society of America, 62*, 1927–1940.

Verhoef, J., W.J. Roest, R. Macnab, J. Arkani-Hamed, and members of the Project Team (1996), Magnetic anomalies of the Arctic and North Atlantic Oceans and adjacent land areas, *Open File 3125b*, Geological Survey of Canada, Dartmouth, Nova Scotia.

Vogt, P.R. (1986), Geophysical and geochemical signatures and plate tectonics, in *The Nordic Seas*, edited by B.G. Hurdle, pp. 413–662, Springer-Verlag, New York.

Vogt, P.R., P.T. Taylor, L.C. Kovacs, and G.L. Johnson (1979), Detailed aeromagnetic investigation of the Arctic Basin, *Journal of Geophysical Research, 84*, 1071–1089.

Vogt, P.R., R.K. Perry, R.H. Feden, H.S. Fleming, and N.Z. Cherkis (1981), The Greenland–Norwegian Sea and Iceland environment: geology and geophysics, in *The Arctic Ocean, The Ocean Basins and Margins*, vol. 5, edited by A.E.M. Nairn et al., pp. 493–598, Plenum Press, New York.

Weigelt, E. (1998), The crustal structure and sedimentary cover of the Eurasian Basin, Arctic Ocean: Results from seismic and gravity measurements, *AWI Reports on Polar Research, 261*, 127 pp.

Wessel, P., and W.H.F. Smith (1991), Free software helps map and display data, *Eos, Transactions, AGU, 72*, 441, 445–446.

Wetmiller, R.J., and D.A. Forsyth (1978), Seismicity of the Arctic, 1908–1975, in *Arctic Geophysical Review,* Publication 45, edited by J.F. Sweeney, pp. 15–24, Earth Physics Branch, Department of Energy, Mines and Resources, Ottawa, Ontario.

White, R.S., T.A. Minshull, M.J. Bickle, and C.J. Robinson (2001), Melt generation at very slow-spreading oceanic ridges: constraints from geochemical and geophysical data, *Journal of Petrology, 42*, 1171–1196.

Wolfe, C.J., E.A. Bergman, and S.C. Solomon (1993), Oceanic transform earthquakes with unusual mechanisms or locations: relation to fault geometry and state of stress in the adjacent lithosphere, *Journal of Geophysical Research, 98*, 16,187–16,211.

Wyss, M. (1973), Towards a physical understanding of the earthquake frequency distribution, *Geophysical Journal of the Royal astronomical Society, 31*, 341–359.

Paper 2

Paper 2

Seismic stratigraphy and basement structure of the Nansen Basin, Arctic Ocean

Øyvind Engen[1], Jakob Andreas Gjengedal[2,3], Jan Inge Faleide[1], Yngve Kristoffersen[2], and Olav Eldholm[1,4]

1) Department of Geosciences, University of Oslo, Norway
2) Department of Earth Science, University of Bergen, Norway
3) *Now at* Future Exploration AS, Stavanger, Norway
4) *Now at* Department of Earth Science, University of Bergen, Norway

Manuscript submitted to *Geophysical Journal International*

Abstract. About 1100 km of 2-D multi-channel seismic data and 50 wide-angle velocity profiles were acquired from the icebreaker *MV Oden* during the Norwegian expedition to the Nansen Basin, Yermak Plateau and Hinlopen margin in 2001. We analyse and model these data to establish a regional seismic stratigraphic framework consistent with sparse previous surveys. High-relief oceanic crust with average velocity 4.1 km s^{-1} is successively filled in by four main turbidite units with typical velocities 2.3, 2.2, 1.9 and 1.8 km s^{-1}. The large velocity and reflection contrast between units 2 and 3 is tentatively dated by basement onlap and sedimentation rates to a Late Miocene (~10 Ma) paleoceanographic event such as the opening of the Fram Strait. The youngest unit, corresponding to prograding sequences on the Hinlopen margin and the onset of major slope failure, may be linked to intensified glacio-fluvial drainage and shelf outbuilding at 2.3 Ma. Integrating new and pre-existing seismic data with mantle Bouguer anomalies and re-identified magnetic anomalies, we interpret the Hinlopen margin as a Paleocene–Early Eocene sheared margin segment including a steep fault at the continent–ocean transition. The current magmatic provinces along the Gakkel Ridge may have been established at Chron 5 times (9.8 Ma) although individual magmatic centres may have originated before Chron 18 (39.9 Ma).

Keywords: Seismic modelling; Seismic velocities; Marine sediments; Crustal structure; Arctic Ocean; Gakkel Ridge

Introduction

The ~4-km-deep Nansen Basin between the Gakkel Ridge and the Barents–Kara continental margin (Figure 2.1) is underlain by oceanic crust accreted along the boundary between the Eurasian and the North American plates [*Karasik*, 1968; *Vogt*

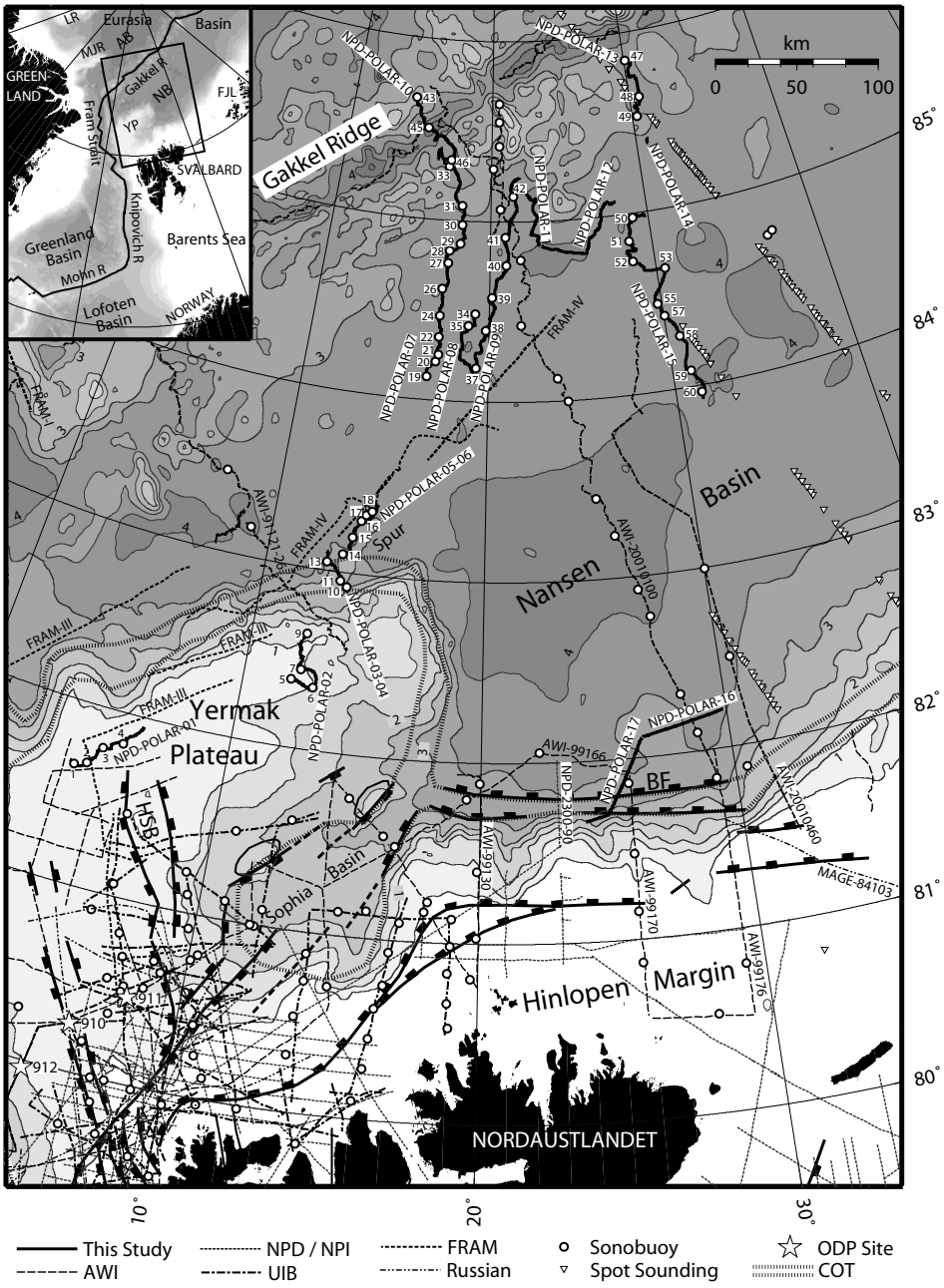

et al., 1979]. To the west the basin is bounded by the Yermak Plateau north of Svalbard and the oblique ridge province extending from the Fram Strait region. The oldest identified magnetic isochron in the Norwegian–Greenland Sea is Chron 24n.3n near the Paleocene–Eocene transition [*Talwani and Eldholm*, 1977; *Tsikalas et al.*, 2002] whereas the Nansen Basin may have been spreading since Chron 25 times [*Kristoffersen*, 1990; *Brozena et al.*, 2003]. Throughout its spreading history, the Nansen Basin has been proximal to plate rotation poles and spread at slow to ultraslow rates [*Vogt et al.*, 1979].

The surface-ship geophysical coverage of the Nansen Basin and the adjacent continental slopes is poor because of perennial sea-ice (Figure 2.1 and Table 2.1), whereas airborne surveying has provided evenly spaced magnetic and gravity profiles [*Vogt et al.*, 1979; *Brozena et al.*, 2003]. Bathymetry and sediment thickness in previously unsurveyed locations are currently being mapped by a Norwegian program aimed at delineating the legal outer shelf limit under the United Nations Convention on the Law of the Sea. The program included a seismic survey in the autumn of 2001 when multi-channel seismic (MCS) and wide-angle sonobuoy (SB) profiles were acquired by the Norwegian Petroleum Directorate (NPD) and the Universities of Bergen and Oslo from the icebreaker *MV Oden* (Figure 2.1). The results from the expedition are presented in two papers. *Gjengedal et al.* [in prep.] document the acquisition and processing of icebreaker seismic data and discuss sedimentary features of the Yermak Plateau. In this paper we determine sediment thicknesses in the Nansen Basin, derive a regional seismic stratigraphy, and propose refined geodynamic constraints from integrated analysis of airborne potential field [*Brozena et al.*, 2003] and the new seismic data.

Sediment Thickness from Seismic Data

While important seismic datasets from the Arctic Ocean have been acquired by drifting ice stations and later by tandem icebreaker operations [e.g., *Kristoffersen and Husebye*, 1985; *Jokat et al.*, 1994], the use of a single icebreaker offers an acceptable balance between data quality and operating costs [*Kristoffersen*, 1997; *Grantz et al.*, 2004]. We collected MCS profiles while icebreaking using robust towing

Figure 2.1 (opposite). Seismic data and major structures in the western Nansen Basin and Yermak Plateau region. IBCAO bathymetry [*Jakobsson et al.*, 2000] contoured every 0.5 km. The segment of the Gakkel Ridge shown is the "sparsely magmatic zone" [*Michael et al.*, 2003]. We define the Hinlopen margin as the portion of the Barents–Kara margin west of 35°E. Continent–ocean transition (COT) on the Yermak Plateau from *Engen and Faleide* [2005, this volume]; other structures from *Faleide et al.* [2003]. MCS lines of this study are denoted in the text by number only (e.g., "Line 15" denotes NPD-POLAR-15). *AB*, Amundsen Basin; *AWI*, Alfred Wegener Institute for Polar and Marine Research, Bremerhaven, Germany; *BF*, boundary fault on Hinlopen margin; *FJL*, Franz Josef Land; *HSB*, H. U. Sverdrup Bank; *LR*, Lomonosov Ridge; *MJR*, Morris Jesup Rise; *NB*, Nansen Basin; *NPD*, Norwegian Petroleum Directorate; *NPI*, Norwegian Polar Institute; *ODP*, Ocean Drilling Program; *UIB*, University of Bergen, Norway; *YP*, Yermak Plateau. Polar stereographic projection.

arrangements and a 12-channel, 300 m active-section hydrophone cable without depth control. The seismic source alternated between a pair of 4 l airguns and a more powerful but lower-frequency, single 20 l airgun for improved signal-to-noise ratio during wide-angle measurements [*Gjengedal et al.*, in prep.]. Wide-angle velocity profiles were recorded simultaneously by sonobuoys dropped in open water behind the ship.

Seismic profiling while icebreaking typically results in crooked-line geometry, delayed ghost effects and variable noise. Therefore, tailored midpoint binning and noise editing procedures were applied to the MCS data, followed by standard 2-D processing routines excluding migration [*Gjengedal et al.*, in prep.]. The sonobuoy data were binned, band-pass filtered and scaled before analysis.

Quality of Sonobuoy Data

The processed sonobuoy profiles are 2.5–28.7 km long, with a median length of 11.9 km for the 50 profiles recorded. All profiles show clear direct-wave arrivals and seafloor-reflection hyperbolas, occasionally interrupted by noisy trace sections. Wide-angle reflections appear from the seafloor down to the top of oceanic basement. Whereas 29 profiles contain near-top-basement refractions, 8 profiles show intra-sedimentary refractions. Sub-basement information is provided by 2 refracted arrivals and 4 wide-angle reflections. We would expect more far-offset arrivals from the larger airgun source than from the smaller setup, but we cannot observe any significant differences.

Table 2.1. Seismic Data Base, Western Nansen Basin and Gakkel Ridge (Figure 2.1)[a]

Expedition	Year	Data[b]	Reduction[c]	Vessel(s)[d]	Reference
A01–A03	1965,72,88	SS	–	ILA	*Blinova et al.* [in press]
FRAM-I	1979	SS; A(U)	T-X	DIS; ILA	*Kristoffersen et al.* [1982]
FRAM-III	1981	OBS	T-X; R	DIS; ILA	*Jackson et al.* [1984]
FRAM-IV	1982	MCS; A(U)	τ-p; I	DIS; ILA	*Kristoffersen, Husebye* [1985]; *Duckworth, Baggeroer* [1985]
Sevmorgeologia	1984-88	MCS	–	Ship	*Baturin* [1987]; *Baturin et al.* [1994]
NP-28	1987-88	MCS	–	DIS	*Sorokin et al.* [1998]; *Blinova et al.* [in press]
NPD-2300-90	1990	MCS	–	Ship	*Riis* [1994]
ARCTIC '91	1991	MCS; SB(U)	T-X; R	2×IB	*Jokat et al.* [1995a]; *Weigelt and Jokat* [2001]
ARKTIS-XV/2	1999	MCS; SB(U)	T-X; R	IB	*Geissler and Jokat* [2004]
AMORE 2001	2001	MCS; A(U); SB(U)	T-X; R	2×IB	*Jokat et al.* [2003]; *Jokat and Micksch* [2004]
NPD-POLAR-2001	2001	MCS, SB(U)	T-X; T^2-X^2; R; I	IB	This study

[a]Data from several of these sources have also been compiled by *Jackson et al.* [1990] and *Eiken* [1994].

[b]*A*, Array: *MCS*, multi-channel seismic; *OBH*, ocean-bottom hydrophone; *SB*, sonobuoy; *SS*, spot soundings; *U*, unreversed

[c]*I*, inversion; *R*, ray tracing; τ-*p*, slant stack; *T-X*, slope–intercept

[d]*DIS*, drifting ice station; *IB*, icebreaker; *ILA*, ice-landing aircraft

1-D and 2-D Velocity Models

Traditionally, velocities have been determined from the moveout of seismic arrivals by assuming plane layer interfaces; however, this 1-D assumption is not optimal in areas of high-relief layer boundaries. Ambiguities arise because sonobuoys drift away from the location of deployment and because our unreversed profiles yield only apparent velocities. Assuming that the 2-D MCS and sonobuoy profiles sample in the same plane, we estimated the influence of sonobuoy drift and layer relief by modelling seismic ray paths through layer geometries interpreted from MCS data [*Bruguier and Minshull*, 1997].

The subsurface was first modelled by plane, homogeneous layers where velocities increased stepwise with depth. Profiles displayed as half-scale wiggle plots in the time-offset-domain were interpreted with respect to direct, reflected and refracted arrivals. The refracted arrivals were approximated by straight lines and correlated along tangent reflection hyperbolas to three regional seismic horizons in the MCS profiles. A staircase velocity-depth model was calculated by the slope–intercept method of *Ewing et al.* [1939]. We assigned 1.48 km s^{-1} constant velocity to the water layer and 1.85 km s^{-1} to the sedimentary top-layer if shallow wide-angle reflections were absent. Layer dips were interpreted from the MCS profiles and used for dip correction of apparent velocities. The refraction solution was augmented by reflected arrivals solved by a standard T^2-X^2 algorithm [e.g., *Sheriff and Geldart*, 1995].

We integrated 1-D velocity models and MCS reflector geometries into preliminary velocity layer models along each MCS line. Seismic wave paths through the layers were then modelled by 2-D seismic ray tracing [*Cerveny et al.*, 1977] as implemented in the ray tracing and travel time inversion procedure of *Zelt and Smith* [1992] which allows irregular layer boundaries and random velocity gradients.

The ray tracing involved three main steps. First, we ray traced direct waves and seafloor reflections, learning that <1.48 km s^{-1} water velocities had to be introduced at depths shallower than 2.2 km. A suitable velocity-depth function for seawater was approximated from acoustic measurements aboard drifting ice stations [*Hunkins et al.*, 1969]. The function comprises two layers with linear velocity gradients defined by 1.43 km s^{-1} velocity at the surface, 1.45 km s^{-1} at 0.4 km depth, and 1.50 km s^{-1} at 4.0 km depth. The monotonic velocity increase with depth is typical for ice-covered Arctic seawater unaffected by frontal mixing and summer heating [*Hurdle*, 1986]. Applying this model, 17 of the 50 sonobuoy models matched the observed travel times. The remaining 33 models had travel-time mismatches proportional to sonobuoy offsets, indicating linear drift of buoys along profiles. Mismatches were fitted to observations by adjusting profile bin spacings by 2.5% on the average.

With profiles now drift-corrected, we evaluated the validity of the 1-D velocity models by ray tracing sedimentary and basement arrivals. Earlier straight-line and hyperbolic fits were adjusted in order to accommodate complex moveouts induced by layer relief. If a sonobuoy arrival did no longer tie to its previously assigned MCS horizon, we tied it to a different horizon or ascribed it to 3-D noise and removed it.

Finally, the re-interpreted velocity models were optimised by weighted least-squares travel time inversion. The inversion proceeded layer by layer from the top [*Zelt and Forsyth*, 1994], keeping velocities in the overlying layers fixed and performing an updated depth conversion before inverting the next layer. The

inversion out-put travel time and model misfit values, allowing us to evaluate the non-uniqueness of the chosen velocity model.

In areas of high-relief basement, some top basement refractions were not reproduced by inversion. These velocity models were fitted to observed travel times by trial-and-error velocity adjustment and forward modelling.

Sediment Thickness Uncertainty

The delineation of legal outer shelf limits relies on sediment thickness data and their uncertainties [*Symonds et al.*, 2000]. However, uncertainties of sonobuoy velocities are difficult to quantify because the largest errors arise from the interpretation of arrivals [*Mooney*, 1989]. Such errors are commonly on the order of one seismic wavelength, i.e. 10–20 ms. However, we observe up to 80 ms differences between sonobuoy arrivals and their assigned MCS horizons. We ascribe these errors to ringing in the seismic signal, masking by overlying reflectors, and sonobuoy drift perpendicular to ray paths, implying that modelled ray paths differ from the true ones. For example, our sonobuoys may have sampled >3 km to the side of the MCS profile at far ranges (Figure 2.2). Where the basement relief is really 3-D but assumed to be 2-D, such geometry problems may cause considerable over-fitting of models in order to match observations [*Bruguier and Minshull*, 1997].

Some uncertainty may arise from the model parameterisation, i.e., whether the block model represents the true earth, and whether the data resolve the model at the desired scale. In fact, *Zelt and Zelt* [1998] demonstrated that no 2-D model along a crooked line is consistent with the real earth in the case of basement topography or other lateral velocity variation.

Noting the above limitations, we tested the non-uniqueness of the sediment velocity model along Line 15, which has the thickest sedimentary cover and favourable sonobuoy coverage (Figure 2.3a–b). We isolated the top basement arrivals and modelled travel times while stepwise perturbing sedimentary velocities and the basement horizon (Figure 2.3c). In each step we perturbed all sedimentary velocities and basement picks by the same percentage and depth converted the line using the perturbed velocities and depths. The significance of each perturbation was assessed by an F-test of travel time residuals [*Zelt and Smith*, 1992]. The normalised value χ^2=1 indicates perfect match between model and data; χ^2<<1 over-fitting; and χ^2>>1 unresolved small-scale heterogeneities, geometry problems, or an inaccurate modelling scheme [*Zelt and Forsyth*, 1994]. Our tests indicate χ^2=1 in a trough spanned by –7% and +17% perturbation of the original velocity and –20 and +210 ms perturbation of the original basement horizon (Figure 2.3c). The minimum value corresponds to 80 ms deeper basement and 5% higher sedimentary velocities than in our model. We ascribe this result to refracted waves, known to travel some distance below the basement surface, and not to errors in the original model. If we fix the original basement interpretation, our model fits data within 7% of the original velocity. Because the relation between depth and velocity is linear, this implies 7% uncertainty of sediment thickness.

Substituting the original 1-D velocity values into the final 2-D model and ray tracing again, we obtained sediment thicknesses within the upper uncertainty limit in cases of smooth basement constrained by both reflection and refraction (Figure 2.3d). However, in the high-relief southern end of Line 15, the 1-D solutions over-

estimated basement depths by up to 0.4 km. We may therefore infer that moving from 1-D to 2-D space improves the reliability of the seismic velocity model.

The final 2-D sediment thickness models (Figure 2.4) include four distinct sedimentary layers with typical velocities 1.8, 1.9, 2.2, and 2.3 km s^{-1}. The velocity models have been sampled in sonobuoy deployment positions (Figure 2.1) and are

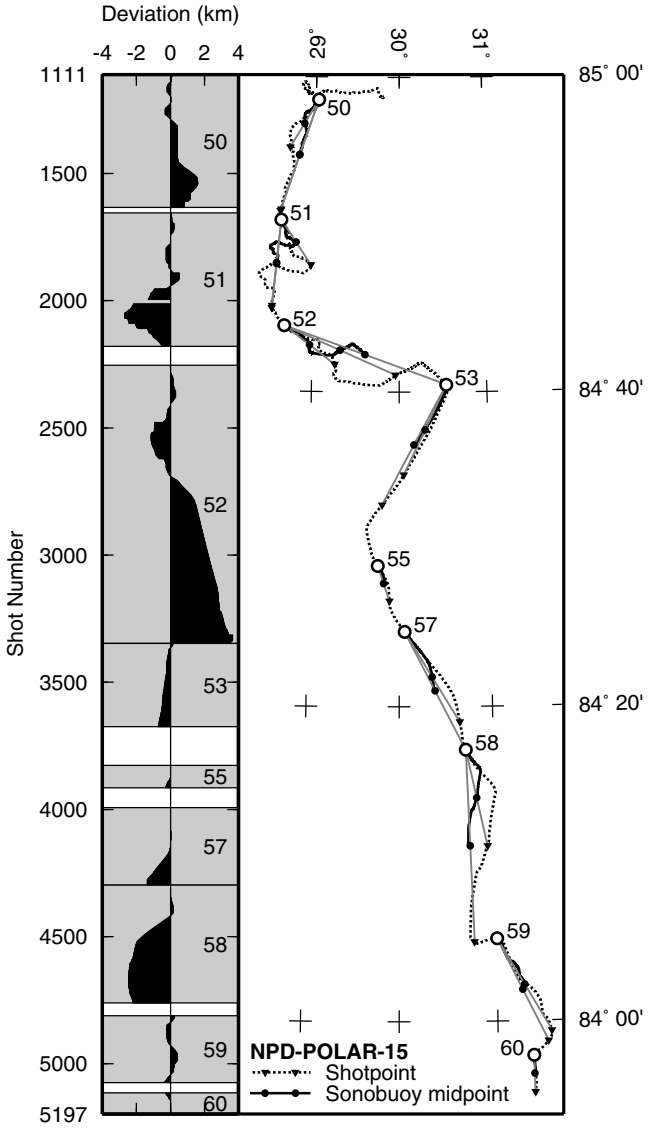

Figure 2.2. Distance between MCS and sonobuoy depth points along Line 15, calculated by neglecting sonobuoy drift and MCS shot–receiver offsets. We have assumed identical coverage of sonobuoy profiles and MCS lines, but in reality, the sonobuoys sampled up to 3.7 km away from the MCS line.

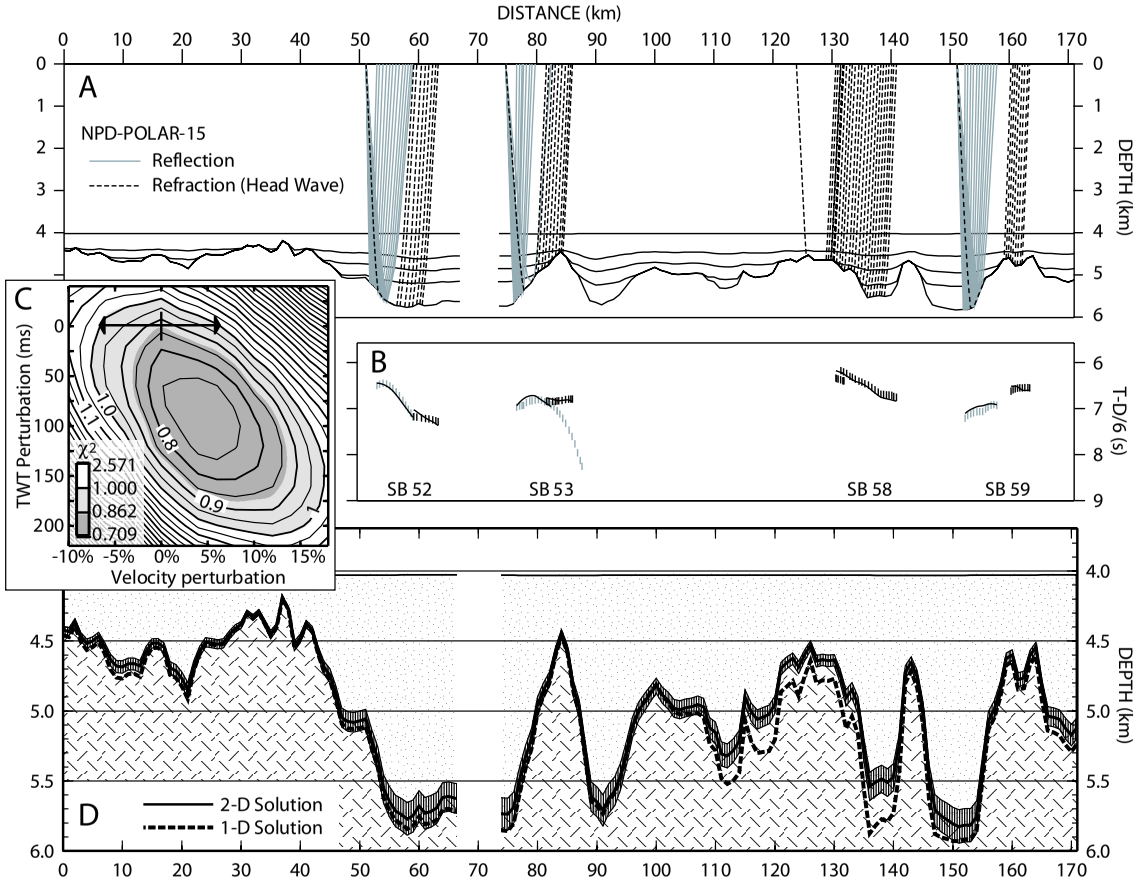

Figure 2.3. Analysis of sediment thickness uncertainty along Line 15. **(A)** Final depth converted MCS line with modelled ray paths used in the analysis. **(B)** Sonobuoy profile readings corresponding to ray paths in (A), displayed at 6 km s^{-1} reduction velocity. Vertical bars indicate travel time picks with uncertainties and bold lines indicate synthetic travel times calculated from (A). **(C)** Sensitivity of model to perturbation of sedimentary velocities and basement depths from (A). χ^2=1 indicate that a range of velocities within 7% of the original value satisfy the travel time picks in (B). **(D)** The resulting 7% sediment thickness uncertainties (stippled area), compared to sediment thickness determined from 1-D and 2-D reduction of sonobuoys.

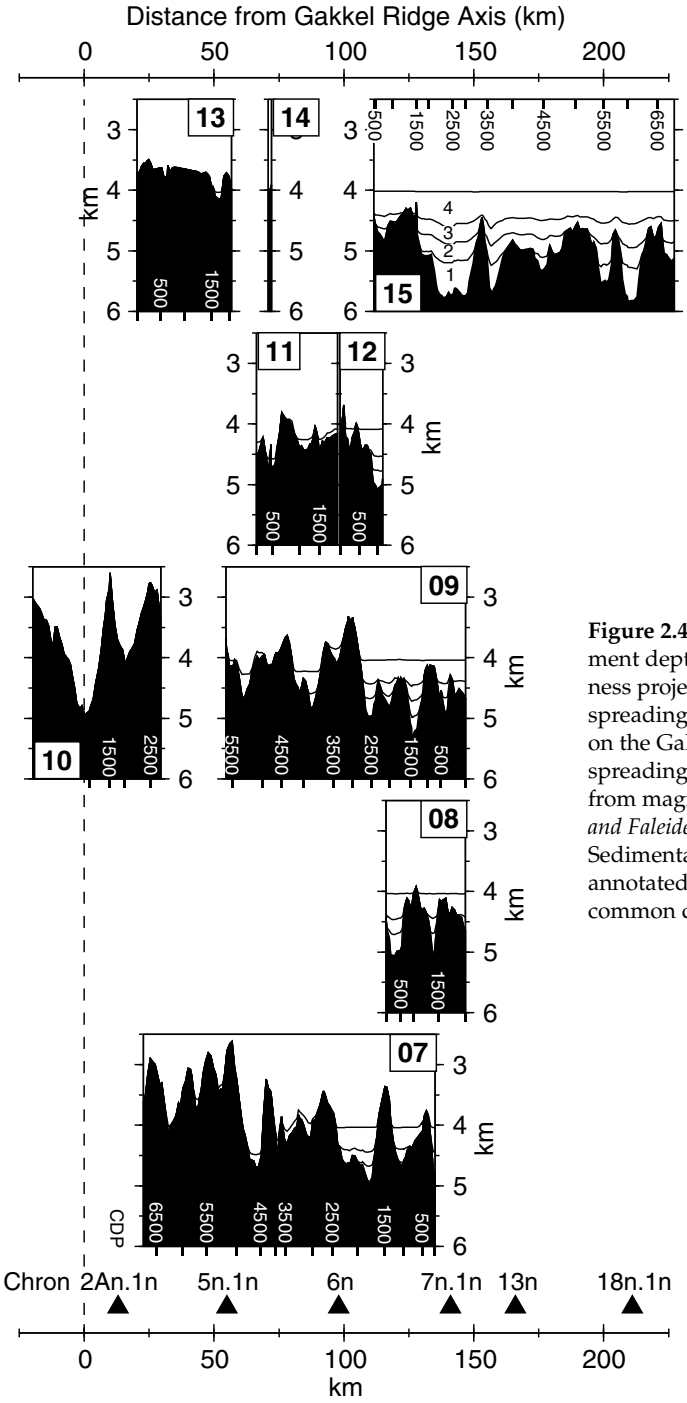

Figure 2.4. Final profiles of basement depth and sediment thickness projected on the Chron 1–5 spreading direction and aligned on the Gakkel Ridge axis. Seafloor spreading isochrons identified from magnetic anomalies [*Engen and Faleide*, 2005, this volume]. Sedimentary units NB-1–NB-4 annotated in Line 15. CDP, common depth point.

given in the Appendix (Table 2.3). On oceanic crust younger than Chron 20 (43.2 Ma), sediment thickness generally increases to the east where a maximum of 1.75±0.12 km is found beneath SB 59 (Figures 2.3c and 2.4).

Sedimentary Units and Basement Structure

The processed MCS data comprise ~1100 km of good-quality sections, sampling to 8 s two-way travel time (TWT) with 25 m trace spacing. Although short intervals are disturbed by noise and variable ghost reflections, we may confidently interpret layered sedimentary rocks and the high-relief basement surface. Because the Nansen Basin has not yet been drilled and regional tie-lines are sparse, we divide the sedimentary section into units based on similar velocities and reflection patterns, rather than into formal seismic sequences [*Mitchum et al.*, 1977]. We correlate our units to previous surveys (Figure 2.5) and group the presentation into the north slope of the Yermak Plateau, the Nansen Basin and Gakkel Ridge, and the Hinlopen margin (Figure 2.1).

North Slope of Yermak Plateau

Lines 3–6 make one transversal and one longitudinal section through a spur projecting NE into the Nansen Basin, at 25° angle with the N plateau flank (Figure 2.1). The spur is made up of conical highs with a diffracted reflection character (Figure 2.6). It shoals to 2.1 km depth, or 1.9 km above the adjacent basin floor, and has near-top basement velocities of 3.2–4.1 km s^{-1}. To the south, the transition to the Yermak Plateau takes place at a 3.3-km-deep saddle where the basement has a weak, blocky character with some internal layering.

Sedimentary rocks on the saddle in Line 3 are 0.9 s thick (TWT implied throughout this paper) and are distinguished into two units (Figure 2.6). The upper unit has 1.7 km s^{-1} velocity and strong but distorted reflections lapping down on the lower boundary. It continues NW onto Line 4, where sedimentary layers are conformal with the high basement topography and terminate on the outer basinward scarp. The lower unit has 2.9 km s^{-1} velocity and a relatively transparent reflection pattern with internal diffractions.

Seaward of the spur, we recognise the acoustic reflection character of the three upper velocity layers in the Nansen Basin. The lower unit (NB-1) is 0.4 s thick with strong reflections; the two middle units (NB-2–3) have weak, parallel reflections and 0.2 s compound thickness; and the upper, 0.3-s-thick unit (NB-4) has strong, parallel reflections (Figure 2.6). NB-4 has 2.0 km s^{-1} velocity whereas deeper sedimentary velocities are not resolved.

We may also correlate reflection patterns to MCS lines ~30 km to the south [*Jokat et al.*, 1995a], showing sedimentary rocks similar to those on the saddle in Lines 3–4 (Figure 2.6). Therefore, we are confident that sedimentary rocks on either side of the seaward scarp in Line 4 are of the same age. The correlation to the FRAM-IV ice-drift MCS line [*Kristoffersen and Husebye*, 1985] ~20 km up-slope to the SW is less straightforward. Our units have similar thickness but nearly opposite reflection character compared to FRAM-IV, where a 0.8-s-thick, semi-transparent basal unit

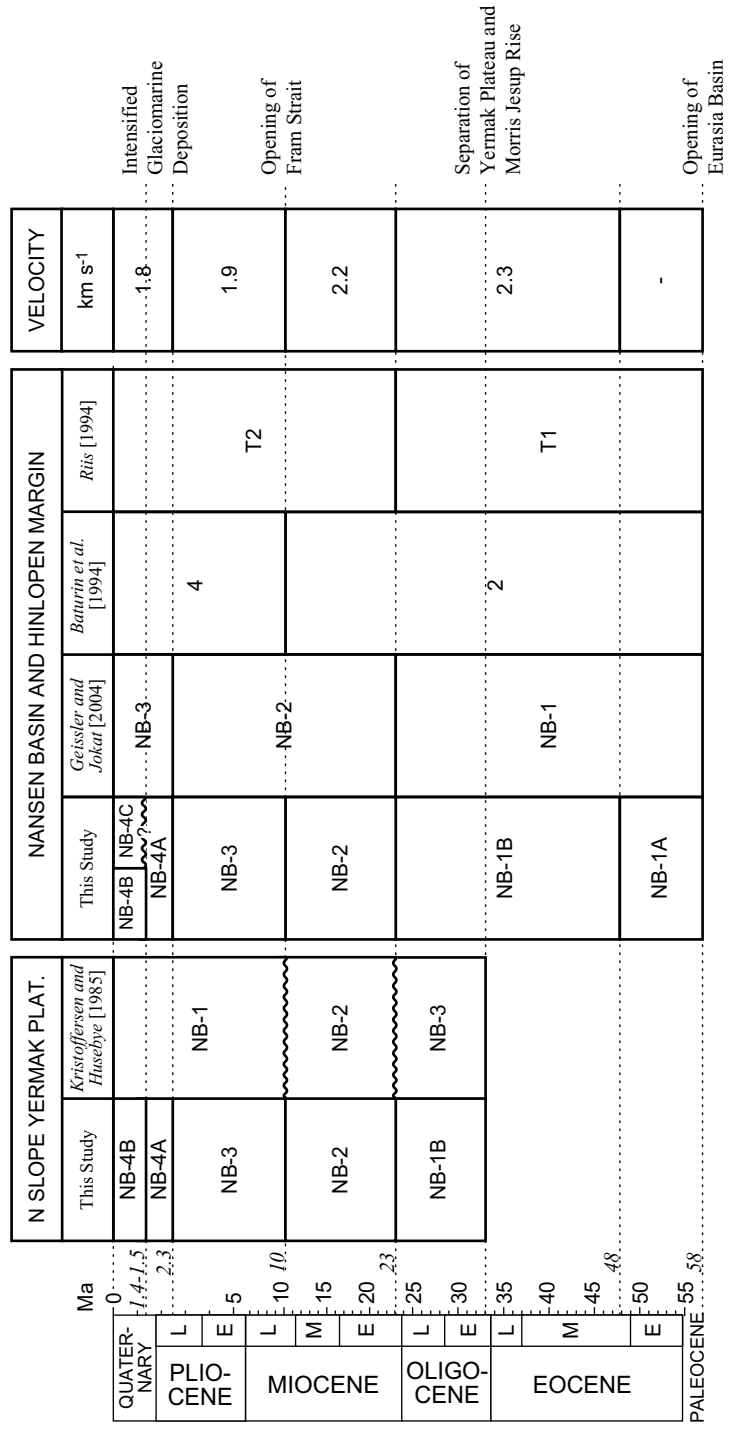

Figure 2.5. Seismic stratigraphic framework of the western Nansen Basin and adjacent margins. Ages proposed by other workers have been revised using our correlations and age estimates. Timescale from *Cande and Kent* [1995].

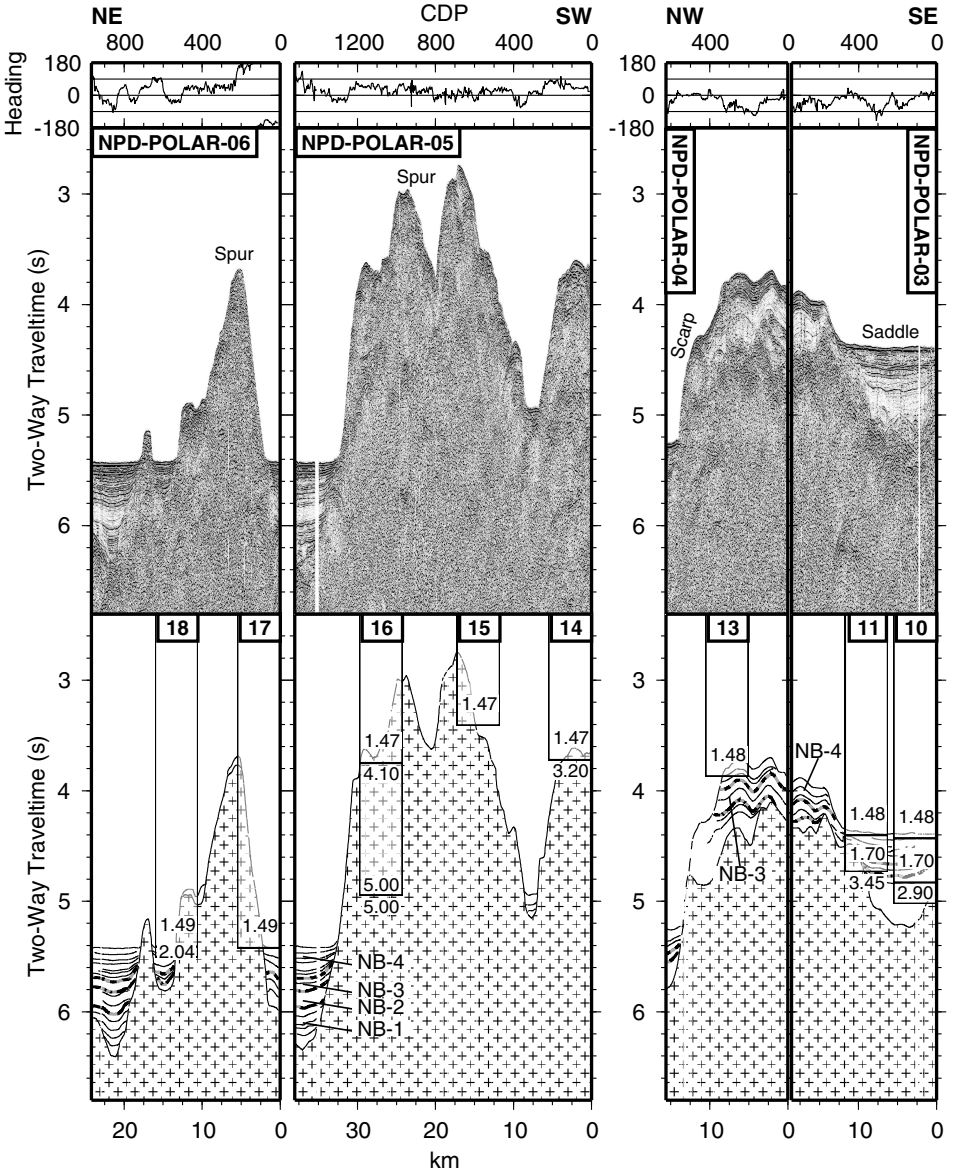

Figure 2.6. Processed MCS lines (middle panel); line drawings (bottom panel); and velocity profiles (annotated columns) from the north slope of the Yermak Plateau. Velocities, in km s^{-1}, are sampled from the 2-D velocity model in the sonobuoy deployment positions. The variable ship's heading, in degrees clockwise from north, illustrates the crooked geometry of seismic lines shot during ice-breaking.

underlies a 0.3-s-thick, strongly reflective middle unit and an upper, 0.3-s-thick, transparent unit. We tentatively propose that these units are equivalent to our units (Figure 2.5) and ascribe different reflection patterns to acquisition and processing parameters; *Kristoffersen and Husebye* [1985] used a 20-channel sonobuoy array and a 2 l airgun suspended through holes in the ice. The correlation of sedimentary units on the Yermak Plateau north slope is discussed further by *Gjengedal et al.* [in prep.].

Nansen Basin and Gakkel Ridge

Nine MCS lines and 33 velocity profiles were acquired between 84–86°N and 14–33°E on oceanic crust younger than Chron 20 (43.2 Ma; Figure 2.1). Line 10 crosses a 4.85-km-deep portion of the axial valley (Figure 2.4). The rugged oceanic basement ranges from 2.6 km depth in Line 10 to 5.8 km in Line 15. 22 of the sonobuoy profiles give near-top basement velocities in the 3.2–6.9 km s^{-1} range, with average velocity 4.3±0.9 km s^{-1}. Three sonobuoys show that the 4.3 km s^{-1} upper basement velocity may be representative for deeper basement rocks as well. In SB 50 the 4.3 km s^{-1} velocity continues 2.3 km into basement where an 8.3 km s^{-1} Moho refractor is indicated (Figure 2.7). In SB 40 on Line 9 it extends from a basement high to a wide-angle reflection 8.3 km further down. SB 48 on the ridge flank indicates 4.3 km s^{-1} upper basement velocity, a 5.0 km s^{-1} refractor 1.6 km further down, and an 8.3 km s^{-1} Moho refractor 2.8 km below the surface.

Sedimentary rocks forming a plain, 4.0-km-deep seafloor terminate against basement older than Chron 6 (19.6 Ma; Figure 2.4). While the oceanic basement topography along Line 7 is only partly covered (Figure 2.8), the entire relief is buried along Line 15 in the east (Figure 2.7). The deepest depocentres in Line 15 are flanked by high-angle extensional faults where the sedimentary hanging walls have slid by ~30 m relative to the footwall (Figure 2.7).

From the velocity layering we interpret four main sedimentary units. The oldest unit, NB-1, has 2.2–2.5 km s^{-1} velocity and is only found below 0.6 km depth in Lines 9 and 15, where its maximum thickness is 0.60 km (Figure 2.7). It has transparent reflection character grading upwards into discrete patches of parallel reflections.

Unit NB-2, with 2.2–2.4 km s^{-1} velocity, conformably overlies NB-1 along an intermediate-amplitude, continuous reflection. The unit is characterised by fairly constant, 0.4 km thickness and internal reflections that bend up markedly near basement onlaps (Figure 2.7). The low-frequency internal reflection pattern varies from blurred and faintly continuous to strong, semi-parallel reflections.

The boundary between NB-2 and NB-3 is a strong reflection corresponding to a velocity increase of up to 0.5 km s^{-1}, which is the largest sedimentary velocity contrast in the Nansen Basin. NB-3 has 1.9–2.1 km s^{-1} velocity and 0.3 km constant thickness. SB 19 in the start of Line 7 shows considerably higher velocity, 2.7 km s^{-1}, but its proximity to steep basement topography makes the velocity uncertain in the same manner as the 2.42 km s^{-1} velocity near basement in SB 30 (Figure 2.8). The acoustic character is a sandwich of two high-amplitude reflections and a number of medium strong, parallel reflections. Reflections bend up at onlap points, but not as strongly as in NB-2.

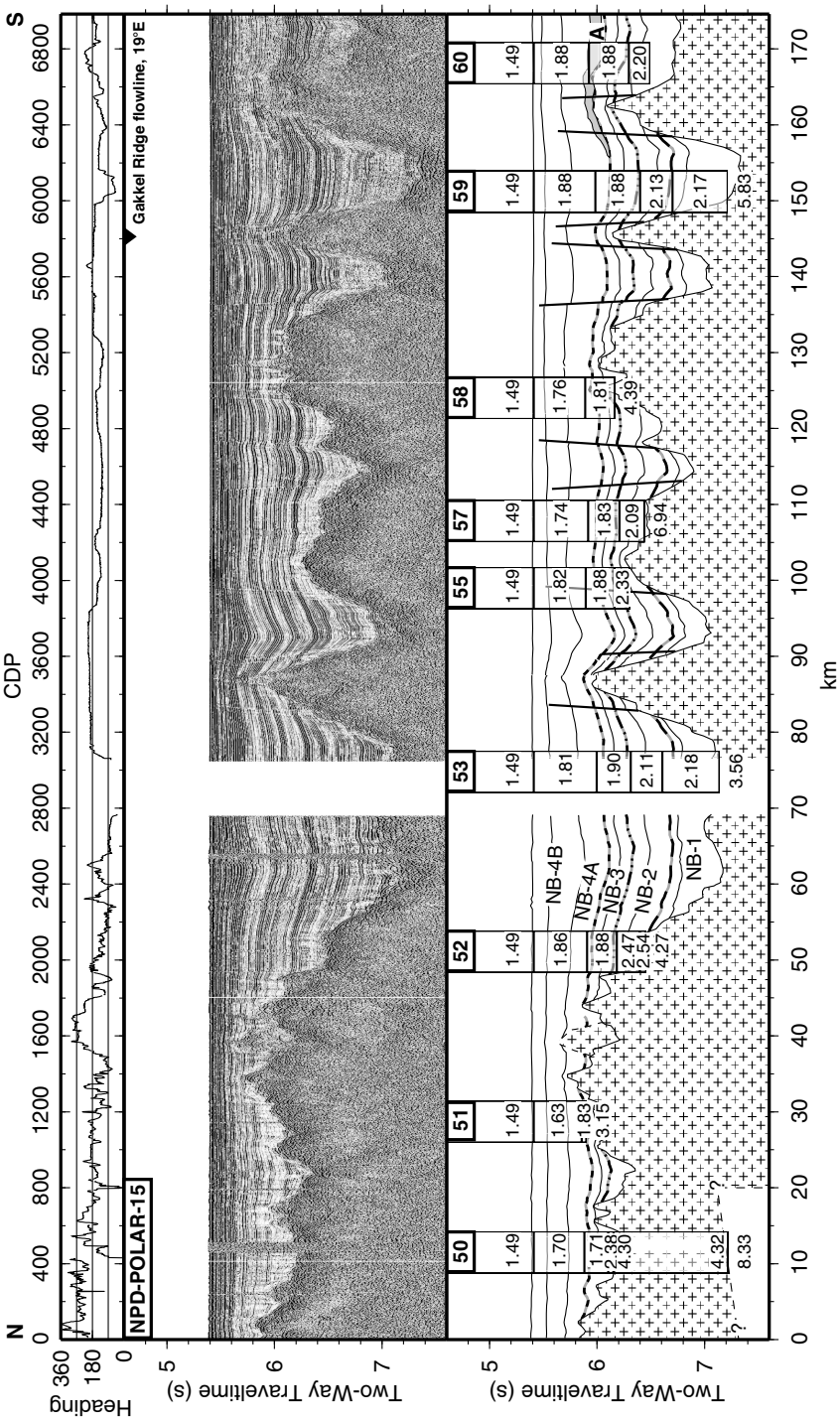

Figure 2.7. Seismic image, line drawing and velocity profiles along Line 15 in the eastern end of the study area.

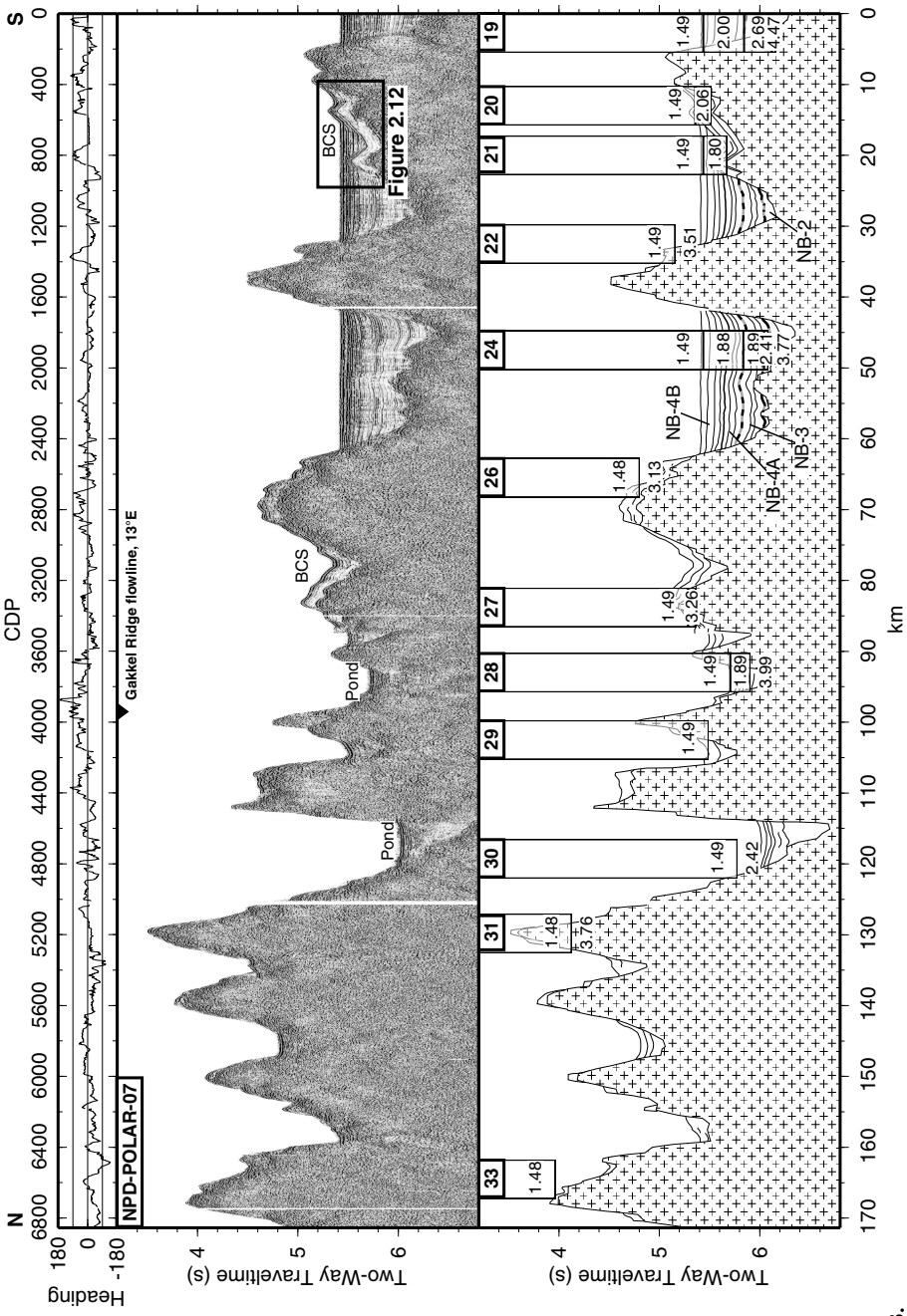

Figure 2.8.
Seismic image, line drawing and velocity profiles along Line 7 in the western end of the study area. BCS, basement-conformal sediments.

An intermediate-amplitude, continuous reflection marks the conformal boundary between NB-3 and NB-4, which is the youngest unit. NB-4 has 1.6–2.0 km s^{-1} velocity, yielding 0.45 km thickness in Line 7 (Figure 2.8) and 0.75 km in Line 15 (Figure 2.7). South of common depth point (CDP) 6200 in Line 15, the base of NB-4 is overlain and perhaps eroded by a chaotic, up to 0.13 km thick body (Body A in Figure 2.7). Based on reflection character, we may divide NB-4 into sub-unit NB-4A of weak reflections, and the overlying NB-4B with sub-parallel reflections that are markedly stronger than both NB-4A and NB-3.

Sparse sediments on oceanic crust younger than Chron 6 (19.6 Ma) fall into two categories. Ponds between basement highs are sediment-filled to different levels than the abyssal plain and contain sub-parallel reflections terminating against basement (Figures 2.4 and 2.8). Sediments on basement highs are conformal with the underlying relief and have finely layered but low-amplitude interiors and reflective caps (Figure 2.8).

The only tie between our lines and previous studies is the intersection between Line 9 and a regional MCS transect [*Jokat and Micksch*, 2004] at 85°0′N 21°12′E, which is unfortunately at a basement high (Figures 2.1 and 2.9). However, we can readily match acoustic reflection patterns of neighbouring sedimentary rocks. Seismic horizons may then be tied to the Hinlopen margin and tied further to previously published seismic stratigraphy of the continental slope (Figure 2.5). We

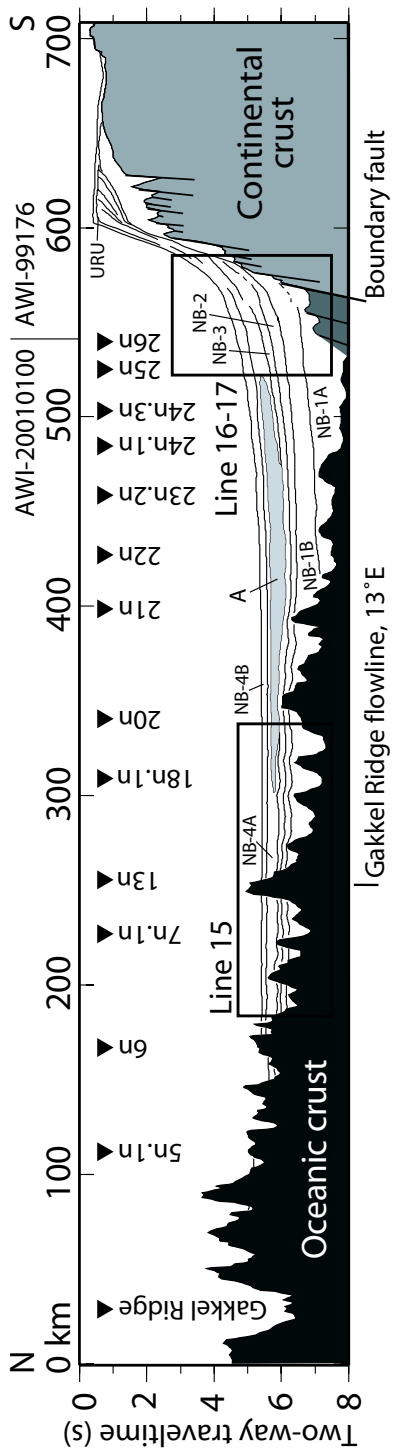

Figure 2.9. MCS transect across the Hinlopen margin and Nansen Basin, modified from *Jokat and Micksch* [2004]. Boxes show the projected positions of Lines 15 (Figure 2.7) and 16–17 (Figure 2.10). Positions of magnetic isochrons shown by triangles. Fault interpretation from *Geissler and Jokat* [2004]. *URU*, Upper Regional Unconformity.

may also correlate reflection patterns to Figure 2.8 and pre-existing MCS lines north of the Yermak Plateau [*Jokat et al.*, 1995a].

Our NB-4B unit is equivalent to the uppermost, 1.8–2.0 km s^{-1} velocity layer of *Jokat and Micksch* [2004], corresponding to a band of strong, parallel reflections [*Micksch*, 2004]. In particular, the chaotic Body A can be traced ~220 km landward from Line 15 (Figures 2.7 and 2.9). Deeper layer boundaries largely correlate with pronounced regional reflections defined by *Micksch* [2004]. The correlation of pre-NB-4 velocities is more difficult. Our velocities for NB-3 (1.9–2.1 km s^{-1}) are consistently lower than the 2.3–2.5 km s^{-1} range of *Jokat and Micksch* [2004]. The same holds for NB-1 and NB-2 where we find 2.2–2.5 km s^{-1} velocities while *Jokat and Micksch* [2004] reported 2.7–3.1 km s^{-1}. There is less disagreement on basement velocities. We note first that discrepancies may arise from more or less favourable sonobuoy locations. Both datasets are based on unreversed profiles which cannot resolve the effects of dipping layers such as high-velocity oceanic basement. On the other hand, there are notable differences in the 2-D ray tracing schemes used. While we implied a direct relationship between the sonobuoy profiles and the corresponding MCS sections, *Jokat and Micksch* [2004] used the MCS sections only as an interpretive guide to the final adjustment of the model [*Micksch*, 2004]. We assumed constant velocities and solved for one layer velocity in each run, whereas *Jokat and Micksch* [2004] simultaneously solved for velocities, depths, and velocity–depth gradients. We do not know the non-uniqueness of the latter approach. The fact that *Jokat and Micksch* [2004] used a constant water velocity and did not correct for sonobuoy drift should not introduce more than ~15% of the observed discrepancy as long as the drift correction would not lead to re-interpretation of arrivals.

Hinlopen Margin

Line 16 runs parallel to the margin on the lower continental slope, turning into Line 17 in an oblique traverse of the upper slope (Figures 2.1 and 2.10). Sonobuoys were not deployed along the lines but approximate depths from nearby velocity measurements [*Geissler and Jokat*, 2004] are given in parentheses. The seafloor shoals from 4.9 to 3.9 s and features a 0.6 s depression on the upper slope. The top basement reflection is blurred by the thick sedimentary cover and we may only map it along Line 17 (Figure 2.10). At CDP 1900, a pronounced fault increases basement depth by 1.2 s (~1.8 km) on the seaward side. In the following discussion we denote it the boundary fault. Up to 2.7 s (~3.6 km) of sediments are accommodated on its seaward side and 1.7 s (~2.1 km) on its landward side.

Sedimentary reflections are more chaotic in Line 16–17 than in Line 15 (Figures 2.7 and 2.10), but the four major units of the Nansen Basin may be interpreted landward to the boundary fault. Unit NB-1 fills in the basement relief and comprises two sub-units. A band of continuous, strong reflections marks the top of sub-unit NB-1A with horizontal onlap of the boundary fault and strong, sub-parallel reflections of variable continuity. The overlying NB-1B is more transparent with some sub-parallel reflections and becomes thicker towards the boundary fault where we observe upward-curving onlap contacts.

NB-2 rests on a medium strong and continuous reflection, drapes the boundary fault, and increases from 0.3 s (~0.4 km) thickness on the lower slope to 0.6 s (~0.8 km) on the upper slope. Its reflection pattern is similar to that of NB-1. In the NE end

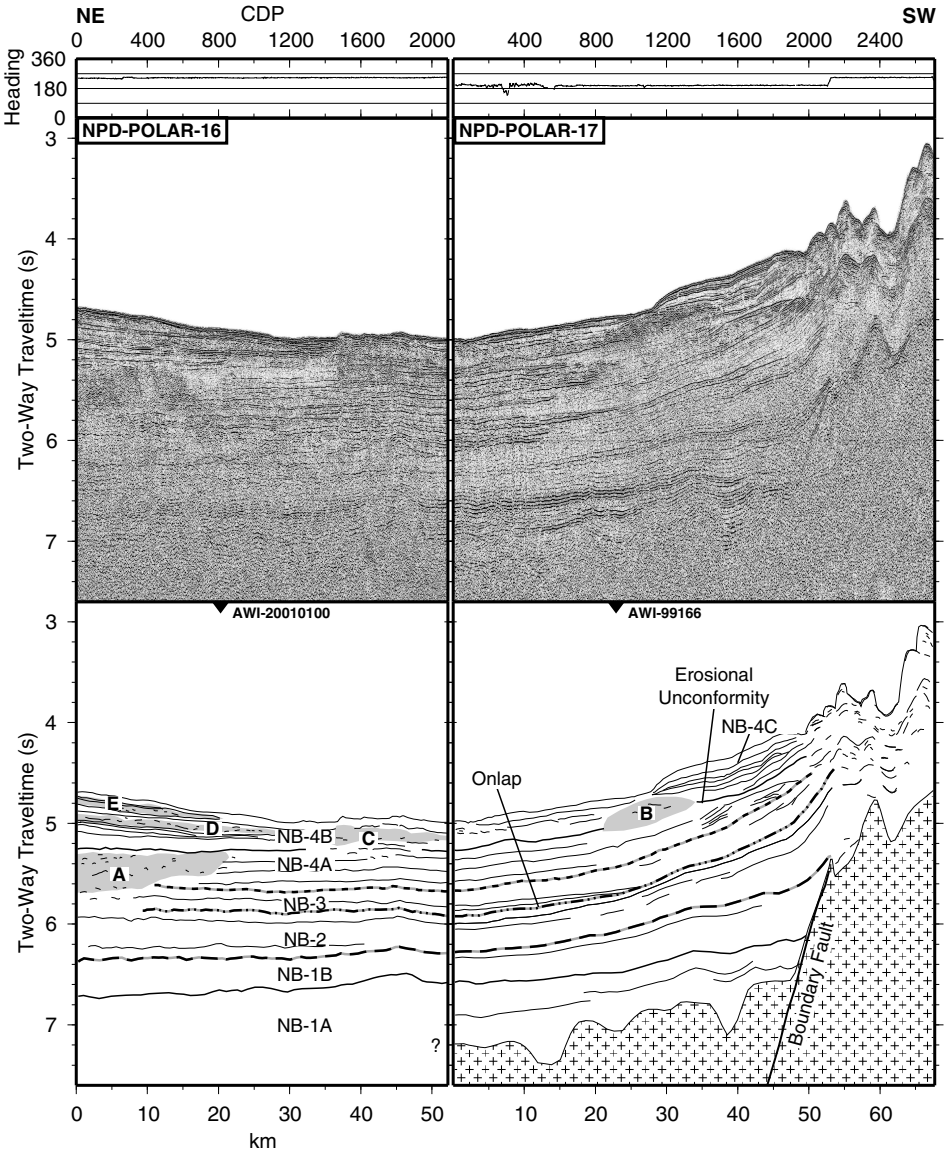

Figure 2.10. Seismic image and line drawing of MCS Lines 16 and 17 on the Hinlopen margin. Letters A–E denote bodies of chaotic reflections within otherwise layered units. The basement surface could not be interpreted along Line 16 because of limited seismic penetration.

of Line 17 some strong internal reflections grade into a chaotic reflection pattern landward of the boundary fault.

The 0.3-s-thick (~0.4 km) NB-3 has sub-parallel reflections of variable amplitude and slightly better continuity than NB-2. It onlaps NB-2 at CDP 200–500 in Line 17

(Figure 2.10). In the NE end of Line 16 it is replaced by the chaotic and diffusely bounded Body A which continues upward into unit NB-4.

The youngest unit, NB-4, has 0.7 s (~0.7 km) constant thickness seaward of the boundary fault and may be divided into three sub-units. NB-4A has sub-parallel reflections of variable amplitude and continuity, distorted by at least three bodies with chaotic reflection patterns (Bodies A–C in Figure 2.10). The overlying NB-4B has a wavy reflection pattern including chaotically textured, sigmoid bodies in the N end of Line 16 (Bodies D–E in Figure 2.10). These bodies have 0.4 s (~0.4 km) combined thickness at the NE end of Line 16 but pinch out and eventually onlap sediment body C at CDP 1400. The uppermost sub-unit, NB-4C, is found on the middle slope in Line 17. It has nearly parallel reflections of high amplitude and good continuity, and apparently overlies an erosional surface.

Our NB-1 unit ties to "NB-1" of *Geissler and Jokat* [2004] and "T1" of *Riis* [1994] (Figure 2.5). The combined NB-2 and NB-3 corresponds to "NB-2" of *Geissler and Jokat* [2004], except in line AWI-99176 where internal boundaries according to *Geissler and Jokat* [2004] are shifted slightly upwards compared to our interpretation. The slight mis-correlation may be due to the many degrees of freedom when tracing seismic horizons along strike of continental slopes. Furthermore, Line 17 is a tie line which *Geissler and Jokat* [2004] did not have. The tie links our survey to line MAGE-84103 (Figure 2.1), where the base of our NB-3 unit is equivalent to the boundary between "Sequence 2" and the transgressive "Sequence 4" of *Baturin et al.* [1994].

Discussion

Sedimentary Cover

Lines 7–15 map distal parts of the large Franz-Victoria Fan and Lines 16–17 a tributary fan at the mouth of the Erik Eriksen Trough (Figure 2.11). The sub-parallel, continuous and relatively strong reflections in Lines 7–15 are compatible with distal sheet-flow turbidites in this submarine fan system. Increasingly random reflection character towards the Hinlopen margin indicates more proximal turbidite facies. Furthermore, NB-4 thins gradually away from the Franz-Victoria Fan so that its thickness off the Yermak Plateau is only half of that on the Hinlopen margin. The turbidites were sourced by Cenozoic uplift and erosion of the Barents Sea where erosion estimates increase to the NW and >3 km of sedimentary strata have been removed from Svalbard [*Rasmussen and Fjeldskaar*, 1996; *Dimakis et al.*, 1998]. The regional thickness trends of NB-1B to NB-3 are less pronounced. Nonetheless, these units flex upwards and thicken at the large fault in Line 17 (Figure 2.10), indicating that sediment sources were proximal to the Hinlopen margin also at pre-NB-4 times. The tendency of younger reflections to be stronger and less continuous suggests an accompanying increase of depositional energy. The horizontal onlap of NB-1A on the boundary fault indicates a distal source and moderate depositional energy during the initial development of the Nansen Basin.

Sediment bodies D and E in Line 16 may be interpreted as abandoned fan lobes on the apron of the Franz-Victoria Fan (Figure 2.10). Detailed bathymetry [*Cherkis et*

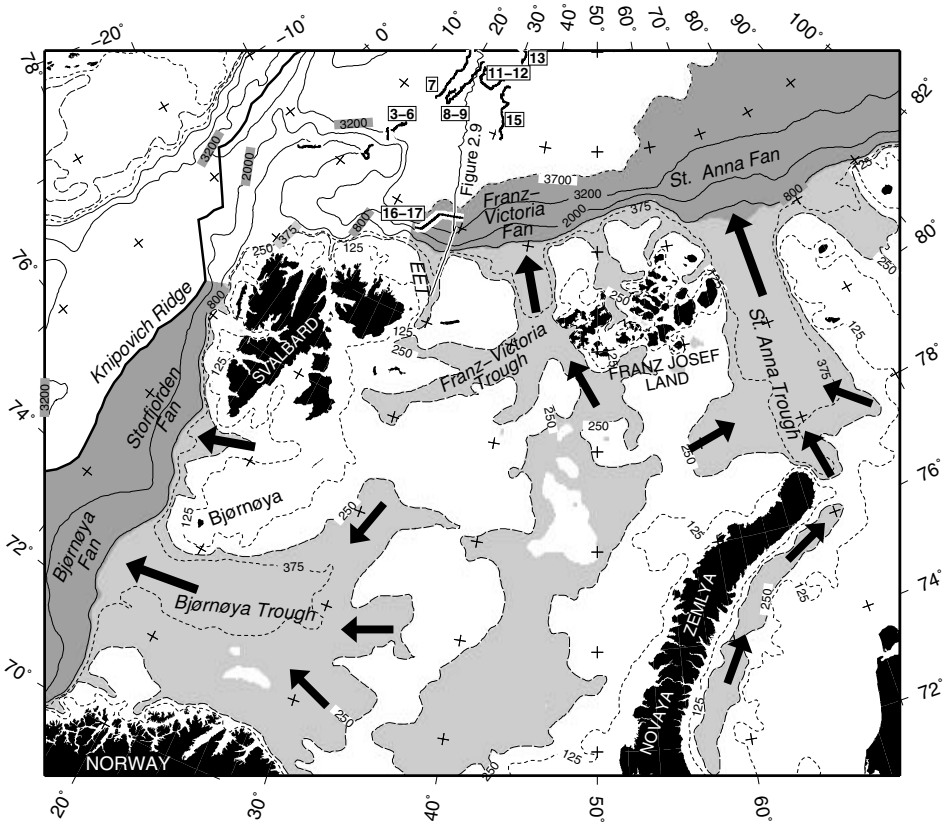

Figure 2.11. Position of our survey (annotated by line number) and Figure 2.9 relative to major Late Cenozoic trough and fan systems on the Barents Sea shelf. The present shelf bathymetry [*Jakobsson et al.*, 2000] is shaped by glacial erosion (arrows) of the underlying basement and structural trends.

al., 1999] shows that the depression in Line 17, CDP 2200–2600, may be a canyon in the Erik Eriksen Trough system (Figures 2.10 and 2.11), but we cannot properly identify levees and erosion patterns. None of the lines farther seaward show channels related to this canyon; however, because our lines run largely parallel to the expected channel direction on the Erik Eriksen and Franz-Victoria fans, the chances of adequately mapping channels are small.

The irregular geometries and mushy internal patterns of sediment bodies A–C may be interpreted as slump deposits (Figure 2.10). In particular, Body A extending for ~220 km across the basin and cutting into the underlying sediments indicates a major mass-wasting episode on the margin (Figure 2.9). There is no stratigraphic connection between Body A and a large slump deposit forming the seafloor only ~40 km farther west [*Cherkis et al.*, 1999]. However, the abundance of young slump deposits as well as deep slide scars on the margin [*Cherkis et al.*, 1999; *Geissler and*

Jokat, 2004] demonstrates the importance of mass wasting during the recent margin development.

NB-4C, containing sub-parallel reflections of high amplitude and good continuity, may be a channel-levee system or a contourite (Figure 2.10). It is unclear whether the erosional unconformity at its base is a slide plane related to Body B, or a surface created by bottom-current erosion and subsequent deposition. Contour currents run along strike and tend to deposit "plastered drifts" prograding landward [*Faugères et al.*, 1999], while submarine channels run down-dip with levees prograding along-strike. NB-4C has a small channel on its upper end and reflections prograding up-dip, but we cannot trace it onto neighbouring lines. Therefore, the sediment body appears to be a local fan deposit, possibly modified by contour currents.

The reflective sedimentary ponds in the ridge province are similar to the turbidites of the abyssal plain (Figure 2.8). However, if the ponds were sourced from the margin, the different surface levels of the ponds show that sediment flow into the ridge province is barred at least in part by basement topography. High reflectivity may also point to turbidites and submarine slide deposits derived from erosion of nearby basement highs.

Basement-conformal sediments in the ridge province (Figure 2.8) may result from either hemipelagic drape or post-depositional basement tectonics. A tectonic origin is supported by the observation that conformal sediments are not evenly distributed in the ridge province but appear to be concentrated on ~12–23-Myr-old basement [see also *Kristoffersen*, 1998]. Block faulting and tilting of oceanic crust may have occurred during or after that time because of plate reorganisation or an episode of amagmatic accretion which may be common on slow- and ultraslow-spreading ridges [*Louden et al.*, 1996]. Furthermore, one conformal unit partly buried below the abyssal plain appears to have higher velocity than the adjacent turbidites (SB 20–21 in Figure 2.8), a surprising observation if the conformal unit is hemipelagic.

On the other hand, a hemipelagic origin is supported by seismic reflection geometries. It is difficult to find any clear evidence that the partly buried conformal unit is fault-bounded and then onlapped by turbidites. Rather, successive turbidite reflections appear to continue into the conformal unit as thin, draping reflectors (Figure 2.12). Such shingled onlap may be explained by the interplay of hemipelagic drape, which affects the entire region, and turbidites which are only deposited in low-standing locations [*Taylor and Huchon*, 2002].

There are signs of recent faulting on the edge of major sediment depocentres in Line 15 (Figure 2.7). Because thinner sediments in the other lines do not appear faulted and we cannot observe faults continuing through the underlying basement, we regard the faulting purely as a result of differential sediment compaction. Compaction is also indicated by upward-bending reflections on depocentre flanks. The amount of bending increases with overburden.

Age of Sediments

Three ODP sites have been drilled into Pliocene sedimentary strata on the inner Yermak Plateau (Figure 2.1) [*Thiede et al.*, 1995], but the drilled horizons are correlated to the Nansen Basin only by matching of acoustic reflection patterns [*Geissler and Jokat*, 2004]. Without direct borehole control, we may consider three

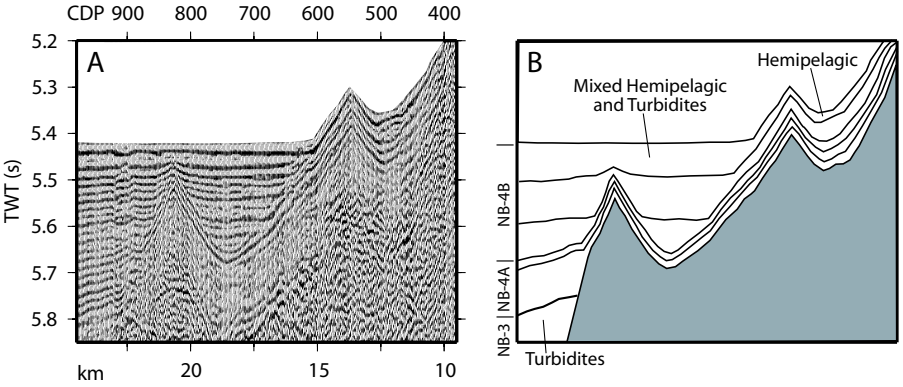

Figure 2.12. Relation between turbidites and the basement-conformal sedimentary unit below SB 20–21 (see Figure 2.8 for location). **(A)** Multi-channel seismic image. **(B)** Line interpretation indicating shingled onlap of basement by turbidites and hemipelagic drape.

simple approaches to estimate the age of the main depositional units: (1) the units may be correlated with regional unconformities on the margin; (2) the sedimentary rocks must be younger than the underlying basement; and (3) changes in reflection character and velocity may relate to paleoceanographic events. Age correlation based on eustatic curves [*Baturin et al.*, 1994] is less useful because of extensive glacial erosion of the Barents Sea shelf [*Solheim et al.*, 1996].

The present-day shelf edge on the Hinlopen margin is composed of an up to 1.0-s-thick, strongly prograding unit that is truncated and overlain by a ~0.15-s-thick, aggrading to slowly prograding unit (Figure 2.9). The truncation surface corresponds to the Upper Regional Unconformity (URU) of the Barents Sea, marking the change from net glacial erosion to net accumulation [*Solheim and Kristoffersen*, 1984]. While the URU is diachronous and has not yet been dated on the Hinlopen margin, the base of the prograding unit is probably equivalent to horizon R7 on the W Barents Sea margin [*Faleide et al.*, 1996], which is the ~2.3-Myr-old regional base of glacial sediments [*Solheim et al.*, 1998].

The correlation of horizon R7 to the Nansen Basin is ambiguous because of chaotic reflections above the boundary fault (Figure 2.10). The strong thickening of NB-4 towards the glacial Franz-Victoria Trough (Figure 2.11) indicates that R7 correlates to the base of NB-4 rather than the base of NB-3. Another key may be found in sediment body A which erodes into NB-3 and marks the onset of several other slide deposits (Figure 2.10). In the Bjørnøya Fan, similar slide deposits emerged shortly after R7 times when intensified glacio-fluvial drainage increased sediment supply to the outer shelf, causing over-steepening and subsequent slope failure [*Faleide et al.*, 1996; *Fiedler and Faleide*, 1996; *Kuvaas and Kristoffersen*, 1996; *Butt et al.*, 2000]. We may therefore assume that the base of NB-4 corresponds to ~2.3 Ma (Table 2.2). Increased reflection amplitudes from NB-4A to NB-4B suggest a link to horizon R5 which is the base of a shallow, chaotic package on the W Barents Sea margin [*Faleide et al.*, 1996]. The age of R5 is estimated to 1.4–1.5 Ma [*Forsberg et al.*, 1999].

Table 2.2. Summary of Nansen Basin Sedimentary Figures[a]

Unit	Base Age (Ma)		Average velocity	Max. Thickness		Sed. Rate
	Onlap[5]	Corrected (method)	km s^{-1}	TWT (s)	km	cm kyr^{-1}
NB-4B	20	1.0 (correlation)	1.8	0.50	0.45	45
NB-4A	20	2.3 (correlation)	1.8	0.33	0.30	23
NB-3	21	10 (sed. rate)	1.9	0.28	0.26	3.3
NB-2	23	–	2.2	0.39	0.43	3.3
NB-1B	48	–	2.3	1.1	1.3	5.2
NB-1A	58	–	–	1.4	–	–

[a]Linearly interpolated between magnetic isochrons; timescale from *Cande and Kent* [1995]

The age of the oceanic crust in the Nansen Basin has been estimated from correlations of magnetic lineations with the geomagnetic time scale [*Karasik*, 1968; *Vogt et al.*, 1979; *Brozena et al.*, 2003]. However, the rugged basement offers poor definition of the youngest basement location where a particular stratigraphic unit wedges out. Also, in an environment with predominantly turbidite deposition, the elevated young ridge flank does not receive turbidites until it has subsided to a level comparable to the abyssal plain. This subsidence lag may be estimated from NB-4 terminating against basement of Chron 6 age (19.6 Ma; Figure 2.4). If the true age of NB-4 is 2.3 Ma, the subsidence lag is ~17 Myr

NB-3 reaches ~21-Myr-old basement (Table 2.2), implying ~4 Ma lag-corrected age and accordingly 18 cm kyr^{-1} sedimentation rate. Because this value is well above the 3 cm kyr^{-1} average for the north slope of the Yermak Plateau [*Kristoffersen and Husebye*, 1985], it is unrealistic for pre-glacial times and casts doubt on the usefulness of lag correction in our survey area. Taking instead the NB-2 onlap age of ~23 Ma at face value (Table 2.2), we calculate 3.3 cm kyr^{-1} average sedimentation rate of NB-2 and NB-3 and an interpolated Late Miocene (~10 Ma) age for the base of NB-3 (Figure 2.5). This estimate is reasonable because the large velocity contrast and strongly reflective boundary between NB-2 and NB-3 may reflect a major paleoceanographic event. The most obvious candidate event is the opening of the Fram Strait gateway between ~15 and ~10 Ma [*Engen and Faleide*, 2005, this volume] or events farther south. The ~10 Ma age as well as the sedimentation rate agrees with the gateway interpretation of *Kristoffersen and Husebye* [1985].

The less distinct boundary between NB-1 and NB-2, marking the transition to more proximal sediment sources on the Hinlopen margin, may have resulted from paleoceanographic changes at the Oligocene–Miocene transition (Table 2.2). *Riis* [1994] suggested that units NB-2 and younger are equivalent to the Plio–Pleistocene wedges of the W Barents Sea margin (<2.3 Ma), while *Geissler and Jokat* [2004] proposed 6–7 Ma from extrapolated glacial sedimentation rates on the Yermak Plateau. These values are probably not correct but demonstrate that the Plio–Pleistocene of the Hinlopen margin is thinner than expected from direct comparison with the W Barents Sea margin. The Hinlopen margin, particularly to the west of Lines 16–17, is less influenced by large submarine fans than any other segment of the western and northern Barents Sea margin (Figure 2.11). The difference in sediment thickness is demonstrated by the free-air gravity which has a large maximum over

the Franz-Victoria Fan but nearly vanishes west of Line 17 (Figure 2.13b) [*Vogt et al.*, 1998].

NB-1A, downlapping on ~48-Myr-old oceanic basement, represents Paleocene to Eocene early infill of the basin (Figure 2.9 and Table 2.2). NB-1B is then of Eocene and Oligocene age and was deposited at ~5 cm kyr^{-1}.

Depositional Patterns of Nansen and Amundsen Basins

In the Amundsen Basin as well as the Nansen Basin, sedimentary reflections on pre-Chron 21 (>47.0 Ma) basement dip seaward because of differential subsidence of originally flat-lying layers (Figure 2.9) [*Jokat et al.*, 1995b]. The deeper Amundsen Basin has the steepest dips, indicating less deposition relative to subsidence. While the Nansen Basin has received sediments from repeated Cenozoic uplift and erosion of the Barents–Kara margin (Figure 2.11) [*Rasmussen and Fjeldskaar*, 1996], the Amundsen Basin was fed by the Lomonosov Ridge until ~50 Ma and later sourced from the continental margins at both ends [*Jokat et al.*, 1995b]. As a result, the Amundsen Basin has 8 sedimentary units which cannot be directly correlated to our units [*Jokat et al.*, 1995b]. Units below 0.9 km depth have higher velocity (>2.9 km s^{-1}) than our units, possibly as a result of different provenance. The velocity and thickness of NB-4 corresponds to the two upper units of the Amundsen Basin, comprising glaciomarine sediments deposited since 2.5 Ma in a pronounced submarine fan system along the lower slope of the Lomonosov Ridge [*Kristoffersen et al.*, 2004].

Oceanic Basement

Our 4.3±0.9 km s^{-1} average upper basement velocity passes as oceanic layer 2 but is somewhat lower than the global range of 4.5–5.5 km s^{-1} [*Ludwig et al.*, 1970; *White et al.*, 1992]. Layer 3 velocity (6.9 km s^{-1}) is interpreted from SB 57. Previous surveying of the Gakkel Ridge flanks have yielded upper basement velocities of 4–5 km s^{-1} [*Duckworth and Baggeroer*, 1985]; 3.4–4.6 km s^{-1} [*Jokat et al.*, 1995a] and >4 km s^{-1} [*Jokat and Micksch*, 2004]. We cannot group our upper basement velocities into oceanic layers 2A, 2B and 2C as demonstrated in the Norwegian–Greenland Sea [*Houtz and Ewing*, 1976; *Myhre and Eldholm*, 1981]. This is perhaps because the majority of our profiles sample crust older than ~7.5 Ma where layer 2A is commonly vanished because of chemical alteration with age [*Carlson*, 1998].

The layer 3 velocity in SB 57 is related to a strongly reflective and low-standing basement province (Figure 2.7, CDP 4100–4900). Elsewhere, the seismic basement character varies from diffractions and semi-continuous reflections on basement highs, to strong, semi-parallel reflections at the bottom of depocentres. The latter occurs near SB 53 where the upper basement velocity is only 3.56 km s^{-1} (Figure 2.7). Because the Eurasia Basin has unusually rough basement [*Weigelt and Jokat*, 2001], such parallel reflections are most likely from igneous or consolidated sedimentary infill of the primary relief [*Ludwig et al.*, 1970]. Ocean drilling has demonstrated interlayered sediments and extrusive basalts in the upper 200–300 m of basement [*Hall and Robinson*, 1979], what would correspond to a 0.11–0.17 s upper basement zone below SB 53.

Our survey area corresponds to a deep, sparsely magmatic segment of the Gakkel Ridge where predominantly mantle peridotites have been dredged, whereas segments on either side consist almost exclusively of basalt (Figure 2.13a) [*Michael et al.*, 2003]. The western segment, extending from ~60 km west of Line 7, has elevated axial topography and >1000 nT magnetic anomalies in the area between the highly magnetic Yermak Plateau and Morris Jesup Rise. *Feden et al.* [1979] interpreted these observations in terms of repeated hotspot activity since Chron 18 times (43.2 Ma), the "Yermak hotspot". However, regional seismic tomography cannot resolve any local mantle hotspot [*Levshin et al.*, 2001]. Farther east, volcanism is focussed where the plate boundary intersects flowline-striking highs underlain by relatively thick magmatic crust [*Cochran et al.*, 2003; *Michael et al.*, 2003]. The highs stand out in the bathymetry to crustal ages of Chron 6 times (~19.6 Ma; Figure 2.13a) while the underlying thickness anomalies have been followed to the 8.3 Ma isochron [*Cochran et al.*, 2003; *Jokat et al.*, 2003]. Models predict that flowline-striking highs may persist for longer time-spans and even be inherited from the initial break-up [*Choblet and Parmentier*, 2001].

Within the sparsely magmatic segment, a shoaling axial valley and a flowline-striking high corresponds to a first-order magmatic centre at 19°E, while a smaller centre at 13°E is not reflected in the axial bathymetry [*Michael et al.*, 2003]. We calculated flowlines of relative plate motion from these locations and found basement highs along them to crustal ages of Chron 18 (39.9 Ma) and Chron 13 (33.3 Ma), respectively (Figures 2.8 and 2.9). The flowlines also point at bathymetric lineaments on the Lomonosov Ridge (Figure 2.13a), but we cannot verify such a link between mid-ocean ridge and margin segmentation. However, there is a link between crustal thickness on the ridge flank and in the axial valley. The relatively thick, 8.3 km, crust beneath SB 40 correlates with the 13°E magmatic centre, and our measurements of thin crust (2.8 km in SB 48 and 2.3 km in SB 50) are adjacent to ~2-km-thick, sparsely magmatic crust in the axial valley (Figure 2.13c) [*Jokat et al.*, 2003]. Our upper basement velocities are invariant to the magmatic segmentation, in accordance with the Mid-Atlantic and Southwest Indian ridges where layer 2 is fairly even and crustal thickness variations are mainly accommodated by the waxing and waning of layer 3 [*Muller et al.*, 1999; *Hooft et al.*, 2000].

Figure 2.13 (overleaf). Geophysical character of the western Eurasia Basin and adjacent margins. Eurasia–North America flowlines [*Roest and Srivastava*, 1989; *Brozena et al.*, 2003] show which parts of the basin floor correspond to the western volcanic (WVZ), sparsely magmatic (SMZ) and eastern volcanic zone (EVZ) of the Gakkel Ridge [*Michael et al.*, 2003]. Dashed flowlines run from magmatic centres on the Gakkel Ridge at 13° and 19°E. Seismic tracklines shown by bold (Figure 2.14) and dashed lines. **(A)** Residual bathymetry calculated by subtracting the *Parsons and Sclater* [1977] age–depth relationship from the IBCAO bathymetry grid [*Jakobsson et al.*, 2000]. **(B)** Free-air gravity anomaly (Arctic Gravity Project; http://earth-info.nima.mil/GandG/agp/). **(C)** Mantle Bouguer anomaly, calculated by removing from (B) the gravity attraction of 6-km-thick crust with 2730 kg m^{-3} density outcropping at the seafloor and overlying mantle with 3330 kg m^{-3} density. Crustal thickness values (in km) from this and previous wide-angle seismic studies (Table 2.1) shown in boxes. **(D)** Magnetic anomalies [*Verhoef et al.*, 1996; *Olesen et al.*, 1997] with identification from Figure 2.14 and *Engen and Faleide* [2005, this volume].

(Figure 2.13)

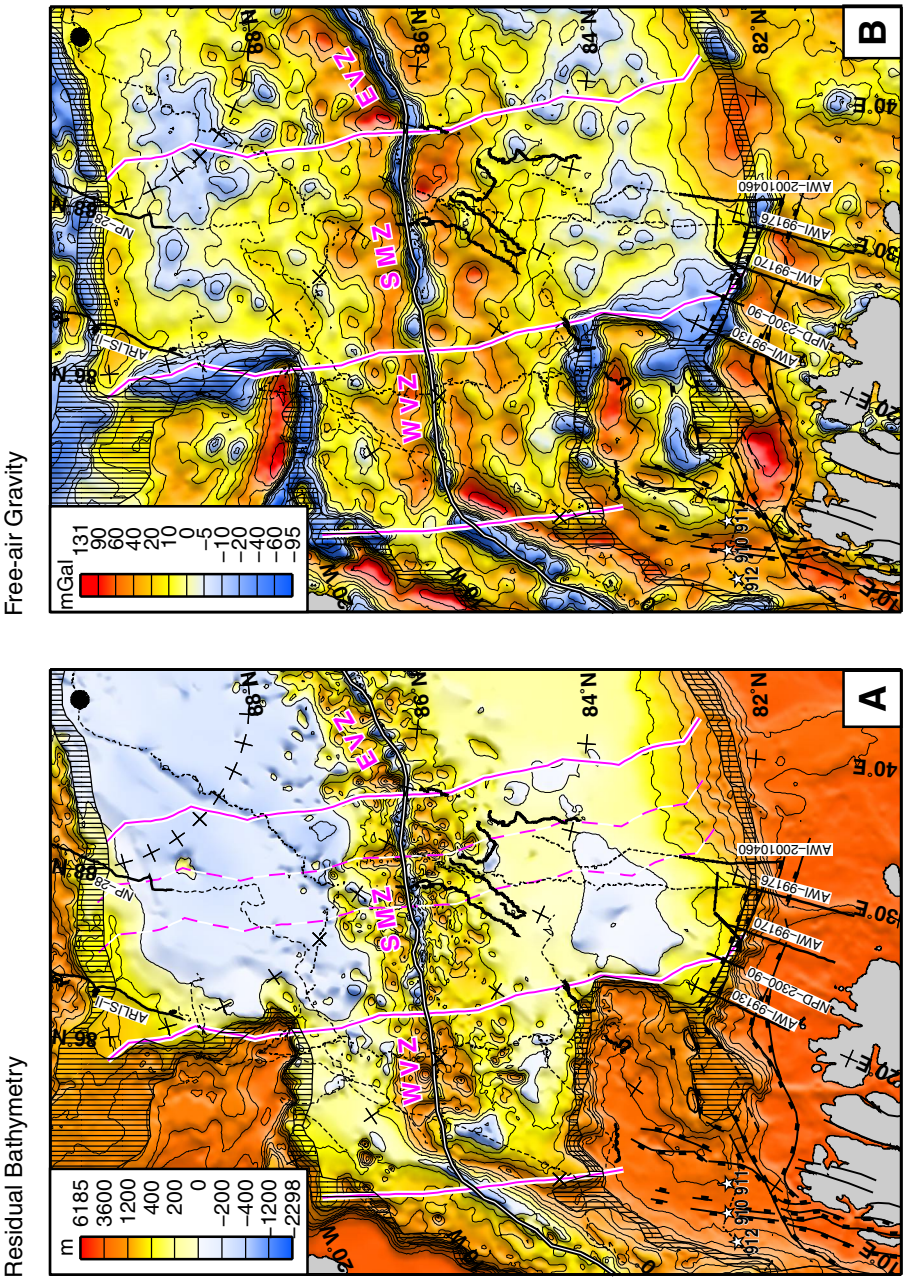
Free-air Gravity
mGal 131 90 60 40 20 10 0 −5 −10 −20 −40 −60 −95
B
EVZ
SMSZ
WVZM
AWI-20010460
AWI-99176
AWI-99170
AWI-99130
NPD-2300-90
912
910
911
Residual Bathymetry
m 6185 3600 1200 400 200 0 −200 −400 −1200 −2298
A
EVZ
SMSZ
WVZM
AWI-20010460
AWI-99176
AWI-99170
AWI-99130
NPD-2300-90
912
910
911

(Figure 2.13)

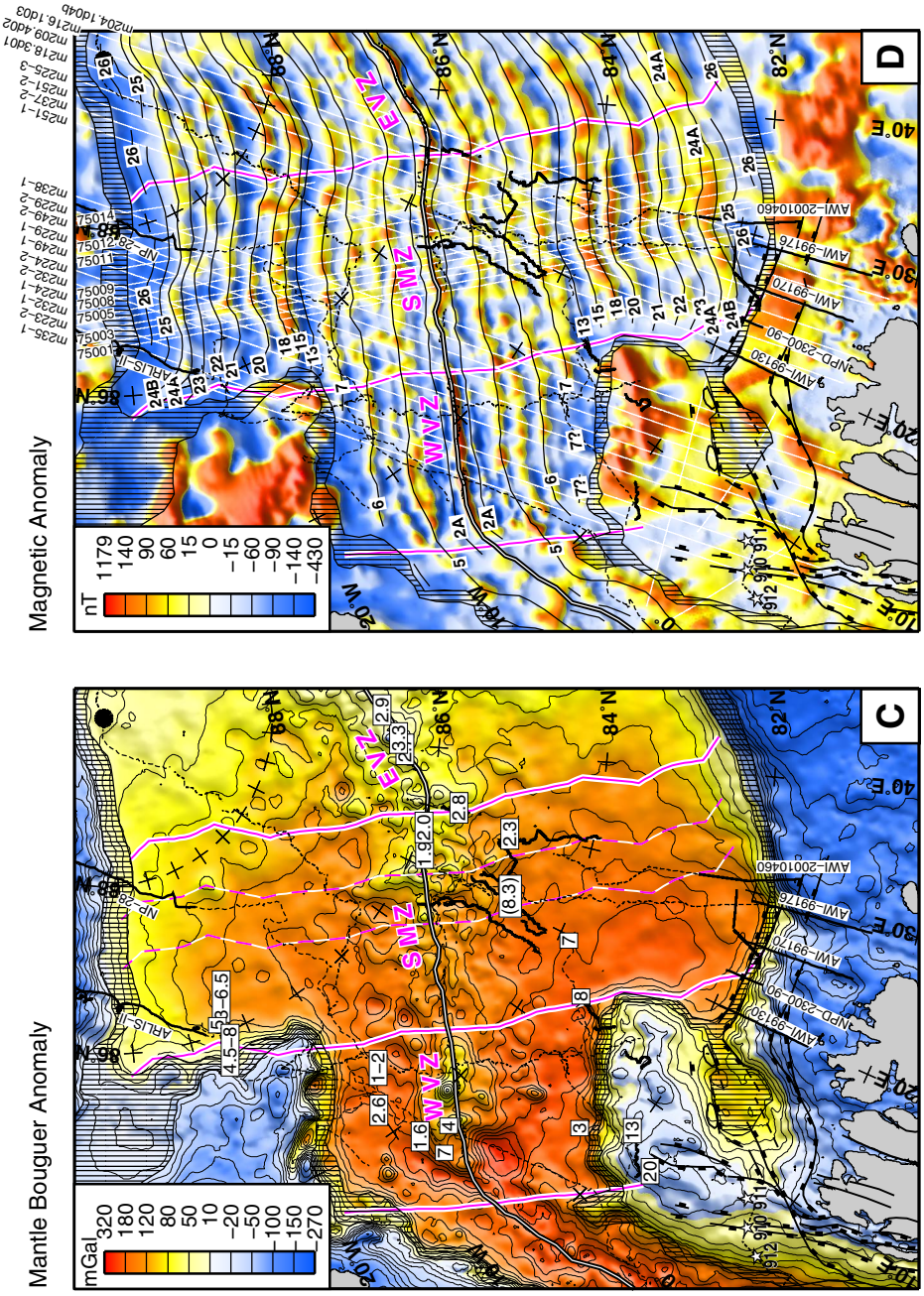
D
Magnetic Anomaly
nT
1179
140
90
60
15
0
−15
−60
−90
−140
−430
C
Mantle Bouguer Anomaly
mGal
320
180
120
80
50
10
−20
−50
−100
−150
−270
ENZ
SMZ
WMZ
SMZ
WVZ
86°N
84°N
82°N
20°W
0°
20°E
40°E
AWI-20010460
AWI-99176
AWI-99170
AWI-99130
NP-26
ARLIS-IP
24B
24A
24
23
22
21
20
18
15
13
7
6
5
2A
26
25

We calculated mantle Bouguer anomalies (MBAs) from recent gravity and bathymetry grids of the Nansen Basin region (Figure 2.13a–c). MBAs reflect lateral density variations in the crust and mantle and should therefore indicate locally thicker crust underneath the flowline-striking highs. The 19°E flowline is associated with a broad MBA low centred on the spreading axis whereas the 13°E flowline is less distinct (Figure 2.13c). Unfortunately, the MBAs fade out where the flowline-striking highs are buried by sediments, probably as a result of low resolution of the gravity data.

Except for the 13°E flowline in Figure 2.9, the flowline-striking basement highs do not stand out from the regional basement relief. A possible explanation is that otherwise persistent flowline-striking highs may temporarily vanish due to the magmatic accretion process. On the slow-spreading Mid-Atlantic Ridge, >20-Myr-old persistent magmatic segments have created >1–2 km crustal thickness changes every 2–3 Myr because of alternating magmatic and amagmatic extension episodes [*Tucholke et al.*, 1997]. Such changes may be larger on the ultraslow-spreading Gakkel Ridge because crustal thickness tends to be more variable at lower spreading rates [*Chen*, 1992]. An alternative explanation may be that the current 2-D pattern of flowline-striking highs replaced an earlier random accretion pattern at Chron 6 times. In that case, the agreement between flowlines and pre-Chron 6 basement highs is coincidental, but we may explain why earlier measurements [*Duckworth and Baggeroer*, 1985] of thin (3 km) and relatively thick (8 km) crust do not correlate with the present ridge segmentation (Figure 2.13c). Moreover, depleted harzburgites in the sparsely magmatic zone indicate that axial mantle melting may have been more fertile at earlier times [*Michael et al.*, 2003].

A narrow MBA low along the spreading axis (Figure 2.13c) probably reflects hot upwelling below the Gakkel Ridge because the constant mantle density implied by the MBAs is too high for the axial province. In the western volcanic zone, the low is wider than in the sparsely magmatic zone, pointing to hotter mantle and/or thicker and less dense crust. The MBA low ends at Chron 5 (9.8 Ma) and coincides with a high-standing ridge block with 4–7 km crustal thickness [*Kristoffersen et al.*, 1982]. Immediately off-axis the crust is 1–3 km thick [*Jackson et al.*, 1982; 1984]. High magnetic amplitudes over the same block led *Feden et al.* [1979] to suggest a rejuvenation of volcanic activity at Chron 5 times. If this is the case, we may suggest that the western volcanic zone was amagmatic as late as ~10 Ma and actually less persistent than the magmatism of the sparsely magmatic zone.

The regional basement level rises to the west, even in the absence of sediment cover (Figure 2.4). Similarly, the oceanic MBAs increase gently towards the Fram Strait (Figure 2.13c). The broad anomaly might reflect increasing sediment thickness to the east, but its shape does not fully overlap with the large submarine fans in the Nansen and Amundsen basins. Moreover, its long wavelength suggests a mantle cause. The average mantle velocity in the eastern end of the high is 8.1 km s^{-1}, based on our 8.2 and 8.3 km s^{-1} values (SB 48 and 50) and one 8.0 km s^{-1} value from the spreading axis [*Jokat et al.*, 2003]. In the western volcanic zone, *Kristoffersen et al.* [1982] and *Jackson et al.* [1982] obtained 7.8 km s^{-1} average velocity within a 7.6–8.1 km s^{-1} range. Horizontal anisotropy in the upper mantle in is commonly 5% [*White et al.*, 1992]; therefore, the notion of a westward decrease in mantle velocities is uncertain but not rejected.

Continent–Ocean Transition and Timing of Break-up

The large fault in Line 17 (Figure 2.10; CDP 1900) is correlated to line NPD-2300-90, ~20 km to the west, where *Riis* [1994] interpreted it in terms of a narrow and steep continent–ocean transition (COT) by analogy to sheared continental margins. *Geissler and Jokat* [2004] found that the boundary fault extends for >200 km along the margin. The fault coincides with the steepest seaward gradient of the MBA field (Figure 2.13c), which is caused mainly by horizontal juxtaposition of thick crust and mantle. We may therefore use the MBA gradient to estimate the COT location between seismic profiles on the Hinlopen margin and the conjugate Lomonosov Ridge.

Vogt et al. [1979] identified seafloor spreading anomalies back to Chron 24n.3n (53.1 Ma) in the Nansen Basin and proposed another 50–100 km of transitional or older oceanic crust seaward of the continental slope. With seismic, MBA and additional magnetic constraints now available, we may review this idea. We re-identified magnetic anomalies, locating Chron 24n.3n ~20 km seaward of the boundary fault in Line 17 (Figure 2.14). The gap between the Chron 24 location and the boundary fault widens to the east and includes a broad magnetic trough with low-amplitude magnetic lineations.

Basement below the magnetic trough has variable relief and dips generally seaward. In the east it may include a ~20 km wide intermediate terrace (Figure 2.9), but this interpretation is uncertain [*Jokat and Micksch*, 2004]. Upper basement velocities are 5.2–5.3 km s^{-1} [*Geissler and Jokat*, 2004], or inconclusive in terms of crustal structure.

To interpret the magnetic trough, we compared observed and synthetic anomalies calculated from crustal block models with spreading rates derived from plate rotation poles (Figure 2.14). Because the marginal structure of the Eurasia Basin is still largely unknown, pre-Chron 24 relative plate motions rely on the assumption that the Lomonosov Ridge has been moving with the North American plate since break-up. As a result, the nearest plate tectonic constraints are sparse locations of Chron 25 in the Labrador Sea.

Published poles for the relative motion of North America with respect to Eurasia yield widely different predictions for the early opening of the Eurasia Basin [*Rowley and Lottes*, 1988]. We tested first the Chron 24 finite rotation pole from the PLATES database [*Brozena et al.*, 2003] combined with the Chron 27 pole for the Labrador Sea [*Roest and Srivastava*, 1989]. These poles predict highly oblique and slow (2.3 cm yr^{-1} half-rate) break-up of the conjugate Hinlopen and Lomonosov Ridge margins slightly before Chron 26 times (see flowlines in Figure 2.13). Observed magnetic anomalies are reproduced reasonably well and we may interpret the pre-Chron 24 lineations on either margin as Chron 25–26 (56.1–57.8 Ma) convolute seafloor spreading anomalies (Figure 2.14). It is, however, difficult to uniquely identify the anomaly as Chron 25–26 because its shape is not as distinct as younger, high-amplitude anomalies. The anomaly terminates against the Hinlopen margin east of Line 17, in accordance with the predicted sheared-margin break-up. The narrow, fault-bounded COT also agrees with a sheared margin setting, while the possible basement terrace in Figure 2.9 may indicate an eastward transition to a rifted margin segment with a more gradual COT.

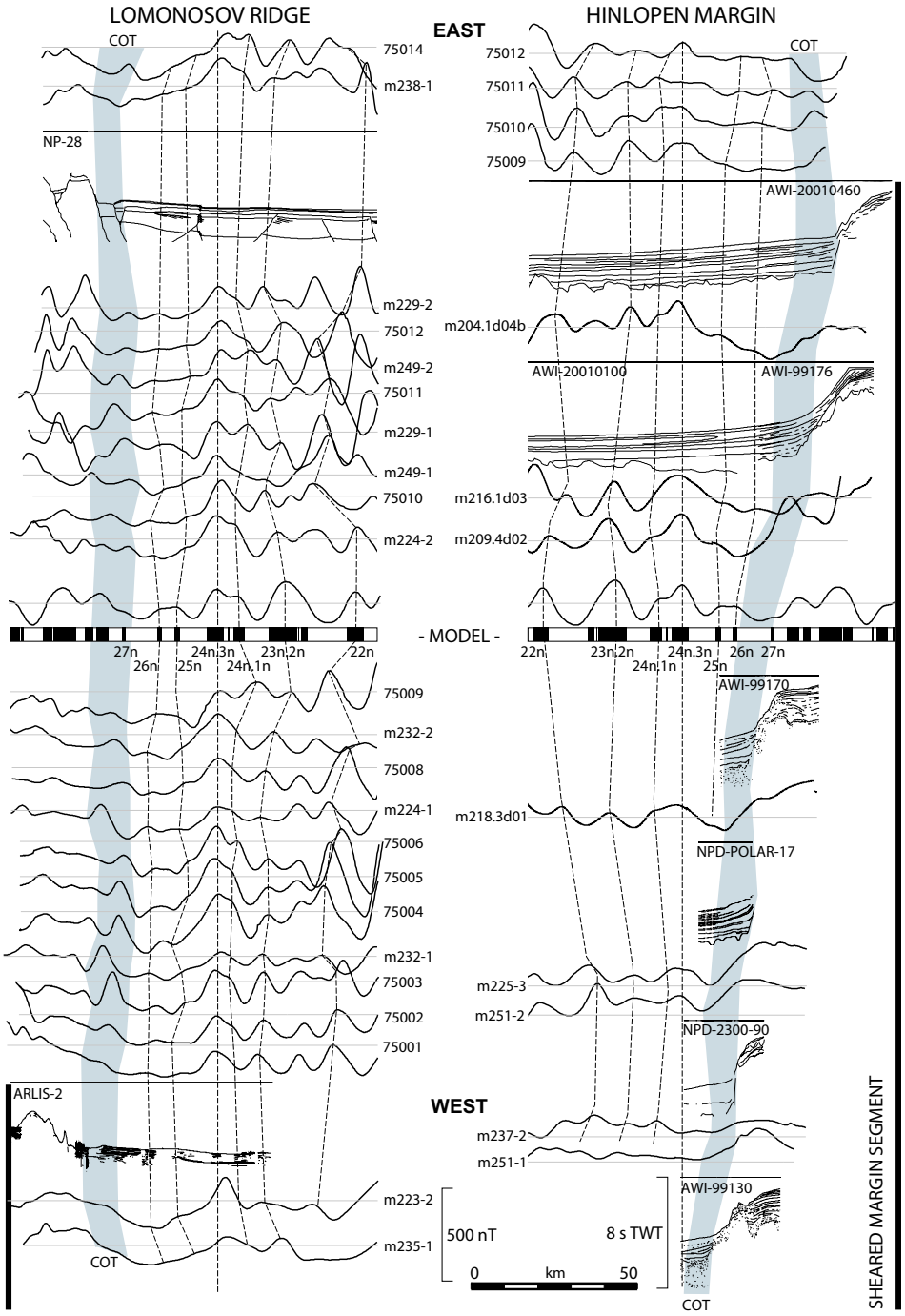
LOMONOSOV RIDGE
EAST
HINLOPEN MARGIN
COT
75014
m238-1
NP-28
m229-2
75012
m249-2
75011
m229-1
m249-1
75010
m224-2
75012
75011
75010
75009
AWI-20010460
m204.1d04b
AWI-20010100
AWI-99176
m216.1d03
m209.4d02
- MODEL -
27n
26n
25n
24n.3n
24n.1n
23n.2n
22n
22n
23n.2n
24n.1n
24n.3n
25n
26n
27n
75009
m232-2
75008
m224-1
75006
75005
75004
m232-1
75003
75002
75001
AWI-99170
m218.3d01
NPD-POLAR-17
m225-3
m251-2
NPD-2300-90
ARLIS-2
WEST
m237-2
m251-1
m223-2
m235-1
500 nT
8 s TWT
0
km
50
AWI-99130
COT
COT
SHEARED MARGIN SEGMENT

Figure 2.14 (opposite). Continent–ocean transition and magnetic isochrons on the conjugate Lomonosov Ridge (left) and Hinlopen margins (right). Seismic sections and aeromagnetic profiles (Figure 2.13) are projected on the Chron 23n.2n–24n.3n spreading direction and aligned on the Chron 24n.3n location. The synthetic magnetic profiles [*Rabinowitz and Labrecque*, 1979] assume a 2-km-thick layer at 4 km depth with 2 A m^{-1} remanent magnetisation induced by the 55 Ma paleopole of *Torsvik et al.* [2001]. Aeromagnetic tracklines from *Vogt et al.* [1979] and *Brozena et al.* [2003]; MCS lines from Table 2.1; and ARLIS-II single-channel seismic profile from *Ostenso and Wold* [1977].

The Chron 24–25 pole from *Gaina et al.* [2002] predicts orthogonal break-up at 6.7 cm yr^{-1} shortly after Chron 25, which is coeval with the break-up of the Norwegian–Greenland Sea [*Tsikalas et al.*, 2002]. Magnetic modelling of these poles yields a wide pre-Chron 24 trough with no superimposed local highs. The observed low-amplitude lineations may then represent continental fault blocks with possible magmatic intrusions as in the Norwegian–Greenland Sea [*Talwani and Eldholm*, 1977]. However, the orthogonal break-up model does not fully account for the sheared-like morphology of the Hinlopen margin. We tentatively prefer the sheared-margin model, noting that the nature of pre-Chron 24 crust is still not verified. Nonetheless, the modelling indicates a link between the Labrador Sea and the onset of seafloor spreading in the Eurasia Basin.

Conclusions

We have acquired a new dataset of 50 wide-angle velocity profiles and ~1100 km of MCS lines elucidating the regional basement and sedimentary structure of the western Nansen Basin. Bulk sediment thickness is constrained within 7% uncertainty, or 0.12 km for the deepest depocenter surveyed. The new data facilitate correlation between previous seismic studies and show four turbidite units with typical velocities 2.3, 2.2, 1.9 and 1.8 km s^{-1} (Figure 2.5). The three lower units have fairly uniform thickness, while the upper unit doubles its thickness towards the Franz-Victoria Fan which fed glaciomarine sediments into the basin from ~2.3 Ma. The deeper, regional velocity contrast from 2.2 to 1.9 km s^{-1} tentatively dates to the Late Miocene (~10 Ma) and may be linked to major paleoceanographic changes during the opening of the Fram Strait gateway.

By integrated analysis of the new data and airborne gravity and magnetic profiles, we propose that the COT on the Hinlopen margin is mainly accommodated by a steep boundary fault consistent with the Hinlopen margin as a sheared margin segment. The sparsely magmatic segment of the Gakkel Ridge has persisted since at least Chron 6 (19.6 Ma) and possibly since before Chron 18 times (39.9 Ma). The presently volcanic segment between the Yermak Plateau and the Morris Jesup Rise may have been amagmatic during Chron 5–13 times (9.8–33.3 Ma).

Acknowledgments. We thank Captain Mats Johansson and his crew aboard *MV Oden*, cruise leader Harald Brekke, and the scientific personnel for their outstanding efforts during the NPD-POLAR-2001 cruise. The Norwegian Defence Research Establishment (FFI) kindly

provided the sonobuoys. We also thank Olvar Løvås, Berit Kuvaas and Brian Taylor for support and advice, and Viktor Poselov and Anton Likhachev for Russian survey locations. Most figures were generated with the Generic Mapping Tools [*Wessel and Smith*, 1991]. Ø. E. received funding from the Norwegian Research Council (grant no. 147541/432) and the NPD.

Appendix

Table 2.3. 2-D Velocity Models Sampled in Sonobuoy Deployment Positions[a]

SB	Lat.˚N	Lon.˚E	Max. offset	Layer 1			Layer 2			Layer 3			Layer 4			Layer 5	
				WD	v_{top}	v_{bot}	z_{top}	v_{top}	v_{bot}	z_{top}	v_{top}	v_{bot}	z_{top}	v_{top}	v_{bot}	z_{top}	v_{top}
1	81.65	4.31	7.3	0.770	1.70	1.70	0.83	1.72	1.72	0.99							
2	81.68	4.77	12.6	0.760	1.61	1.61	0.83	1.81	1.81	0.97	2.00	2.00	1.13	2.20	2.20	1.64	3.24
3	81.78	5.20	11.3	0.790	1.82	1.82	1.31	1.82	1.82	1.31	2.23	2.23	1.64	2.30			
4	81.83	5.93	14.6	0.812	1.88	1.88	1.23	1.89	1.89	1.54	2.00	2.00	1.83	2.30	2.30	3.12	4.61
6	82.34	12.94	12.4	1.047	1.60	1.60	1.33	1.75	1.75	1.79	4.60						
7	82.44	12.33	14.8	0.860	3.88												
9	82.64	12.38	2.5	1.320													
10	82.92	13.82	5.3	3.270	1.70	1.70	3.61	2.90	2.90	3.89							
11	82.95	13.50	7.7	3.250	1.70	1.70	3.53	3.45									
13	83.05	12.78	6.6	2.855													
14	83.10	13.44	11.9	2.730	3.20	7.00	5.72										
15	83.20	13.81	10.8	2.500													
16	83.29	14.13	7.6	2.750	4.10	5.00	5.72										
17	83.33	14.32	4.1	4.030													
18	83.35	14.59	6.7	4.020	2.04	2.04	4.12										
19	84.13	16.68	10.3	4.040	2.00	2.00	4.45	2.69	2.69	4.82	4.47	4.47	4.90				
20	84.22	17.11	5.0	3.980	2.06	2.06	4.14										
21	84.25	17.24	9.7	4.040	1.80	1.80	4.25										
22	84.35	17.21	11.9	3.830	3.51												
24	84.47	17.18	15.2	4.040	1.88	1.88	4.42	1.89	1.89	4.61	2.41	2.41	4.66	3.77			
26	84.62	17.23	15.2	3.545	3.13												
27	84.76	17.48	7.4	3.928	3.26	3.26	4.05										
28	84.83	17.52	8.0	4.240	1.89	1.89	4.43	3.99									
29	84.87	18.17	10.7	4.080													
30	84.98	18.22	11.7	4.293	2.42												
31	85.08	18.18	24.1	3.045	3.76												
33	85.30	17.18	6.3	2.925													
34	84.49	19.22	8.6	4.030	1.80	1.80	4.45										
35	84.42	18.85	28.7	4.040	1.80	1.80	4.44	1.90	1.90	4.66	2.40	2.40	4.97	4.27			
37	84.19	19.34	23.7	4.040	1.74	1.74	4.39	1.87	1.87	4.63	4.21						
38	84.40	19.84	19.8	4.040	1.74	1.74	4.43	1.87	1.87	4.66	2.15	2.15	4.88	4.67			
39	84.58	20.17	20.3	4.040	1.74	1.74	4.41	1.87	1.87	4.62	2.25	2.25	4.65	3.65			

[a] *SB*, sonobuoy number; *WD*, water depth. Depths and offset in km, velocities in km s^{-1}.

Table 2.3 continued.

SB	Lat.°N	Lon.°E	Max. offset	Layer 1			Layer 2			Layer 3			Layer 4			Layer 5	
				WD	v_{top}	v_{bot}	z_{top}	v_{top}	v_{bot}	z_{top}	v_{top}	v_{bot}	z_{top}	v_{top}	v_{bot}	z_{top}	v_{top}
40	84.76	21.00	16.9	3.671	1.76	1.76	3.70	4.30	4.31	12.0							
41	84.91	20.95	25.8	4.230	1.92	1.92	4.51	4.13									
42	85.14	21.47	9.6	4.240	1.67	1.67	4.37										
43	85.67	14.44	21.1	3.118	4.17												
45	85.50	15.54	25.4	4.898													
46	85.33	17.28	4.4	2.820													
47	85.84	30.11	14.1	3.632	2.74												
48	85.64	30.70	12.8	3.710	1.80	1.80	3.72	4.30	4.30	5.31	5.00	5.00	6.50	8.20			
49	85.53	30.33	2.9	3.750													
50	84.98	29.03	14.9	4.020	1.70	1.70	4.42	1.71	1.71	4.61	2.38	2.38	4.67	4.30	4.32	6.97	8.33
51	84.85	28.61	12.3	4.020	1.63	1.63	4.38	1.83	1.83	4.42	3.15						
52	84.74	28.67	13.1	4.020	1.86	1.86	4.48	1.88	1.88	4.74	2.47	2.47	5.01	2.54	2.54	5.08	4.27
53	84.67	30.54	21.5	4.020	1.81	1.81	4.55	1.90	1.90	4.85	2.11	2.11	5.16	2.18	2.18	5.74	3.56
55	84.48	29.77	5.0	4.020	1.82	1.82	4.46	1.88	1.88	4.71	2.33	2.33	4.88				
57	84.41	30.06	16.1	4.020	1.74	1.74	4.46	1.83	1.83	4.73	2.09	2.09	4.97	6.94			
58	84.29	30.71	22.5	4.020	1.76	1.76	4.44	1.81	1.81	4.69	4.39						
59	84.09	31.01	14.1	4.020	1.88	1.88	4.56	1.88	1.88	4.95	2.13	2.13	5.27	2.17	2.17	5.83	5.83
60	83.96	31.36	4.6	4.020	1.88	1.88	4.50	1.88	1.88	4.85	2.20	2.20	5.07				

References

Baturin, D. (1987), Evolution of the Northern Barents Sea in the area of junction with the Eurasian Ocean Basin, *Oceanology, 27* (3), 308–312.

Baturin, D., T. Fedukhina, L. Savostin, and A. Yunov (1994), A geophysical survey of the Spitsbergen margin and surrounding areas, *Marine Geophysical Researches*, *16* (6), 463–484.

Blinova, M.K., L.G. Poselova, L.A. Dragan-Sushchova, A.D. Pavlenkin, V.V. Butsenko, and V.A. Poselov (in press), Bathymetric and seismic study of Arctic Ocean and isopach draft-map of sedimentary cover of Russian sector, in *Proceedings of the 4th International Conference on Arctic Margins*, edited by D. Thurston and R.F. Scott, Dartmouth, Nova Scotia, Canada.

Brozena, J.M., V.A. Childers, L.A. Lawver, L.M. Gahagan, R. Forsberg, J.I. Faleide, and O. Eldholm (2003), New aerogeophysical study of the Eurasia Basin and Lomonosov Ridge: Implications for basin development, *Geology, 31* (9), 825–828.

Bruguier, N.J., and T.A. Minshull (1997), Accurate modelling of sonobuoy refraction data to determine velocity variations in oceanic crust, *Marine Geophysical Researches*, *19* (1), 25–36.

Butt, F.A., A. Elverhøi, A. Solheim, and C.F. Forsberg (2000), Deciphering late Cenozoic development of the western Svalbard margin from ODP Site 986 results, *Marine Geology, 169* (3–4), 373–390.

Cande, S.C., and D.V. Kent (1995), Revised calibration of the geomagnetic polarity timescale for the Late Cretaceous and Cenozoic, *Journal of Geophysical Research*, *100* (B4), 6093–6095.

Carlson, R.L. (1998), Seismic velocities in the uppermost oceanic crust: Age dependence and the fate of layer 2A, *Journal of Geophysical Research*, *103* (B4), 7069–7077.

Cerveny, V., I. Molotkov, and I. Psencík (1977), *Ray Method in Seismology*, University of Karlova, Prague, Czechoslovakia.

Chen, Y.J. (1992), Oceanic crustal thickness versus spreading rate, *Geophysical Research Letters*, *19* (8), 753–756.

Cherkis, N.Z., M.D. Max, P.R. Vogt, K. Crane, A. Midthassel, and E. Sundvor (1999), Large-scale mass wasting on the north Spitsbergen continental margin, Arctic Ocean, *Geo-Marine Letters*, *19* (1–2), 131–142.

Choblet, G., and E.M. Parmentier (2001), Mantle upwelling and melting beneath slow spreading centers: effects of variable rheology and melt productivity, *Earth and Planetary Science Letters*, *184* (3–4), 589–604.

Cochran, J.R., G.J. Kurras, M.H. Edwards, and B.J. Coakley (2003), The Gakkel Ridge: Bathymetry, gravity anomalies, and crustal accretion at extremely slow spreading rates, *Journal of Geophysical Research*, *108* (B2), 2116, doi:10.1029/2002JB001830.

Dimakis, P., B.I. Braathen, J.I. Faleide, A. Elverhøi, and S.T. Gudlaugsson (1998), Cenozoic erosion and the preglacial uplift of the Svalbard–Barents Sea region, *Tectonophysics*, *300* (1–4), 311–327.

Duckworth, G.L., and A.B. Baggeroer (1985), Inversion of refraction data from the Fram and Nansen Basins of the Arctic Ocean, *Tectonophysics*, *114* (1–4), 55–102.

Eiken, O. (ed.) (1994), *Seismic Atlas of Western Svalbard: A Selection of Seismic Transects*, *Meddelelser 130*, 73 pp., Norsk Polarinstitutt, Oslo, Norway.

Engen, Ø., and J.I. Faleide (2005), Plate tectonic reconstruction of the North Atlantic–Arctic gateway, *Tectonophysics*, submitted. This volume, p. 127.

Ewing, W.M., G.P. Woollard, and A.C. Vine (1939), Geophysical investigations in the emerged and submerged Atlantic Coastal Plain; Part 3, Barnegat Bay, New Jersey, section, *Geological Society of America Bulletin*, *50* (2), 257–296.

Faleide, J.I., A. Solheim, A. Fiedler, B.O. Hjelstuen, E.S. Andersen, and K. Vanneste (1996), Late Cenozoic evolution of the western Barents Sea–Svalbard continental margin, *Global and Planetary Change*, *12* (1–4), 53–74.

Faleide, J.I., F. Tsikalas, A.J. Breivik, Ø. Engen, O. Eldholm, and S. Ren (2003), Late Mesozoic–Cenozoic evolution of the NE Atlantic region and links to the Arctic, *4th International Conference on Arctic Margins (ICAM IV)*, Dartmouth, Nova Scotia, Canada, 30 Sept–3 Oct.

Faugères, J.-C., D.A.V. Stow, P. Imbert, and A. Viana (1999), Seismic features diagnostic of contourite drifts, *Marine Geology*, *162*, 1–38.

Feden, R.H., P.R. Vogt, and H.S. Fleming (1979), Magnetic and bathymetric evidence for the Yermak Hot Spot northwest of Svalbard in the Arctic Basin, *Earth and Planetary Science Letters*, *44* (1), 18–38.

Fiedler, A., and J.I. Faleide (1996), Cenozoic sedimentation along the southwestern Barents Sea margin in relation to uplift and erosion of the shelf, *Global and Planetary Change*, *12* (1–4), 75–93.

Forsberg, C.F., A. Solheim, A. Elverhøi, E. Jansen, J.E.T. Channell, and E.S. Andersen (1999), The depositional environment of the western Svalbard margin during the late Pliocene and the Pleistocene; sedimentary facies changes at Site 986, in *North Atlantic–Arctic Gateways II*, *Proceedings of the Ocean Drilling Program, Scientific Results*, vol. 162, edited by M.E. Raymo et al., pp. 233–246, Texas A & M University, Ocean Drilling Program, College Station, TX, United States.

Gaina, C., W.R. Roest, and R.D. Muller (2002), Late Cretaceous–Cenozoic deformation of northeast Asia, *Earth and Planetary Science Letters*, *197* (3–4), 273–286.

Geissler, W.H., and W. Jokat (2004), A geophysical study of the northern Svalbard continental margin, *Geophysical Journal International*, *158* (1), 50–66.

Gjengedal, J.A., Y. Kristoffersen, and Ø. Engen (in prep.), Sediment deposition on the northern Yermak Plateau at the gateway to the Arctic Ocean.

Grantz, A., P.E. Hart, and S.D. May (2004), Seismic Reflection and Refraction Data Acquired in the Canada Basin, Northwind Ridge and Northwind Basin, Arctic Ocean in 1988, 1992 and 1993, Open-File Report 2004-1243, 34 pp., U. S. Geological Survey, Menlo Park, CA.

Hall, J.M., and P.T. Robinson (1979), Deep crustal drilling in the North Atlantic Ocean, *Science*, *204* (4393), 573–586.

Hooft, E.E.E., R.S. Detrick, D.R. Toomey, J.A. Collins, and J. Lin (2000), Crustal thickness and structure along three contrasting spreading segments of the Mid-Atlantic Ridge, 33.5˚N–35˚N, *Journal of Geophysical Research*, *105* (B4), 8205–8226.

Houtz, R.E., and J. Ewing (1976), Upper crustal structure as a function of plate age, *Journal of Geophysical Research*, *81*, 2490–2498.

Hunkins, K.L., H.W. Kutschale, and J.K. Hall (1969), Studies in Marine Geophysics and Underwater Sound from Drifting Ice Stations, Report No. 266(82), 102 pp., Lamont–Doherty Geological Observatory of Columbia University, New York, NY.

Hurdle, B.G. (1986), The sound-speed structure, in *The Nordic Seas*, edited by B.G. Hurdle, pp. 155–182, Springer-Verlag, New York, NY.

Jackson, H.R., I. Reid, and R.K.H. Falconer (1982), Crustal structure near the Arctic Mid-Ocean Ridge, *Journal of Geophysical Research*, *87* (B3), 1773–1783.

Jackson, H.R., G.L. Johnson, E. Sundvor, and A.M. Myhre (1984), The Yermak Plateau – formed at a triple junction, *Journal of Geophysical Research*, *89* (B5), 3223–3232.

Jackson, H.R., D.A. Forsyth, J.K. Hall, and A. Overton (1990), Seismic reflection and refraction, in *The Arctic Ocean Region*, *The Geology of North America*, vol. L, edited by A. Grantz et al., pp. 153–170, Geol. Soc. Am., Boulder, CO.

Jakobsson, M., N. Cherkis, J. Woodward, R. Macnab, and B. Coakley (2000), New grid of Arctic bathymetry aids scientists and mapmakers, *Eos, Transactions, American Geophysical Union*, *81* (9), 89, 93, 96.

Jokat, W., and U. Micksch (2004), Sedimentary structure of the Nansen and Amundsen basins, Arctic Ocean, *Geophysical Research Letters*, *31*, L02603, doi:10.1029/2003GL018352.

Jokat, W., V.Y. Buravtsev, and H. Miller (1994), Marine seismic profiling in ice covered regions, *Polarforschung*, *64* (1), 9–17.

Jokat, W., E. Weigelt, Y. Kristoffersen, T. Rasmussen, and T. Schöne (1995a), New geophysical results from the south-western Eurasian Basin (Morris Jesup Rise, Gakkel Ridge, Yermak Plateau) and the Fram Strait, *Geophysical Journal International*, *123* (2), 601–610.

Jokat, W., E. Weigelt, Y. Kristoffersen, T. Rasmussen, and T. Schöne (1995b), New Insights into the Evolution of the Lomonosov Ridge and the Eurasian Basin, *Geophysical Journal International*, *122* (2), 378–392.

Jokat, W., O. Ritzmann, M.C. Schmidt-Aursch, S. Drachev, S. Gauger, and J. Snow (2003), Geophysical evidence for reduced melt production on the Arctic ultraslow Gakkel mid-ocean ridge, *Nature*, *423* (6943), 962–965.

Karasik, A.M. (1968), Magnetic anomalies of the Gakkel Ridge and origin of the Eurasian subbasin of the Arctic Ocean, English Translation, in *Geophysical Methods of Prospecting in the Arctic*, vol. 5, pp. 8–19, Nauchno-Issled. Inst. Geologii Arktiki, Leningrad.

Kristoffersen, Y. (1990), Eurasia Basin, in *The Arctic Ocean Region*, *The Geology of North America*, vol. L, edited by A. Grantz et al., pp. 365–378, Geological Society of America, Boulder, CO.

Kristoffersen, Y. (1997), Seismic reflection surveys during Arctic Ocean-96, in *Yearbook 1995/96*, pp. 75–77, Swedish Polar Research Secretariat, Stockholm.

Kristoffersen, Y. (1998), The Eurasia Basin: An update from a decade of geoscientific research, *Polarforschung*, *68*, 11–18 (published 2000).

Kristoffersen, Y., and E.S. Husebye (1985), Multi-channel seismic reflection measurements in the Eurasian Basin, Arctic Ocean, from U.S. ice station FRAM-IV, *Tectonophysics*, *114* (1–4), 103–115.

Kristoffersen, Y., E.S. Husebye, H. Bungum, and S. Gregersen (1982), Seismic investigations of the Nansen Ridge during the FRAM I experiment, *Tectonophysics*, *82*, 57–68.

Kristoffersen, Y., M.Y. Sorokin, W. Jokat, and O. Svendsen (2004), A submarine fan in the Amundsen Basin, Arctic Ocean, *Marine Geology*, *204* (3–4), 317–324.

Kuvaas, B., and Y. Kristoffersen (1996), Mass movements in glaciomarine sediments on the Barents Sea continental slope, *Global and Planetary Change*, *12* (1–4), 287–307.

Levshin, A.L., M.H. Ritzwoller, M.P. Barmin, A. Villaseñor, and C.A. Padgett (2001), New constraints on the arctic crust and uppermost mantle: surface wave group velocities, Pn, and Sn, *Physics of the Earth and Planetary Interiors*, *123* (2–4), 185–204.

Louden, K.E., J.C. Osler, S.P. Srivastava, and C.E. Keen (1996), Formation of oceanic crust at slow spreading rates: New constraints from an extinct spreading center in the Labrador Sea, *Geology*, *24* (9), 771–774.

Ludwig, J.W., J.E. Nafe, and C.L. Drake (1970), Seismic refraction, in *The Sea*, vol. 4, edited by A.E. Maxwell, pp. 53–84, John Wiley, New York, NY.

Michael, P.J., C.H. Langmuir, H.J.B. Dick, J.E. Snow, S.L. Goldstein, D.W. Graham, K. Lehnert, G. Kurras, W. Jokat, R. Mühe, and H.N. Edmonds (2003), Magmatic and amagmatic seafloor generation at the ultraslow-spreading Gakkel ridge, Arctic Ocean, *Nature*, *423* (6943), 956–961.

Micksch, U. (2004), Sedimentary structure, subsidence history and roughness analysis of Nansen and Amundsen Basin, Arctic Ocean, Diploma thesis, 113 pp., University of Karlsruhe, Karlsruhe, Germany.

Mitchum, R.M., Jr., P.R. Vail, and J.B. Sangree (1977), Seismic stratigraphy and global changes of sea level, Part 6: Stratigraphic interpretation of seismic reflection patterns and depositional sequences, in *Seismic Stratigraphy – Applications to Hydrocarbon Exploration*, *Memoir*, vol. 26, edited by C.E. Payton, pp. 117–133, American Association of Petroleum Geologists, Tulsa, OK.

Mooney, W.D. (1989), Seismic methods for determining earthquake source parameters and lithospheric structure, in *Geophysical Framework of the Continental United States*, *Memoir*, vol. 172, edited by L. Pakiser and W.D. Mooney, pp. 11–34, Geological Society of America, Boulder, CO.

Muller, M.R., T.A. Minshull, and R.S. White (1999), Segmentation and melt supply at the Southwest Indian Ridge, *Geology*, *27* (10), 867–870.

Myhre, A.M., and O. Eldholm (1981), Sedimentary and crustal velocities in the Norwegian–Greenland Sea, *Journal of Geophysical Research*, *86* (B6), 5012–5022.

Olesen, O., J. Gellein, H. Håbrekke, O. Kihle, J.R. Skilbrei, and M.A. Smethurst (1997), Magnetic anomaly map, Norway and adjacent ocean areas, map scale 1:3,000,000, Geological Survey of Norway, Trondheim, Norway.

Ostenso, N.A., and R.J. Wold (1977), A seismic and gravity profile across the Arctic Ocean basin, *Tectonophysics*, *37*, 1–24.

Parsons, B., and J.G. Sclater (1977), Analysis of variation of ocean floor bathymetry and heat flow with age, *Journal of Geophysical Research*, *82* (5), 803–827.

Rabinowitz, P.D., and J. Labrecque (1979), Mesozoic South Atlantic Ocean and evolution of Its continental margins, *Journal of Geophysical Research*, *84* (B11), 5973–6002.

Rasmussen, E., and W. Fjeldskaar (1996), Quantification of the Pliocene–Pleistocene erosion of the Barents Sea from present-day bathymetry, *Global and Planetary Change*, *12* (1–4), 119–133.

Riis, F. (1994), North of Nordaustlandet, in *Seismic Atlas of Western Svalbard: A Selection of Seismic Transects*, *Meddelelser*, vol. 130, edited by O. Eiken, pp. 30–31, Norsk Polarinstitutt, Oslo, Norway.

Roest, W.R., and S.P. Srivastava (1989), Sea-floor spreading in the Labrador Sea – a new reconstruction, *Geology*, *17* (11), 1000–1003.

Rowley, D.B., and A.L. Lottes (1988), Plate kinematic reconstructions of the North Atlantic and Arctic – Late Jurassic to present, *Tectonophysics*, *155* (1–4), 73–120.

Sheriff, R.E., and L.P. Geldart (1995), *Exploration Seismology*, 592 pp., Cambridge University Press, New York, NY.

Solheim, A., and Y. Kristoffersen (1984), *The Physical Environment, Western Barents Sea: Sediments above the Upper Regional Unconformity: Thickness, Seismic Stratigraphy and Outline of the Glacial History, Skrifter*, vol. 179B, 26 pp., Norsk Polarinstitutt, Oslo, Norway.

Solheim, A., E.S. Andersen, A. Elverhøi, and A. Fiedler (1996), Late Cenozoic depositional history of the western Svalbard continental shelf, controlled by subsidence and climate, *Global and Planetary Change*, *12* (1–4), 135–148.

Solheim, A., J.I. Faleide, E.S. Andersen, A. Elverhøi, C.F. Forsberg, K. Vanneste, G. Ünzelmann-Neben, and J.E.T. Channell (1998), Late Cenozoic seismic stratigraphy and glacial geological development of the East Greenland and Svalbard–Barents Sea continental margins, *Quaternary Science Reviews*, *17* (1–3), 155–184.

Sorokin, M.Y., Y.Y. Zamansky, A.Y. Languinen, H. Brekke, M. Sand, and N.B. Sørenes (1998), North Pole - 28 ice drift seimic line, *3rd International Conference on Arctic Margins (ICAM III)*, Celle, Germany.

Symonds, P.A., O. Eldholm, J. Mascle, and G.F. Moore (2000), Characteristics of continental margins, in *Continental Shelf Limits: The Scientific and Legal Interface*, edited by P.J. Cook and C.M. Carleton, pp. 25–63, Oxford University Press, New York, NY.

Talwani, M., and O. Eldholm (1977), Evolution of the Norwegian–Greenland Sea, *Geological Society of America Bulletin*, *88* (7), 969–999.

Taylor, B., and P. Huchon (2002), Active continental extension in the western Woodlark Basin: A synthesis of Leg 180 results, in *Active Continental Extension in the Western Woodlark Basin, Papua New Guinea, Proceedings of the Ocean Drilling Program, Scientific Results*, edited by P. Huchon et al., pp. 1–36, Texas A&M University, Ocean Drilling Program, College Station, TX.

Thiede, J., A.M. Myhre, J.V. Firth, and the Shipboard Scientific Party (1995), Cenozoic Northern Hemisphere polar and subpolar ocean paleoenvironments (summary of ODP Leg 151 drilling results), in *North Atlantic–Arctic Gateways I, Proceedings of the Ocean Drilling Program, Initial Reports*, vol. 151, edited by A.M. Myhre et al., pp. 397–420, Texas A & M University, Ocean Drilling Program, College Station, TX.

Torsvik, T.H., J. Mosar, and E.A. Eide (2001), Cretaceous–Tertiary geodynamics: a North Atlantic exercise, *Geophysical Journal International*, *146*, 850–866.

Tsikalas, F., O. Eldholm, and J.I. Faleide (2002), Early Eocene sea floor spreading and continent–ocean boundary between Jan Mayen and Senja fracture zones in the Norwegian–Greenland Sea, *Marine Geophysical Researches*, *23* (3), 247–270.

Tucholke, B.E., J. Lin, M.C. Kleinrock, M.A. Tivey, T.B. Reed, J. Goff, and G.E. Jaroslow (1997), Segmentation and crustal structure of the western Mid-Atlantic Ridge flank, 25°25'–27°10'N and 0–29 m.y., *Journal of Geophysical Research*, *102* (B5), 10,203–10,223.

Verhoef, J., W.J. Roest, R. Macnab, J. Arkani-Hamed, and members of the Project Team (1996), Magnetic Anomalies of the Arctic and North Atlantic Oceans and Adjacent Land Areas, Open File 3125b, Geological Survey of Canada, Dartmouth, NS, Canada.

Vogt, P.R., W.Y. Jung, and J. Brozena (1998), Arctic margin gravity highs: Deeper meaning for sediment depocenters?, *Marine Geophysical Researches*, *20* (5), 459–477.

Vogt, P.R., P.T. Taylor, L.C. Kovacs, and G.L. Johnson (1979), Detailed aeromagnetic investigation of the Arctic Basin, *Journal of Geophysical Research*, *84* (B3), 1071–1089.

Weigelt, E., and W. Jokat (2001), Peculiarities of roughness and thickness of oceanic crust in the Eurasian Basin, Arctic Ocean, *Geophysical Journal International*, *145* (2), 505–516.

Wessel, P., and W.H.F. Smith (1991), Free software helps map and display data, *Eos, Transactions, American Geophysical Union*, *72*, 441, 445–446.

White, R.S., D. McKenzie, and R.K. O'Nions (1992), Oceanic crustal thickness from seismic measurements and rare-earth element inversions, *Journal of Geophysical Research*, *97* (B13), 19,683–19,715.

Zelt, C.A., and D.A. Forsyth (1994), Modeling wide-angle seismic data for crustal structure; southeastern Grenville Province, *Journal of Geophysical Research*, *99* (B6), 11,687–11,704.

Zelt, C.A., and R.B. Smith (1992), Seismic traveltime inversion for 2-D crustal velocity structure, *Geophysical Journal International*, *108* (1), 16–34.

Zelt, C.A., and B.C. Zelt (1998), Study of out-of-plane effects in the inversion of refraction wide-angle reflection traveltimes, *Tectonophysics*, *286* (1–4), 209–221.

Paper 3

Paper 3

Inversion of gravity data for sediment thickness: Case study Norwegian–Greenland Sea

Øyvind Engen[1,*], L. Neil Frazer[2], Pål Wessel[2], and Jan Inge Faleide[1]

1) Department of Geosciences, University of Oslo, Norway
2) Department of Geology and Geophysics, School of Ocean and Earth Science and Technology (SOEST), University of Hawai'i at Manoa, Honolulu, USA

Manuscript submitted to *Journal of Geophysical Research – Solid Earth*

Abstract. We explore the feasibility of using freely available gravity and bathymetry grids in a 3-D prediction of sediment thickness between seismic calibration points. The method requires that the gravity signal of the sedimentary layer can be fully separated from the observed free-air gravity. In particular, the separation has to account for thermal mantle structure beneath mid-ocean ridges and continental margins, which we approximate by a stack of 125-km-deep, 2-D finite-element models of seafloor spreading and cooling. As the gravity signal of the Moho cannot be separated from the gravity signal of the sediment–basement interface, we assume constant-thickness crystalline basement. The inversion searches for crustal parameters that produce a sediment-thickness map in minimum disagreement with observed seismic and gravity data. The map calculation is iterative, finding (1) increments to the base of the sedimentary layer by dampened downward continuation of residual gravity; and (2) an updated gravity residual from forward calculation of model gravity. The predicted sediment thickness map is constrained by depths and density estimates from an extensive seismic velocity database. It faithfully predicts the locations of >20–25-km-wide depocenters and basement highs in the Norwegian–Greenland Sea, but predicted sediment thickness values depend strongly on model assumptions and are commonly ~1 km in error. Therefore, our method is feasible for rapid, 3-D exploration of oceanic structure and gross sedimentation patterns in poorly surveyed areas such as the Arctic Ocean and several of the world's outer continental margins.

Keywords: Potential fields; Gravity anomalies and Earth structure; Gravity and isostasy; Inverse theory; Arctic region

Introduction

Bathymetry can be predicted from dense satellite-derived gravity calibrated against sparse shipboard depth soundings [*Smith and Sandwell*, 1994]. Then, if the bathymetry is already known, it should be possible to predict sediment thickness from dense gravity and sparse seismic calibration points. The idea is especially tempting in the deep ocean where the boundary between sedimentary rocks and the underlying basement represents a pronounced density contrast and existing seismic profiles may be spaced hundreds of kilometres apart.

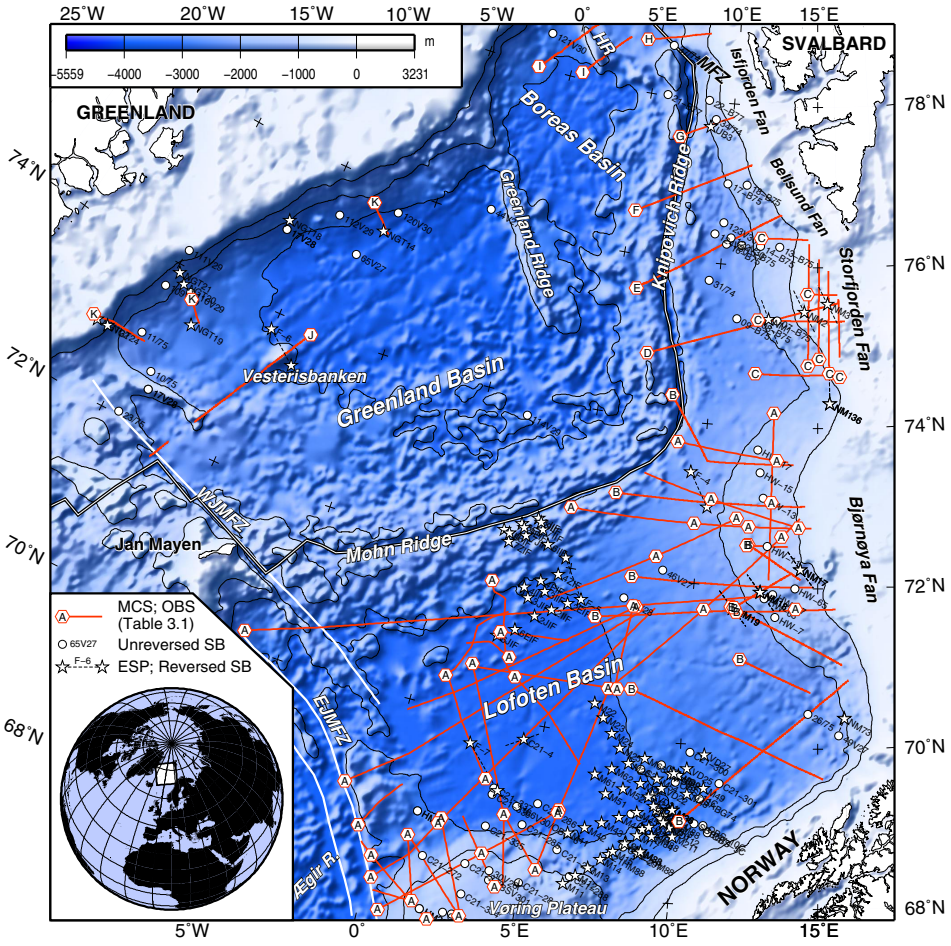

Figure 3.1. Seismic wide-angle and depth-converted multi-channel data used in this study. Only profile portions showing oceanic basement are included. Capital letters correspond to profile references in Table 3.1. IBCAO bathymetry [*Jakobsson et al.*, 2000]. Structures from *Breivik et al.* [2004]. Universal Transverse Mercator (UTM) zone 33 projection. *EJMFZ* and *WJMFZ*, East and West Jan Mayen Fracture Zone, respectively; *HR*, Hovgård Ridge; *MFZ*, Molloy Fracture Zone.

The Norwegian–Greenland Sea comprises three basins (Figure 3.1). The Lofoten and Greenland basins formed by slow seafloor spreading across the Mohn Ridge from the earliest Eocene, while the Boreas Basin emerged from Eocene–Oligocene northward propagation of the Knipovich Ridge [*Talwani and Eldholm*, 1977]. The Lofoten Basin is relatively well studied in relation to petroleum exploration on the Norwegian continental margin and might serve to calibrate predictions about the poorly surveyed Greenland Basin (Figure 3.1 and Table 3.1). High-quality bathymetry and gravity data are readily available for the entire region.

The aim of this study is to evaluate the predictive power of gravity inversion for oceanic sediment thickness. We base our work on existing techniques, primarily the well known power-series formula for the gravity of a three-dimensional density interface [*Parker*, 1972]. The formula has been adapted for inversion [*Oldenburg*, 1974] and subsequently applied to, e.g., heterogeneous basins [*Granser*, 1987; *Cowie and Karner*, 1990] and mid-ocean ridge structure [*Blackman and Forsyth*, 1991; *Phipps Morgan and Blackman*, 1993].

Most inversion schemes seek to minimise a cost or objective function that rapidly increases in value outside of the limits of measurement uncertainty and a priori geological knowledge. Therefore, the accuracy of the final solution depends strongly on pre-determined tolerances. We start by discussing the quality of our input data and the choice of earth model, then explore the resulting model space, and finally relate our findings to the depositional history of the Norwegian–Greenland Sea.

Table 3.1. Seismic Data Used in This Study[a]

Type	Coverage	Figure 3.1 letter	Reference
MCS	Lofoten Basin	A	*Vidje* [2003]
MCS; SCS	Bjørnøya Fan	B	*Fiedler* [1992]; *Fiedler and Faleide* [1996]
MCS	Storfjorden Fan	C	*Hjelstuen* [1993]; *Hjelstuen et al.* [1996]
MCS	Storfjorden Fan	D	*Breivik et al.* [1999; 2003]
MCS; OBS	SW Svalbard margin	E	*Ljones et al.* [2004]
MCS; OBS	SW Svalbard margin	F	*Ritzmann et al.* [2002]
MCS; SB	Isfjorden Fan	G	*Sundvor and Eldholm* [1979]
MCS; OBS	W Svalbard margin	H	*Ritzmann et al.* [2004]
MCS	Hovgård Ridge	I	*Karlberg* [1995]
MCS	Vesterisbanken	J	*Hempel et al.* [1991]
MCS; ESP	East Greenland margin	K	*Hinz et al.* [1987]; *Eldholm and Grue* [1994]
ESP; SB; SB-R	Regional	–	VELO Database [*Planke*, 1993]

[a]Major constituents of the VELO Database presented by *Myhre and Eldholm* [1981] and *Jackson et al.* [1990]. *ESP*, expanding spread profile; *MCS*, multi-channel seismic; *OBS*, ocean-bottom seismometer; *SB/SB-R*, unreversed/reversed sonobuoy; *SCS*, single-channel seismic.

Data

Sources and Uncertainties

Multi-channel seismic (MCS) profiles are the authoritative source of sediment and basement information, but their depth conversion depends on wide-angle P-wave velocities with significant uncertainties depending on experimental setup, signal-to-noise ratio, and subsurface heterogeneity. We classify the uncertainties of the seismic data according to the type of wide-angle measurements used. Velocities from expanding spread profiles (ESPs) are constrained by a setup that largely eliminates dipping-layer effects, and deep velocities must be considered averages over wide regions. We assign 0.2 km uncertainty to basement depths from ESPs [*Nissen et al.*, 1995] as well as reversed sonobuoys (Table 3.2). Standard ocean bottom seismometer (OBS) surveying enables detailed 2-D velocity modelling and inversion with quantitative uncertainty estimates [*Zelt and Smith*, 1992]. We follow two OBS studies in the Norwegian–Greenland Sea, indicating ~3% velocity uncertainty above upper basement levels [*Klingelhöfer et al.*, 2000; *Breivik et al.*, 2003]. Traditional plane-layer reduction of unreversed sonobuoys involves large scatter of values [*White et al.*, 1992], whereas detailed modelling indicates ~7% uncertainty of sedimentary velocities in the Arctic Ocean [*Engen et al.*, 2005, this volume]. The MCS data contain small cross-over errors which were averaged. If only refraction data are available, a major question is whether velocities in the 3–5 km s^{-1} range represent upper basaltic crust or consolidated or calcareous sedimentary rocks. In such cases the most probable basement level was picked by comparison with the nearest reflection profile along-strike [*Myhre and Eldholm*, 1981].

Table 3.2. Input Data and Model Parameters

Data Type	Uncertainty
Bathymetry	–
Age of basement	–
Seismic basement depth	0.2 km (ESP; SB-R); 3% (OBS); 7% (SB)
Seismic Moho depth	1 km (ESP; SB-R); 0.7 km (OBS); 2 km (SB)
Gravity	3 mGal

Model Parameter	A Priori Value	A Priori Uncertainty
Crystalline crustal thickness	7.08 km	0.78 km
Crystalline crustal density	2.89 Mg m^{-3}	0.23 Mg m^{-3}
Density of upper sediments	1.90 Mg m^{-3}	0.26 Mg m^{-3}
Compaction coefficient	0.15 km^{-1}	0.15 km^{-1}

A smaller number of profiles constrain depths to Moho, here defined as the top of layers with more than 7.9 km s^{-1} velocity. Based on the same sources as above, we assign 1.0 km depth uncertainty to ESP and reversed sonobuoy data, 0.7 km to OBS data, and 2.0 km to unreversed sonobuoy data (Table 3.2). These uncertainties are not

unexpected because the geological Moho is a transitional zone commonly >1 km thick [e.g., *Jarchow and Thompson*, 1989].

Gravity derived from satellite altimetry is essential for oceanic crustal studies because of its nearly uniform sampling of all seas below 81.5° latitude [*Smith*, 1998]. We employed the comprehensive grid by *Sandwell and Smith* [1997] to its 72°N northern limit where we merged it with the less detailed grid by *Andersen and Knudsen* [1998] based on the European Remote Sensing (ERS) satellites (Figure 3.2). The resolution of the grid by *Sandwell and Smith* [1997] has been tested against detailed bathymetry on the Southeast Indian Ridge, where ~4 mGal anomalies over ~9-km-wide ridges can be barely distinguished from the ambient noise [*Goff and Smith*, 2003]. Altimetric resolution should increase with higher latitudes because of better crossing angles between satellite tracks, but is limited by the altimeter footprint which is commonly 5–10 km across. Moreover, the generally higher sea states near the polar fronts decrease resolution. In the Norwegian–Greenland Sea, estimated resolution values decline linearly from ~25 km half-wavelength in the southeast to ~12.5 km in the northwest [*Yale et al.*, 1995]. Altimeter readings over sea ice, e.g. on the east Greenland shelf, are dominated by noise, but special processing has extracted gravity anomalies with resolution down to ~15 km [*Laxon and McAdoo*, 1994; *Childers et al.*, 2001]. Overlapping altimeter-derived and surface gravity measurements in the Arctic Ocean differ by 2.64–3.11 mGal [*Childers et al.*, 2001] so we may assume 3 mGal uncertainty of the satellite grid.

To increase high-wavenumber information, we merged the satellite grid with shipborne gravity data from the National Geophysical Data Center (Figure 3.2). The marine data were pre-processed by quadratic trend removal, instead of the customary level and drift correction of crossing tracks [*Wessel and Watts*, 1988], giving a better fit to the satellite data. Notwithstanding, the drift analysis yielded 2.8 mGal average crossover error, which does not change our initial uncertainty figure (Table 3.2).

The IBCAO bathymetry grid [*Jakobsson et al.*, 2000] resolves the seafloor in 2.5 km detail. Being constructed from variably spaced surface-ship and submarine soundings, it is accurate near the Norway–Svalbard continental margin and in some locations on the mid-ocean ridge, but contains a large proportion of interpolated values elsewhere. On plain, sediment-covered seafloor the interpolation does not pose any problem, but in axial locations the gridded bathymetry may be locally several hundred meters in error. We regard the bathymetric uncertainties as negligible compared to those of the seismic and gravity data.

Basement ages of the Norwegian–Greenland Sea were obtained from correlation of seafloor spreading anomalies with the geomagnetic polarity timescale of *Cande and Kent* [1995]. The age of the continent–ocean boundary was set to 55 Ma in the Lofoten and Greenland basins [*Tsikalas et al.*, 2002] and interpreted from plate flowlines further north. Locations of seafloor spreading anomalies and the continent–ocean boundary were taken from the works of *Skogseid and Eldholm* [1987] and *Åkermoen* [1989] south of Jan Mayen Fracture Zone; *Talwani and Eldholm* [1977] and *Tsikalas et al.* [2002] in the Lofoten and Greenland basins; and *Engen and Faleide* [2005, this volume] north of the Greenland Ridge (Figure 3.3). The resulting age model has uncertainties related to: (1) ambiguous, low-amplitude magnetic anomalies north of Greenland Ridge; (2) navigational errors of 10–15 km in the

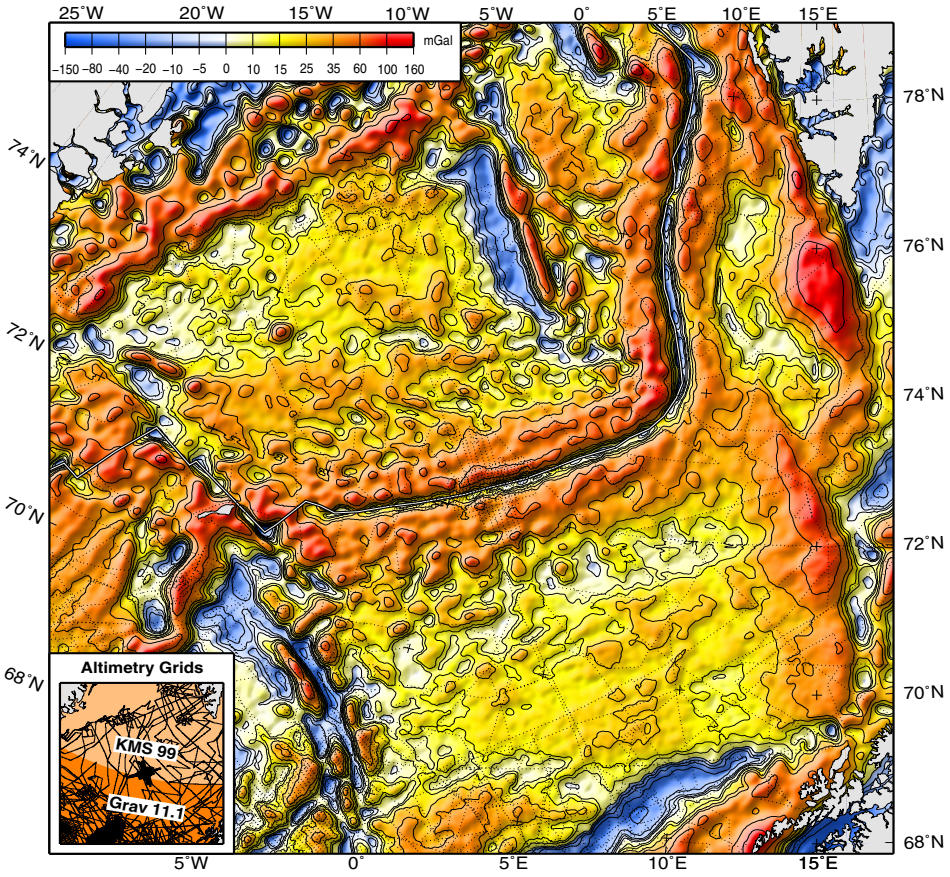

Figure 3.2. Free-air gravity of the Norwegian–Greenland Sea from combined altimetry-derived and shiptrack values. Grav 11.1 1×1 min. grid from *Sandwell and Smith* [1997]; KMS 99 2×2 min. grid from *Andersen and Knudsen* [1998]; and shiptrack gravity (dotted lines) from the National Geophysical Data Center (http://www.ngdc.noaa.gov/mgg).

magnetic data [*Brozena et al.*, 2003]; and (3) the fact that seafloor spreading anomalies are caused by a crustal region wider than the interpreted isochron line. However, the combined influence of these uncertainties on the subsequent modelling is beyond the scope of this paper and we are forced to assume it is small.

Geological Features Revealed

The ocean basins narrow to the north, reflecting progressively younger times of break-up, and are compartmentalised by the Greenland and Hovgård ridges which are continental slivers rifted off the Norway–Svalbard continental margin [*Engen and Faleide*, 2005, this volume]. The regional ocean depth is 1 km above the global average, increases gently towards Iceland, and has been attributed to a regional, hot asthenospheric lens connected to the Iceland hotspot [*Cochran and Talwani*, 1978; *Vogt*

et al., 1981]. The ridge valleys and flanks of the Mohn and Knipovich ridges stand out in the bathymetry as well as in the free-air gravity. Amplitudes of second-order gravity anomalies indicate asymmetric axial profiles with polarities changing every 120–150 km, not unlike inside–outside corner complexes on the Mid-Atlantic Ridge and in the Eurasia Basin [*Cochran et al.*, 2003]. Negative bathymetry and gravity anomalies in the Jan Mayen Fracture Zone are the only direct indications of fracture zone crust in the Norwegian–Greenland Sea.

The Knipovich Ridge has asymmetric flank relief because its eastern flank is buried by the Bjørnøya and Storfjorden submarine fans resulting from Cenozoic uplift and erosion of the Barents Sea shelf. The fans are up to 7 km thick and contain ~788,000 km^3 of sedimentary rock of which two thirds were deposited during the glacial period (<2.3 Ma) [*Faleide et al.*, 1996; *Fiedler and Faleide*, 1996; *Hjelstuen et al.*, 1996]. The rapid shelf outbuilding has created oval, ~50–150-mGal, margin-parallel free-air gravity anomalies typical of glacial margins [*Vogt et al.*, 1998; *Breivik et al.*, 1999; 2003]. Seismic profiles on the east Greenland continental slope show 1–2 km sedimentary cover [*Hinz et al.*, 1987]. Noting narrower shelf-edge gravity anomalies and rougher ridge topography we expect that less sediment has been transported across the east Greenland continental shelf than across the Barents Sea.

A particular feature of the Greenland Basin is the Vesterisbanken seamount which is neither part of any seamount chain nor mirrored across the spreading axis. Seismic and petrologic analysis indicates a <1-Myr-old, once sub-aerial volcanic emplacement on ~44-Myr-old oceanic crust [*Cherkis et al.*, 1994; *Haase and Devey*, 1994].

Data Reduction

Using a spline-in-tension algorithm [*Smith and Wessel*, 1990], we sampled all data into grids with 2×2 km cell size and Cartesian coordinates given by the UTM zone 33 projection. The gravity grids were extended to 1024 cells in each direction and linearly tapered to zero on their edges. The seismic data (Table 3.1) were obtained as depth-converted line-drawings except for the MCS profile over Vesterisbanken which we interpreted and depth-converted using seismic velocities from two nearby sonobuoy profiles (Figure 3.1). In grid cells with multiple seismic depth values we picked the median depth.

The free-air gravity field is similar to low-pass filtered bathymetry because the seafloor commonly represents a large density contrast and is less smoothed by upward continuation than the deeper crustal boundaries. To recover the weaker signal from sediment-covered basement relief, we removed the gravity effect of the seafloor using four terms of the formula of *Parker* [1972]. The resulting Bouguer anomalies are assumed to result from lateral density contrasts in sediments, oceanic crystalline crust, and the upper mantle.

Upper mantle temperatures decrease with oceanic crustal age because of heat loss vertically to the seafloor and laterally to the adjacent continental lithosphere. Neglecting increased mantle densities due to 1 Myr of near-axis cooling leads to ~10 mGal gravity misfit with the observed data, which might be mis-interpreted as a ~1.5-km-deep sediment depocenter [*Phipps Morgan and Blackman*, 1993]. In continental margin settings, the misfit made by assuming constant mantle density may exceed 150 mGal [*Breivik et al.*, 1999]. Such misfits are long-wavelength, but we

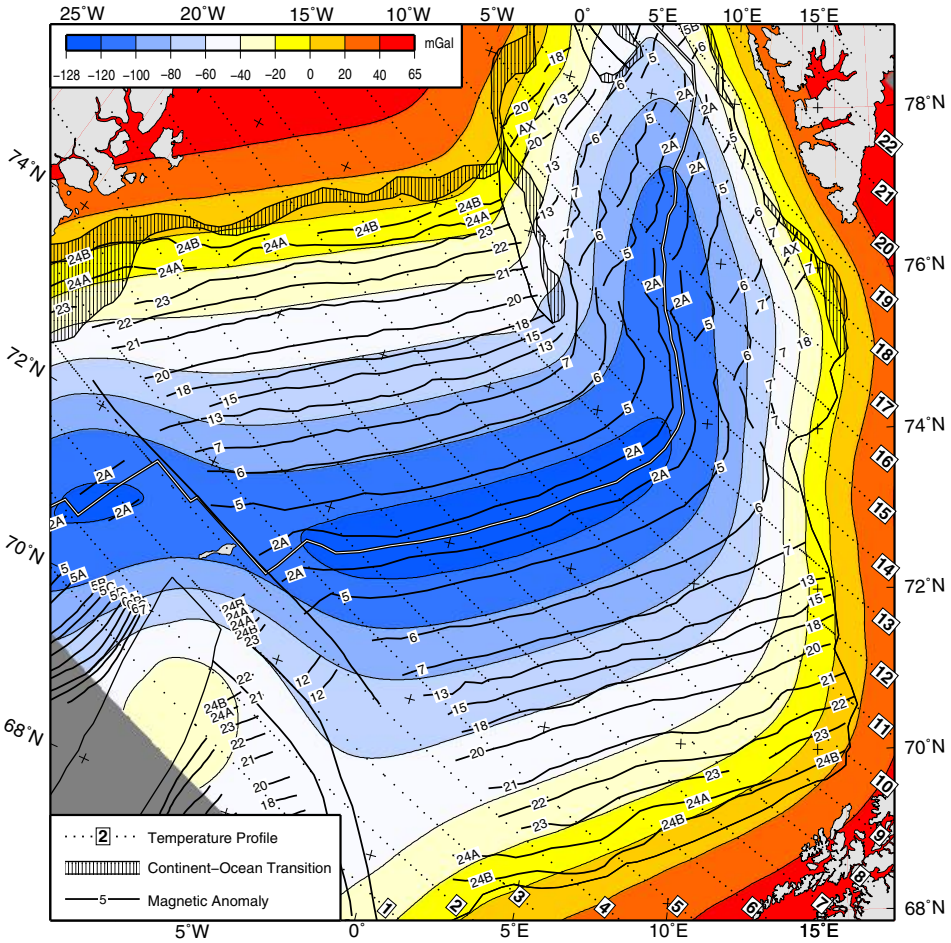

Figure 3.3. Gravity field due to mantle thermal structure. Temperatures were estimated down to 125 km depth in the synthetic profile points shown, based on basement ages indicated by magnetic anomalies and the mantle parameters in Table 3.3.

recommend against their removal by simple high-pass filtering. Depths to oceanic isotherms show a square-root dependence of age [*Parsons and Sclater*, 1977], and because square-root functions have a wide frequency spectrum, frequency cut-off would either leave a remainder of mantle gravity signal or remove some of the precious sediment/basement signal.

We prefer instead to model the gravity effect of some reasonable mantle density structure. We defined ~60-km-spaced synthetic temperature profiles running from the spreading axis and >150 km into continental crust along the current plate spreading direction (Figure 3.3). Each profile was sampled at 1 Myr intervals in the horizontal direction, i.e. with node spacing depending on the rate and direction of seafloor spreading, while the vertical direction was sampled every 6.25 km from the seafloor to 125 km depth. We modelled the present temperature distribution along

profiles [*Breivik et al.*, 1999] by (1) assuming a linear geothermal gradient and no radiogenic heat production in continental lithosphere; (2) emplacing columns of hot, new lithosphere for every 1 Myr of seafloor spreading; and (3) computing the subsequent cooling by a 2-D finite element routine [*Lee et al.*, 1980] using the mantle parameters in Table 3.3.

The final temperature distribution is sensitive to the chosen thermal diffusivity value but largely invariant to thermal conductivity within realistic ranges for mantle rock. Comparing modelled and observed heat flow values along profiles (Figure 3.4), we observe that model values are acceptable on the ridge flanks but too high near the spreading axis. This is probably because axial mantle temperatures are lowered by convection and not only by the assumed conductive cooling. The outcome may be somewhat too low mantle densities in the ridge province, yielding too much thermal correction of the gravity field and consequently local overprediction of sediment thickness.

We converted temperatures to densities using a constant thermal expansion coefficient for mantle rock (Table 3.3). In our model, density decreases monotonically with depth while in reality, pressure and mineral phase changes start to outweigh thermal expansion at ~30 km depth [*Kimbell et al.*, 2004]. However, we may assume that pressure and phase changes occur at constant depths and therefore do not significantly affect lateral density contrasts which are the cause of gravity anomalies. The estimated 'thermal' gravity field

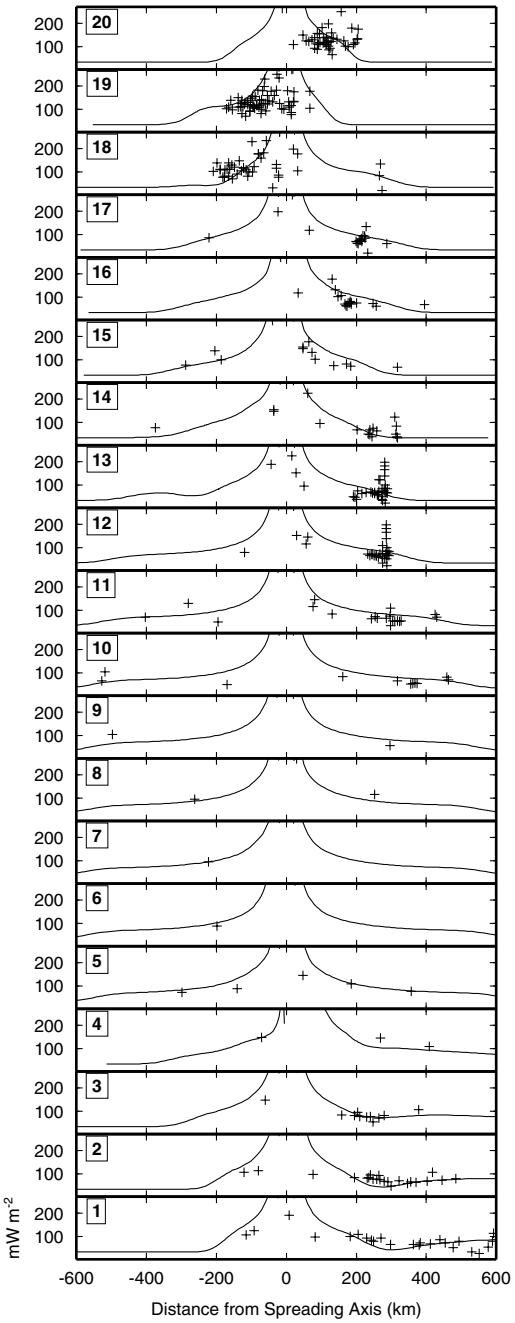

Figure 3.4. Modelled (lines) and observed (crosses) heat flow values along synthetic temperature profiles (location in Figure 3.3). Observed values from *Sundvor et al.* [2000].

was computed [*Parker*, 1972] from density contrasts between 25 and 125 km depth (Figure 3.3) and subtracted from the complete Bouguer anomalies. The so computed residual Bouguer anomalies (Figure 3.5) serve as input for the inversion.

Table 3.3. Mantle Parameters, Thermal Modelling

Parameter	Value
Compensation depth	125 km
Temperature at top	0°C
Temperature at compensation depth	1330°C
Thermal conductivity	3.1 W m^{-1} K^{-1}
Thermal diffusivity	7.5×10^{-7} m^2 s^{-1}
Internal heat production	0 W
Volume thermal expansion coefficient	3.2×10^{-5} K^{-1}
Density at 0°C	3.33 Mg m^{-3}

Earth Model

Assuming that the gravity effects of all other density contrasts have been successfully removed, we propose that the residual Bouguer anomalies are caused by density contrasts at the top and bottom of the oceanic crystalline crust. The crustal model may be tentatively parameterised by (1) the thickness of the basement layer; (2) the density of basement rocks; (3) the density of the uppermost sedimentary rocks; and (4) its variation with overburden (Figure 3.6). Variations in the density of sea-water are an order of magnitude lower than that of rock so we may regard it as constant.

Crystalline Crustal Thickness

The globally averaged thickness of oceanic crystalline crust is 7.08±0.78 km [*White et al.*, 1992] while 3–4 km thickness may be common along the Mohn Ridge [*Klingelhöfer et al.*, 2000]. Density contrasts at the top and bottom of such a thin layer produce interfering gravity anomalies and we cannot resolve the top of the crystalline crust without a model relating it to the Moho. A natural assumption would be that the crust is locally compensated at the Moho level, so that a basement high would be underlain by a Moho low 2–3 times as large. However, oceanic lithosphere along the western Barents Sea margin has ≥15 km effective elastic thickness [*Breivik et al.*, 1999] and the long-wavelength isostatic compensation depth may be as deep as 125 km [*Parsons and Sclater*, 1977]. OBS models in the same area (Table 3.1) suggest that basement relief is not fully compensated by the Moho. It is nonetheless difficult to assign one type of crustal compensation to the entire Norwegian–Greenland Sea because it is likely affected by several loading mechanisms. The above lack of shallow compensation may be a consequence of rapidly emplaced glaciomarine fans on rigid oceanic lithosphere. Moreover, high flexural rigidity may be expected from low regionally averaged melt supply

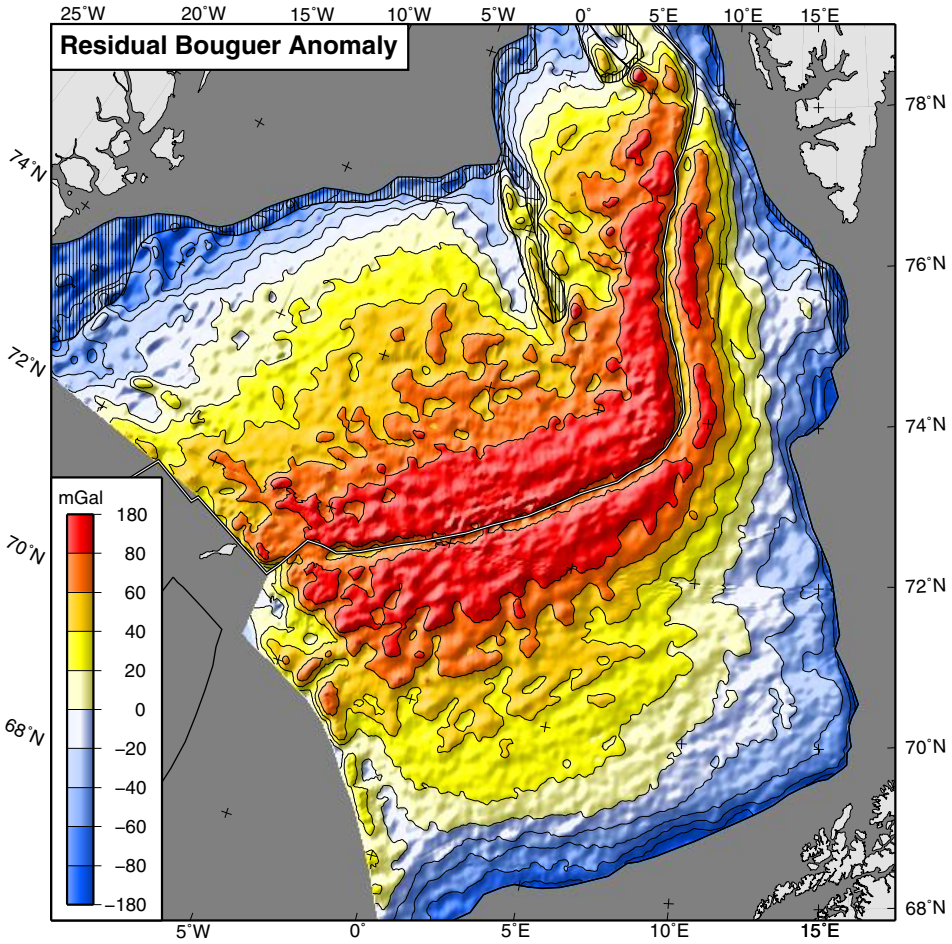

Figure 3.5. Residual Bouguer anomalies, calculated from the free-air gravity (Figure 3.2) by subtracting the gravity effect of the seafloor and mantle thermal structure (Figure 3.3).

associated with ultraslow spreading ridges [*Cannat et al.*, 2003]. Seamounts such as Vesterisbanken also involve flexural isostasy.

Assuming constant-thickness crystalline crust gives the best initial fit to the observed gravity. The seismic data (Table 3.1) indicate 8.6±3.3 km thickness, but because they mainly sample marginal oceanic crust, we consider them non-representative and prefer the *White et al.* [1992] values (Table 3.2).

Crystalline Crustal Density

The upper oceanic basement has typical layer 2 seismic velocities, 4.70±0.88 km s^{-1}, corresponding to 2.89±0.23 Mg m^{-3} density [*Ludwig et al.*, 1970]. Drilling constraints from within the area do not yet exist, but well logs from the central Atlantic show 2.62–2.69 Mg m^{-3} densities of layer 2 and 2.86±0.3 Mg m^{-3} of layer 2

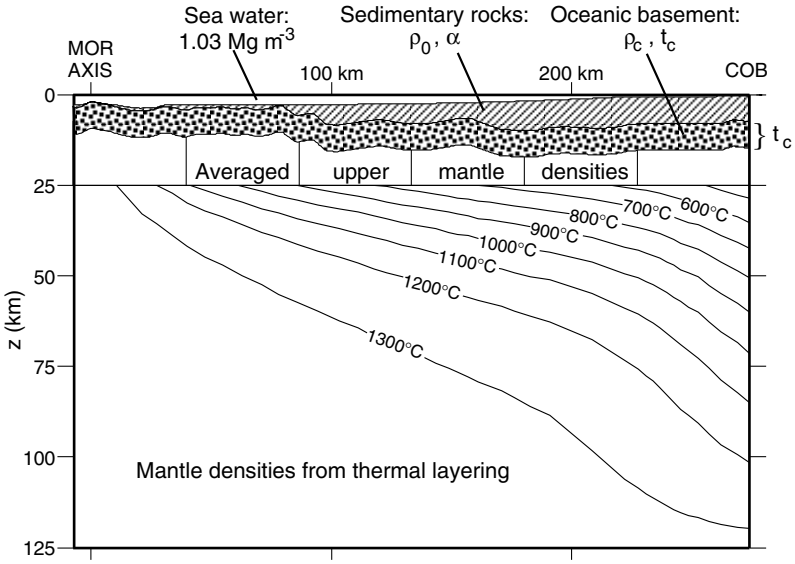

Figure 3.6. Earth model for sediment thickness inversion.

and 3 combined [*Carlson and Herrick*, 1990]. A major question is how the large spread of top basement velocities in the Norwegian–Greenland Sea translates into density. Velocities are lower than average (3.9 km s^{-1}) in crust younger than 10 Ma [*Myhre and Eldholm*, 1981] and significantly higher (5.6–7.1 km s^{-1}) in the Eocene basement underneath the Bjørnøya and Storfjorden fans [*Myhre and Eldholm*, 1988; *Jackson et al.*, 1990]. However, all these velocities are appropriate for basalt at different alteration stages and sustain the claim that basement velocity is influenced by crustal age and sediment overburden [*Purdy*, 1987; *Jacobson*, 1992]. The corresponding influence on density may be far lower because basalt porosity manifests itself mainly as small cracks which readily close under hydrochemical alteration and lithostatic pressure; in fact, a doubling of seismic velocity may reflect only 5% porosity loss [*Wilkens et al.*, 1991]. If the lowest basement velocities do correspond to 2.6 Mg m^{-3} density, the highest velocities may correspond to 2.8 Mg m^{-3}.

Densities increase downward into oceanic layer 3. We nonetheless prefer a homogeneous basement layer because the gravity difference of a one-layer and a two-layer basement model is typically only ~1 mGal as long as the layering is smooth and the total density contrast between seawater and mantle is maintained [*Blackman and Forsyth*, 1991]. Our homogeneous basement assumption is violated by lateral density contrasts in the lower crust. Magmatism at slow- and ultraslow-spreading ridges is focused at segment centres, creating well-developed crystalline layering, while layer 3 appears thin or absent at segment boundaries [*Muller et al.*, 1999; *Hooft et al.*, 2000; *Klingelhöfer et al.*, 2000]. However, we do not have sufficient data to include such density contrasts in our model. We settle on 2.89 Mg m^{-3} as an average basement density (Table 3.2).

Densities of the uppermost mantle were taken from the thermal modelling. Between the seafloor and 25 km depth, we computed column averages in order to reduce the influence of hypothetical thermal boundaries on the inversion (Figure 3.6). Therefore, the density contrast across the Moho is variable in our model.

Sedimentary Density as a Function of Overburden

Densities in the 1.2–2.0 Mg m^{-3} range can be inferred from ODP and DSDP drillholes penetrating the uppermost kilometer of sedimentary rocks [*Talwani et al.*, 1976; *Thiede et al.*, 1995]. The deeper sedimentary densities were obtained from seismic velocities [*Ludwig et al.*, 1970] with the precaution that one particular velocity corresponds to a range of equally probable densities [*Barton*, 1986]. Sampling staircase velocity–depth functions mid-way between break points (Figure 3.7a), we observe a higher velocity–depth gradient in the Storfjorden Fan than in the Bjørnøya Fan [*Myhre et al.*, 1982; *Fiedler and Faleide*, 1996; *Hjelstuen et al.*, 1996], but these regional differences are reduced in the conversion from velocity to density (Figure 3.7b). The distribution of converted densities agrees with in situ density–depth curves for Miocene sedimentary rocks [*Gregory*, 1977]. Given the 2.89 Mg m^{-3}

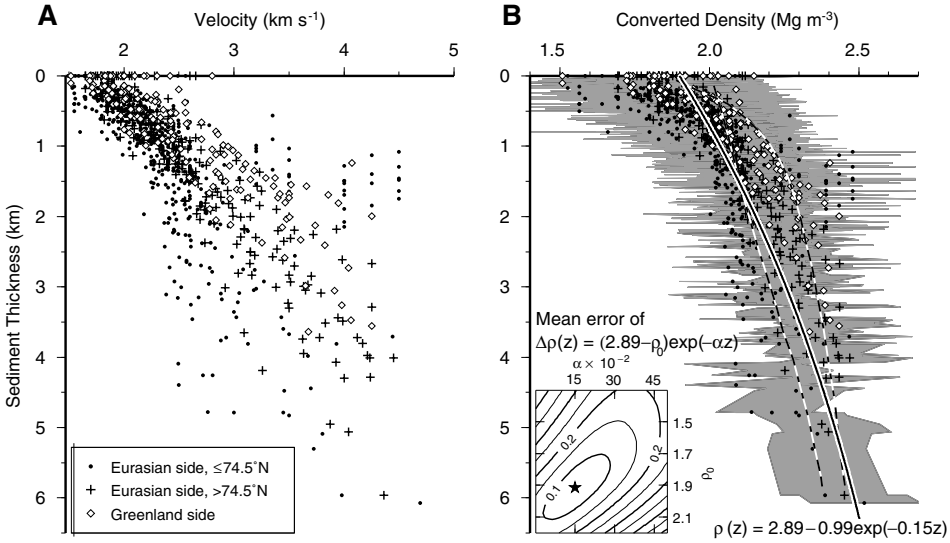

Figure 3.7. (A) Distribution of sedimentary seismic velocities in the Norwegian–Greenland Sea with respect to depth below seafloor (z). Data points were sampled mid-way between break points of staircase velocity–depth functions stored in the VELO database (Table 3.1). Velocities increase more rapidly with depth in the northern and western part of the basin than in the southern part. **(B)** Estimated density distribution calculated from (A) using the velocity–density relationship of *Ludwig et al.* [1970]. Grey-shaded area shows the range of densities possible for each velocity [*Barton*, 1986]. Best-fit density–depth curve (bold line) obtained by inversion for density of uppermost sediments (ρ_0) and sedimentary compaction coefficient (α). 2.89 Mg m^{-3} basement density assumed. Inset shows contoured misfit for different values of ρ_0 and α. In situ density–depth curves from well logs [*Gregory*, 1977] shown by dashed lines.

basement density, we crudely approximated these curves by assuming that the density contrast to the underlying basement is given by $\Delta\rho(z) = (2.89-\rho_0) \times \exp(-\alpha z)$ where ρ_0 is the density of the uppermost sediments, α is the compaction coefficient, and z is distance downward from the top of the sediments (Figure 3.7b). An L1 inversion where weights increased proportionally with depth yielded ρ_0=1.9 Mg m^{-3} and α=0.15 km^{-1} (Figure 3.7b and Table 3.2). These values are robust as to the predetermined basement density; if basement density increases by 5% from top to bottom of Figure 3.7b, the density contrast is not altered by more than 0.06 Mg m^{-3} anywhere.

Inversion Procedure

Parameter Search

The inversion for sediment thickness consists of two separate inversions. First, we want to find sediment thickness from gravity, bathymetry and seismic calibration points. Second, we do not know what reasonable values of the model parameters (Figure 3.6) create the most probable of an infinite number of possible sediment thickness models.

The calculation of sediment thickness is based on the recipe of *Phipps Morgan and Blackman* [1993] and comprises:

1. Remove from free-air gravity the attraction of the seafloor and mantle thermal structure;
2. First time through, obtain a candidate basement surface by interpolation between seismic calibration points; in later iterations, calculate increments to this surface by filtered downward continuation of the residual gravity;
3. Set Moho to equal the most recent basement surface plus crystalline crustal thickness;
4. Calculate the gravity effect of the basement increment, using the formula of *Parker* [1972] modified for depth-dependent density contrasts [*Granser*, 1987];
5. Calculate the gravity effect of the Moho increment from the formula of *Parker* [1972];
6. Remove the gravity contributions of steps 4 and 5 from the residual gravity.
7. Repeat steps 2–6 until the average residual gravity is <1 mGal or, alternatively, <1% less than the residual gravity from the previous iteration.
8. Find sediment thickness from the difference between seafloor and basement depths.

The inverse calculation in step 2 is stabilised by a filter penalizing high slopes of the surface [*Phipps Morgan and Blackman*, 1993], thereby preventing high-frequency noise which is otherwise a consequence of downward continuation.

The inversion for the most probable model parameters should evaluate the probability density function of the problem, as constructed from the residuals and prior density distributions of the data and model parameters. However, because we are interested in where the maximum probability is, rather than the absolute

probability values, we simplified the problem to finding the minimum of the cost function ϕ,

$$\varphi(\boldsymbol{m}) \propto W_g \left\| \boldsymbol{C}_{gg}^{-1/2} (\boldsymbol{g}_{obs} - \boldsymbol{g}_{mod}) \right\| + W_s \left\| \boldsymbol{C}_{ss}^{-1/2} (\boldsymbol{s}_{obs} - \boldsymbol{s}_{mod}) \right\| + W_n \left\| \boldsymbol{C}_{nn}^{-1/2} (\boldsymbol{n}_{obs} - \boldsymbol{n}_{mod}) \right\| + W_m \left\| \boldsymbol{C}_{mm}^{-1/2} (\boldsymbol{m} - \boldsymbol{m}_{ref}) \right\| \quad (3.1)$$

Here, the vectors $\boldsymbol{g}_{mod}$, $\boldsymbol{s}_{mod}$ and $\boldsymbol{n}_{mod}$ are the gravity, basement surface and Moho, respectively, calculated from the model parameter set **m**. The vectors $\boldsymbol{g}_{obs}$, $\boldsymbol{s}_{obs}$ and $\boldsymbol{n}_{obs}$ are the corresponding observed data and $\boldsymbol{m}_{ref}$ is the a priori set of model parameters (Table 3.2). The **C**'s are covariance matrices; because we assume independent data, these contain inverse squared uncertainties of each data point or model parameter. The ‖…‖ brackets denote L1 vector norms and the W's are weights designed to bring each term to the same order of magnitude. We chose an L1 norm rather than the least-squares criterion in hopes of reducing the influence of outliers. The value of the cost function is large if the modelled data are outside the bounds of measurement uncertainty, and if the model parameters are geologically unreasonable. Thus, the inversion works as an automated extrapolation procedure, seeded by seismic calibration points and aided by gravity, bathymetry and prior geological knowledge.

Because there are only four parameters in the model, we preferred to compute the cost function for the entire model space near the a priori parameter values, and then do a grid search for the parameter set corresponding to the minimum value. This method is less elegant and more time-consuming than direct search algorithms, but allows the precision of the solution to be visualised.

Sensitivity to Model Parameters

In order to test how the above inversion scheme illuminates different model parameters, we devised a synthetic model with 3-km-high and 80-km-wide basement ridges buried underneath a plain seafloor, and crustal properties as given in Table 3.2. We calculated the gravity attraction of the model and added 3 mGal Gaussian noise to simulate observed gravity data. Contours of the cost function around the a priori parameter values show that the solution is sensitive to the choice of upper sedimentary density, and somewhat less sensitive to upper basement density and compaction coefficient (Figure 3.8). However, the cost function does not have any closed minimum for crystalline crustal thickness and the grid search fails to locate the true value. Accordingly, crystalline crustal thickness can be skipped in the inversion of observed data. This result is not unexpected since the gravity fields of two depth-shifted but otherwise identical surfaces have the same overall shape.

Sediment Thickness Map

The inversion found a set of optimal model parameters near the a priori determined parameter values and well within their associated uncertainties (Figure

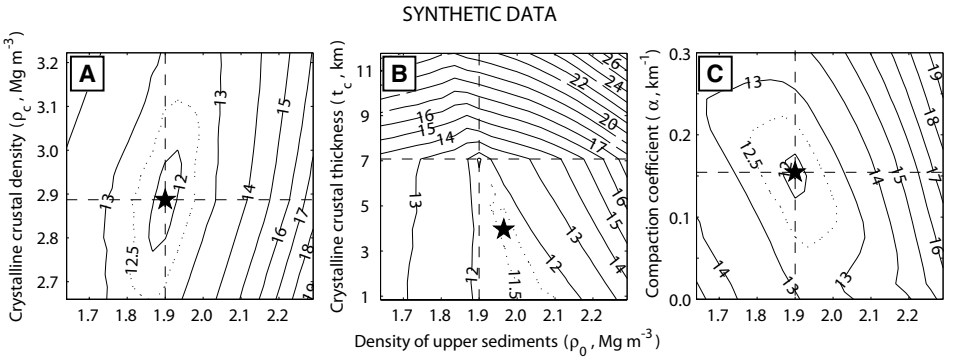

Figure 3.8. Ability of the inversion to recover geologically reasonable model parameters. Synthetic gravity was calculated from the earth model (Figure 3.6) using the a priori parameter values indicated by dashed lines. Recovered parameter values (stars) and contours of the cost function show the influence of the pre-determined earth model on the inversion. **(A)** The inversion is sensitive to the chosen density of upper sediments (ρ_0) and slightly less sensitive to crystalline crustal density (ρ_c). **(B)** Choice of crystalline crustal thickness (t_c) is insignificant. **(C)** Compaction coefficient (α) is about as significant as crystalline crustal density (A).

3.9). These optimal parameters predict realistic basement topography with depocenters and highs at spatial scales >20–25 km (Figures 3.10 and 3.11). However, the absolute depths and thicknesses do not everywhere agree with seismic calibration points.

The first-order errors take place near the continental margins (Figure 3.11) and relate to incorrect model assumptions (Figure 3.6). Along the Vøring Plateau margin, up to 4 km thickness errors correlate with the area of a lower crustal body at the continent–ocean transition [*Eldholm and Grue*, 1994]. In this case, the assumption of constant crystalline crustal thickness implies too large mass of the lower crust which has to be incorrectly compensated by low-density sediments in order to match the gravity field. On the conjugate east Greenland margin, Figure 3.11 predicts >5 km sediment thickness in a wide area below the shelf while magnetic and seismic refraction data are consistent with 20–22-km-thick crust including dike complexes and shallow break-up lavas [*Hinz et al.*, 1987; *Schlindwein and Jokat*, 1999; *Tsikalas et al.*, 2002]. Because of the conjugate margin setting we expect thickness errors comparable to the Vøring Plateau margin; however, the region is not masked in Figure 3.11 because MCS calibration points are lacking. Along the Vøring Plateau margin the misfit area extends to the East Jan Mayen Fracture Zone, where it corresponds to an area of ~15 km igneous crustal thickness created by Late Miocene underplating possibly coming from the Ægir Ridge [*Breivik et al.*, 2004]. Smaller thickness errors at the Vesterisbanken seamount and the northern Hovgård Ridge may arise from locally incorrect assumptions about basement density or isostatic compensation.

In the thickest parts of the Bjørnøya and Storfjorden fans, ~1 km thickness errors indicate too low assumed density contrasts at the bottom of the sedimentary layer. The primary cause appears to be that densities of deeply buried sedimentary rocks are overestimated because the fitted density–depth curve is too low-order (Figure

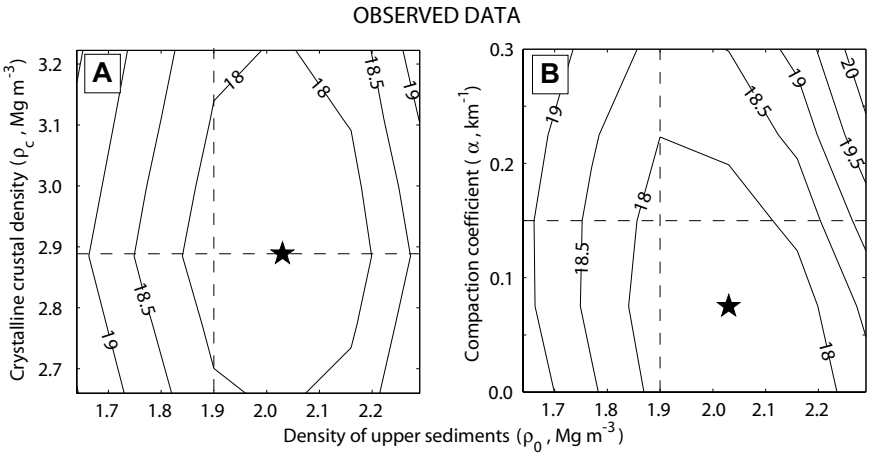

Figure 3.9. Contours of the cost function for the inversion of real gravity data (Figure 3.5). A priori model parameters shown by dashed lines; inverted (minimum-cost) parameters shown by star. Broad minima indicate that a range of parameter values are almost equally probable within pre-determined uncertainty limits (Table 3.2). **(A)** Inverted crystalline crustal density agrees with prior information while upper sediments are probably denser than assumed. **(B)** Compaction of sediments with depth may be slower than calculated from Figure 3.7.

3.7). In addition, the gravity inversion has low resolution at the largest sedimentary depths.

Second-order thickness errors are related to the over-simplifying assumption that bathymetry and the thermal gravity field are exact. On the mid-ocean ridge flanks, there is >3 mGal gravity misfit because the inverted basement surface is not allowed to cross the seafloor even if higher basement is required to match the gravity. Predicted basement at the Greenland Ridge is ~1 km below its actual outcrop and predicted sediment thickness is too large below the mid-ocean ridge axis (Figure 3.12). At several locations close to the continent–ocean boundary, predicted sediment thickness increases landward by 0.5–2 km. These observations point to the thermal mantle model, where we assumed that the Greenland Ridge originated as a continental sliver and we know that temperatures near the spreading axis are over-estimated (Figure 3.3). In addition, if we allow an Airy isostatic crustal root beneath the Greenland Ridge, the inversion would be given more mass to distribute at the basement surface, and local basement level would be closer to the seafloor. If assumed temperatures of the continental lithosphere are too high, the modelled mantle cooling is too low near the continental margins and the inversion is given too little mass for distribution. Alternatively, the crystalline crust close to the continental margin is thicker than assumed because of transitional rift zones or thickened initial oceanic crust.

Thickness errors tend to increase with increasing crustal age (Figure 3.12), showing that the slope of basement should have been steeper and consequently that our residual Bouguer gravity field is too flat. However, the explanation here is more complex. One possibility is that too high slopes were removed by the thermal gravity correction because we may have assumed too large a density reduction towards the

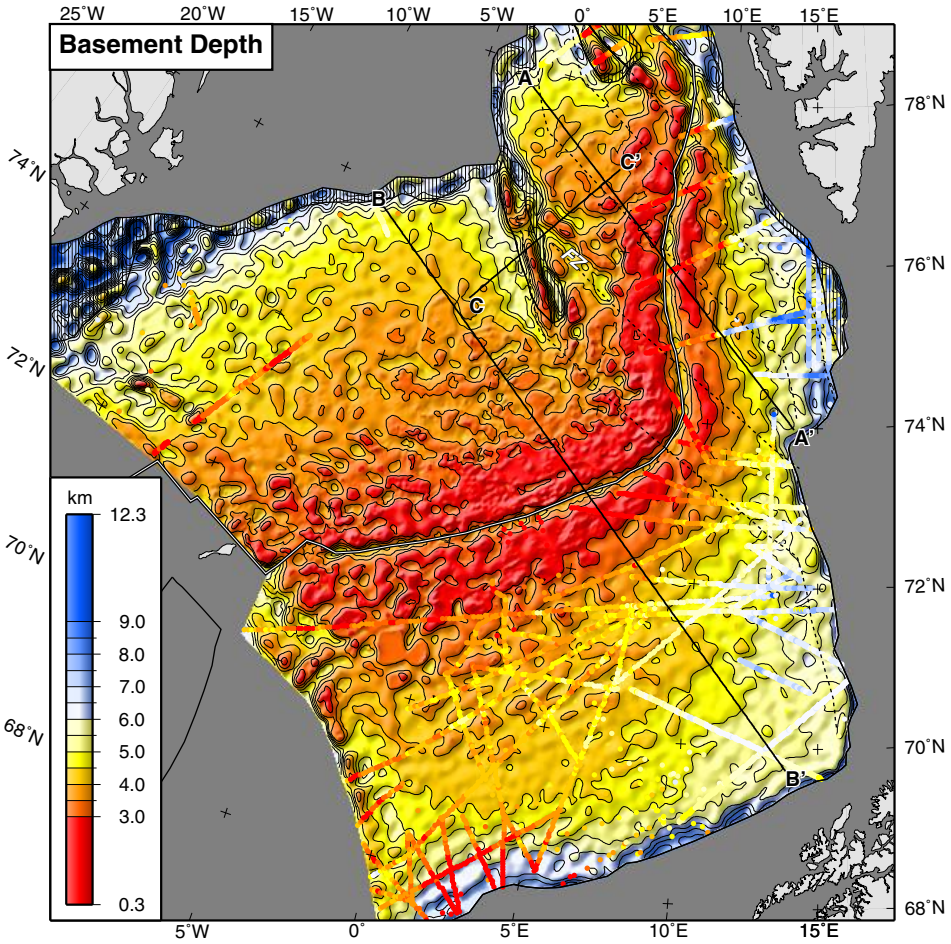

Figure 3.10. Depth to oceanic basement from gravity inversion using the minimum-cost model parameters from Figure 3.9. Seismic calibration points (Figure 3.1 and Table 3.1) overlain for comparison. Flowlines of relative plate motion between Greenland and Eurasia [*Lawver et al.*, 2002] shown by dashed lines. Location of transects (Figure 3.12) shown by annotated bold lines. *FZ*, extinct fracture zone east of Greenland Ridge.

spreading axis. The underlying cause may be that pressure is a stronger-than-assumed moderator of thermal expansion, or, as discussed above, that temperatures near the spreading axis are over-estimated (Figure 3.3). Another possibility is that long wavelengths of the sediment thickness distribution are simply not recoverable from gravity inversion. *Smith and Sandwell* [1994] showed that >160 km wavelengths of seafloor topography are isostatically compensated, produce little or no gravity anomalies, and have to be supplied by actual depth measurements.

The gravity field due to a uniform slab is constant. Because the inversion only accounts for residual heights of the basement surface, it cannot distinguish between two candidate surfaces at slightly different depths, and the regional basement level

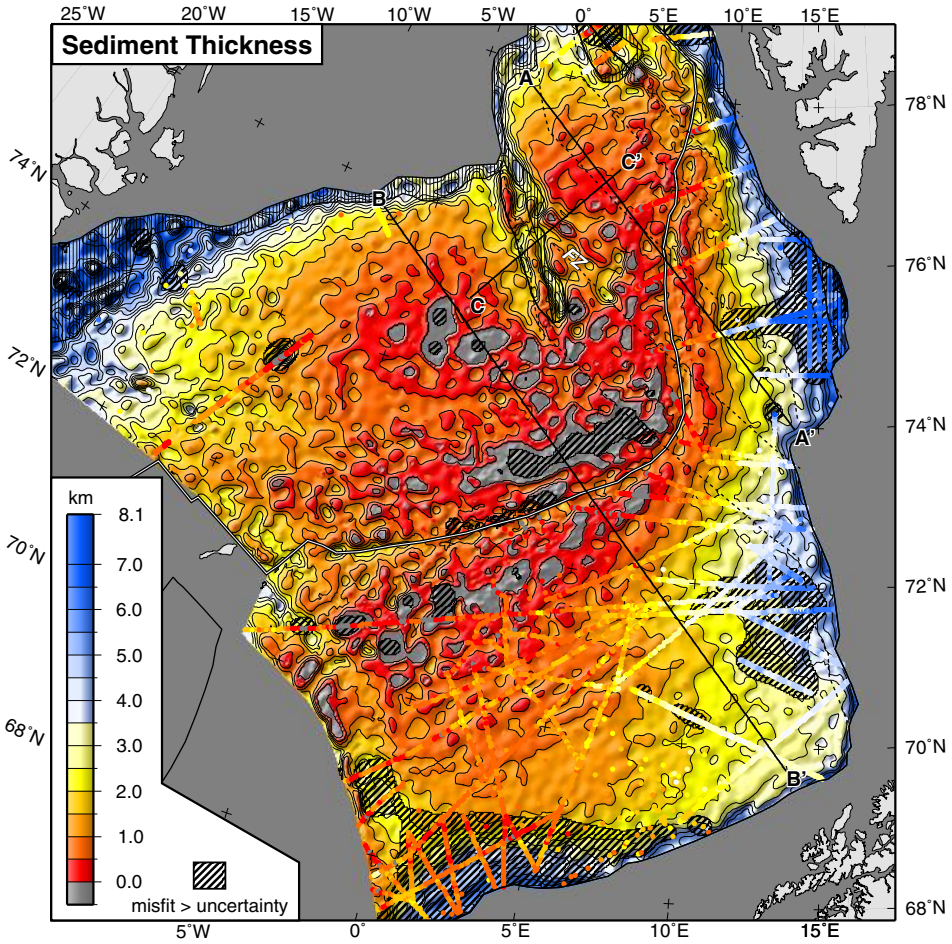

Figure 3.11. Sediment thickness from gravity inversion and the minimum-cost model parameters from Figure 3.9. Flowlines and seismic calibration points as in Figure 3.10.

has to be pre-determined from sparse seismic data. Different choices of regional level yield different sedimentary depths and basement outcrops. We may conclude that absolute sediment thickness values are generally unreliable, with uncertainties of 1 km or more. However, noting that the thermal gravity correction is mainly long-wavelength, we may safely assume that locations of basement highs and sediment depocenters are faithfully predicted. From the present method we recommend using Figures 3.10–3.12 for mapping basement trends such as fracture zones, extinct spreading axes and abyssal hills, but not for volume calculations.

It is beyond uncertainty that the Eurasian side of the Norwegian–Greenland Sea has received 2–3 km more of sediments than the Greenland side (Figure 3.12). The Mohn and Knipovich ridges have dammed up sediment flow from the western Barents Sea shelf, while submarine fan systems on the Greenland side appear to be smaller.

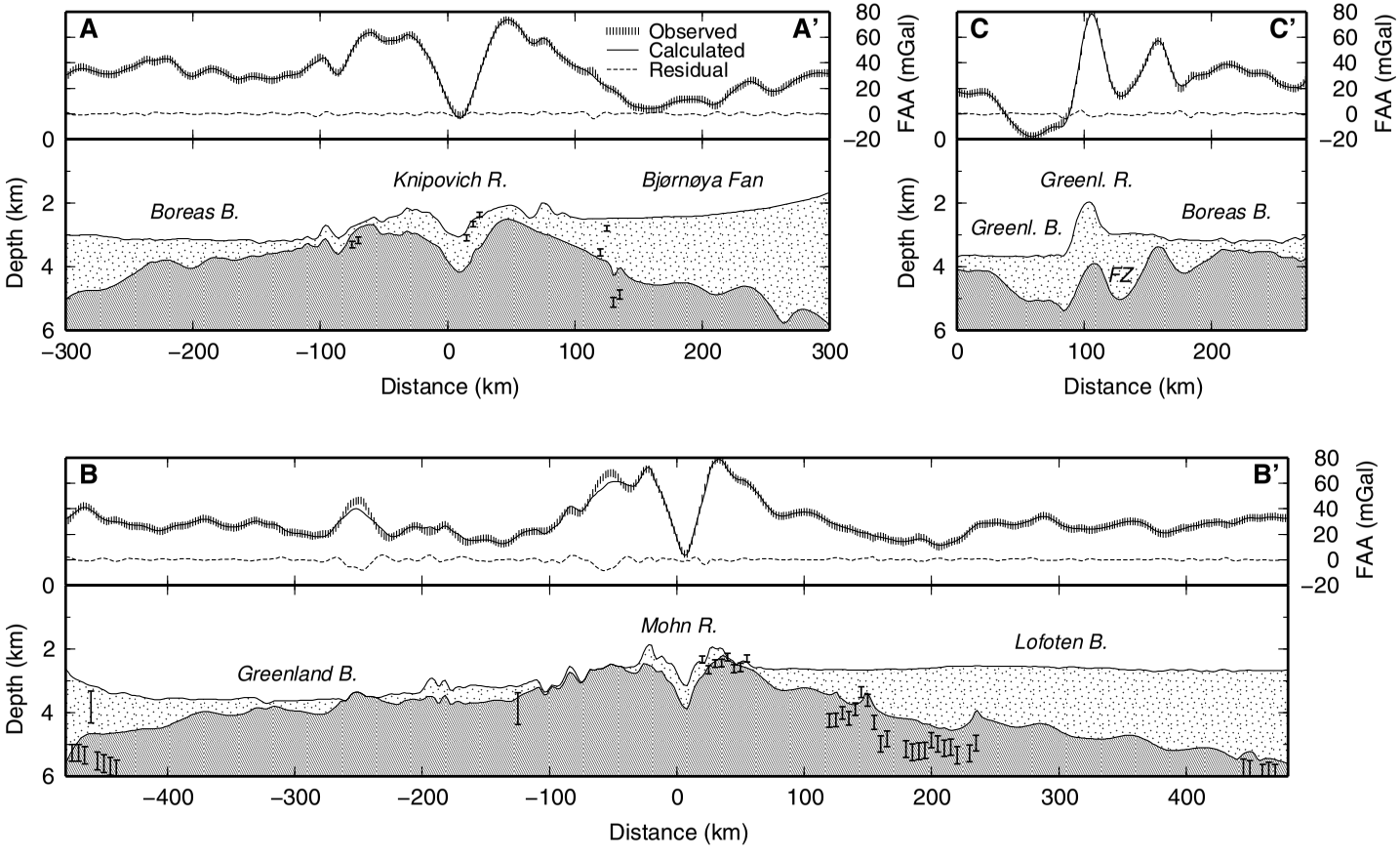

Figure 3.12. Sediment thickness and free-air gravity anomaly (*FAA*) along transects in Figures 3.10 and 3.11. Seismic calibration points within 20 km from transects are projected and shown by error bars. *FZ*, extinct fracture zone east of Greenland Ridge.

Differential sediment loading has depressed the crystalline crust of the Lofoten Basin while the Greenland Basin has numerous basement outcrops extending from the mid-ocean ridge province to crustal ages of Chron 21 times (47 Ma). The existence of an elevated basement province is supported by rugged bathymetry southwest of the Greenland Ridge, correlating with a free-air gravity high (Figures 3.1 and 3.2). We do not observe any similar basement province at the corresponding location in the Lofoten Basin, as would be the consequence if the elevated province were due to magmatic variability during symmetric seafloor spreading. Asymmetric basement elevation has been inferred previously from bathymetry [*Vogt et al.*, 1982] and magnetic depth-to-source analysis [*Kovacs and Vogt*, 1982]. If the province results from secondary uplift, e.g. due to post-Chron 21 hotspot activity, we do not yet have seismic data to demonstrate any uplift and erosion of older sedimentary rocks. However, we know that secondary magmatism created the Vesterisbanken seamount so we cannot rule out secondary mantle processes as a shaping factor of the Greenland Basin.

Post-Chron 7 abyssal hills on the Mohn Ridge appear to have broad V-shapes pointing away from Jan Mayen (Figure 3.10). The pattern, which may be inferred also from the free-air gravity (Figure 3.2), would be expected from migrating asthenosphere zones moving along the spreading axis at ~5 mm yr^{-1}. On the Reykjanes and Kolbeinsey ridges adjacent to Iceland, similar ridges point away from Iceland and may relate to temporal variations in magma production combined with along-axis asthenospheric flow [*Vogt et al.*, 1980; *Ito*, 2001; *Jones et al.*, 2002]. Alternatively, V-shaped patterns result from propagating rifts correlated with regionally decreasing gravity or bathymetry along some slow-spreading ridges [*Phipps Morgan and Sandwell*, 1994].

On the younger side of Greenland Ridge, two linear depocenters and an intermediate basement high align with plate-motion flowlines, suggesting the presence of one or two fossil fracture zones (Figures 3.10–3.12). Limited resolution precludes mapping the conjugate parts underneath the Storfjorden Fan, but seafloor spreading anomalies are offset across the southern depocenter (Figure 3.3) [*Engen and Faleide*, 2005, this volume]. The depocenter can be traced to crustal ages younger than Chron 5 (9.8 Ma). However, the present Knipovich Ridge is continuous and oblique [*Okino et al.*, 2002], suggesting that the ridge reorganised post-Chron 5 from an earlier, more segmented configuration. A recent axial reorganization was also inferred by *Sundvor and Eldholm* [1979] from the steeply bounded ridge province in the area.

Conclusions

Provided that the bathymetry and crustal age of an ocean basin is fairly well known, sediment thickness can be predicted from altimeter-derived gravity and a few seismic calibration points. The locations of sediment depocentres and basement highs are credible down to spatial scales of 20–25 km, while absolute sediment thickness values typically have ~1 km uncertainty because of their strong dependence of model assumptions. For that reason, our method gives insight

primarily into basement structure and to some degree into first-order sedimentation patterns, such as (1) strongly asymmetric sediment distribution in the Norwegian–Greenland Sea, where submarine fans on the western Barents Sea margin reach the mid-ocean ridge axis while the East Greenland Shelf has supplied far less sediment; (2) an anomalous elevated basement province occupying the central Greenland Basin; (3) V-shaped abyssal hills on the Mohn Ridge, indicating northward-migrating asthenosphere zones or propagating oceanic rifts since Chron 7 times; and (4) extinct Knipovich Ridge segmentation on the younger side of the Greenland Ridge.

Appendix: Sediment Thickness from Gravity

We consider a Cartesian coordinate system with the z axis pointing upward and the plane z = 0 at sea level. Following *Parker* [1972], the gravitational attraction $g(\boldsymbol{x})$ at level z_0 due to a surface with topography $h(\boldsymbol{x})$ and density contrast $\Delta\rho(\boldsymbol{x})$ can be expressed as

$$F[g(\boldsymbol{x})] = 2\pi\gamma e^{|\boldsymbol{k}|(s-z_0)} \sum_{n=1}^{\infty} \frac{|\boldsymbol{k}|^{n-1}}{n!} F[\Delta\rho(\boldsymbol{x})h^n(\boldsymbol{x})] \tag{3.2}$$

where $F[\ldots]$ denotes the Fourier transform, γ is Newton's gravitational constant (6.6732×10^{-11} Nm^2 kg^{-2}), and $\boldsymbol{k}$ is an array of wavenumbers corresponding to the spatial vector $\boldsymbol{x}$. To ensure rapid convergence, the topography $h(\boldsymbol{x})$ is treated as undulations about a regional level s. The topography must be tapered to zero outside the region of interest and z_0 must lie entirely above it. We note that the density contrast may be either constant or variable. If $\boldsymbol{x}$ spans a plane rather than a line, the Fourier transforms are two-dimensional and $\boldsymbol{k}$ denotes radial wavenumbers. We terminate the series after four terms because in a typical oceanic setting, the fourth and higher terms contribute < 1 mGal to the calculated gravity [*Blackman and Forsyth*, 1991]. The error of not formulating equation (3.2) in spherical coordinates is also <1 mGal [*Kimbell et al.*, 2004].

If the density contrast $\Delta\rho(\boldsymbol{x})$ is an exponential function of depth below seafloor, e.g. $\Delta\rho(\boldsymbol{x}) = \rho_0\exp\{-\alpha[b(\boldsymbol{x}) + r - h(\boldsymbol{x}) - s]\}$ where $b(\boldsymbol{x})$ is the bathymetry with respect to its median level r, equation (3.2) translates to [*Granser*, 1987]:

$$F[g(\boldsymbol{x})] = \frac{2\pi\gamma}{|\boldsymbol{k}| + \alpha} e^{|\boldsymbol{k}|(s-z_0)} \sum_{n=0}^{\infty} \frac{|\boldsymbol{k}|^n}{n!} F[\Delta\rho_0 e^{\alpha\{s-r+h(\boldsymbol{x})-b(\boldsymbol{x})\}} h^n(\boldsymbol{x})] \tag{3.3}$$

Calculating topography from gravity implies that the upward continuation term $\exp[|\boldsymbol{k}|(s - z_0)]$ in equations (3.2) and (3.3) is replaced by downward continuation, $\exp[|\boldsymbol{k}|(z_0 - s)]$, which exponentially amplifies short-wavelength noise relative to the geologic signal, demonstrating that an infinite number of noisy topographies satisfy a given gravity field. To ensure that the smoothest candidate surface is found,

we apply a downward continuation filter with weight Λ_1 on surface slope and Λ_2 on curvature change [*Phipps Morgan and Blackman*, 1993]:

$$F[h(\boldsymbol{x})] = F[g(\boldsymbol{x})]\frac{2\pi\gamma e^{|\boldsymbol{k}|(z_0 - s)}}{\Lambda_1|\boldsymbol{k}|^2 + \Lambda_2|\boldsymbol{k}|^4 + (2\pi\gamma)^2 e^{2|\boldsymbol{k}|(z_0 - s)}} \tag{3.4}$$

For long wavelengths, the filter acts as normal downward continuation, while the short wavelengths are dominated by the weighting terms. Λ_1 and Λ_2 could be treated as model parameters to be found by inversion, but *Phipps Morgan and Blackman* [1993] did not succeed in doing so. By trial and error we found that $\Lambda_1 = 0.05$ and $\Lambda_2 = 0$ gives a satisfactory balance between basement relief and noise, i.e., our inverse problem does not require a penalty on curvature change. The weighting filter has a narrower centre lobe and smaller sidelobes than a conventional low-pass cosine-tapered filter [*Oldenburg*, 1974; *Phipps Morgan and Blackman*, 1993] so that the calculated basement surface is less dominated by circular noise.

Acknowledgments. We thank Fernando Martinez for kind support and Walter H. F. Smith for valuable comments on satellite altimetry resolution. Ø. E. greatly acknowledges Evelyn Norris and the Department of Geology and Geophysics at the University of Hawai'i for providing research training and facilities. Marte Vidje kindly made available seismic data points in the Lofoten Basin. We are grateful to Asbjørn Breivik for reviewing an earlier version of the manuscript. Ø. E. was supported by a doctoral research fellowship and a travel grant from the Norwegian Research Council (grant no. 147541/432).

References

Åkermoen, T. (1989), Jan Mayen-ryggen: Et seismisk stratigrafisk og strukturelt studium, Cand. Scient. thesis, 174 pp., University of Oslo, Norway (in Norwegian).

Andersen, O.B., and P. Knudsen (1998), Global marine gravity field from the ERS-1 and Geosat geodetic mission altimetry, *Journal of Geophysical Research*, *103* (C4), 8129–8137.

Barton, P.J. (1986), The relationship between seismic velocity and density in the continental crust – a useful constraint?, *Geophysical Journal of the Royal astronomical Society*, *87* (1), 195–208.

Blackman, D.K., and D.W. Forsyth (1991), Isostatic compensation of tectonic features of the Mid-Atlantic Ridge: 25–27°30'S, *Journal of Geophysical Research*, *96* (B7), 11,741–11,758.

Breivik, A.J., J. Verhoef, and J.I. Faleide (1999), Effect of thermal contrasts on gravity modeling at passive margins: Results from the western Barents Sea, *Journal of Geophysical Research*, *104* (B7), 15,293–15,311.

Breivik, A.J., R. Mjelde, P. Grogan, H. Shimamura, Y. Murai, and Y. Nishimura (2003), Crustal structure and transform margin development south of Svalbard based on ocean bottom seismometer data, *Tectonophysics*, *369* (1–2), 37–70.

Breivik, A.J., J.I. Faleide, and R. Mjelde (2004), Late magmatic underplating of oceanic crust at the outer Vøring margin, Norway, Euromargins 2003 OBS experiment, *Eos, Transactions, American Geophysical Union*, *85* (47), Fall Meeting Supplement, Abstract V31B-1432.

Brozena, J.M., V.A. Childers, L.A. Lawver, L.M. Gahagan, R. Forsberg, J.I. Faleide, and O. Eldholm (2003), New aerogeophysical study of the Eurasia Basin and Lomonosov Ridge: Implications for basin development, *Geology*, *31* (9), 825–828.

Cande, S.C., and D.V. Kent (1995), Revised calibration of the geomagnetic polarity timescale for the Late Cretaceous and Cenozoic, *Journal of Geophysical Research*, *100* (B4), 6093–6095.

Cannat, M., C. Rommevaux-Jestin, and H. Fujimoto (2003), Melt supply variations to a magma-poor ultra-slow spreading ridge (Southwest Indian Ridge 61˚ to 69˚E), *Geochemistry Geophysics Geosystems*, *4* (8), 9104, doi:10.1029/2002GC000480.

Carlson, R.L., and C.N. Herrick (1990), Densities and porosities in the oceanic crust and their variations with depth and age, *Journal of Geophysical Research*, *95* (B6), 9153–9170.

Cherkis, N.Z., S. Steinmetz, R. Schreiber, J. Thiede, and J. Theiner (1994), Vesteris Seamount: An enigma in the Greenland Basin, *Marine Geophysical Researches*, *16*, 287–301.

Childers, V.A., D.C. McAdoo, J.M. Brozena, and S.W. Laxon (2001), New gravity data in the Arctic Ocean: Comparison of airborne and ERS gravity, *Journal of Geophysical Research*, *106* (B5), 8871–8885.

Cochran, J.R., and M. Talwani (1978), Gravity anomalies, regional elevation, and the deep structure of the North Atlantic, *Journal of Geophysical Research*, *83* (B10), 4907–4924.

Cochran, J.R., G.J. Kurras, M.H. Edwards, and B.J. Coakley (2003), The Gakkel Ridge: Bathymetry, gravity anomalies, and crustal accretion at extremely slow spreading rates, *Journal of Geophysical Research*, *108* (B2), 2116, doi:10.1029/2002JB001830.

Cowie, P.A., and G.D. Karner (1990), Gravity effect of sediment compaction: examples from the North Sea and the Rhine Graben, *Earth and Planetary Science Letters*, *99*, 141–153.

Eldholm, O., and K. Grue (1994), North Atlantic volcanic margins – dimensions and production rates, *Journal of Geophysical Research*, *99* (B2), 2955–2968.

Engen, Ø., and J.I. Faleide (2005), Plate tectonic reconstruction of the North Atlantic–Arctic gateway, *Tectonophysics*, submitted. This volume, p. 127.

Engen, Ø., J.A. Gjengedal, J.I. Faleide, Y. Kristoffersen, and O. Eldholm (2005), Seismic stratigraphy and basement structure of the Nansen Basin, Arctic Ocean, *Geophysical Journal International*, submitted. This volume, p. 57.

Faleide, J.I., A. Solheim, A. Fiedler, B.O. Hjelstuen, E.S. Andersen, and K. Vanneste (1996), Late Cenozoic evolution of the western Barents Sea–Svalbard continental margin, *Global and Planetary Change*, *12* (1–4), 53–74.

Fiedler, A. (1992), Kenozoisk sedimentasjon i Lofotenbassenget langs vestlige Barentshavmarginen, Cand. Scient. thesis, 114 pp., University of Oslo, Norway (in Norwegian).

Fiedler, A., and J.I. Faleide (1996), Cenozoic sedimentation along the southwestern Barents Sea margin in relation to uplift and erosion of the shelf, *Global and Planetary Change*, *12* (1–4), 75–93.

Goff, J.A., and W.H.F. Smith (2003), A correspondence of altimetric gravity texture to abyssal hill morphology along the flanks of the Southeast Indian Ridge, *Geophysical Research Letters*, *30* (24), 2269, doi:10.1029/2003GL018913.

Granser, H. (1987), Three-dimensional interpretation of gravity data from sedimentary basins using an exponential density–depth function, *Geophysical Prospecting*, *35* (9), 1030–1041.

Gregory, A.R. (1977), Aspects of rock physics from laboratory and log data that are important to seismic interpretation, in *Seismic Stratigraphy – Applications to Hydrocarbon Exploration*, *Memoir*, vol. 26, edited by C.E. Payton, pp. 15–46, American Association of Petroleum Geologists, Tulsa, OK.

Haase, K.M., and C.W. Devey (1994), The petrology and geochemistry of Vesteris Seamount, Greenland Basin: An intraplate alkaline volcano of non-plume origin, *Journal of Petrology, 35* (2), 295–328.

Hempel, P., R. Schreiber, L. Johnson, and J. Thiede (1991), The Vesterisbanken Seamount (Greenland Basin): Patterns of morphology and sediment distribution, *Marine Geology, 96*, 175–185.

Hinz, K., J.C. Mutter, C.M. Zehnder, and the NGT Study Group (1987), Symmetrical conjugation of continent–ocean boundary structures along the Norwegian and East Greenland margins, *Marine and Petroleum Geology, 4* (3), 166–187.

Hjelstuen, B.O. (1993), Sein-kenozoisk utvikling av Storfjordvifta, basert på reprosesserte multikanals data, Cand. Scient. thesis, 111 pp., University of Oslo, Norway (in Norwegian).

Hjelstuen, B.O., A. Elverhøi, and J.I. Faleide (1996), Cenozoic erosion and sediment yield in the drainage area of the Storfjorden Fan, *Global and Planetary Change*, *12* (1–4), 95–117.

Hooft, E.E.E., R.S. Detrick, D.R. Toomey, J.A. Collins, and J. Lin (2000), Crustal thickness and structure along three contrasting spreading segments of the Mid-Atlantic Ridge, 33.5°N–35°N, *Journal of Geophysical Research*, *105* (B4), 8205–8226.

Ito, G. (2001), Reykjanes 'V'-shaped ridges originating from a pulsing and dehydrating mantle plume, *Nature*, *411* (6838), 681–684.

Jackson, H.R., J.I. Faleide, and O. Eldholm (1990), Crustal structure of the sheared southwestern Barents Sea continental margin, *Marine Geology, 93* (1–4), 119–146.

Jacobson, R.S. (1992), Impact of crustal evolution on changes of the seismic properties of the uppermost ocean crust, *Reviews of Geophysics*, *30* (1), 23–42.

Jakobsson, M., N. Cherkis, J. Woodward, R. Macnab, and B. Coakley (2000), New grid of Arctic bathymetry aids scientists and mapmakers, *Eos, Transactions, American Geophysical Union*, *81* (9), 89, 93, 96.

Jarchow, C.M., and G.A. Thompson (1989), The nature of the Mohorovicic discontinuity, *Annual Review of Earth and Planetary Sciences*, *17*, 475–506.

Jones, S.M., N. White, and J. Maclennan (2002), V-shaped ridges around Iceland: Implications for spatial and temporal patterns of mantle convection, *Geochemistry Geophysics Geosystems*, *3* (10), 1059, doi:10.1029/2002GC000361.

Karlberg, T. (1995), En geofysisk undersøkelse av Hovgårdryggen, Cand. Scient. thesis, 104 pp., University of Oslo, Norway (in Norwegian).

Kimbell, G.S., R.W. Gatliff, J.D. Ritchie, A.S.D. Walker, and J.P. Williamson (2004), Regional three-dimensional gravity modelling of the NE Atlantic margin, *Basin Research*, *16* (2), 259–278.

Klingelhöfer, F., L. Géli, L. Matias, N. Steinsland, and J. Mohr (2000), Crustal structure of a super-slow spreading centre: a seismic refraction study of Mohns Ridge, 72°N, *Geophysical Journal International*, *141* (2), 509–526.

Kovacs, L.C., and P.R. Vogt (1982), Depth to magnetic source analysis of the Arctic Ocean region, *Tectonophysics*, *89* (1–3), 255–294.

Lawver, L.A., A. Grantz, and L.M. Gahagan (2002), Plate kinematic evolution of the present Arctic region since the Ordovician, in *Tectonic Evolution of the Bering Shelf–Chukchi Sea–Arctic Margin and Adjacent Landmasses*, *Special Paper*, edited by E.L. Miller et al., pp. 333–358, Geological Society of America, Boulder, CO.

Laxon, S., and D. McAdoo (1994), Arctic Ocean gravity field derived from ERS-1 satellite altimetry, *Science*, *265* (5172), 621–624.

Lee, T.-C., A.J. Rudman, and A. Sjoreen (1980), Application of finite element analysis to terrestrial heatflow, Occasional Paper 20, 53 pp., Department of Natural Resources, Geological Survey of Indiana, Bloomington, IN.

Ljones, F., A. Kuwano, R. Mjelde, A. Breivik, H. Shimamura, Y. Murai, and Y. Nishimura (2004), Crustal transect from the North Atlantic Knipovich Ridge to the Svalbard margin west of Hornsund, *Tectonophysics*, *378* (1–2), 17–41.

Ludwig, J.W., J.E. Nafe, and C.L. Drake (1970), Seismic refraction, in *The Sea*, vol. 4, edited by A.E. Maxwell, pp. 53–84, John Wiley, New York, NY.

Muller, M.R., T.A. Minshull, and R.S. White (1999), Segmentation and melt supply at the Southwest Indian Ridge, *Geology, 27* (10), 867–870.

Myhre, A.M., and O. Eldholm (1981), Sedimentary and crustal velocities in the Norwegian–Greenland Sea, *Journal of Geophysical Research*, *86* (B6), 5012–5022.

Myhre, A.M., and O. Eldholm (1988), The western Svalbard margin (74°–80°N), *Marine and Petroleum Geology, 5* (2), 134–156.

Myhre, A.M., O. Eldholm, and E. Sundvor (1982), The margin between Senja and Spitsbergen fracture zones: Implications from plate tectonics, *Tectonophysics*, *89* (1–3), 33–50.

Nissen, S.S., D.E. Hayes, P. Buhl, J. Diebold, Yao Bochu, Zeng Weijun, and Chen Yongqin (1995), Deep penetration seismic soundings across the northern margin of the South China Sea, *Journal of Geophysical Research*, *100* (B11), 22,407–22,433.

Okino, K., D. Curewitz, M. Asada, K. Tamaki, P. Vogt, and K. Crane (2002), Preliminary analysis of the Knipovich Ridge segmentation: influence of focused magmatism and ridge obliquity on an ultraslow spreading system, *Earth and Planetary Science Letters*, *202* (2), 275–288.

Oldenburg, D.W. (1974), The inversion and interpretation of gravity anomalies, *Geophysics*, *39* (4), 526–536.

Parker, R.L. (1972), The rapid calculation of potential anomalies, *Geophysical Journal of the Royal astronomical Society*, *31*, 447–455.

Parsons, B., and J.G. Sclater (1977), Analysis of variation of ocean floor bathymetry and heat flow with age, *Journal of Geophysical Research*, *82* (5), 803–827.

Phipps Morgan, J., and D.K. Blackman (1993), Inversion of combined gravity and bathymetry data for crustal structure: A prescription for downward continuation, *Earth and Planetary Science Letters*, *119*, 167–179.

Phipps Morgan, J., and D.T. Sandwell (1994), Systematics of ridge propagation south of 30°S, *Earth and Planetary Science Letters*, *121* (1–2), 245–258.

Planke, S. (1993), VELO Seismic refraction/wide-angle reflection velocity data base program, Computer Program/Data Base Documentation Series no. 1, 14 pp., Department of Geology, University of Oslo, Norway.

Purdy, G.M. (1987), New observations of the shallow seismic structure of young oceanic crust, *Journal of Geophysical Research*, *92* (B9), 9351–9362.

Ritzmann, O., W. Jokat, R. Mjelde, and H. Shimamura (2002), Crustal structure between the Knipovich Ridge and the Van Mijenfjorden (Svalbard), *Marine Geophysical Researches*, *23* (5–6), 379–401.

Ritzmann, O., W. Jokat, W. Czuba, A. Guterch, R. Mjelde, and Y. Nishimura (2004), A deep seismic transect from Hovgard Ridge to northwestern Svalbard across the continental–ocean transition: A sheared margin study, *Geophysical Journal International*, *157* (2), 683–702.

Sandwell, D.T., and W.H.F. Smith (1997), Marine gravity anomaly from Geosat and ERS 1 satellite altimetry, *Journal of Geophysical Research*, *102* (B5), 10,039–10,054.

Schlindwein, V., and W. Jokat (1999), Structure and evolution of the continental crust of northern east Greenland from integrated geophysical studies, *Journal of Geophysical Research*, *104* (B7), 15,227–15,245.

Skogseid, J., and O. Eldholm (1987), Early Cenozoic crust at the Norwegian continental margin and the conjugate Jan Mayen Ridge, *Journal of Geophysical Research*, *92* (B11), 11,471–11,491.

Smith, W.H.F. (1998), Seafloor tectonic fabric from satellite altimetry, *Annual Review of Earth and Planetary Sciences*, *26*, 697–747.

Smith, W.H.F., and D.T. Sandwell (1994), Bathymetric prediction from dense satellite altimetry and sparse shipboard bathymetry, *Journal of Geophysical Research*, *99* (B11), 21,803–21,824.

Smith, W.H.F., and P. Wessel (1990), Gridding with continuous curvature splines in tension, *Geophysics*, *55* (3), 293–305.

Sundvor, E., and O. Eldholm (1979), The western and northern margin off Svalbard, *Tectonophysics*, *59* (1–4), 239–250.

Sundvor, E., O. Eldholm, T.P. Gladczenko, and S. Planke (2000), Norwegian–Greenland Sea thermal field, in *Dynamics of the Norwegian margin*, *Special Publications*, vol. 167, edited by A. Nøttvedt et al., pp. 397–410, Geological Society, London, UK.

Talwani, M., and O. Eldholm (1977), Evolution of the Norwegian–Greenland Sea, *Geological Society of America Bulletin*, *88* (7), 969–999.

Talwani, M., G.B. Udintsev, and S.M. White (1976), Introduction and explanatory notes, Leg 38, Deep Sea Drilling Project, in *Dublin, Ireland to Amsterdam, The Netherlands; Aug.–Sept.1974*, *Initial Reports of the Deep Sea Drilling Project*, vol. 38, pp. 3–19, Texas A & M University, Ocean Drilling Program, College Station, TX.

Thiede, J., A.M. Myhre, J.V. Firth, and the Shipboard Scientific Party (1995), Cenozoic Northern Hemisphere polar and subpolar ocean paleoenvironments (summary of ODP Leg 151 drilling results), in *North Atlantic–Arctic Gateways I, Proceedings of the Ocean Drilling Program, Initial Reports*, vol. 151, edited by A.M. Myhre et al., pp. 397–420, Texas A & M University, Ocean Drilling Program, College Station, TX.

Tsikalas, F., O. Eldholm, and J.I. Faleide (2002), Early Eocene sea floor spreading and continent–ocean boundary between Jan Mayen and Senja fracture zones in the Norwegian–Greenland Sea, *Marine Geophysical Researches*, *23* (3), 247–270.

Vidje, M. (2003), Sedimentfordeling i Lofotenbassenget, Cand. Scient. thesis, 112 pp., University of Oslo, Norway (in Norwegian).

Vogt, P.R., G.L. Johnson, and L. Kristjansson (1980), Morphology and magnetic anomalies north of Iceland, *Journal of Geophysics*, *47* (1–3), 67–80.

Vogt, P.R., R.K. Perry, R.H. Feden, H.S. Fleming, and N.Z. Cherkis (1981), The Greenland–Norwegian Sea and Iceland environment: Geology and geophysics, in *The Arctic Ocean*, *The Ocean Basins and Margins*, vol. 5, edited by A.E.M. Nairn et al., pp. 493–598, Plenum Press, New York, NY.

Vogt, P.R., L.C. Kovacs, C. Bernero, and S.P. Srivastava (1982), Asymmetric geophysical signatures in the Greenland–Norwegian and southern Labrador seas and the Eurasia Basin, *Tectonophysics*, *89*, 95–160.

Vogt, P.R., W.Y. Jung, and J. Brozena (1998), Arctic margin gravity highs: Deeper meaning for sediment depocenters?, *Marine Geophysical Researches*, *20* (5), 459–477.

Wessel, P., and A.B. Watts (1988), On the accuracy of marine gravity measurements, *Journal of Geophysical Research*, *93* (B1), 393–413.

White, R.S., D. McKenzie, and R.K. O'Nions (1992), Oceanic crustal thickness from seismic measurements and rare-earth element inversions, *Journal of Geophysical Research*, *97* (B13), 19,683–19,715.

Wilkens, R.H., G.J. Fryer, and J. Karsten (1991), Evolution of porosity and seismic structure of upper oceanic crust: Importance of aspect ratios, *Journal of Geophysical Research*, *96* (B11), 17,981–17,995.

Yale, M.M., D.T. Sandwell, and W.H.F. Smith (1995), Comparison of along-track resolution of stacked Geosat, ERS 1, and TOPEX satellite altimeters, *Journal of Geophysical Research*, *100* (B8), 15,117–15,127.

Zelt, C.A., and R.B. Smith (1992), Seismic traveltime inversion for 2-D crustal velocity structure, *Geophysical Journal International*, *108* (1), 16–34.

Paper 4

Paper 4

Plate tectonic reconstruction of the North Atlantic–Arctic gateway

Øyvind Engen and Jan Inge Faleide

Department of Geosciences, University of Oslo, Norway

Manuscript submitted to *Tectonophysics*

Abstract. The Fram Strait deep-water gateway between Svalbard and NE Greenland formed by Oligocene–Miocene propagation of seafloor spreading between Eurasia and North America. Coevally deteriorating climates suggest that the age of the gateway is a main boundary condition for Cenozoic environmental change. We constrain the gateway opening by Miocene–present plate reconstructions using new seismic, gravity, and bathymetry data along with existing poles of relative plate motion. The continent–ocean transition and conjugate margin structures are located from seismic profiles and the relation between crustal thickness and mantle Bouguer anomalies. Magnetic seafloor spreading anomalies are re-identified by modelling along aeromagnetic tracklines. Results of the analysis include new delineations of the continental Hovgård and Greenland ridges, and the possibility that the Yermak Plateau and the Morris Jesup Rise are entirely continental. A pre-condition for gateway opening was the change from strike-slip to oblique extension between Svalbard and Greenland at the Eocene–Oligocene transition (33.3 Ma). A continuous corridor of immature seafloor spreading formed by Chron 5B times (14.8 Ma), indicating up to ~18 Myr of extensive pre-drift crustal thinning. The gateway may have been further delayed until the present-day seafloor spreading regime was established at Chron 5 times (9.8 Ma). The age of the gateway agrees with the regional sedimentary record of Late Cenozoic deep-water exchange and climatic cooling. However, the changes were controlled also by the Greenland–Scotland Ridge. Abrupt, middle–late Miocene uplift of the NW Barents Sea shelf coincided with the gateway opening and indicates that the Fram Strait is also a gateway for asthenospheric flow.

Keywords: Crustal structure; Plate tectonics; Paleoceanography; Tectonic uplift; Fram Strait; Arctic Ocean

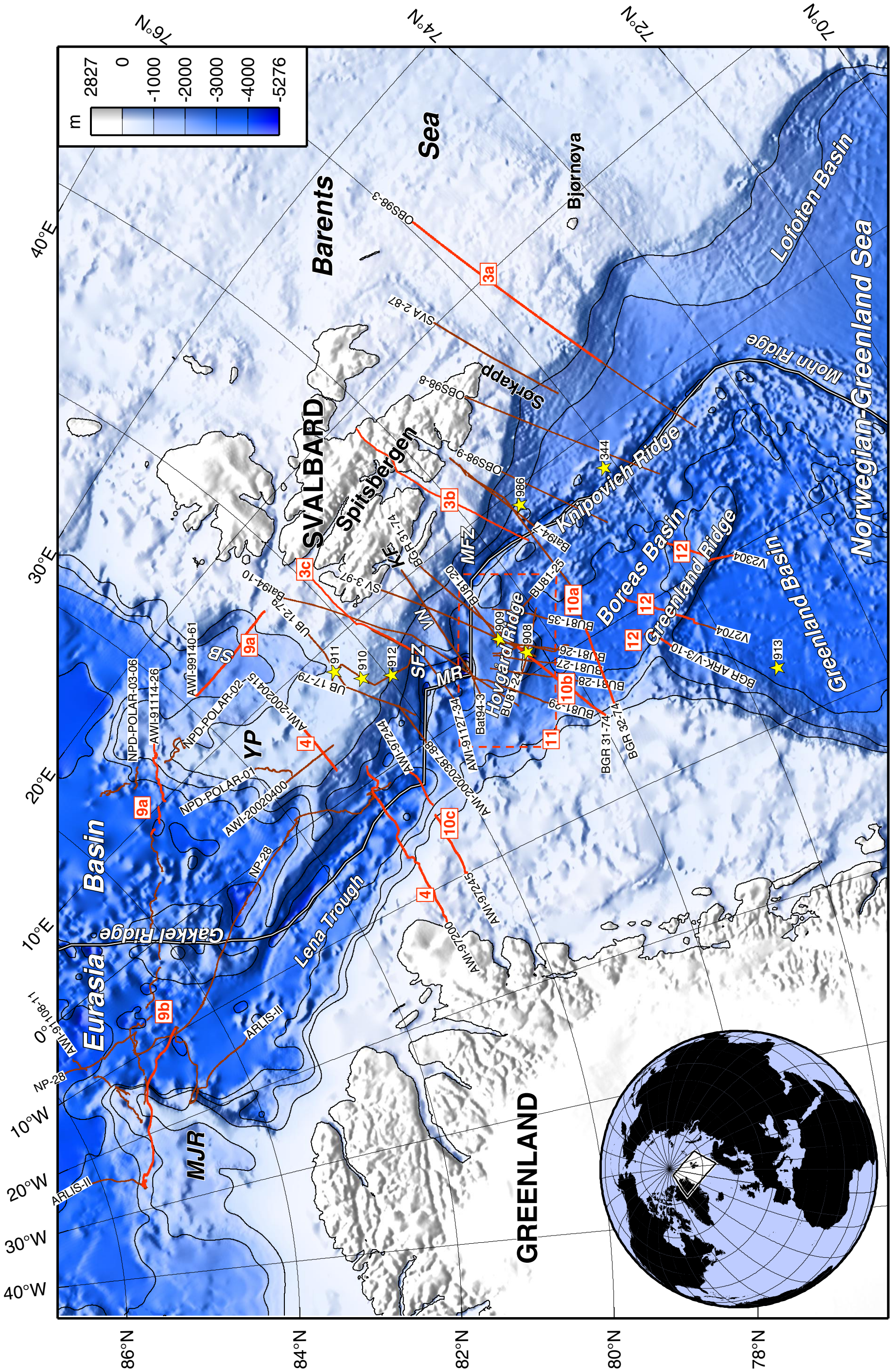
76°N
74°N
72°N
70°N
40°E
30°E
20°E
10°E
0°
10°W
20°W
30°W
40°W
86°N
84°N
82°N
80°N
78°N
m
2827
0
-1000
-2000
-3000
-4000
-5276
Barents
Sea
Bjørnøya
SVALBARD
Spitsbergen
Sørkapp
Knipovich Ridge
Mohn Ridge
Lofoten Basin
Norwegian-Greenland Sea
Boreas Basin
Greenland Ridge
Greenland Basin
Hovgård Ridge
GREENLAND
Lena Trough
Gakkel Ridge
Eurasia
Basin
MJR
YP
SFZ
MR
MFZ
KF
VV
SB
3a
3b
3c
4
9a
9b
10a
10b
10c
11
12
OBS98-3
OBS98-8
OBS98-9
SVA 2-87
SV 3-97
BGR 31-74
BGR 32-74
Bat94-1
Bat94-3
Bat94-10
BU81-20
BU81-24
BU81-25
BU81-26
BU81-27
BU81-28
BU81-29
BU81-35
UB 12-79
UB 17-79
V2304
V2704
BGR ARK-V/3-10
AWI-99140-61
AWI-91114-26
AWI-91127-34
AWI-91108-1
AWI-97244
AWI-97245
AWI-97200
AWI-20020387-88
AWI-20020415
AWI-20020400
NPD-POLAR-03-06
NPD-POLAR-02
NPD-POLAR-01
NP-28
ARLIS-II
344
986
908
909
910
911
912
913

Introduction

The Fram Strait between Svalbard and NE Greenland is the only gateway for deep-water exchange between the Arctic Ocean and the other world oceans (Figure 4.1). Its oceanic part, the Lena Trough, is an oblique segment of the Eurasia–North America plate boundary currently spreading at 7 mm yr^{-1} half-rate [*DeMets et al.*, 1990]. Seafloor spreading in the central Eurasia Basin and the Norwegian–Greenland Sea was established by the earliest Eocene and involved Greenland as a separate plate [*Karasik*, 1968; *Pitman and Talwani*, 1972; *Talwani and Eldholm*, 1977; *Vogt et al.*, 1979]. The plate boundary between Svalbard and NE Greenland developed within the De Geer megashear region [*Harland*, 1969] and included the sheared Senja and Hornsund margins offset by a volcanic rifted segment west of Bjørnøya [*Eldholm et al.*, 1987; *Faleide et al.*, 1991]. At the Eocene–Oligocene transition, Greenland became attached to North America and relative plate motions between Svalbard and NE Greenland changed to oblique extension [*Talwani and Eldholm*, 1977]. The present margin geometry is an end product of the complex shear-rift development [*Faleide et al.*, 1991; 1993].

The eventual break-up of the Lena Trough is poorly dated because the structure of the NE Greenland margin has been largely unknown and magnetic seafloor spreading anomalies have not been identified with confidence [*Vogt et al.*, 1981]. In a segmented plate boundary region such as the Fram Strait, the formation of a continuous oceanic corridor is delayed from the time of break-up and until the time when continental crust separates across the largest-offset transform fault [*LePichon and Hayes*, 1971]. Plate tectonic reconstructions assuming that the continent–ocean transition (COT) is represented by bathymetric contours indicate an oceanic passageway by middle [*Kristoffersen*, 1990] or late Miocene times [*Lawver et al.*, 1990]. However, extensive contourites in the Lena Trough [*Eiken and Hinz*, 1993] imply that the relation between slope bathymetric contours and the COT is uncertain. In order to reconstruct the gateway more precisely, the past and present segmentation of the Lena Trough plate boundary should be better constrained, notions of asymmetric seafloor spreading [*Sundvor and Eldholm*, 1979] should be investigated, and the continental Hovgård and Greenland ridges [*Myhre et al.*, 1982; *Tsikalas et al.*, 2002] should be more precisely delineated.

The opening of the Lena Trough coincided with Late Cenozoic cooling and eventual glaciation of the northern hemisphere. Ice-rafted sediments were deposited in the Fram Strait from 14.0 Ma [*Wolf-Welling et al.*, 1996] and on the mid-Norwegian margin from 12.6 Ma onwards [*Fronval and Jansen*, 1996]. A regional cooling event is dated to 9.8 Ma in Iceland [*Mudie and Helgason*, 1983]. At 5.5 Ma, Scandinavian glaciers reached sea level, and northern Europe was extensively glaciated at 2.57 Ma [*Jansen and Sjøholm*, 1991]. Because dating of plate tectonic events is imprecise

---

Figure 4.1 (opposite). Seismic profiles used in this study (Table 4.1). This and subsequent maps are on the oblique Mercator projection about the Chron 5–present plate rotation pole (Table 4.2); hence, recent flowlines horizontal. IBCAO bathymetry [*Jakobsson et al.*, 2000]. Figure number suffixes annotated in boxes (e.g., "3a" denotes Figure 4.3a). *MJR*, Morris Jesup Rise; *MFZ*, Molloy Fracture Zone; *MR*, Molloy Ridge; *KF*, Kongsfjorden; *SB*, Sophia Basin; *SFZ*, Spitsbergen Fracture Zone; *VN*, Vestnesa; *YP*, Yermak Plateau.

compared to the sedimentary record of climate change [*Berger et al.*, 1981], it is difficult to demonstrate a causal link between the opening of the Lena Trough and these cooling events. Furthermore, an incipient gateway across the Greenland–Scotland Ridge adjacent to Iceland may have controlled ocean circulation during the same time interval [*Eldholm et al.*, 1994]. The gateways are reasonable causes of the paleoclimatic deterioration because of the increased latitudinal heat transfer facilitated by a deep-water conduit. Furthermore, several Cenozoic uplift events on the Barents Sea shelf [*Vågnes*, 1997; *Dimakis et al.*, 1998] might have had the potential to disrupt atmospheric circulation patterns, initiate glacial–interglacial cycles, and alter the balance of evaporation and precipitation [*Raymo and Ruddiman*, 1992; *Wright and Miller*, 1996].

To place plate tectonic constraints on the opening of the Fram Strait gateway, we (1) estimate the COT on the W Barents Sea–Svalbard and NE Greenland margins as well as around the Hovgård and Greenland ridges; (2) locate present and extinct spreading axes and fracture zones; (3) identify magnetic seafloor spreading anomalies; and (4) test these new structural constraints in a series of Miocene to present plate reconstructions. We then discuss the reconstruction of the gateway with respect to the regional sedimentary record of paleoenvironmental change.

New Structural Constraints

Airborne gravity surveying has covered the latitudinal gap of satellite altimetry north of 81.5°N [*Childers et al.*, 2001; *Brozena et al.*, 2003] and made possible the first gravity grid of the Arctic Ocean region (Figure 4.2a). We calculated mantle Bouguer anomalies (MBAs) by removing the gravity attraction of the seafloor [*Jakobsson et al.*, 2000] and a 6-km-thick, homogeneous basement layer from the free-air gravity (Figure 4.2b). The MBA reduction successfully removed large positive free-air gravity anomalies associated with the shelf break and glaciomarine fan deposits on the W Barents Sea–Svalbard margin [*Vogt et al.*, 1998]. The underlying crustal thinning and rising of the Moho across the COT is reflected by a seaward positive MBA gradient. Comparing MBA profiles and deep seismic transects across the W Barents Sea–Svalbard margin, we observe a steep MBA gradient on the sheared-margin COT northwest of Bjørnøya and a more diffuse gradient where the COT is wider due to rifting (Figure 4.3). Furthermore, the MBA contour defining the COT at a sheared segment predicts the COT with 40 km or better precision on neighbouring rifted segments.

The W Barents Sea–Svalbard margin has been mapped in detail by multi-channel (MCS) and wide-angle seismic profiles, but the dense data coverage ends at ~80°N because of prevailing sea ice farther north (Figure 4.1 and Table 4.1). Recent seismic expeditions into the ice have returned structural information on the slopes of the Yermak Plateau, Morris Jesup Rise, and the NE Greenland margin. In particular, new seismic profiles across the Lena Trough image the crustal structure of the gateway for the first time (Figure 4.4). We calibrated the gravimetric COT against seismic profiles where we defined the COT between the seaward limit of faulted

Table 4.1. Seismic Data Used in This Study

Line Name (Figure 4.1)	Type, Format[a]	Province[b]					Reference
		NEG	WBS	MJR	YP	G/HR	
ARLIS-II	SL			x			*Ostenso and Wold* [1977]
AWI-20020387–20020415	MI				x		*Medow* [2004]
AWI-91108–91126	MIL			x	x		*Jokat et al.* [1995]; *Kristoffersen* [1998]
AWI-97200–97245	MI	x	x				*Jokat* [1998]
AWI-99140–99161	MIL				x		*Geissler and Jokat* [2004]
BGR ARK-V/3-10	MIL					x	*Hinz et al.* [1993]
BGR-31-74	ML	x	x			x	*Hinz et al.*[1993]; *Ritzmann et al.* [2004]
BGR-32-74	ML	x	x				*Nøttvedt et al.* [1994]
BU-81-28–81-35	MIL					x	*Karlberg* [1995]
Bat94-3–10	ML		x			x	*Baturin et al.* [1994]
NP-28	MIL			x	x		*Sorokin et al.* [1998]
NPD-POLAR-01–06	MIL				x		*Engen et al.* [2005b][c]; *Gjengedal* [2004]
OBS-98-3	MOIL		x				*Breivik et al.* [2003]
OBS-98-8	MOL		x				*Ljones et al.* [2004]
OBS-98-9	MOIL		x				*Ritzmann et al.* [2002]
SVA-2-87	MIL		x		x		*Eiken* [1994]
UB-12-79	MIL				x		*Eiken* [1994]
V2304–2704	SI					x	*Hammernes* [1998]

[a]*I*, Seismic image (uninterpreted); *L*, Line drawing; *M*, multi-channel seismic; *O*, ocean-bottom seismometer; *S*, single-channel seismic

[b]*NEG*, northeast Greenland margin; *WBS*, western Barents Sea–Svalbard margin; *MJR*, Morris Jesup Rise; *YP*, Yermak Plateau; *G/HR*, Greenland and Hovgård ridges

[c]This volume

basement blocks with internal reflections, and the landward limit of rugged, strongly reflective and acoustically opaque basement.

Dense aeromagnetic surveying during the 1970s revealed low-amplitude seafloor spreading anomalies that have been only tentatively identified in the northern Norwegian–Greenland Sea [*Vogt et al.*, 1981]. By comparing aeromagnetic profiles with marine magnetic tracklines [*Talwani and Eldholm*, 1977] and a gridded dataset including profiles across the W Barents Sea–Svalbard margin [*Olesen et al.*, 1997], we found distinct anomalies masked by long-wavelength noise. We enhanced anomaly information by removing a quadratic trend from each track and normalising the magnetic amplitudes. The processed anomalies were then identified by comparison with synthetic anomalies derived from a 2-D magnetic block model of the oceanic basement (Figures 4.5–4.8) [*Rabinowitz and Labrecque*, 1979]. The model featured 2-km-thick blocks at 4 km depth with 2 A m^{-1} remanent magnetisation aligned with the present-day magnetic field. The width of each block and hence the shape of the synthetic anomalies is a function of time-averaged spreading rates derived from the rotation poles in Table 4.2.

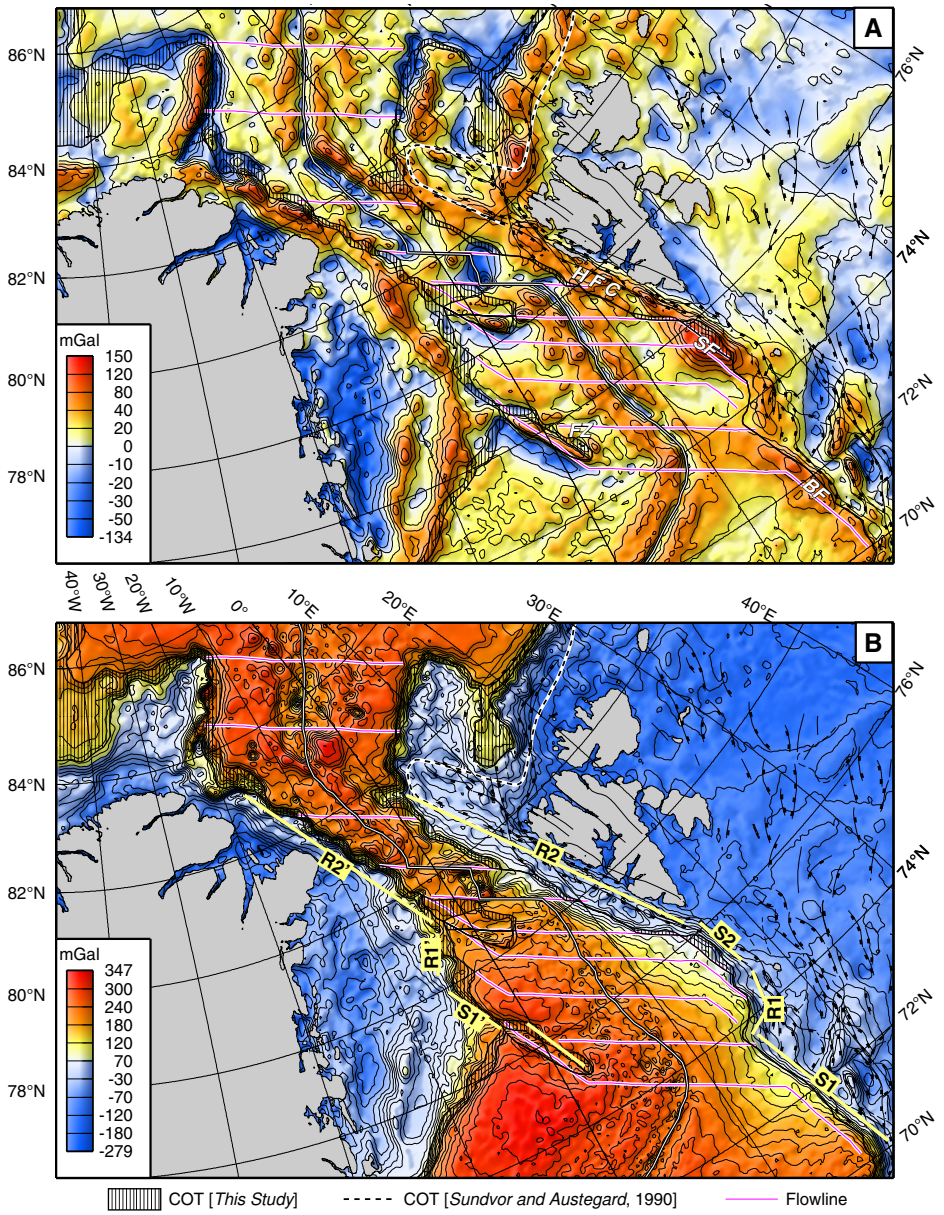

Figure 4.2. (A) Free-air gravity from the Arctic Gravity Project 5×5 min. grid (http://earth-info.nima.mil/GandG/agp/). Note large positive anomalies associated with the Bjørnøya (*BF*) and Storfjorden (*SF*) fans. *FZ*, extinct fracture zone east of the Greenland Ridge; *HFC*, Hornsund Fault Complex. **(B)** Mantle Bouguer anomalies (MBAs) calculated assuming a 6-km-thick basement layer at the seafloor. Basement and mantle densities of 2730 kg m^{-3} and 3330 kg m^{-3}, respectively. *S1*, Senja sheared margin segment; *R1*, volcanic rifted segment west of Bjørnøya; *R2*, obliquely rifted segment. Conjugate NE Greenland margin segments denoted by primes.

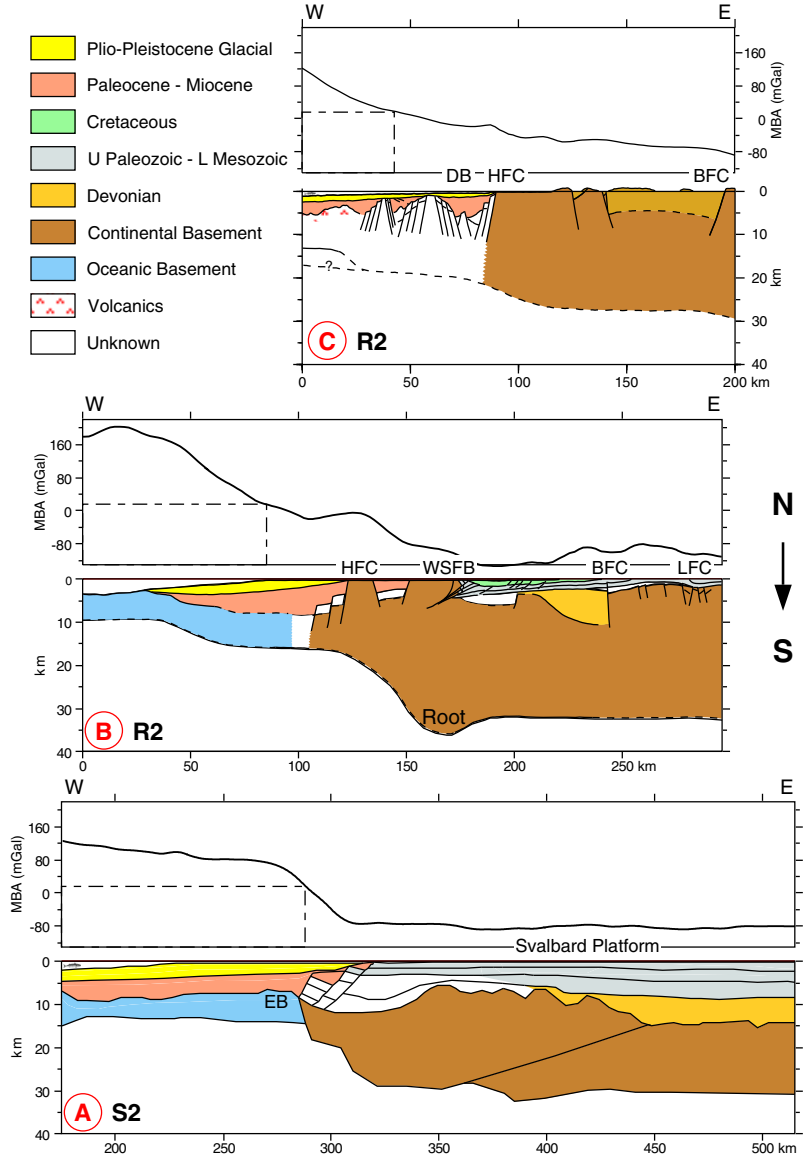

Figure 4.3. Deep seismic transects and MBA profiles across main segments of the W Barents Sea–Svalbard margin north of Bjørnøya. **(A)** Sheared segment NW of Bjørnøya with elevated basement province (*EB*) seaward of the main boundary fault [*Breivik et al.*, 2003]; **(B)** Obliquely rifted segment with crustal root due to Eocene fold-and-thrust belt between Sørkapp and Kongsfjorden [*Faleide et al.*, 1991]; **(C)** Obliquely rifted segment at the transition between the NW Svalbard margin and the Yermak Plateau [*Eiken*, 1994; *Andreassen*, 1998]. Predicted COT location, based on MBA contour from (A), shown by dashed lines. *BFC*, Billefjorden Fault Complex; *DB*, Danskøya Basin; *HFC*, Hornsund Fault Complex; *LFC*, Lomfjorden Fault Complex; *WSFB*, West Spitsbergen fold-and-thrust belt.

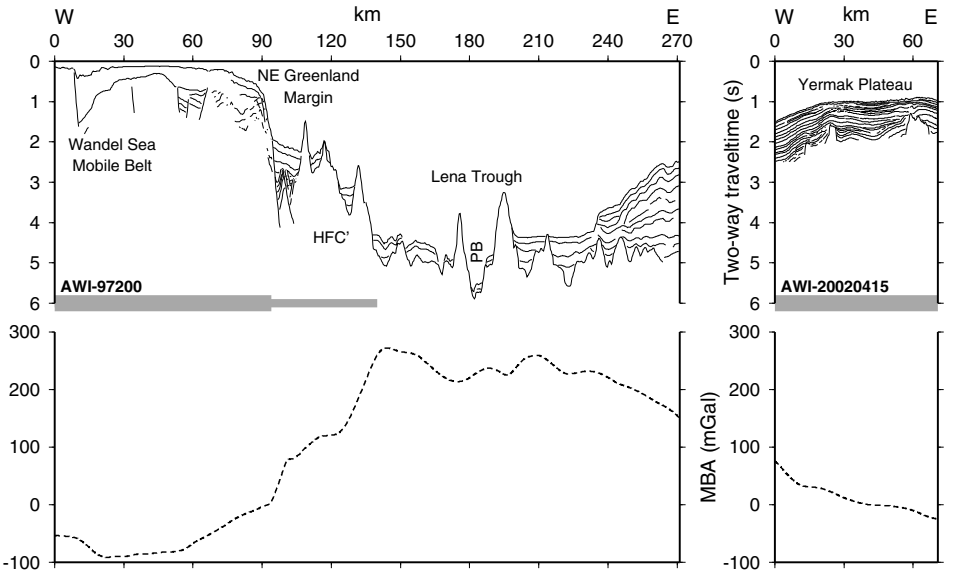

Figure 4.4. Seismic and MBA profiles across the Lena Trough. Line AWI-97200 interpreted from *Jokat* [1998] and line AWI-20020415 from *Medow* [2004]. Continental crust denoted by thick grey bars and transitional or uncertain crust by thin bars. *HFC'*, conjugate to Hornsund Fault Complex; *PB*, plate boundary.

Margin Structure

Western Barents Sea–Svalbard Margin

The sheared Senja margin (S1 in Figure 4.2b) has a steep and well defined COT aligned with plate-motion flowlines [*Faleide et al.*, 1991; *Tsikalas et al.*, 2002]. To the north it transforms into a volcanic rifted segment (R1) including the Vestbakken Volcanic province.

The Hornsund margin between Bjørnøya and northern Spitsbergen was subject to shear during the Eocene and was later obliquely rifted. It comprises a mainly sheared segment (S2) between Bjørnøya and Sørkapp (the southern tip of Spitsbergen) and a rifted segment (R2) north of Sørkapp (Figure 4.2b). The sheared segment has a <5-km-wide COT and the crustal thinning from the Paleozoic–Mesozoic Svalbard Platform to the COT takes place across a ~35-km-wide zone (Figure 4.3a). A 20–60-km-wide basement province seaward of the main boundary fault is elevated >1 km with respect to the adjacent oceanic basement, is magnetically indistinct, and approximately outlined by pre-Chron 13 (33.3 Ma) flowlines (Figure 4.6). We might speculate if the anomalous elevation and magnetic properties reflect a pull-apart basin formed by Eocene shear. However, the seismic reflection and velocity structure of the basement province is similar to that of deeply buried oceanic crust [*Myhre and Eldholm*, 1988; *Breivik et al.*, 2003] so the anomalous elevation may be

due to different basement ages across an oceanic fracture zone. We mark the crustal structure as uncertain in Figure 4.6.

The part of the rifted segment R2 between Sørkapp and Kongsfjorden is characterised by a ~36-km-deep crustal root underneath the Svalbard Platform (Figures 4.2b and 4.3b). The root is related to the W Spitsbergen fold-and-thrust belt which developed in response to crustal overlap during Eocene shear between NE Greenland and Svalbard. The crust was thinned post-Eocene by oblique rifting accommodated by the linear, 60–70-km-wide Hornsund Fault Complex. The initially thickened continental crust is thinned to ~8 km thickness near the COT [*Faleide et al.*, 1991].

North of Kongsfjorden the continental crust is ~30 km thick and did not undergo Eocene shortening [*Ritzmann et al.*, 2004]. The zone of crustal thinning includes the Hornsund Fault Complex and widens to ~180 km north of Spitsbergen [*Czuba et al.*, 2005]. *Ritzmann et al.* [2004] argued that the generally rifted margin includes a minor Oligocene–Miocene sheared segment landward of the Spitsbergen Fracture Zone. At the transition to the Yermak Plateau (Figure 4.3c), two elongate horsts and the probably pull-apart-related Danskøya Basin [*Eiken*, 1992] may indicate a right step of the Eocene megashear zone similar to the volcanic rifted segment west of Bjørnøya (R1). A magnetic high ~80 km landward of the COT overlies a buried volcano on the eastern horst (Figure 4.7) [*Andreassen*, 1998]. Seismic basement reflections near the COT are interpreted as volcanic rocks [*Eiken*, 1994; *Jokat et al.*, 1995].

Yermak Plateau

Sedimentary sequences of the NW Svalbard shelf continue across the inner Yermak Plateau to at least 81.5°N. Seismic velocity structure and low magnetic anomalies indicate continental basement rocks [*Sundvor and Austegard*, 1990; *Ritzmann and Jokat*, 2003]. Therefore, the W slope of the Yermak Plateau is a continental margin. A gentle MBA gradient (Figure 4.4) indicates a wide zone of crustal rifting and thinning and predicts a COT along the trend of the Hornsund Fault Complex (Figure 4.2b). In this way the structural style off NW Spitsbergen (Figure 4.3c) appears to continue north along the W margin of the Yermak Plateau. At the transition to the Eurasia Basin a bathymetric high projects from the NW Yermak Plateau. The inner part of the high may be interpreted as a continental basement horst [*Sorokin et al.*, 1998] but a possible identification of magnetic anomaly 6 in the same area leads us to mark the basement structure as uncertain (Figure 4.7).

MBAs (Figure 4.2b) and seismic refraction [*Jackson et al.*, 1984] indicate that the intermediate crustal thickness of the inner plateau continue onto the outer plateau. The outer plateau is separated from the N Svalbard margin by the Sophia Basin (Figure 4.9a) where ~9 km of sediments are deposited on basement with seismic velocities similar to the continental basement in northern Spitsbergen [*Sundvor et al.*, 1978; *Geissler and Jokat*, 2004]. The basin is flanked by rotated fault blocks [*Geissler and Jokat*, 2004]. Magnetic seafloor spreading anomalies 24B–13 (53.1–33.3 Ma) terminate east of the Sophia Basin and the outer Yermak Plateau. The steep eastern flank of the plateau indicates a sheared margin segment. On this background we interpret the Sophia Basin as a continental rift zone that did not evolve into seafloor spreading. We mark the basin as part of the COT (Figure 4.2b).

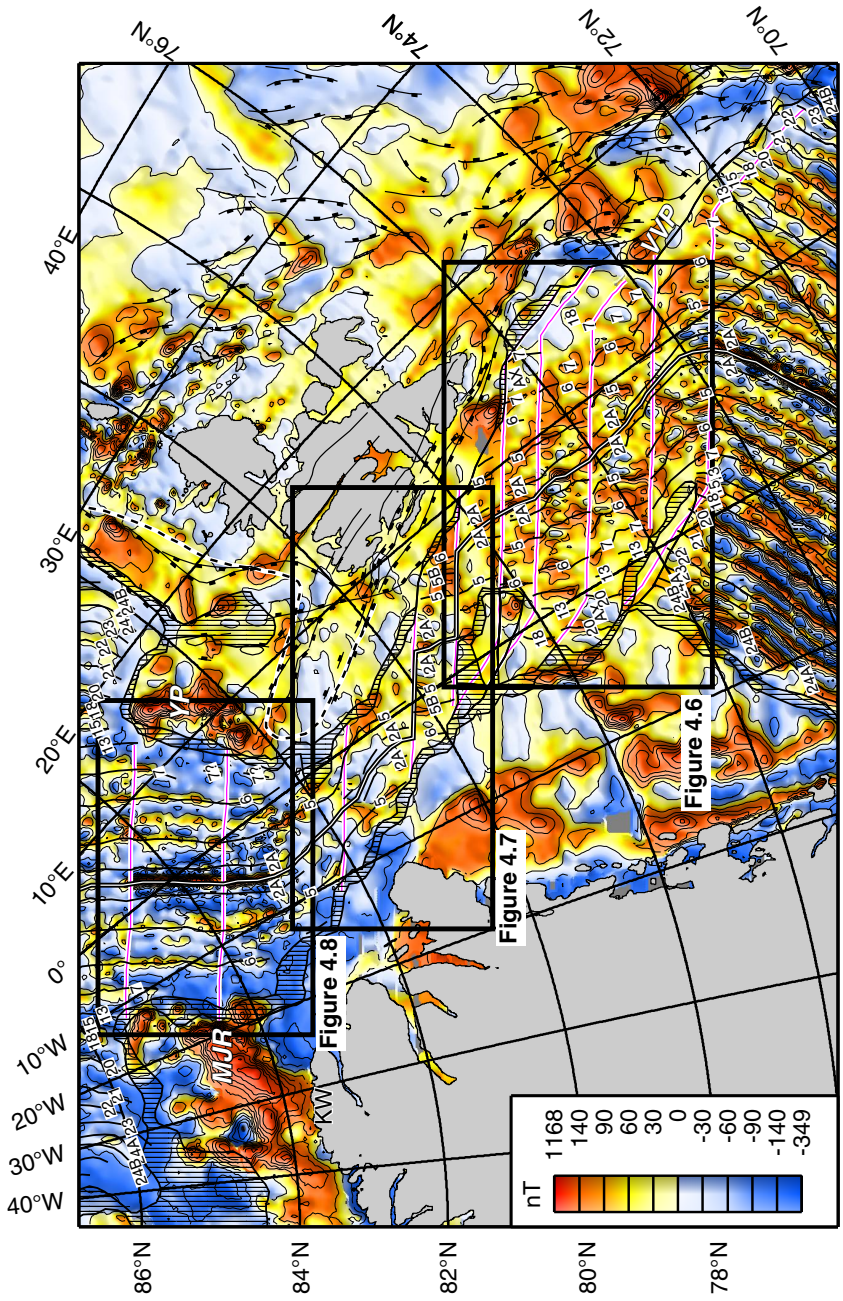

Figure 4.5. Magnetic anomaly field compiled from *Olesen et al.* [1997] in the Norwegian–Greenland and Barents seas and *Verhoef et al.* [1996] elsewhere. Anomaly identifications from Figures 4.6–4.8; legend in Figure 4.2b. *AX*, extinct spreading axis; *KW*, Kap Washington volcanic group; *MJR*, Morris Jesup Rise; *VVP*, Vestbakken Volcanic Province; *YP*, Yermak Plateau.

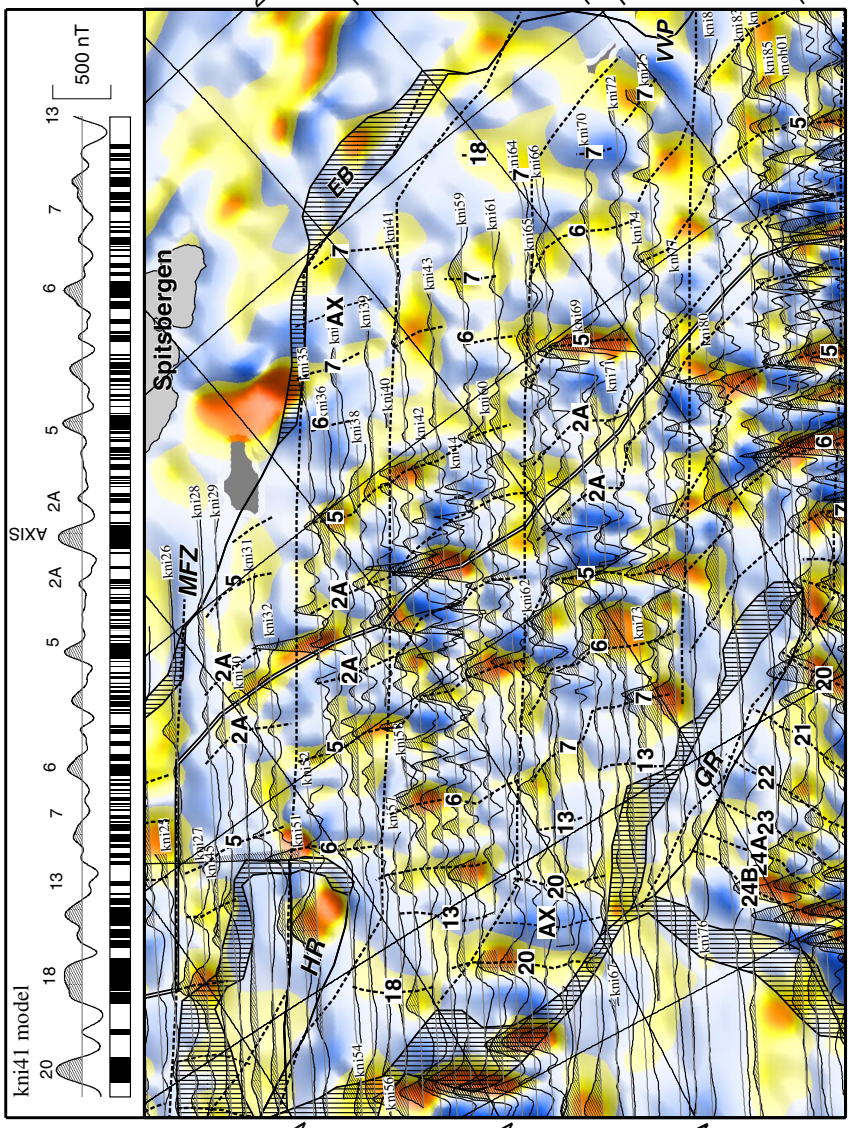

Figure 4.6. Identification of magnetic seafloor spreading anomalies along the Knipovich Ridge. Synthetic anomalies [*Rabinowitz and Labrecque*, 1979] with anomaly numbers indicated (top) assume 2-km-thick blocks at 4 km depth with 2 A m^{-1} remanent magnetisation in the direction of the present-day magnetic field (black) or opposite of it (white). Gridded anomalies (Figure 4.5) are 200 km high-pass Gaussian filtered. *AX*, extinct spreading axis; *EB*, elevated basement province (Figure 4.3a); *GR*, Greenland Ridge; *HR*, Hovgård Ridge; *MFZ*, Molloy Fracture Zone.

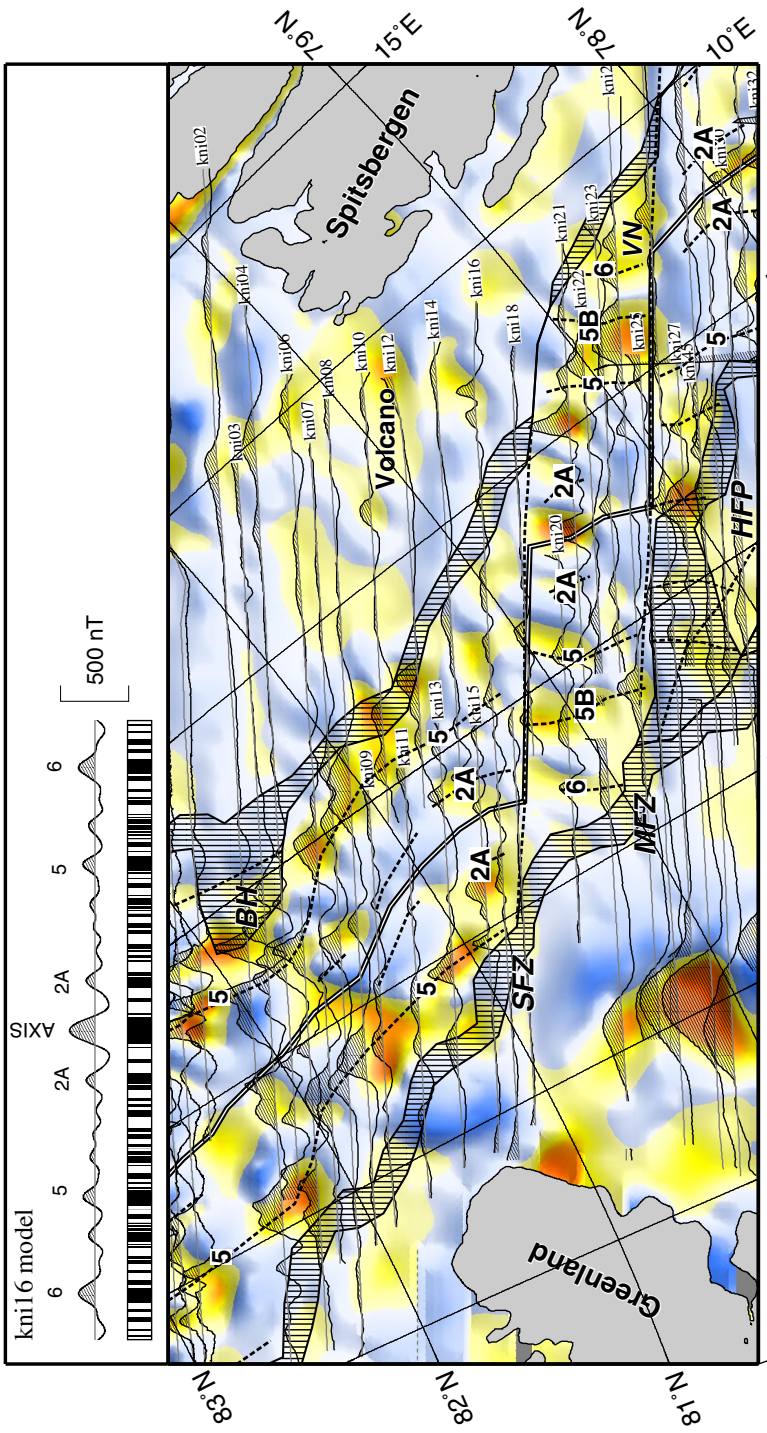

Figure 4.7. Identification of magnetic seafloor spreading anomalies in the Lena Trough. Magnetic high off NW Spitsbergen is associated with a buried volcano [*Andreassen,* 1998]. Synthetic anomalies and filtering as in Figure 4.6. *BH,* bathymetric high of uncertain origin on the NW Yermak Plateau; *HFP,* Hovgård Fault Province; *MFZ,* Molloy Fracture Zone; *SFZ,* Spitsbergen Fracture Zone; *VN,* Vestnesa.

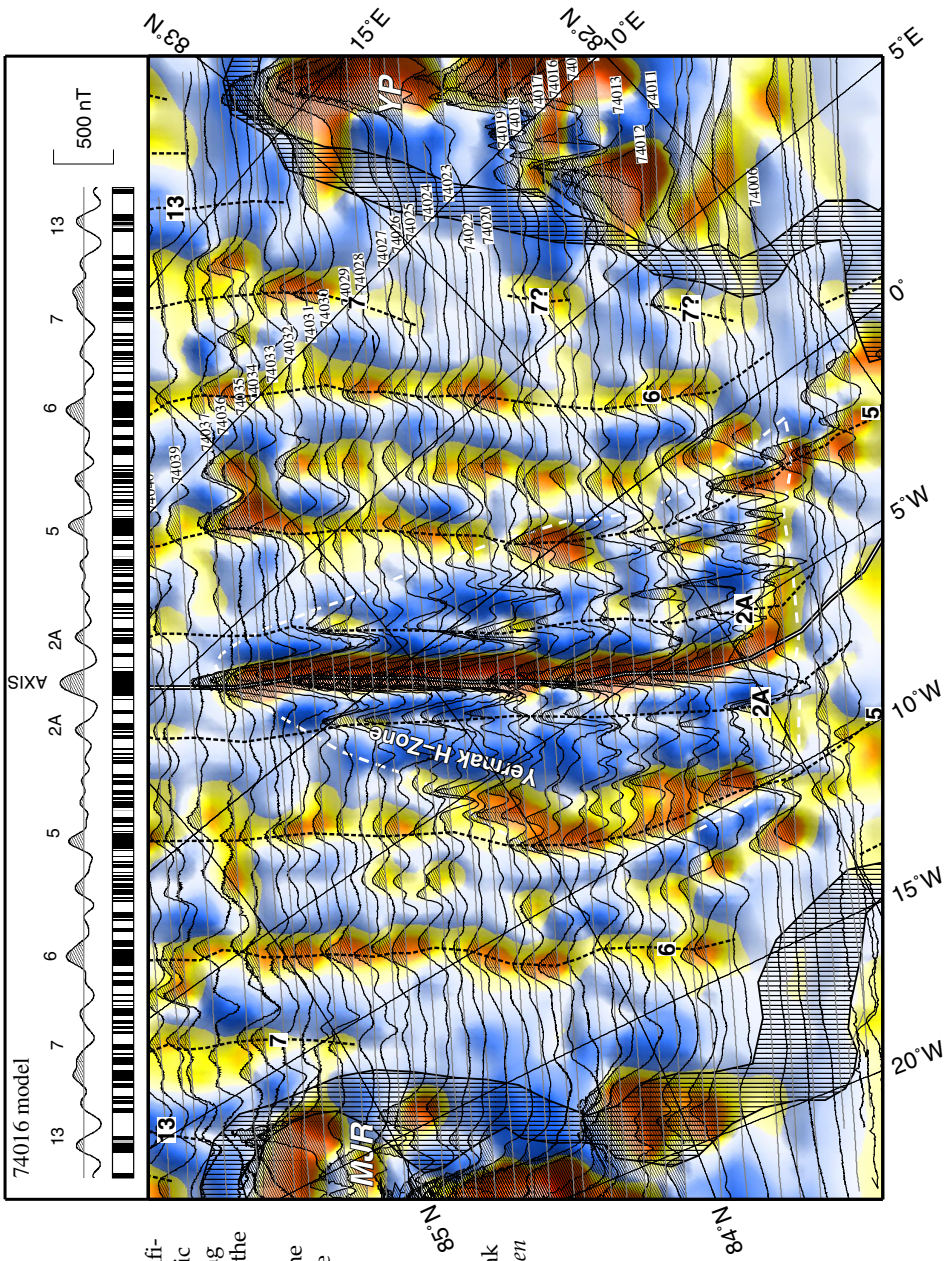

Figure 4.8. Identification of magnetic seafloor spreading anomalies along the western Gakkel Ridge between the Morris Jesup Rise (*MJR*) and the Yermak Plateau (*YP*). Synthetic anomalies and filtering as in Figure 4.6. Yermak H-Zone from *Feden et al.* [1979].

Table 4.2. Total Opening Poles of Greenland and North America Relative to Eurasia[a]

Anomaly	Chron	Age, Ma	Lat., °N	Lon., °E	Angle, °
5	5n.1n	9.8	68.06	132.47	2.54
6	6n	19.6	69.77	128.76	4.93
7	7n.1n	24.8	68.59	129.48	6.25
13	13n	33.3	68.60	130.17	7.84

[a]Poles from *Lawver et al.*[2002]; Age correlations from *Cande and Kent* [1995].

From Figure 4.9 we interpret that the outer Yermak Plateau is as well underlain by block-faulted basement terminating against a possible boundary fault facing the Eurasia Basin [*Jokat et al.*, 1995; *Engen et al.*, 2005b, this volume]. We therefore propose a COT around the lower slope of the Yermak Plateau rather than between the inner and outer plateau at ~81.5°N (Figure 4.2) as suggested by *Sundvor and Austegard* [1990]. In our opinion, the previous COT location represents the known minimum extent of continental crust as of 1990. There is a northward increase of magnetic amplitudes and basement velocities to levels appropriate for 26–41-Myr-old oceanic crust (Figure 4.5) [*Jackson et al.*, 1984]. However, high-amplitude magnetic anomalies may also relate to shallow magmatic intrusions in continental crust. The latter alternative is supported by the irregular shape of magnetic anomalies in the Sophia Basin and the outer Yermak Plateau compared to the linear and easily identified anomalies in the Eurasia Basin (Figure 4.8). The lack of a crustal thickness or density boundary at the previous COT location (Figure 4.2b) is, at best, coincidental. We cannot resolve any other thickness boundaries through the outer plateau, so a continental Sophia Basin implies that a COT around the outer plateau is the most likely alternative. However, because of sparse data and lack of direct evidence, our interpretation is preliminary.

Morris Jesup Rise

The Morris Jesup Rise comprises a steep, outer basement block to the southeast and a lower-lying, faulted province to the northwest (Figure 4.9b). The sedimentary cover comprises syn-rift infill of basement grabens and a thin draping unit [*Ostenso and Wold*, 1977; *Jokat et al.*, 1995]. Moderate MBA amplitudes indicate crustal thicknesses intermediate between the adjacent NE Greenland margin and oceanic crust. The crustal thinning from the Morris Jesup Rise to the Eurasia Basin is accommodated almost entirely by a single fault, in contrast to the gradually down-stepping fault terraces of the conjugate Yermak Plateau. However, a buried block of thin continental or transitional crust may be present farther seaward.

Similar to on the Yermak Plateau, high-amplitude and irregular magnetic anomalies over the SE part of the Morris Jesup Rise are separated and distinct from the adjacent seafloor spreading anomalies. The magnetic character is furthermore reminiscent of continental magmatic rocks [*Dawes*, 1990]. In fact, the magnetic high continues east along the N Greenland margin and coincides with the onshore Kap Washington Group (Figure 4.5) which is a 4–5-km-thick pile of basalts and

pyroclastic rocks erupted at the Cretaceous–Paleogene boundary [*Dawes*, 1973; *Riddihough et al.*, 1973; *Estrada et al.*, 1999]. Noting possible errors introduced by large compressive faults in the area, we are confident that the magnetic high on the SE Morris Jesup Rise corresponds to the onshore volcanics. Because seafloor spreading between the Morris Jesup Rise and the Yermak Plateau commenced at Chron 13 times (~33.3 Ma), we infer that the magnetic high on the outer Yermak Plateau may be also related to the Kap Washington Group.

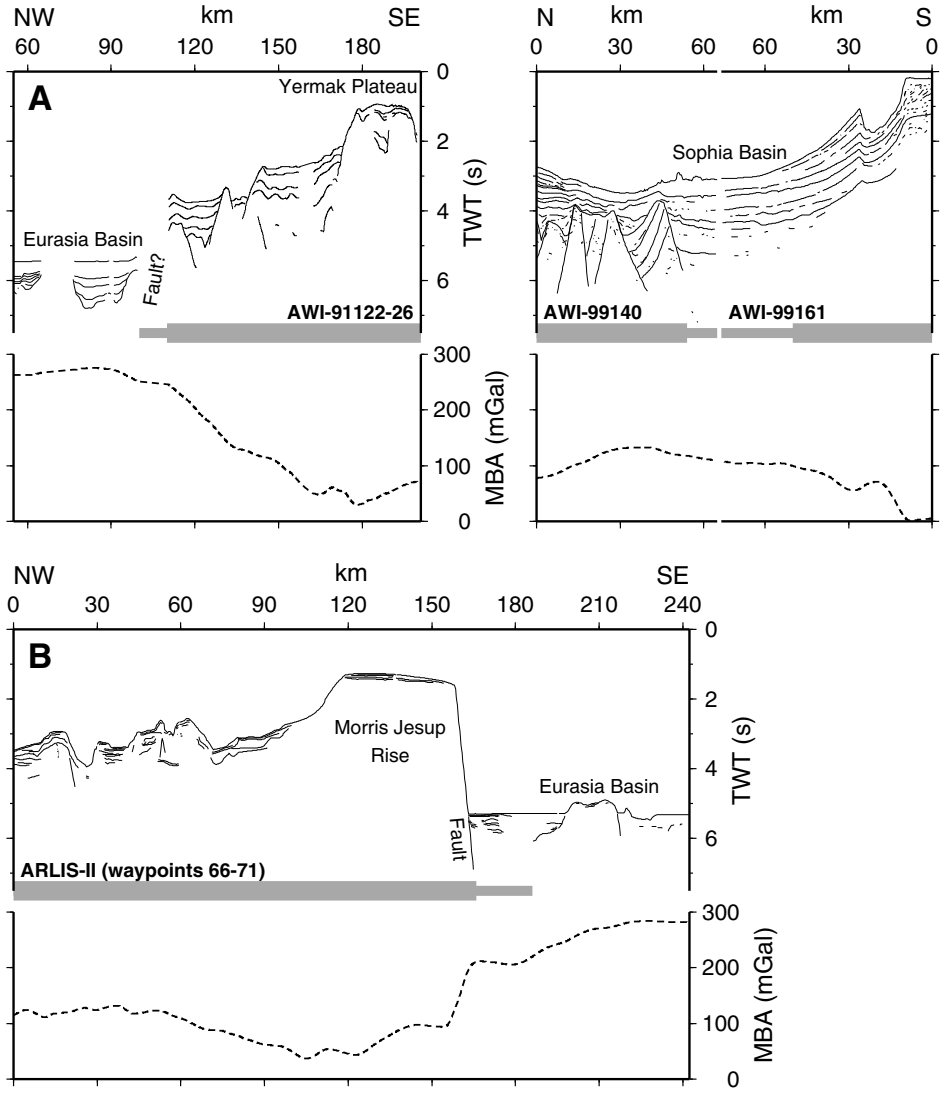

Figure 4.9. (A) MCS and MBA profiles from the Eurasia Basin across the Yermak Plateau to the N Svalbard margin, interpreted from *Kristoffersen* [1998], *Jokat et al.* [1995], and *Geissler and Jokat* [2004]. **(B)** Single-channel seismic [*Ostenso and Wold*, 1977] and MBA profile across the conjugate segment of the Morris Jesup Rise. Crustal structure outlined by grey bars as in Figure 4.4.

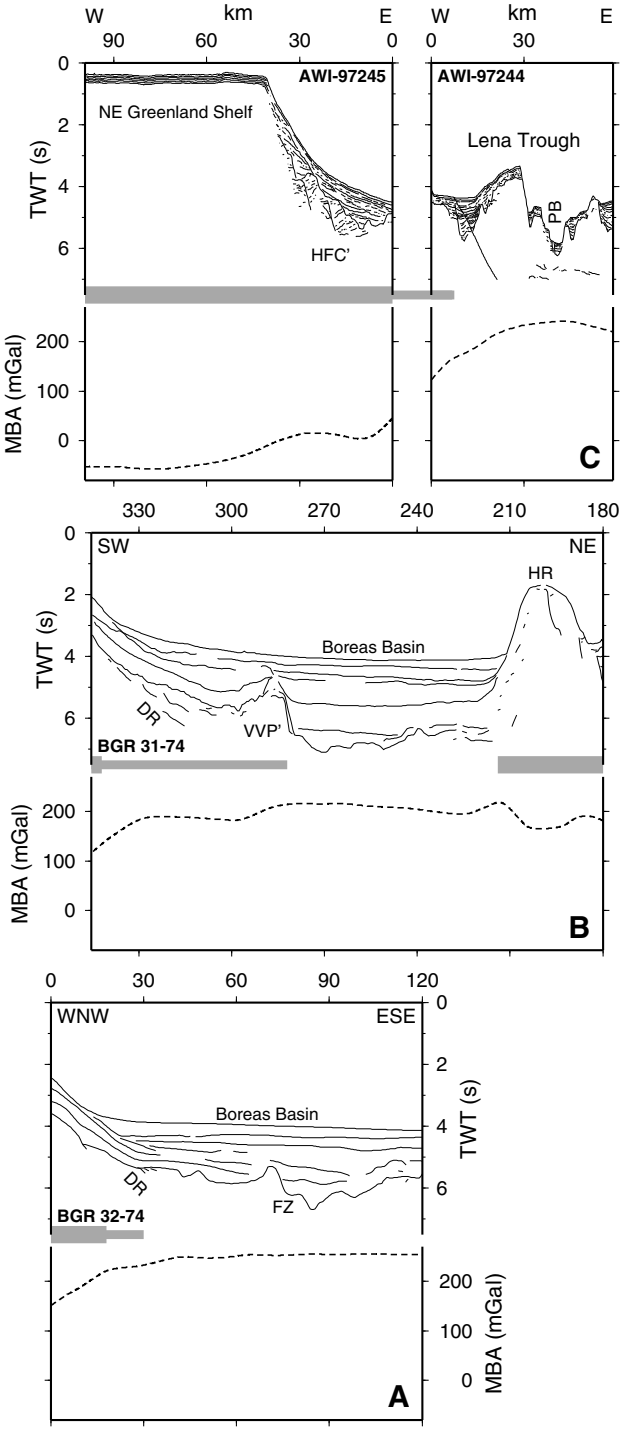

Figure 4.10. MCS and MBA profiles across the NE Greenland margin. **(A)** Volcanic rifted segment R1′ [*Nøttvedt et al.*, 1994]. **(B)** Volcanic rifted segment R1′ with conjugate to the Vestbakken Volcanic Province (*VVP′*) [*Eiken*, 1994]; **(C)** Obliquely rifted segment R2′, interpreted from *Jokat* [1998]. Margin segmentation outlined in Figure 4.2b. Crustal structure outlined by grey bars as in Figure 4.4. *DR*, dipping reflectors; *FZ*, extinct fracture zone in Boreas Basin; *HFC′*, conjugate to Hornsund Fault Complex; *HR*, Hovgård Ridge; *PB*, plate boundary.

Northeast Greenland Margin

The COT is pinpointed along two MCS lines in the Lena Trough and two lines in the Boreas Basin (Figures 4.4 and 4.10). Between these points, conjugate margin segmentation on the NE Greenland and W Barents Sea–Svalbard margins is tentatively mapped by MBA gradients (Figure 4.2b). The margin segment south of 78°N (S1′) is flanked by Chron 20 oceanic crust and may have formed by shear between the Greenland Ridge and the adjacent continental margin.

Between 80°N and the Hovgård Ridge (R1′) the margin corresponds in a plate reconstruction to the rifted volcanic segment west of Bjørnøya (Figure 4.2b). Dipping basement reflectors and (Figure 4.10a–b) and high-amplitude magnetic anomalies (Figure 4.6) indicates break-up-related magmatism. The southern part of the margin segment has a gradual COT (Figure 4.10a) while the COT of the middle segment includes an outer, fault-bounded high probably formed by shear (Figure 4.10b). This structural setting appears conjugate to the western flank of the Vestbakken Volcanic Province on the W Barents Sea–Svalbard margin, although flowlines do not exactly connect the two locations.

The margin north of the Hovgård Ridge (R2′) developed by Oligocene–Miocene oblique rifting of previously sheared provinces. On the continental slope we interpret a 40–50-km-wide zone of crustal thinning conjugate to the Hornsund Fault Complex (Figures 4.4 and 4.10c). The margin landward of the fault complex is narrow and dominated by Cretaceous–Paleogene strike-slip faults of the Wandel Sea mobile belt [*Dawes*, 1990]. The projection of the Eocene Eurekan fold-and-thrust belt [*von Gosen and Piepjohn*, 2003] intersects the margin at ~83°N but this possible northward structural transition is unresolved in our data.

We cannot locate any sheared margin segment conjugate to S2 on the W Barents Sea–Svalbard margin (Figure 4.2b). Because the sheared margin is older than the rifted margin, it may have been altered during rifting. Alternatively, the conjugate sheared margin is embedded in the Hovgård Ridge microcontinent.

Ocean Structure

Present-Day Plate Boundary

The plate boundary comprises the Knipovich Ridge in the Norwegian–Greenland Sea and the Gakkel Ridge in the Eurasia Basin, linked by transform segments and oblique ridges in the Lena Trough province. We keep the plate boundary location of *Engen et al.* [2003, this volume] which was based primarily on gravity and earthquake epicentre locations; however we revise their interpretation of two small-offset fracture zones in the northern Lena Trough. From the more comprehensive dataset available to us, we observe a continuous free-air gravity low from the Spitsbergen Fracture Zone to the Gakkel Ridge and interpret it as a single, highly oblique and curved ridge segment (Figure 4.2a).

The axial magnetic anomaly is continuous and high-amplitude on the Gakkel and Mohn ridges but weak and partly absent along the Lena Trough and the Knipovich Ridge (Figure 4.5). Because the latter segments are highly oblique, axial

magnetic amplitudes may be correlated with ridge obliquity. The magnetic modelling shows that a low axial anomaly may also result from a slightly asymmetric distribution of magnetised bodies.

Magnetic Seafloor Spreading Anomalies

Seafloor spreading across the Knipovich Ridge has generated a pattern of discontinuous and short magnetic anomalies (Figure 4.6). Nonetheless, we may identify magnetic anomalies at least back to Chron 13 (33.3 Ma) south of the Hovgård Ridge and possibly back to Chron 6 (19.6 Ma) farther north. Anomalies are more distinct on the NE Greenland side than on the W Barents Sea–Svalbard side where the oceanic basement is deeper due to large sediment input from the Barents Sea shelf and Svalbard. Anomalies younger than Chron 2A (2.8 Ma) cross-cut older anomalies and indicate that the present spreading axis has smoothed an older, more segmented plate boundary. Re-organisations of the plate boundary are also indicated by two possible fracture zones in the Boreas Basin. On the eastern side of the Greenland Ridge, anomalies 13 through 5 are offset across a flowline-striking basement depression associated with a free-air gravity low (Figure 4.2a) [*Engen et al.*, 2005a, this volume]. In the central Boreas Basin, offset magnetic anomalies correlate with a shift in basement elevation (Figure 4.10a). The Knipovich Ridge between 76° and 77°N is fairly symmetric with respect to the continental margins and has had nearly the same location since break-up. Along the ridge segment between 77° and 77.5°N, anomaly 6 is located close to the Hovgård Ridge on the NE Greenland side but >100 km seaward of the COT on the W Barents Sea–Svalbard side (Figure 4.6). We tentatively interpret an extinct, pre-Chron 6 spreading axis that shifted to the present plate boundary location at the time of break-up between the Hovgård Ridge microcontinent and the W Barents Sea–Svalbard continental margin. The presence of such an extinct ridge is difficult to assess by seismic data; however relatively elevated oceanic basement in the area [*Myhre and Eldholm*, 1988; *Eiken*, 1994] leaves some possibility for it.

Pre-Chron 13 anomalies are only identified with confidence on the NE Greenland side (Figure 4.6). We identify an anomaly 20 (43.2 Ma) pair north of the Greenland Ridge with a different trend and higher amplitudes than the younger anomalies. Anomaly 20 may also be present on the southwest side of the Hovgård Ridge, but the quiet magnetic field in the area precludes identification of anomalies older than Chron 18 (39.9 Ma). There is room for post-Chron 13 seafloor spreading only between the Greenland Ridge and the W Barents Sea margin.

The northernmost segment of the Knipovich Ridge is flanked by weak magnetic anomalies (Figure 4.6). At the junction with the Molloy FZ, anomaly 5 (9.8 Ma) is directly seaward of the COT. The ridge segment immediately to the south has space for an earlier segmented or highly oblique plate boundary. The Molloy Ridge segment shows distinct anomalies back to Chron 6 (19.6 Ma; Figure 4.7). On the Svalbard side, anomalies 5 and older form a convolute positive anomaly over Vestnesa which is a depocentre overlying an oceanic basement high [*Eiken and Hinz*, 1993; *Baturin et al.*, 1994].

The Lena Trough has curved anomalies approximately following the geometry of the COT (Figure 4.7). Anomaly 5 (9.8 Ma) is the oldest anomaly found along all segments of the trough. The ridge segment just north of the Spitsbergen Fracture

Zone appears to be shifted towards the NE Greenland margin. However, post-Chron 5 magnetic anomalies are symmetric with respect to the spreading axis, indicating either that the COT location is inaccurate, or that the asymmetric position of the axis was created during the initial stages of seafloor spreading. The latter alternative is supported by the irregular shape of anomalies older than Chron 5. In the NE part of the Lena Trough, we observe irregular magnetic highs landward of anomaly 5 in the same manner as on the Molloy Ridge segment.

Seafloor spreading anomalies in the W Eurasia Basin are linear and well defined (Figure 4.8). The anomalies indicate that the Yermak Plateau and the Morris Jesup Rise were a continuous plateau prior to Chron 13 times and were separated by southward propagation of seafloor spreading. We follow the anomaly 13 pair (33.3 Ma) from the central basin to near the NE tips of the Yermak Plateau and the Morris Jesup Rise. Anomaly 7 (24.8 Ma) continues at least 60 km farther westward. In the western part of the basin two scattered linear magnetic highs on the Yermak Plateau side may be interpreted as anomaly 7, suggesting an early asymmetric position of the plate boundary. Anomaly 5 (9.8 Ma) is the oldest anomaly completely separating the plateaus and continuing into the Lena Trough. A ~200-km-long V-shaped region of >1000 nT magnetic amplitudes is centred on the spreading axis, enclosed by anomaly 5, and corresponds to an elevated ridge province. The region was termed the Yermak H-Zone by *Feden et al.* [1979].

Submarine Ridges in the Norwegian–Greenland Sea

The Norwegian–Greenland Sea is compartmentalised by the elongate Greenland and Hovgård ridges, situated where the ocean basin to the north is narrower than that to the south. This geometrical observation suggests that the ridges are related to fracture zones formed when the Eocene propagation of seafloor spreading temporarily stalled and was translated along the megashear region between Svalbard and NE Greenland [*Eldholm et al.*, 1987; *Faleide et al.*, 1993; *Tsikalas et al.*, 2002].

The Hovgård Ridge proper is defined by the 2.4 km depth contour as a triangular, ~100-km-long high rising to 1.2 km depth (Figure 4.11). The ridge and a smaller, isolated high to the east separate the ~2.5-km-deep Fram Strait Sill to the north from the ~3.0-km-deep Boreas Basin to the south. The SW ridge flank is steep and aligns approximately with the Chron 18–20 plate motion flowline (39.9–43.2 Ma), suggesting that it formed as a sheared margin segment during that time. A sheared origin is further supported by magnetic anomaly 18 terminating against a linear basement trough along the foot of the SW ridge flank. The trough is associated with a free-air gravity low and may represent an extinct fracture zone (Figure 4.2a). On the nearly as steep NE ridge flank, a linear valley which we denote the Central Valley trends along the Chron 6–13 flowline (19.6–33.3 Ma) and turns south at the isolated eastern high (Figure 4.11). The eastern high has a pronounced, circular magnetic anomaly at the northward termination of a linear anomaly identified as anomaly 6 (Figure 4.6). Acoustic reflection patterns and onlap geometries indicate that the high is a seamount [*Johansen*, 1985] denoted the Hovgård Seamount (Figure 4.11).

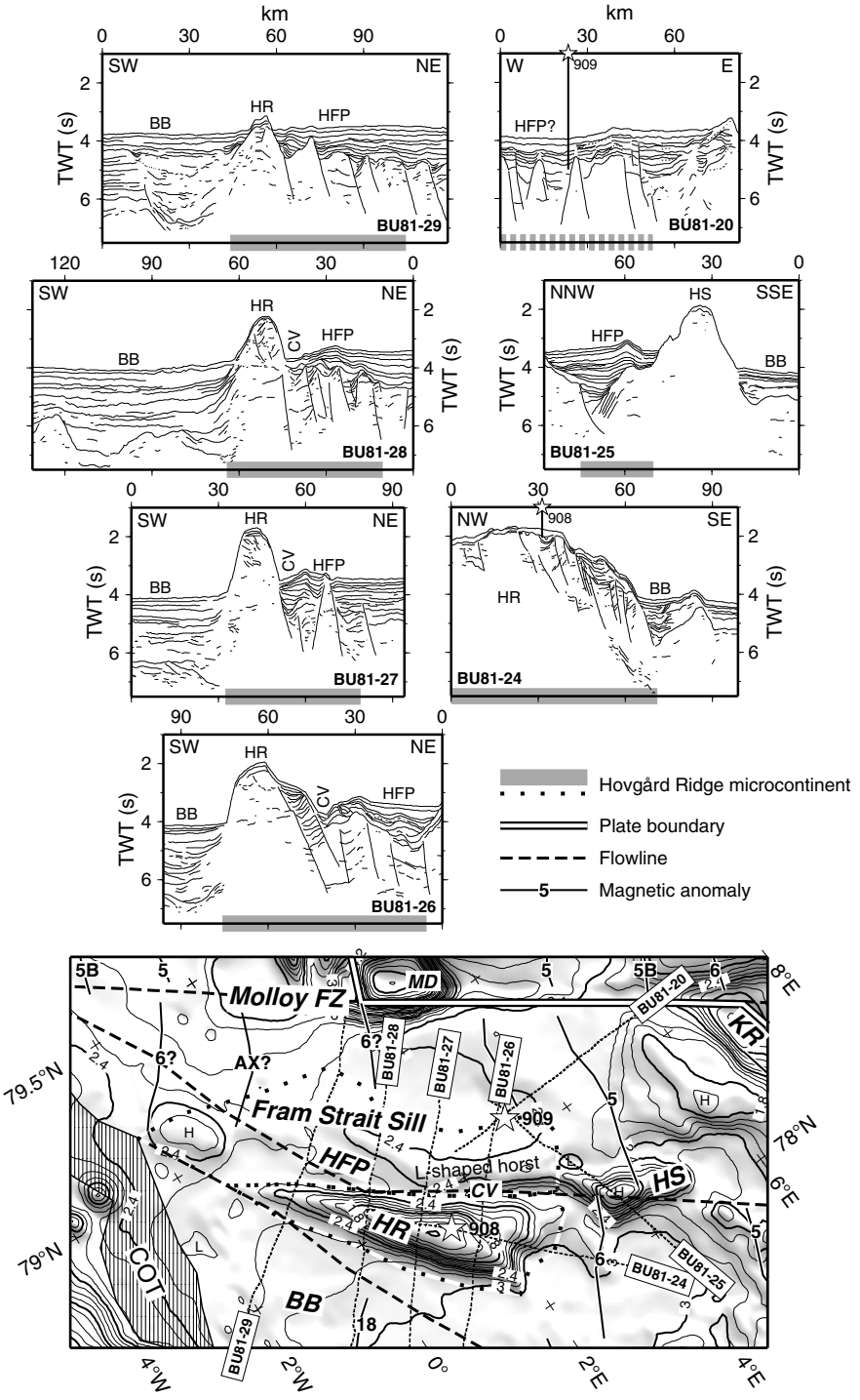
km
SW
NE
BB
HR
HFP
BU81-29
W
909
E
HFP?
BU81-20
CV
BU81-28
NNW
HS
SSE
BU81-25
NW
908
SE
BU81-24
BU81-27
BU81-26
TWT (s)
Hovgård Ridge microcontinent
Plate boundary
Flowline
5 Magnetic anomaly
Molloy FZ
MD
AX?
Fram Strait Sill
L-shaped horst
KR
COT
BU81-29
79.5°N
79°N
78°N
8°E
6°E
4°W
2°W
0°
2°E
4°E

Figure 4.11 (opposite). MCS profiles [*Karlberg*, 1995] and 0.15-km contoured bathymetry [*Jakobsson et al.*, 2000] across the Hovgård Ridge microcontinent (location in Figure 4.1). The microcontinent comprises the Hovgård Ridge proper (*HR*) and the Hovgård Fault Province (*HFP*), separated by the flowline-striking Central Valley (*CV*). The type of basement along profile BU81-20 is uncertain but probably belongs to the HFP. *BB*, Boreas Basin; *HS*, Hovgård Seamount; *KR*, Knipovich Ridge; *MD*, Molloy Deep.

MCS profiles show that the Hovgård Ridge proper consists of a single continental block with sparse internal reflections [*Karlberg*, 1995]. Across the Central Valley, the basement block becomes strongly faulted and continues as the low-lying and reflective Hovgård Fault Province (HFP) underneath large parts of the Fram Strait Sill (Figure 4.11). Sediments overlying the HFP date from the Late Oligocene (~24 Ma) [*Thiede et al.*, 1995]. Upper basement velocities are in the 3.3–3.6 km s^{-1} range both beneath the Hovgård Ridge proper and the HFP [*Johansen*, 1985; *Ritzmann et al.*, 2004], supporting that the two provinces consist of similar basement rocks. However, the HFP has only 4–6-km-thick basement [*Ritzmann et al.*, 2004], which is extremely thin for continental crust. Therefore, we might interpret that the HFP is oceanic and was faulted due to migration of the Molloy Fracture Zone, but seismic refection character as well as seismic velocities of the HFP are clearly distinct from those of the adjacent oceanic basement [*Karlberg*, 1995; *Ritzmann et al.*, 2004]. The reflection character of the HFP is furthermore similar to the rifted continental terraces of the Hornsund Fault Complex [*Myhre and Eldholm*, 1988]. The quiet magnetic field over the HFP supports a continental origin whereas high-amplitude anomalies over the southern end of the Hovgård Ridge proper are associated with magmatic intrusions into continental crust. By including the HFP in the Hovgård Ridge microcontinent, the area of the microcontinent is more than doubled with respect to earlier interpretations [*Myhre et al.*, 1982; *Lawver et al.*, 1990].

The outline of a major horst within the HFP can be traced from the bathymetry as a wide L-shape aligned with pre-Chron 13 flowlines to the west (Figure 4.11). We may speculate if the shape was previously aligned with the SW flank of the Hovgård Ridge and later offset by right-lateral translation along the central valley; however, the seismic data cannot further constrain such a kinematic interpretation.

The HFP is terminated to the NE by increasing basement reflectivity and velocity to oceanic levels [*Karlberg*, 1995; *Ritzmann et al.*, 2004]. To the NW, the quiet magnetic field over the HFP changes into a province with faint, linear anomalies (Figures 4.6 and 4.7). If these anomalies are related to seafloor spreading, a post-Chron 13 and now extinct transform fault is required along the Central Valley. However, linear anomalies may also result from magmatic intrusion of continental fault blocks, so we regard the crustal structure as uncertain. The NW extension of the HFP towards the NE Greenland margin cannot be further constrained because of the lack of seismic data. Consequently, we cannot yet determine if the Hovgård Ridge is a microcontinent surrounded by oceanic crust, or a continental sliver attached to the NE Greenland margin.

The Greenland Ridge is characterised by a 1.5-km-high escarpment on the SW side and a gentle slope on the NE side (Figure 4.12). Seismic reflection profiles show that the escarpment-bounded ridge proper consists of homogeneous basement while the NE slope is underlain by a fault province which is difficult to demarcate against

the adjacent ocean basin. By analogy to the Hovgård Ridge we interpret the seismic character of the ridge proper as well as the fault province in terms of continental crust. The eastward extent of the fault province is based on a gentle MBA low and magnetic quiet zone. The ridge proper is associated with an elongate free-air gravity high with two local maxima, indicating two basement blocks separated by the 0° meridian. Magnetic seafloor spreading anomalies 24B–20 (53.1–43.2 Ma) terminate against the SW escarpment whereas anomalies 18–13 (39.9–33.3 Ma) indicate gradual propagation past the southern tip of the ridge (Figure 4.6). A free-air gravity low strikes along the SW flank. These observations are consistent with the Greenland Ridge as a continental sliver formed between two successive sheared margin segments [*Tsikalas et al.*, 2002]. The absence of pre-Chron 13 seafloor spreading anomalies and the diffuse COT on the NE side indicates that the final separation between the Greenland Ridge and the SW Barents Sea margin was achieved by Oligocene rifting of the previously sheared margin segment. Oligocene rifting and volcanism is well documented in the conjugate Vestbakken Volcanic Province [*Jebsen*, 1998].

The linearity of the adjacent NE Greenland margin (segment S1' in Figure 4.2b) and the identification of anomaly 20 (43.2 Ma) to the north of the Greenland Ridge imply that the ridge slid past the margin during the Eocene. Nonetheless, from bathymetry and free-air gravity (Figures 4.1 and 4.2b) it appears that the ridge is still attached to the margin and hence classifies as a continental sliver. The transition between the ridge and the margin consists of fault blocks similar to those of the outer ridge (Figure 4.12).

Plate Tectonic Reconstructions

We test our new location of the spreading axis, seafloor spreading isochrons and the COT in a plate tectonic reconstruction of the Fram Strait gateway. We keep Eurasia fixed and use previously published poles for the relative motion of Greenland and North America based on isochrons and flowlines from the North Atlantic and Arctic oceans (Table 4.2). We apply these poles instead of deriving new ones because (1) the strike of the present-day Molloy and Spitsbergen fracture zones agrees with the Chron 1–5 pole; (2) the linear SW flanks of the Hovgård and Greenland Ridges align with pre-Chron 13 flowlines; and (3) the relatively straight magnetic anomalies in the Lena Trough provide little additional constraints on the poles in Table 4.2.

At Chron 6 times (~19.6 Ma), the two continents were in contact from the Spitsbergen Fracture Zone to the northern end of the Lena Trough (Figure 4.13). The Molloy Ridge and adjacent fracture zones probably existed but the irregular shape of the oldest magnetic anomalies in the area (Figure 4.7) indicates immature seafloor spreading in an oceanic, landlocked pond, perhaps analogous to the current magmatism in the Salton Trough of SE California [*Parsons and McCarthy*, 1996]. The reconstruction indicates crustal overlap and highly oblique rifting between the northern Hovgård Fault Province and the conjugate Hornsund margin, but crustal

overlap may be expected from the strongly faulted and thinned continental basement on both sides.

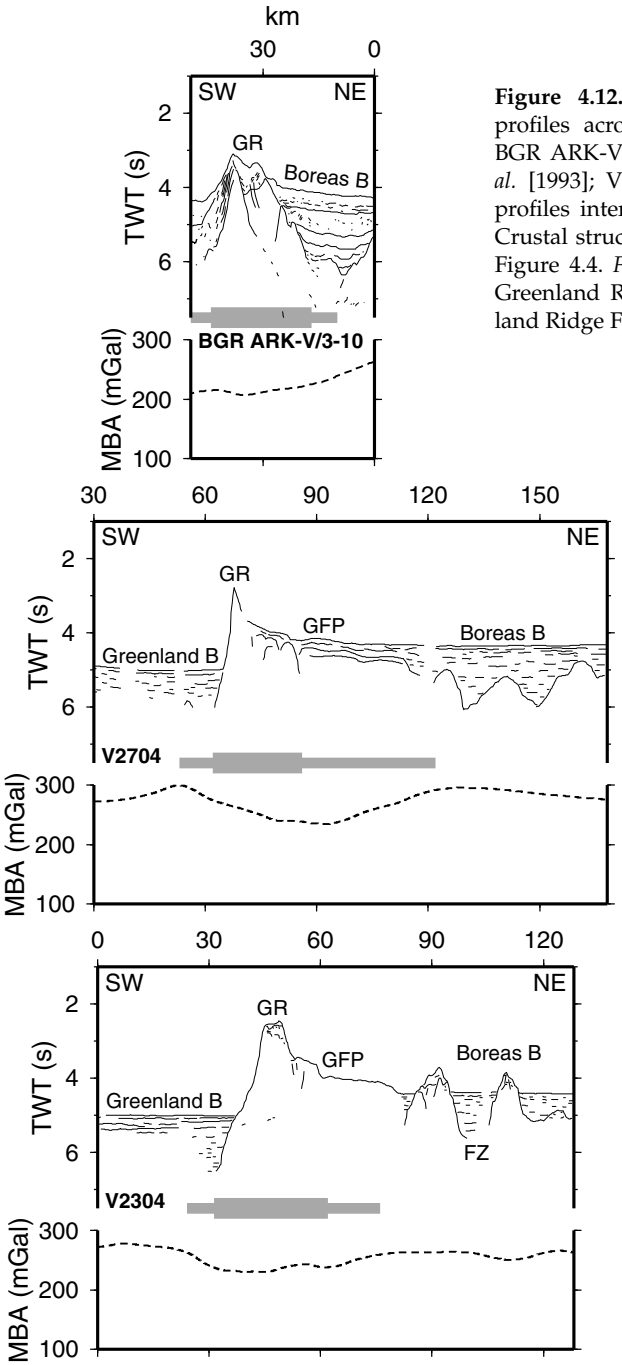

Figure 4.12. MBA and seismic reflection profiles across the Greenland Ridge (*GR*). BGR ARK-V/3-10 MCS profile after *Hinz et al.* [1993]; V2304 and V2704 single-channel profiles interpreted from *Hammernes* [1998]. Crustal structure outlined by grey bars as in Figure 4.4. *FZ*, extinct fracture zone east of Greenland Ridge (Figure 4.2a); *GFP*, Greenland Ridge Fault Province.

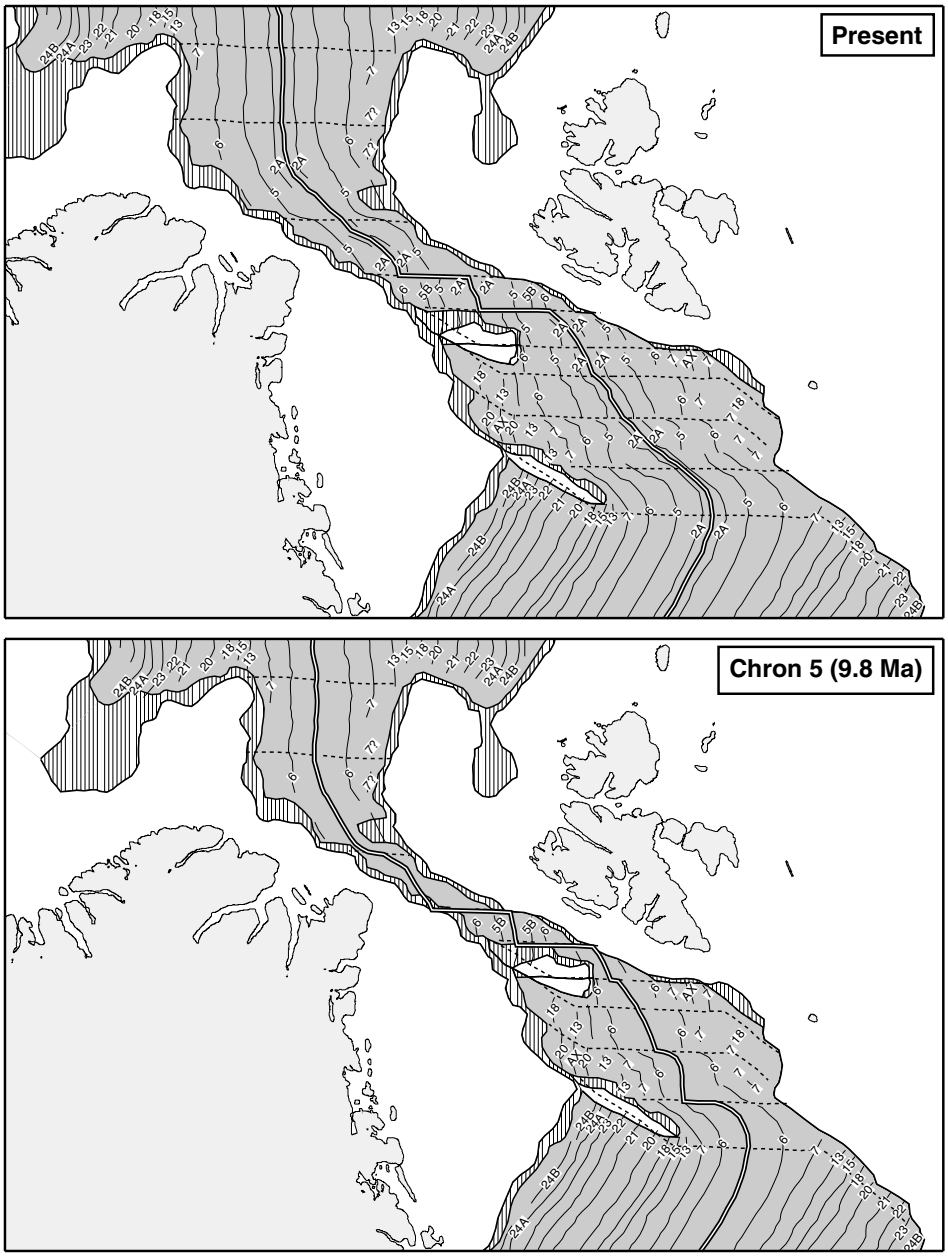

Figure 4.13. Plate tectonic reconstructions of the Fram Strait gateway. Eurasia is kept fixed and Greenland and North America are rotated by the poles in Table 4.2. Oceanic crust is grey-shaded and magnetic seafloor spreading anomalies annotated by number.

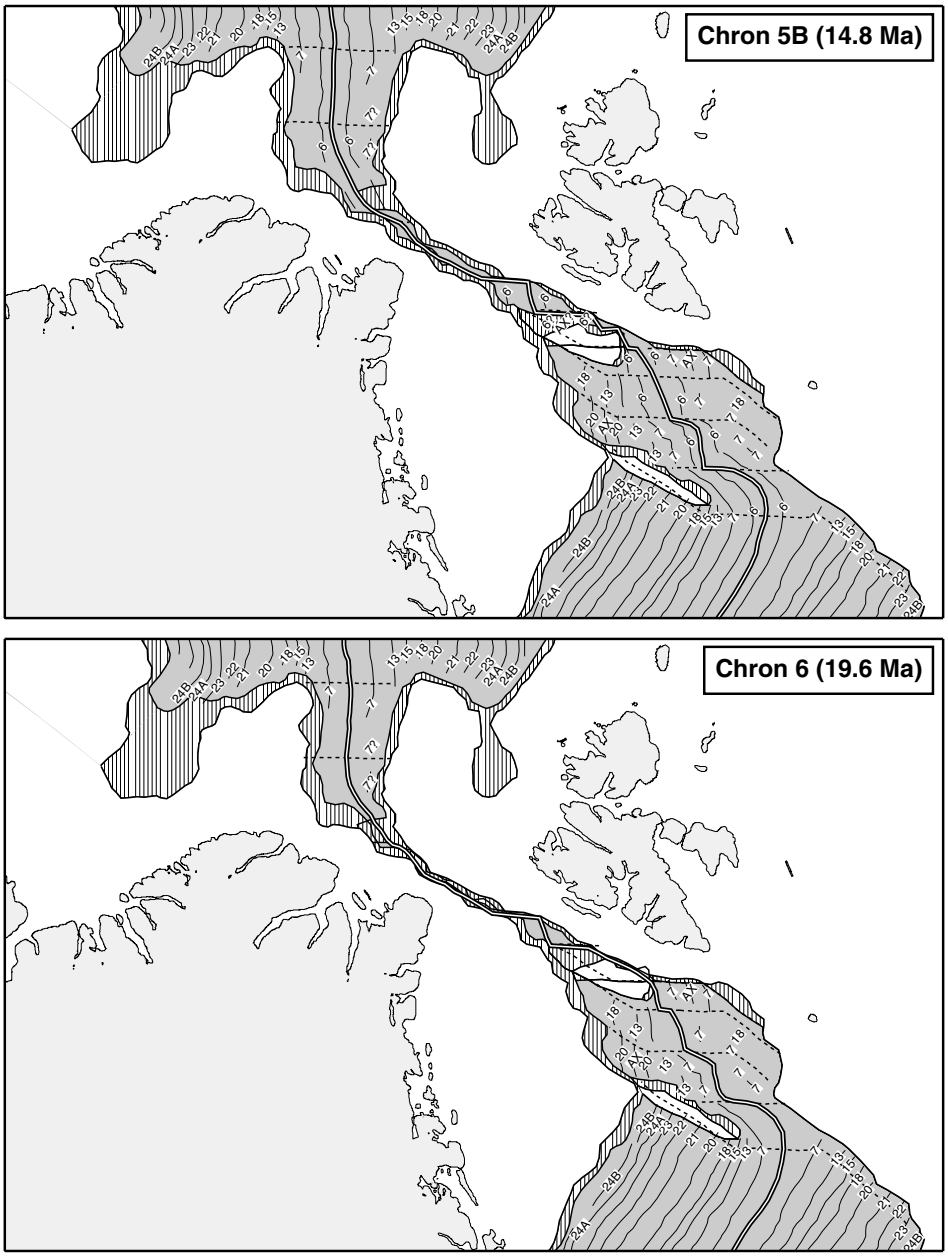

Figure 4.13 continued.

At Chron 5B times (~14.8 Ma) a narrow proto-oceanic channel existed along the trend of the Eocene megashear zone from the Hovgård Ridge to the Eurasia Basin (Figure 4.13). Irregular magnetic anomalies both on the Molloy Ridge and in the Lena Trough suggest that the present-day mode of seafloor spreading was not yet established. The channel may have been nearly blocked by transform faults and kinks in the plate boundary, but given the uncertainty of our COT location the duration of the possible blockage is insignificant.

At Chron 5 times (~9.8 Ma), the present plate boundary configuration of the Lena Trough was established and anomaly 5 was formed as the oldest magnetic anomaly extending from the Norwegian–Greenland Sea to the Eurasia Basin (Figure 4.13). The regular shape of anomaly 5 compared to the older anomalies indicates that the present-day mode of seafloor spreading was established at that time, i.e., ~5 Myr after the onset of magmatic accretion in the Lena Trough.

Discussion

Subsidence and Uplift of the Fram Strait Region

We may discuss the validity of assuming that the opening of the gateway depended on the formation of a continuous oceanic corridor through the Lena Trough. On one hand, the strongly rifted continental basement west of the Hornsund Fault Complex has subsided to nearly the same depth as oceanic crust (Figure 4.3b). Therefore, if continental and oceanic crust is not mechanically coupled, the gateway may have reached its present depth independently of the time of break-up. If coupling exists, the opening of the gateway depended on the time of break-up as well as thermal subsidence of oceanic crust. The proximity to uplifted and eroded continental margins implies that sediments are deposited on young oceanic crust and in some locations even in the axial valley. These sediments may have depressed the oceanic lithosphere but also inhibited heat conduction and pore water flow and thereby slowed down thermal subsidence. To the contrary, cold continental lithosphere on either side of the spreading axis may have enhanced thermal subsidence because heat is transferred to the adjacent continental lithosphere as well as to the surface. However, even in the Lena Trough the vertical temperature gradients are probably greater than the horizontal gradients; consequently, thermal subsidence is likely to be dominated by vertical heat flow. Measured heat flow values in the Fram Strait are comparable to measurements in the Norwegian–Greenland Sea [*Sundvor et al.*, 2000]. We may therefore assume that the subsidence of the Lena Trough followed the regional oceanic subsidence curve. Seafloor spreading probably took place at the present-day 3.2–4.4 km axial depths since at least Chron 5 times (9.8 Ma) when the first continuous magnetic anomaly formed.

Currently, about half of Atlantic water flow into the Arctic Ocean goes through the Barents Sea [*Simonsen and Haugan*, 1996]. Although deep water masses cannot be exchanged across the 0.25 km sill depth of the Barents Sea shelf, the efficiency of latitudinal heat transfer clearly depends on water masses flowing through the Barents Sea. Cenozoic uplift of the Barents Sea shelf is demonstrated by NW

increasing erosion values to ~3 km in Svalbard [*Rasmussen and Fjeldskaar*, 1996; *Dimakis et al.*, 1998]. Because the isostatic response to glacial erosion can only account for ~1 km [*Vågnes and Amundsen*, 1993], the erosion values require that the Barents Sea shelf was above sea-level when extensive glaciations started at 2.57 Ma [*Dimakis et al.*, 1998; *Butt et al.*, 2000; 2002]. We may then ask if the Barents Sea was elevated also at the time when the Lena Trough opened.

In theory, the pre-glacial relief of the Barents Sea shelf might be ascribed to rift flank uplift along the northern and western margins [*Weissel and Karner*, 1989; *Rasmussen and Fjeldskaar*, 1996]. However, the >500 km wavelength of the uplifted region points to a mantle thermal source rather than rift flank uplift [*Dimakis et al.*, 1998]. The space-time distribution of rift flank uplift is linked to the propagation of seafloor spreading. A ~150-km-wide area on the SW Barents Sea margin was uplifted during the Early Eocene [*Vågnes*, 1997] and the rifted volcanic segment west of Bjørnøya during the earliest Eocene and early Oligocene times [*Eidvin et al.*, 1993; *Sættem et al.*, 1994; *Jebsen*, 1998]. Marginal highs at the transition between the NW Svalbard margin and the Yermak Plateau were uplifted post-Eocene but probably pre-Miocene [*Andreassen*, 1998]. Rift flank uplift may have maintained an elongate along-margin relief inherited from the Eocene W Spitsbergen fold-and-thrust belt. However, Eocene strata in central Spitsbergen were buried by 2.7 km of sediments prior to erosion and uplift [*Manum and Throndsen*, 1978]. This requires (1) a significant sedimentary basin that cannot be reconciled with an elevated margin from the time of rifting to the onset of glaciations; and (2) significant time of deposition and subsequent erosion. Thus, the pre-glacial relief was probably caused by Neogene uplift of a largely submarine NW Barents Sea shelf.

Vågnes and Amundsen [1993] found ~50-km-thick lithosphere beneath N Spitsbergen. The implied lithospheric thinning is incompatible with rift flank uplift and by itself sufficient to explain the pre-glacial uplift. A middle–late Miocene age of thinning and uplift was inferred from 9–12-Myr-old plateau basalts in northern Spitsbergen [*Prestvik*, 1978; *Vågnes and Amundsen*, 1993] and heat flow indicating thermal uplift of the inner Yermak Plateau at 10–16 Ma [*Crane et al.*, 1982]. These observations may be linked to a possibly volcanic layer draping an erosional unconformity and a buried volcano off NW Spitsbergen (Figure 4.7) [*Andreassen*, 1998]. Miocene sedimentary strata in the Vestbakken Volcanic Province were pre-glacially uplifted to the NW [*Jebsen*, 1998]. The middle–late Miocene uplift of the Barents Sea shelf coincides with similar uplifts around the North Atlantic, suggesting it is caused by interaction between a regional, hot asthenospheric lens around Iceland [*Cochran and Talwani*, 1978] and cold continental lithosphere [*Vågnes and Amundsen*, 1993].

Because the middle–late Miocene uplift is coeval also with the opening of the gateway (Figure 4.13), we may speculate about the role of the gateway in mantle dynamics. Cold continental lithosphere was in contact across the Fram Strait prior to the Oligocene and may have dammed up the North Atlantic regional asthenospheric lens. At the same time, the North Atlantic Volcanic Province formed [*Eldholm and Grue*, 1994]. Northward propagation of the Norwegian–Greenland Sea may have paved the way for asthenospheric flow from the Iceland hotspot and initiated thinning and uplift. Considering this scenario, it is interesting to note that the highly

magnetic, V-shaped Yermak H-Zone (Figure 4.8) emerged on the western Gakkel Ridge at Chron 5 times (9.8 Ma) and migrated NE at ~1 cm yr^{-1} [*Feden et al.*, 1979].

The Last Gateway: Fram Strait or Greenland–Scotland Ridge?

The present-day water circulation between the North Atlantic and Arctic oceans is restricted by the Greenland–Scotland Ridge (GSR) as well as the Fram Strait. The formation of seaways across the GSR is an equally important boundary condition for paleoceanographic change because the present 0.5–0.9 km sill depth is sensitive to small vertical motions. *Kristoffersen* [1990] noted low bottom current activity in the Fram Strait relative to other deep ocean gateways and ascribed the difference to blocking of deep-water exchange by the GSR after the Fram Strait gateway had opened. The GSR was first overflowed during early Oligocene times (~35 Ma) when the SE Faeroes Drift started forming [*Davies et al.*, 2001]. The distribution of benthic foraminifera indicates that the Norwegian–Greenland Sea was later periodically isolated from deep Atlantic water masses, notably during middle Miocene and early Pliocene times [*Wright and Miller*, 1996]. The repeated opening and closure of the GSR gateway may be correlated to pulses of buoyant asthenospheric material flowing from a dynamic Iceland hotspot [*Vogt*, 1971], creating renewed thermal uplift of the otherwise subsiding GSR [*Wright and Miller*, 1996]. Therefore, the GSR blocked the exchange of deep water both prior to and after the middle–late Miocene formation of the Fram Strait gateway.

The marine sedimentary record of the Fram Strait gateway is indirect but nonetheless consistent with our plate tectonic reconstructions (Figure 4.13). ODP hole 909C in the Hovgård Fault Province (Figure 4.11) shows restricted ocean circulation between ~17 and ~20 Ma [*Shipboard Scientific Party*, 1995]. At 11.2 Ma, the kaolinite/illite ratio of sediments decreased abruptly while the bulk accumulation rate increased correspondingly and benthic foraminifera became more abundant. These changes may be interpreted in terms of increased ice-rafting of sediments from the Arctic Ocean and higher rate of ice melting in the Fram Strait, i.e., a change of source area because of a newly formed gateway [*Winkler et al.*, 2002]. At ~10 Ma, marine conditions were established [*Shipboard Scientific Party*, 1995] and at the same time, the calcium compensation depth (CCD) in the Norwegian–Greenland Sea deepened significantly [*Bohrmann et al.*, 1990]. The change of CCD was probably a response to globally increasing sediment recycling, decreasing organic carbon reservoirs, and increasing latitudinal temperature gradients which may have been initiated by the opening of a North Atlantic–Arctic gateway [*Thiede et al.*, 1998]. Foraminiferal assemblages in the central Arctic Ocean indicate that the gateway was well established by Pliocene times [*Mullen and McNeil*, 1995].

Prior Tectonic Constraints

A plate reconstruction to Chron 13 (33.3 Ma) at the Eocene–Oligocene transition demonstrates closure between Eurasia and Greenland from the Hovgård Ridge to the Yermak Plateau and the Morris Jesup Rise (Figure 4.14). There is considerable crustal overlap along the Lena Trough margins, reflecting the crustal thinning accommodated by the Hornsund Fault Complex, its northern extension along the W Yermak Plateau, and the conjugate fault complex on the NE Greenland margin. The

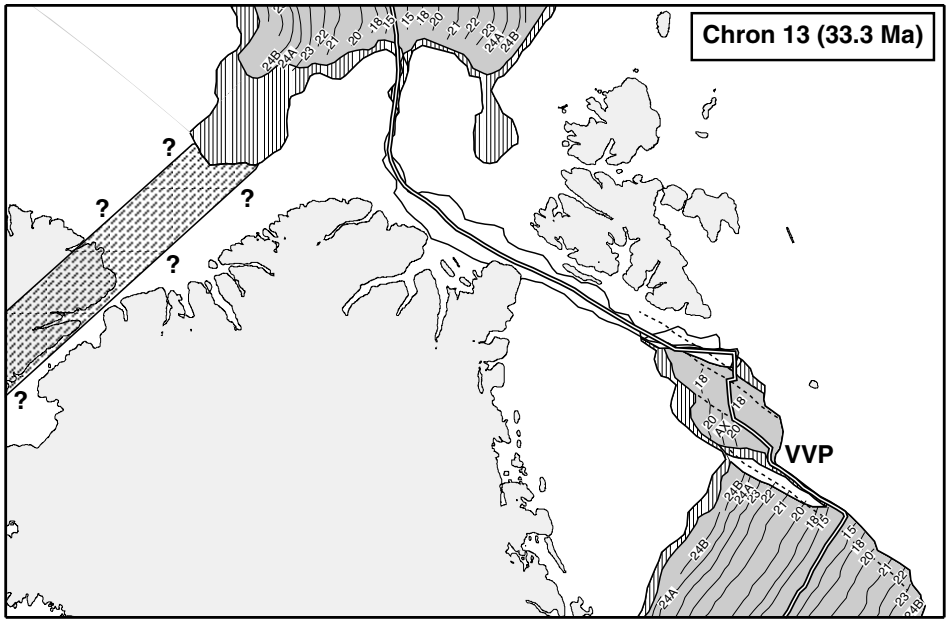

Figure 4.14. Chron 13 plate tectonic reconstruction. Hachured area north of Greenland indicates possible location of the diffuse pre-Chron 13 plate boundary between Greenland and North America. *VVP*, Vestbakken Volcanic Province.

Chron 5B (14.8 Ma) or slightly earlier break-up of the Lena Trough (Figure 4.13) implies an ~18 Myr period of rifting and crustal thinning prior to the first seafloor spreading.

The Greenland Ridge fits in as a continental sliver cut off from the SW Barents Sea margin during the Eocene (Figure 4.14). The reconstruction yields little crustal overlap, implying a sheared break-up and little extension of the crust. The pre-Chron 13 opening of the Boreas Basin was connected to the Norwegian–Greenland Sea along a transform fault on the western side of the Greenland Ridge. The basin appears to have been surrounded by land or shallow water from its time of formation until the Eocene–Oligocene transition.

The reconstructed Hovgård Ridge has more overlap, implying that the microcontinent is significantly rifted and thinned. A Chron 13–7 (33.3–24.8 Ma) transform fault through the Central Valley of the ridge (Figure 4.11) improves the fit of reconstruction. For the same reason, the elevated basement province seaward of the boundary fault between Bjørnøya and Sørkapp (Figures 4.3a and 4.6) is probably oceanic.

The new COT location around the Yermak Plateau and the Morris Jesup Rise yields good fit between the conjugate plateaus (Figure 4.14). The rifted structure of the plateaus and their lower-lying, landward sides (Figure 4.9) indicates that considerable crustal overlap is allowed in pre-Chron 13 reconstructions. If the plateaus are indeed continental, a transform fault existed along the eastern margin of

the plateaus and linked the Eurasia Basin to the Labrador Sea and Baffin Bay west of Greenland. The extinct plate boundary between Greenland and North America is complex and no single fault can account for the implied strike-slip motion and compression [*Dawes*, 1990]. With new constraints now placed on regional crustal structure, future work should aim at a full plate tectonic reconstruction of the Eurasia–Greenland–North America three-plate system back to opening.

Conclusions

We have derived the regional crustal structure, oceanic age distribution, and conjugate margin segmentation on either side of the Eurasia–North America plate boundary between the Mohn and Gakkel Ridges. These constraints yield new information on the timing of the Fram Strait gateway.

1. The margins facing the Knipovich Ridge developed from Chron 20 times (~43.2 Ma) and show conjugate sheared and rifted segments. The Greenland Ridge continental sliver slid past the W Barents Sea margin until it was rifted off at Chron 13 times (33.3 Ma). The Hovgård Ridge microcontinent or continental sliver originated from the margin further north but was probably not fully separated from Svalbard until Chron 6 times (~19.6 Ma).
2. The margins between the Molloy Fracture Zone and the Gakkel Ridge developed by extensive Oligocene–Miocene rifting of different structural provinces related to the Eocene megashear region.
3. The Yermak Plateau and the Morris Jesup Rise may be continental marginal plateaus separated by southward propagation of seafloor spreading between Chrons 13 and 6 (33.3 and 19.6 Ma); however, further study is needed on their faulted basement blocks, high-amplitude magnetic field, and role in pre-Chron 13 plate reconstructions.
4. The Fram Strait gateway formed by simultaneous north- and southward propagation of seafloor spreading through a largely submarine Barents Sea shelf. A narrow and fairly linear channel formed by Chron 5B times (14.8 Ma) but irregular early magnetic anomalies suggest a Chron 5 (9.8 Ma) onset of the present-day seafloor spreading. This implies a ~18 Myr period of pre-drift crustal thinning along the Lena Trough.
5. The 10–15 Ma reconstructed age of the gateway is uncertain compared to the sedimentary record of paleoceanographic change. Nonetheless, it agrees with evidence from the Hovgård Ridge of sediment ice rafting at 11.2 Ma and open-marine conditions from ~10 Ma onwards, coinciding with regional deepening of the calcium compensation depth.
6. The Greenland–Scotland Ridge underwent dynamic uplift and subsidence both before and after the formation of the Fram Strait gateway, and may have represented the last barrier for North Atlantic–Arctic deep-water exchange.
7. The NW Barents Sea shelf was thermally uplifted at the same time as the Fram Strait gateway formed. Similar Miocene uplifts around the North Atlantic lead to the speculation that the gateway opened up a northward migration pathway for the regional hot asthenospheric lens around Iceland.

Acknowledgments. We are grateful to Toril Karlberg, Trine E. S. Andreassen, Pernille Hammernes, and Christopher Jebsen for use of their results. We also thank Olav Eldholm, Filippos Tsikalas, and Knut Bjørlykke for constructive ideas and support. Anton Likhachev and Vladimir Glebovsky kindly prepared magnetic data from the Eurasia Basin. All figures were generated with the Generic Mapping Tools [*Wessel and Smith*, 1991]. Ø. E. was supported by a doctoral fellowship from the Norwegian Research Council (grant no. 147541/432).

References

Andreassen, T.E.S. (1998), En geofysisk undersøkelse av Yermakplatået, Cand. Scient. thesis, 132 pp., University of Oslo, Norway (in Norwegian).

Baturin, D., T. Fedukhina, L. Savostin, and A. Yunov (1994), A geophysical survey of the Spitsbergen margin and surrounding areas, *Marine Geophysical Researches*, *16* (6), 463–484.

Berger, W.H., E. Vincent, and H.R. Thierstein (1981), The deep-sea record: Major steps in Cenozoic ocean evolution, in *The Deep Sea Drilling Project: A Decade of Progress*, *Special Publication*, vol. 32, edited by J.E. Warme et al., pp. 489–504, Society of Economic Paleontologists and Mineralogists, Tulsa, OK.

Bohrmann, G., R. Henrich, and J. Thiede (1990), Miocene to Quaternary paleoceanography in the northern North Atlantic: Variability in carbonate and biogenic opal accumulation, in *Geological History of the Polar Oceans: Arctic Versus Antarctic*, *NATO ASI Series*, vol. C 308, edited by U. Bleil and J. Thiede, pp. 647–675, Kluwer Academic Publishers, Dordrecht, Netherlands.

Breivik, A.J., R. Mjelde, P. Grogan, H. Shimamura, Y. Murai, and Y. Nishimura (2003), Crustal structure and transform margin development south of Svalbard based on ocean bottom seismometer data, *Tectonophysics*, *369* (1–2), 37–70.

Brozena, J.M., V.A. Childers, L.A. Lawver, L.M. Gahagan, R. Forsberg, J.I. Faleide, and O. Eldholm (2003), New aerogeophysical study of the Eurasia Basin and Lomonosov Ridge: Implications for basin development, *Geology*, *31* (9), 825–828.

Butt, F.A., A. Elverhøi, A. Solheim, and C.F. Forsberg (2000), Deciphering late Cenozoic development of the western Svalbard margin from ODP Site 986 results, *Marine Geology*, *169* (3–4), 373–390.

Butt, F.A., H. Drange, A. Elverhøi, O.H. Otterå, and A. Solheim (2002), Modelling Late Cenozoic isostatic elevation changes in the Barents Sea and their implications for oceanic and climatic regimes: preliminary results, *Quaternary Science Reviews*, *21* (14–15), 1643–1660.

Cande, S.C., and D.V. Kent (1995), Revised calibration of the geomagnetic polarity timescale for the Late Cretaceous and Cenozoic, *Journal of Geophysical Research*, *100* (B4), 6093–6095.

Childers, V.A., D.C. McAdoo, J.M. Brozena, and S.W. Laxon (2001), New gravity data in the Arctic Ocean: Comparison of airborne and ERS gravity, *Journal of Geophysical Research*, *106* (B5), 8871–8885.

Cochran, J.R., and M. Talwani (1978), Gravity anomalies, regional elevation, and the deep structure of the North Atlantic, *Journal of Geophysical Research*, *83* (B10), 4907–4924.

Crane, K., O. Eldholm, A.M. Myhre, and E. Sundvor (1982), Thermal implications for the evolution of the Spitsbergen Transform Fault, *Tectonophysics*, *89* (1–3), 1–32.

Czuba, W., O. Ritzmann, Y. Nishimura, M. Grad, R. Mjelde, A. Guterch, and W. Jokat (2005), Crustal structure of northern Spitsbergen along the deep seismic transect between the Molloy Deep and Nordaustlandet, *Geophysical Journal International*, *161* (2), 347–364.

Davies, R., J. Cartwright, J. Pike, and C. Line (2001), Early Oligocene initiation of North Atlantic Deep Water formation, *Nature*, *410* (6831), 917–920.

Dawes, P.R. (1973), The North Greenland fold belt: A clue to the history of the Arctic Ocean Basin and the Nares Strait lineament, in *Implications of Continental Drift to the Earth*

Sciences, vol. 2, edited by D.H. Tarling and S.K. Runcorn, pp. 925–947, Academic Press, London.

Dawes, P.R. (1990), The north Greenland continental margin, in *The Arctic Ocean Region*, *The Geology of North America*, vol. L, edited by A. Grantz et al., pp. 211–226, Geological Society of America, Boulder, CO.

DeMets, C., R.G. Gordon, D.F. Argus, and S. Stein (1990), Current plate motions, *Geophysical Journal International*, *101* (2), 425–478.

Dimakis, P., B.I. Braathen, J.I. Faleide, A. Elverhøi, and S.T. Gudlaugsson (1998), Cenozoic erosion and the preglacial uplift of the Svalbard–Barents Sea region, *Tectonophysics*, *300* (1–4), 311–327.

Eidvin, T., E. Jansen, and F. Riis (1993), Chronology of Tertiary fan deposits off the western Barents Sea: Implications for the uplift and erosion history of the Barents Shelf, *Marine Geology*, *112* (1–4), 109–131.

Eiken, O. (1992), An outline of the northwestern Svalbard continental margin, in *Arctic Geology and Petroleum Potential*, *Special Publication*, vol. 2, edited by T.O. Vorren et al., pp. 619–629, Norwegian Petroleum Society/Elsevier, Amsterdam.

Eiken, O. (ed.) (1994), *Seismic Atlas of Western Svalbard: A Selection of Seismic Transects*, *Meddelelser 130*, 73 pp., Norsk Polarinstitutt, Oslo, Norway.

Eiken, O., and K. Hinz (1993), Contourites in the Fram Strait, *Sedimentary Geology*, *82*, 15–32.

Eldholm, O., and K. Grue (1994), North Atlantic volcanic margins – dimensions and production rates, *Journal of Geophysical Research*, *99* (B2), 2955–2968.

Eldholm, O., J.I. Faleide, and A.M. Myhre (1987), Continent–ocean transition at the western Barents Sea/Svalbard continental margin, *Geology*, *15* (12), 1118–1122.

Eldholm, O., A.M. Myhre, and J. Thiede (1994), Cenozoic tectono-magmatic events in the Northern Atlantic: Potential paleoenvironmental implications, in *Cenozoic Plants and Climates of the Arctic*, *NATO ASI Series*, vol. I 27, edited by M.C. Boulter and H.C. Fischer, pp. 35–55, Springer-Verlag, Berlin.

Engen, Ø., O. Eldholm, and H. Bungum (2003), The Arctic plate boundary, *Journal of Geophysical Research*, *108* (B2), 2075, doi:10.1029/2002JB001809. This volume, p. 23.

Engen, Ø., L.N. Frazer, P. Wessel, and J.I. Faleide (2005a), Inversion of gravity data for sediment thickness: Case study Norwegian–Greenland Sea, *Journal of Geophysical Research*, submitted. This volume, p. 97.

Engen, Ø., J.A. Gjengedal, J.I. Faleide, Y. Kristoffersen, and O. Eldholm (2005b), Seismic stratigraphy and basement structure of the Nansen Basin, Arctic Ocean, *Geophysical Journal International*, submitted. This volume, p. 57.

Estrada, S., A. Höhndorf, and F. Henjes-Kunst (1999), Cretaceous/Tertiary volcanism in north Greenland: The Kap Washington Group, *Polarforschung*, *69*, 17–23 (published 2001).

Faleide, J.I., S.T. Gudlaugsson, O. Eldholm, A.M. Myhre, and H.R. Jackson (1991), Deep seismic transects across the sheared western Barents Sea–Svalbard continental margin, *Tectonophysics*, *189* (1–4), 73–89.

Faleide, J.I., E. Vågnes, and S.T. Gudlaugsson (1993), Late Mesozoic–Cenozoic evolution of the South-Western Barents Sea in a regional rift–shear tectonic setting, *Marine and Petroleum Geology*, *10* (3), 186–214.

Feden, R.H., P.R. Vogt, and H.S. Fleming (1979), Magnetic and bathymetric evidence for the Yermak Hot Spot northwest of Svalbard in the Arctic Basin, *Earth and Planetary Science Letters*, *44* (1), 18–38.

Fronval, T., and E. Jansen (1996), Late Neogene paleoclimates and paleoceanography in the Iceland–Norwegian Sea: Evidence from the Iceland and Vøring plateaus, ODP Leg 151 and 104, in *Proceedings of the Ocean Drilling Program, Scientific Results*, vol. 151, edited by J. Thiede et al., pp. 455–468, Ocean Drilling Program, College Station, TX.

Geissler, W.H., and W. Jokat (2004), A geophysical study of the northern Svalbard continental margin, *Geophysical Journal International*, *158* (1), 50–66.

Gjengedal, J.A. (2004), Prosessering og tolkning av seismiske data frå Nansenbassenget og Yermakplatået, Cand. scient. thesis, University of Bergen, Norway (in Norwegian).

Hammernes, P. (1998), En analyse av strukturelementer i Norske–Grønlandshavet med basis i moderne potensialfeltdata, Cand. Scient. thesis, 182 pp., University of Oslo, Norway (in Norwegian).

Harland, W.B. (1969), Contribution of Spitsbergen to understanding of tectonic evolution of the North Atlantic region, in *North Atlantic geology and continental drift*, *Memoir*, vol. 12, edited by M. Kay, pp. 817–851, American Association of Petroleum Geologists, Tulsa, OK.

Hinz, K., O. Eldholm, M. Block, and J. Skogseid (1993), Evolution of North Atlantic volcanic continental margins, in *Petroleum Geology of Northwest Europe: Proceedings of the 4th Conference*, edited by J.R. Parker, pp. 901–913, Geological Society, London, UK.

Jackson, H.R., G.L. Johnson, E. Sundvor, and A.M. Myhre (1984), The Yermak Plateau – formed at a triple junction, *Journal of Geophysical Research*, *89* (B5), 3223–3232.

Jakobsson, M., N. Cherkis, J. Woodward, R. Macnab, and B. Coakley (2000), New grid of Arctic bathymetry aids scientists and mapmakers, *Eos, Transactions, American Geophysical Union*, *81* (9), 89, 93, 96.

Jansen, E., and J. Sjøholm (1991), Reconstruction of glaciation over the past 6 Myr from iceborne deposits in the Norwegian Sea, *Nature*, *349* (6310), 600–603.

Jebsen, C. (1998), Kenozoisk utvikling av Vestbakkvulkanittprovinsen på den vestlige Barentshavsmarginen, Cand. Scient. thesis, 160 pp., University of Oslo, Norway (in Norwegian).

Johansen, S.E. (1985), Hovgaardbruddsonen, Cand. Scient. thesis, 145 pp., University of Bergen, Norway (in Norwegian).

Jokat, W. (1998), The sediment distribution below the North Greenland continental margin and the adjacent Lena Trough, *Polarforschung*, *68*, 71–82 (2000).

Jokat, W., E. Weigelt, Y. Kristoffersen, T. Rasmussen, and T. Schöne (1995), New geophysical results from the south-western Eurasian Basin (Morris Jesup Rise, Gakkel Ridge, Yermak Plateau) and the Fram Strait, *Geophysical Journal International*, *123* (2), 601–610.

Karasik, A.M. (1968), Magnetic anomalies of the Gakkel Ridge and origin of the Eurasian subbasin of the Arctic Ocean, English Translation, in *Geophysical Methods of Prospecting in the Arctic*, vol. 5, pp. 8–19, Nauchno-Issled. Inst. Geologii Arktiki, Leningrad.

Karlberg, T. (1995), En geofysisk undersøkelse av Hovgårdryggen, Cand. Scient. thesis, 104 pp., University of Oslo, Norway (in Norwegian).

Kristoffersen, Y. (1990), On the tectonic evolution and paleoceanographic significance of the Fram Strait gateway, in *Geological History of the Polar Oceans: Arctic Versus Antarctic*, *NATO ASI Series*, vol. C 308, edited by U. Bleil and J. Thiede, pp. 63–76, Kluwer Academic Publishers, Dordrecht, Netherlands.

Kristoffersen, Y. (1998), The Eurasia Basin: An update from a decade of geoscientific research, *Polarforschung*, *68*, 11–18 (published 2000).

Lawver, L.A., R.D. Müller, S.P. Srivastava, and W. Roest (1990), The opening of the Arctic Ocean, in *Geological History of the Polar Oceans: Arctic Versus Antarctic*, *NATO ASI Series*, vol. C 308, edited by U. Bleil and J. Thiede, pp. 29–62, Kluwer Academic Publishers, Dordrecht, Netherlands.

Lawver, L.A., A. Grantz, and L.M. Gahagan (2002), Plate kinematic evolution of the present Arctic region since the Ordovician, in *Tectonic Evolution of the Bering Shelf–Chukchi Sea–Arctic Margin and Adjacent Landmasses*, *Special Paper*, edited by E.L. Miller et al., pp. 333–358, Geological Society of America, Boulder, CO.

LePichon, X., and D.E. Hayes (1971), Marginal offsets, fracture zones, and early opening of South Atlantic, *Journal of Geophysical Research*, *76* (26), 6283–6293.

Ljones, F., A. Kuwano, R. Mjelde, A. Breivik, H. Shimamura, Y. Murai, and Y. Nishimura (2004), Crustal transect from the North Atlantic Knipovich Ridge to the Svalbard margin west of Hornsund, *Tectonophysics*, *378* (1–2), 17–41.

Manum, S.B., and T. Throndsen (1978), Rank of coal and dispersed organic matter and its geological bearing in the Spitsbergen Tertiary, in *Norsk Polarinstitutt Årbok 1977*, pp. 159–172.

Medow, A. (2004), Die Sedimentstruktur des nördlichen Yermak Plateaus (N-Svalbard), Diploma thesis, 95 pp., Christian-Albrecht University, Kiel, Germany (in German).

Mudie, P.J., and J. Helgason (1983), Palynological evidence for Miocene climatic cooling in eastern Iceland about 9.8 Myr ago, *Nature*, *303* (5919), 689–692.

Mullen, M.W., and D.H. McNeil (1995), Biostratigraphic and paleoclimatic significance of a new Pliocene foraminiferal fauna from the central Arctic Ocean, *Marine Paleontology, 26* (1–4), 273-280.

Myhre, A.M., and O. Eldholm (1988), The western Svalbard margin (74°–80°N), *Marine and Petroleum Geology, 5* (2), 134–156.

Myhre, A.M., O. Eldholm, and E. Sundvor (1982), The margin between Senja and Spitsbergen fracture zones: Implications from plate tectonics, *Tectonophysics*, *89* (1–3), 33–50.

Nøttvedt, A., O. Eiken, and P.S. Midbøe (1994), Boreas Basin – Bellsund – Van Mijenfjorden – Heer Land – Storfjorden, in *Seismic Atlas of Western Svalbard: A Selection of Seismic Transects*, *Meddelelser*, vol. 130, edited by O. Eiken, pp. 17–19, Norsk Polarinstitutt, Oslo, Norway.

Olesen, O., J. Gellein, H. Håbrekke, O. Kihle, J.R. Skilbrei, and M.A. Smethurst (1997), Magnetic anomaly map, Norway and adjacent ocean areas, map scale 1:3,000,000, Geological Survey of Norway, Trondheim, Norway.

Ostenso, N.A., and R.J. Wold (1977), A seismic and gravity profile across the Arctic Ocean basin, *Tectonophysics*, *37*, 1–24.

Parsons, T., and J. McCarthy (1996), Crustal and upper mantle velocity structure of the Salton Trough, southeast California, *Tectonics*, *15* (2), 456–471.

Pitman, W.C., III, and M. Talwani (1972), Sea-floor spreading in the North Atlantic, *Geological Society of America Bulletin*, *83* (3), 619–645.

Prestvik, T. (1978), Cenozoic plateau lavas of Spitsbergen – A geochemical study, in *Årbok 1977*, pp. 129–143, Norsk Polarinstitutt, Oslo, Norway.

Rabinowitz, P.D., and J. Labrecque (1979), Mesozoic South Atlantic Ocean and evolution of its continental margins, *Journal of Geophysical Research*, *84* (B11), 5973–6002.

Rasmussen, E., and W. Fjeldskaar (1996), Quantification of the Pliocene–Pleistocene erosion of the Barents Sea from present-day bathymetry, *Global and Planetary Change*, *12* (1–4), 119–133.

Raymo, M.E., and W.F. Ruddiman (1992), Tectonic forcing of Late Cenozoic climate, *Nature*, *359* (6391), 117–122.

Riddihough, R.P., G.V. Haines, and W. Hannaford (1973), Regional magnetic anomalies of the Canadian Arctic, *Canadian Journal of Earth Sciences*, *10*, 157–163.

Ritzmann, O., and W. Jokat (2003), Crustal structure of northwestern Svalbard and the adjacent Yermak Plateau: evidence for Oligocene detachment tectonics and non-volcanic breakup, *Geophysical Journal International*, *152* (1), 139–159.

Ritzmann, O., W. Jokat, R. Mjelde, and H. Shimamura (2002), Crustal structure between the Knipovich Ridge and the Van Mijenfjorden (Svalbard), *Marine Geophysical Researches*, *23* (5–6), 379–401.

Ritzmann, O., W. Jokat, W. Czuba, A. Guterch, R. Mjelde, and Y. Nishimura (2004), A deep seismic transect from Hovgard Ridge to northwestern Svalbard across the continental–ocean transition: A sheared margin study, *Geophysical Journal International*, *157* (2), 683–702.

Sættem, J., T. Bugge, S. Fanavoll, R.M. Goll, A. Mørk, M.B.E. Mork, M. Smelror, and J.G. Verdenius (1994), Cenozoic margin development and erosion of the Barents Sea: Core evidence from southwest of Bjørnøya, *Marine Geology, 118* (3–4), 257–281.

Shipboard Scientific Party (1995), Site 909, in *North Atlantic–Arctic Gateways I, Proceedings of the Ocean Drilling Program, Initial Reports*, vol. 151, edited by A.M. Myhre et al., pp. 159–220, Texas A & M University, Ocean Drilling Program, College Station, TX.

Simonsen, K., and P.M. Haugan (1996), Heat budgets of the Arctic Mediterranean and sea surface heat flux parameterizations for the Nordic Seas, *Journal of Geophysical Research*, *101* (C3), 6553–6576.

Sorokin, M.Y., Y.Y. Zamansky, A.Y. Languinen, H. Brekke, M. Sand, and N.B. Sørenes (1998), North Pole - 28 ice drift seimic line, *3rd International Conference on Arctic Margins (ICAM III)*, Celle, Germany.

Sundvor, E., and A. Austegard (1990), The evolution of the Svalbard margins: Synthesis and new results, in *Geological History of the Polar Oceans: Arctic Versus Antarctic*, *NATO ASI Series*, vol. C 308, edited by U. Bleil and J. Thiede, pp. 77–94, Kluwer Academic Publishers, Dordrecht, Netherlands.

Sundvor, E., and O. Eldholm (1979), The western and northern margin off Svalbard, *Tectonophysics*, *59* (1–4), 239–250.

Sundvor, E., A. Gidskehaug, A.M. Myhre, and O. Eldholm (1978), Marine geophysical survey on the northern Svalbard margin, Scientific Report 5, 14 pp., University of Bergen Seismological Observatory, Bergen, Norway.

Sundvor, E., O. Eldholm, T.P. Gladczenko, and S. Planke (2000), Norwegian–Greenland Sea thermal field, in *Dynamics of the Norwegian margin*, *Special Publications*, vol. 167, edited by A. Nøttvedt et al., pp. 397–410, Geological Society, London, UK.

Talwani, M., and O. Eldholm (1977), Evolution of the Norwegian–Greenland Sea, *Geological Society of America Bulletin*, *88* (7), 969–999.

Thiede, J., A.M. Myhre, J.V. Firth, and the Shipboard Scientific Party (1995), Cenozoic Northern Hemisphere polar and subpolar ocean paleoenvironments (summary of ODP Leg 151 drilling results), in *North Atlantic–Arctic gateways I, Proceedings of the Ocean Drilling Program, Initial Reports*, vol. 151, edited by A. Marin Jennifer, pp. 397–420, Texas A & M University, Ocean Drilling Program, College Station, TX.

Thiede, J., A. Winkler, T.C.W. Wolf-Welling, O. Eldholm, A.M. Myhre, K.H. Baumann, R. Henrich, and R. Stein (1998), Late Cenozoic history of the Polar North Atlantic: Results from ocean drilling, *Quaternary Science Reviews*, *17* (1–3), 185–208.

Tsikalas, F., O. Eldholm, and J.I. Faleide (2002), Early Eocene sea floor spreading and continent–ocean boundary between Jan Mayen and Senja fracture zones in the Norwegian–Greenland Sea, *Marine Geophysical Researches*, *23* (3), 247–270.

Vågnes, E. (1997), Uplift at thermo-mechanically coupled ocean–continent transforms: Modeled at the Senja Fracture Zone, southwestern Barents Sea, *Geo-Marine Letters*, *17* (1), 100–109.

Vågnes, E., and H.E.F. Amundsen (1993), Late Cenozoic uplift and volcanism on Spitsbergen: Caused by mantle convection?, *Geology*, *21*, 251–254.

Verhoef, J., W.J. Roest, R. Macnab, J. Arkani-Hamed, and members of the Project Team (1996), Magnetic Anomalies of the Arctic and North Atlantic Oceans and Adjacent Land Areas, Open File 3125b, Geological Survey of Canada, Dartmouth, NS, Canada.

Vogt, P.R. (1971), Asthenosphere motion recorded by the ocean floor south of Iceland, *Earth and Planetary Science Letters*, *13* (1), 153–160.

Vogt, P.R., P.T. Taylor, L.C. Kovacs, and G.L. Johnson (1979), Detailed aeromagnetic investigation of the Arctic Basin, *Journal of Geophysical Research*, *84* (B3), 1071–1089.

Vogt, P.R., R.K. Perry, R.H. Feden, H.S. Fleming, and N.Z. Cherkis (1981), The Greenland–Norwegian Sea and Iceland environment: Geology and geophysics, in *The Arctic Ocean*, *The Ocean Basins and Margins*, vol. 5, edited by A.E.M. Nairn et al., pp. 493–598, Plenum Press, New York, NY.

Vogt, P.R., W.Y. Jung, and J. Brozena (1998), Arctic margin gravity highs: Deeper meaning for sediment depocenters?, *Marine Geophysical Researches*, *20* (5), 459–477.

von Gosen, W., and K. Piepjohn (2003), Eurekan transpressive deformation in the Wandel Hav Mobile Belt (northeast Greenland), *Tectonics*, *22* (4), 1039, doi:10.1029/2001TC901040.

Weissel, J.K., and G.D. Karner (1989), Flexural uplift of rift flanks due to mechanical unloading of the lithosphere during extension, *Journal of Geophysical Research*, *94* (B10), 13,919–13,950.

Wessel, P., and W.H.F. Smith (1991), Free software helps map and display data, *Eos, Transactions, American Geophysical Union*, *72*, 441, 445–446.

Winkler, A., T.C.W. Wolf-Welling, K. Stattegger, and J. Thiede (2002), Clay mineral sedimentation in high northern latitude deep-sea basins since the Middle Miocene (ODP Leg 151, NAAG), *International Journal of Earth Sciences*, *91* (1), 133–148.

Wolf-Welling, T.C.W., M. Cremer, S. O'Connell, A. Winkler, and J. Thiede (1996), Cenozoic Arctic Gateway paleoclimate variability: indications from changes in coarse-fraction composition (ODP Leg 151), in *Proceedings of the Ocean Drilling Program, Scientific Results*, vol. 151, edited by J. Thiede et al., pp. 515–567, Ocean Drilling Program, College Station, TX.

Wright, J.D., and K.G. Miller (1996), Control of North Atlantic deep water circulation by the Greenland–Scotland Ridge, *Paleoceanography*, *11* (2), 157–170.

Appendix

Appendix 1

Seismic data acquisition in the Nansen Basin, Arctic Ocean

Øyvind Engen[1], Jakob Andreas Gjengedal[2,3], Olav Eldholm[1,4], and Yngve Kristoffersen[2]

1) Department of Geosciences, University of Oslo, Norway
2) Department of Earth Science, University of Bergen, Norway
3) *Now at* Future Exploration AS, Stavanger, Norway
4) *Now at* Department of Earth Science, University of Bergen, Norway

Revised manuscript submitted to *Proceedings of the 4th International Conference on Arctic Margins, 30 September–3 October 2003, Dartmouth, Nova Scotia, Canada*, edited by D. Thurston and R. A. Scott

Abstract. During the NPD-POLAR-2001 expedition to the Arctic Ocean in the fall of 2001 a multi-channel seismic (MCS) and sonobuoy acquisition program was carried out in the sea ice on the Hinlopen margin north of Svalbard and in the Nansen Basin. For this purpose, specially adapted acquisition and processing techniques were developed, resulting in ~1100 km of 2-D MCS profiles and 50 wide-angle velocity profiles. The data may be interpreted in terms of four main sedimentary units with distinct seismic velocities and reflection character.

Keywords: Seismic acquisition and processing; Seismic velocities; Marine sediments; Arctic Ocean; United Nations Convention on the Law of the Sea

Introduction

The Nansen Basin (Figure A-1) has formed by seafloor spreading along the Gakkel Ridge, the Arctic end-member of the Mid-Atlantic Ridge system, since the late Paleocene (~55 Ma) [*Karasik*, 1968]. Due to perennial sea ice, only a few MCS and wide-angle seismic profiles sample the ocean basin north of 81°N [*Duckworth and Baggeroer*, 1985; *Kristoffersen and Husebye*, 1985; *Jokat et al.*, 1995]. Following Norway's ratification of the United Nations Convention on the Law of the Sea in 1996, the Norwegian Petroleum Directorate (NPD) has initiated a research program to map sediment thickness and the foot of slope for the purpose of delineating legal outer

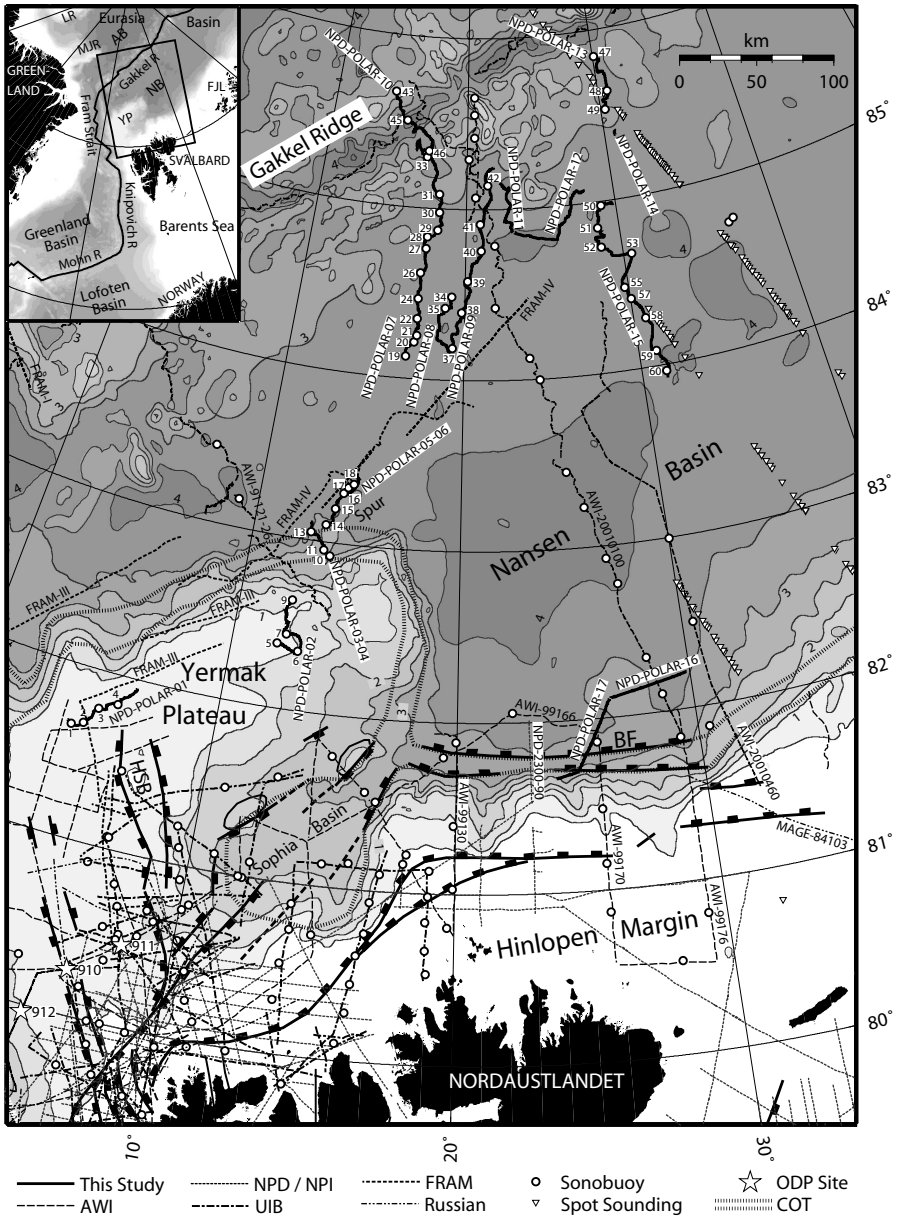

Figure A-1. Existing seismic database and new lines of the NPD-POLAR-2001 survey in the Nansen Basin (*NB*) and adjacent margins. IBCAO bathymetry [*Jakobsson et al.*, 2000], contoured every 0.5 km. *AB*, Amundsen Basin; *AWI*, Alfred Wegener Institute for Polar and Marine Research, Bremerhaven, Germany; *COT*, continent–ocean transition [*Engen and Faleide*, 2005, this volume]; *FJL*, Franz Josef Land; *LR*, Lomonosov Ridge; *MAGE*, Marine Arctic Geological Expedition, Murmansk, Russia; *MJR*, Morris Jesup Rise; *NPD*, Norwegian Petroleum Directorate; *NPI*, Norwegian Polar Institute; *UIB*, University of Bergen, Norway; *YP*, Yermak Plateau.

shelf boundaries beyond 200 nautical miles. As a part of this program, the NPD and the Universities of Bergen and Oslo conducted a seismic survey aboard the Swedish icebreaker *MV Oden* in the autumn of 2001. Here, we present some preliminary results and refer to *Engen et al.* [2005, this volume] for details and further discussion.

Data Acquisition and Processing

Major breakthroughs in seismic exploration of the Nansen Basin have been achieved during the two-ship expeditions ARCTIC-91 [*Fütterer*, 1992] and AMORE [*Thiede and the Shipboard Scientific Party*, 2002], where the icebreaker *PFS Polarstern* collected seismic data in a trail cut open by another icebreaker ahead. However, such operations are costly and involve inefficient sharing of ship-time between two scientific parties. On the other hand the *MV Oden*, with its 30 m wide bow, is an adequate platform for simultaneous icebreaking and seismic surveying, provided that the seismic equipment is robust and flexible [*Kristoffersen*, 1997]. Because the trail of open water rapidly closes, the airguns and hydrophone cable have to enter the water in the turbulent zone just behind the ship, where variable speed, bouncing ice and high noise is a challenge to the acquisition. The airguns (2×4 l or 1×20 l) and hydrophone cable (300 m active section, 12 channels) were suspended from a light depressor device which was able to move around ice fragments and effectively kept the airguns and the hydrophone cable separated in the water.

The raw seismic data contain geometrical and noise effects typical for ice-acquired data. Because the vessel had to navigate around pressure ridges and speed varied because of ice resistance, the shotpoint distances are not constant and the traces had to be stacked in 25 m bins along the ship track. Furthermore, trace-to-trace noise variation and delayed ghost effects from the lack of hydrophone cable depth control had to be filtered out. Further processing steps involved geometrical spreading correction, predictive deconvolution and normal move-out correction, stacking, and filtering. The processing significantly reduced ringing of seismic reflections. The sonobuoy profiles were not processed after the geometrical binning.

Velocity Modelling

Of the 60 sonobuoys dropped, 50 had sufficient quality and range (up to 28 km) for reduction. Most profiles contained both refracted arrivals from the top of basement and intra-sedimentary reflections. These arrivals were solved for initial velocities using standard slope-intercept and T^2-X^2 methods assuming 1-D conditions (plane-layers). Then, velocities were combined with interpreted reflector geometries into 2-D velocity models which were modified by raytracing and traveltime inversion [*Zelt and Smith*, 1992]. By perturbing the final sediment velocities while recording the traveltime and model χ^2 misfits, we calculated uncertainty in sediment thickness of about 7%. The 2-D models also show that the original 1-D reduction over-estimates sediment thickness in areas of high basement relief.

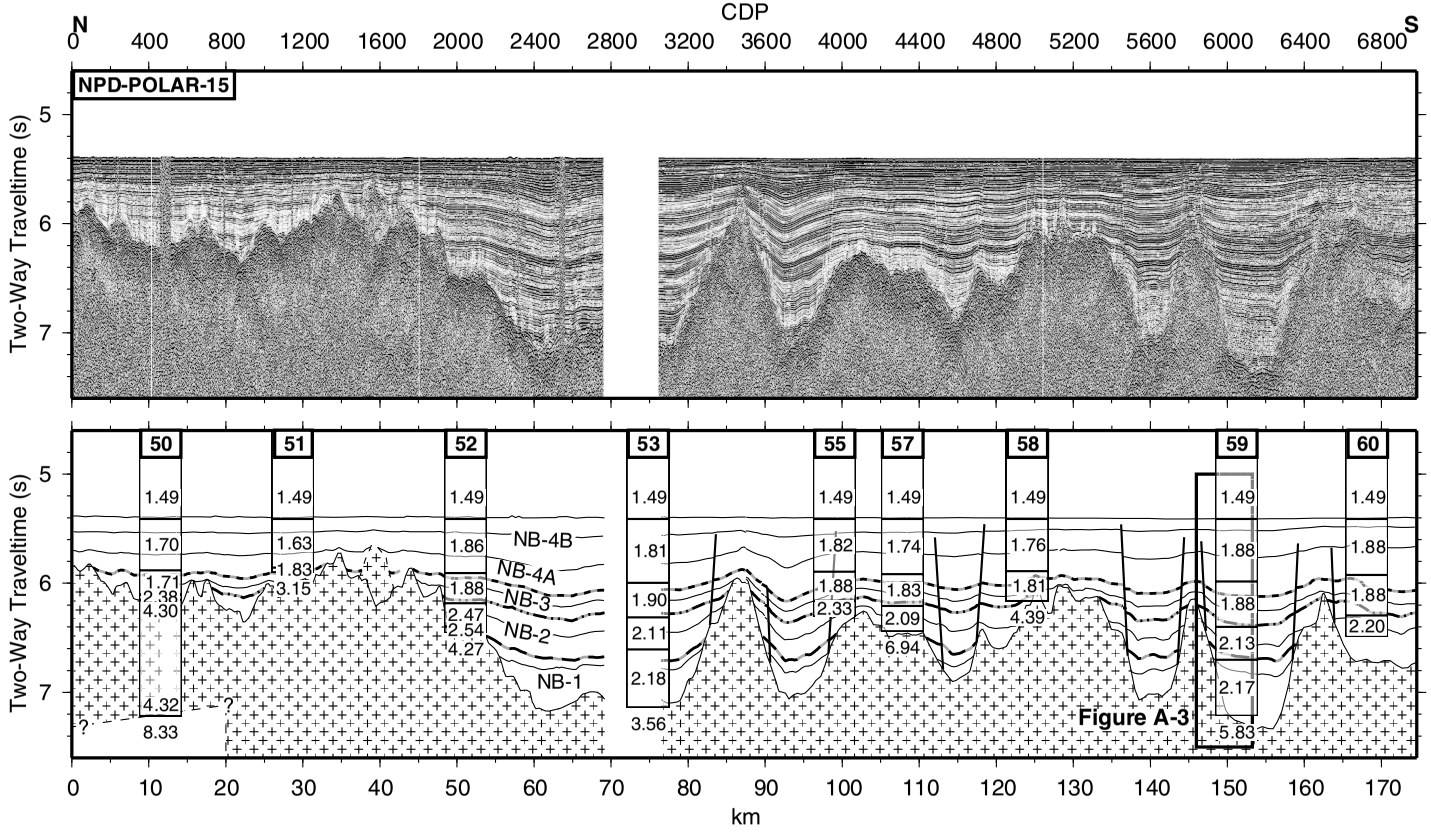

Figure A-2. Seismic data example and line drawing of the easternmost profile, line NPD-POLAR-15. Four sedimentary units (NB-1–NB-4) overlie oceanic basement. Annotated columns show velocities, in km s^{-1}, sampled from the 2-D velocity model in the sonobuoy deployment positions. *CDP*, common depth point.

Results

The processing yielded ~1100 km of good-quality MCS data imaging the basement surface and the main sedimentary sequences. Sediment thickness increases both from the Gakkel Ridge to the margins and from west to east, where the sharp basement relief is completely covered (Figure A-2). There is good agreement between the velocity models and the seismic stratigraphy that the sediments can be subdivided, from bottom to top, into four regional units (Figure A-3). The boundaries between units probably correspond to major paleoceanographic events such as the onset of late Cenozoic glacial deposition and the opening of the Fram Strait gateway between the Arctic and North Atlantic oceans [*Engen et al.*, 2005, this volume]. Faults cut the sediments from basement to shallow levels, indicating recent tectonism (Figure A-2).

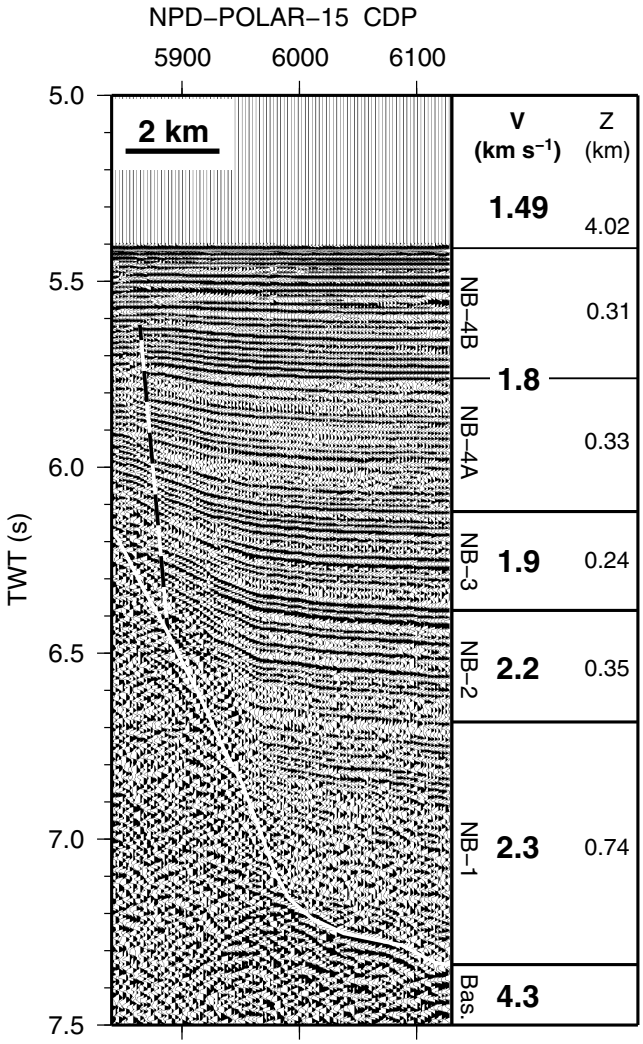

Figure A-3. Typical seismic reflection character, velocity (V), and thickness (Z) of the four sedimentary units of the Nansen Basin. Top of basement (Bas.) marked by white line; fault by dashed line. Location of section in Figure A-2. *CDP,* common depth point.

Acknowledgments. We thank Captain Mats Johansson and his crew aboard *MV Oden* for their professional and kind cooperation, cruise leader Harald Brekke for support and funding, and Olvar Løvås for processing the sonobuoy data. We also thank Stephen M. Jones for thoughtfully reviewing the manuscript and Jan Inge Faleide for comments.

References

Duckworth, G.L., and A.B. Baggeroer (1985), Inversion of refraction data from the Fram and Nansen Basins of the Arctic Ocean, *Tectonophysics*, *114* (1–4), 55–102.

Engen, Ø., and J.I. Faleide (2005), Plate tectonic reconstruction of the North Atlantic–Arctic gateway, *Tectonophysics*, submitted. This volume, p. 127.

Engen, Ø., J.A. Gjengedal, J.I. Faleide, Y. Kristoffersen, and O. Eldholm (2005), Seismic stratigraphy and basement structure of the Nansen Basin, Arctic Ocean, *Geophysical Journal International*, submitted. This volume, p. 57.

Fütterer, D.K. (ed.) (1992), *The Expedition ARK VIII/3 of RV Polarstern in 1991*, *Reports on Polar Research,* vol. 107, 267 pp., Alfred Wegener Institute for Polar and Marine Research, Bremerhaven, Germany.

Jakobsson, M., N. Cherkis, J. Woodward, R. Macnab, and B. Coakley (2000), New grid of Arctic bathymetry aids scientists and mapmakers, *Eos, Transactions, American Geophysical Union*, *81* (9), 89, 93, 96.

Jokat, W., E. Weigelt, Y. Kristoffersen, T. Rasmussen, and T. Schöne (1995), New geophysical results from the south-western Eurasian Basin (Morris Jesup Rise, Gakkel Ridge, Yermak Plateau) and the Fram Strait, *Geophysical Journal International*, *123* (2), 601–610.

Karasik, A.M. (1968), Magnetic anomalies of the Gakkel Ridge and origin of the Eurasian subbasin of the Arctic Ocean, English Translation, in *Geophysical Methods of Prospecting in the Arctic*, vol. 5, pp. 8–19, Nauchno-Issled. Inst. Geologii Arktiki, Leningrad.

Kristoffersen, Y. (1997), Seismic reflection surveys during Arctic Ocean-96, in *Yearbook 1995/96*, pp. 75–77, Swedish Polar Research Secretariat, Stockholm.

Kristoffersen, Y., and E.S. Husebye (1985), Multi-channel seismic reflection measurements in the Eurasian Basin, Arctic Ocean, from U.S. ice station FRAM-IV, *Tectonophysics*, *114* (1–4), 103–115.

Thiede, J., and the Shipboard Scientific Party (2002), *POLARSTERN ARKTIS XVII/2 Cruise Report: AMORE 2001 (Arctic Mid-Ocean Ridge Expedition)*, *Reports on Polar Research*, vol. 421, 397 pp., Alfred Wegener Institute for Polar and Marine Research, Bremerhaven, Germany.

Zelt, C.A., and R.B. Smith (1992), Seismic traveltime inversion for 2-D crustal velocity structure, *Geophysical Journal International*, *108* (1), 16–34.

Appendix 2

Sedimentary thickness estimations from magnetic data in the Nansen Basin

Vladimir Glebovsky[1], Anton Likhachev[1], Yngve Kristoffersen[2], Øyvind Engen[3], Jan Inge Faleide[3], and Harald Brekke[4]

1) VNIIOkeangeologia, St. Petersburg, Russia
2) Department of Earth Science, University of Bergen, Norway
3) Department of Geosciences, University of Oslo, Norway
4) Norwegian Petroleum Directorate, Stavanger, Norway

Revised manuscript submitted to *Proceedings of the 4th International Conference on Arctic Margins, 30 September–3 October 2003, Dartmouth, Nova Scotia, Canada*, edited by D. Thurston and R. A. Scott

Abstract. In spite of several geophysical expeditions during the past decade, the seismic documentation of sediments in the Nansen Basin is still sparse. At the same time, airborne surveys conducted by the US Naval Research Laboratory in 1974–75 and 1998–99 make up a grid of magnetic profiles spaced by 18 to 10 km in the western half of the basin. It is known that the depth to oceanic basement may be calculated from magnetic data by a multiple-source Werner deconvolution method (MSW). Recent bathymetry compilations provide relatively good control of the seafloor. Sediment thickness represents the difference between depths of basement and seafloor. Results of analysis regarding the possibility to use MSW calculations as a support to seismic lines in the mapping of sediment thickness in the study area are presented. The study area, at 80–86°N, 11–35°E, includes the Nansen Basin, Gakkel Ridge flank, Yermak Plateau, and north Svalbard margin. Principles of analysis and sorting of MSW solutions are discussed in detail. Uncertainty of the method is estimated. It is established that in general, both the magnetic basement surface and the sediment thickness values estimated from magnetic data fit well with seismic data from icebreakers *Oden* and *Polarstern* (2001). Possible reasons for differences between magnetic and acoustic basements revealed along seismic lines are discussed. The regional map of the sediment thickness in the study area shows that in general the thickness of sediments decreases from the Barents Sea shelf towards the Gakkel Ridge. Least thickness or absence of sediments is observed in the axial zone of the Ridge. The largest accumulation of sediments (4–5 km) is discovered on the continental shelf

and slope, north and south of Yermak Plateau, and in the southern part of Litke Trough. The thickness of sedimentary cover on the Yermak Plateau varies from 1 to 2 km.

Keywords: Estimated magnetic source depths; Sediment thickness; Integrated geophysical modelling; Arctic Ocean; United Nations Convention on the Law of the Sea

Introduction

Information on the sediment thickness is important for both the regional study and modelling of geological processes related to development of sedimentary basins and the assessment of oil and gas reserves. Moreover, sediment thickness of the ocean floor has become a major concern to many coastal states in relation to the revision of outer limits of the legal continental shelf in accordance with Article 76 of the United Nations Convention on the Law of the Sea.

Existent maps of sediment thickness in the Arctic Ocean [e.g., *Gramberg and Puscharovsky*, 1989; *Jackson and Oakey*, 1990; *Gramberg et al.*, 1999] are mainly based on widely spaced and irregular seismic lines. Thus, wide areas of the maps are based on interpolation of seismic data. The most effective method of sediment thickness mapping is obviously based on the integrated analysis of seismic, gravity, magnetic, and bathymetry information.

For both scientific and Article 76 purposes, Norwegian and Russian institutions (Norwegian Petroleum Directorate; Department of Geosciences, University of Oslo; VNIIOkeangeologia; and Polar Marine Geological Research Expedition) entered into a collaborative project to study the feasibility of using potential field data integrated with seismic and bathymetry data to determine the ocean floor and sediment thickness in the Arctic Ocean. The area 83°50′–86°N, 13–34°E in the western part of the Nansen Basin (Figure A-4b, small box) was chosen as the test area. This part of the basin has the best coverage of seismic data in addition to high-quality digital aeromagnetic and aerogravity information. Later, the area of investigation was extended to the south (Figure A-4b, large box). This paper summarises results of the mapping of oceanic basement relief and estimated sedimentary thickness from aeromagnetic data integrated with bathymetry.

Mass depth to magnetic source estimations is the common technology to study the geomagnetic structure of oceanic crust. Euler deconvolution [*Nabighian*, 1974] and Werner deconvolution [*Werner*, 1953] are the most widely used methods of estimation. The former method is usually considered as a fast one for rapid estimation of depths to magnetic sources (upper edges) from gridded magnetic data. The latter method is more laborious and needs magnetic anomaly profile data. At the same time, it allows estimation of parameters of magnetic sources more precisely. That is why it was used in this project. Seismic data were used both to calibrate and to check results of independent estimations from magnetic anomalies.

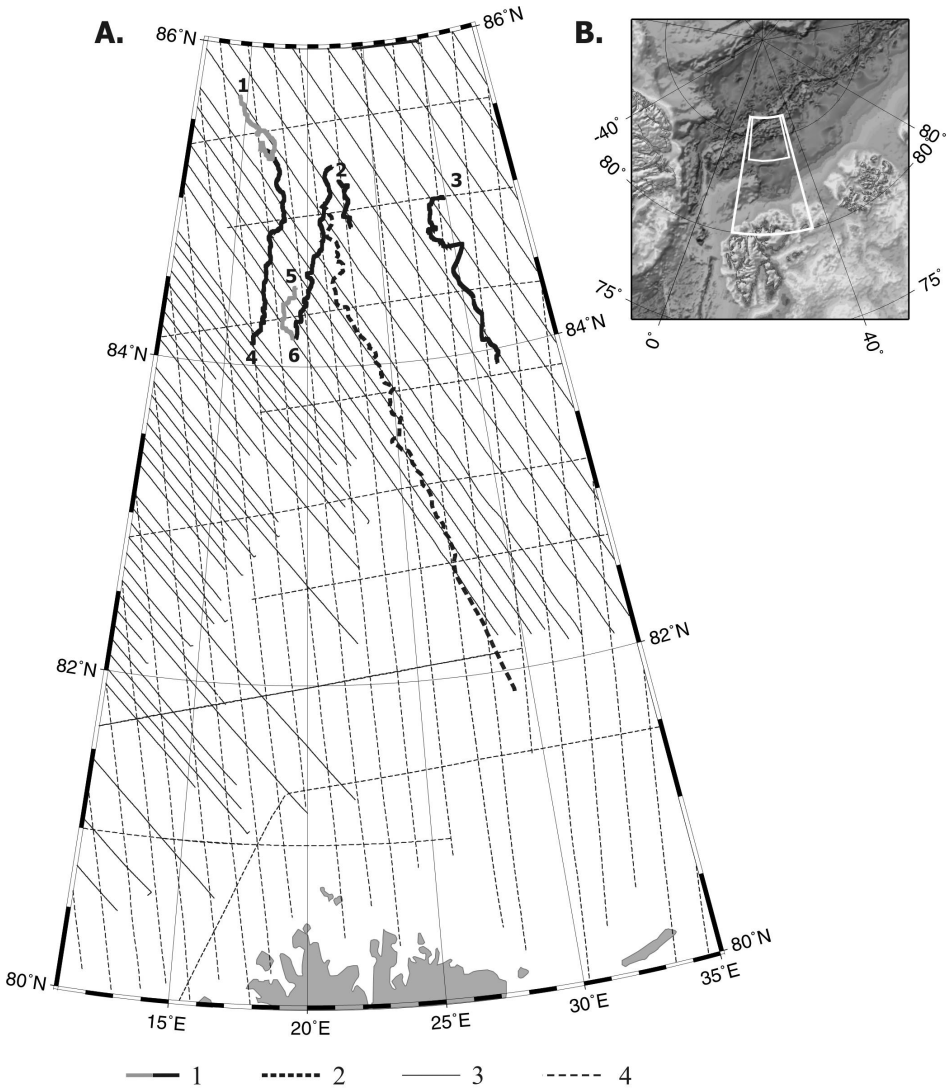

Figure A-4. Data coverage and area of study. **(A)** Position of seismic lines from *Oden*-2001 (1) and line 20010100 from *Polarstern*-2001 (2), aeromagnetic tracklines of NRL 1974–75 (3) and NRL 1998–99 (4). **(B)** Positions of the initial test area (small box) and the extended study area (large box).

Data Processing and Interpretation

Several geophysical data sets from the Nansen Basin were used under the project (Figure A-4a): seismic data collected in 2001 from the icebreakers *Oden* and

Polarstern [*Gjengedal*, 2004; *Jokat and Micksch*, 2004; *Engen et al.*, 2005, this volume]; and free air gravity and magnetic profiles collected by the Naval Research Laboratory (NRL). Bathymetry information was presented by the latest version of the IBCAO grid [*Jakobsson et al.*, 2000], by a paper copy of the Russian map "Bottom Relief of the Arctic Ocean" at scale 1:5,000,000 [*HDNO-VNIIOkeangeologia,* 1999], and by bathymetry observations along profiles acquired in 2001 from the icebreakers *Oden* and *Polarstern.*

The preliminary processing and analysis of the data sets included:

- Seismic interpretation and construction of depth sections.
- Levelling, adjustment and compilation of NRL 1998–99 aerogravity data sets [*Brozena et al.*, 2003], satellite data [*Laxon and McAdoo*, 1998], and Norwegian marine gravity observations to construct an updated grid and map of gravity anomalies.
- Digitising and gridding of isobaths from the Russian bathymetry map and comparison of the resulting grid and the IBCAO grids with shiptrack bathymetry [*Thiede and the Shipboard Scientific Party,* 2002] and Russian profiles to upgrade existent information and/or to select the most reliable grid values among multiple sources.
- Levelling and adjustment of aeromagnetic data sets; adjustment included navigational correction (shift) of old (NRL 1974–75) magnetic anomaly profiles with poor navigation using recent data sets (NRL 1998–99) with excellent navigation as reference information. The average magnitude of shift was about 1–2 km and the maximum value ran up to 5 km. The final, coherent magnetic database was used both for mapping and for mass depth to magnetic source estimations.

Depths to oceanic basement were calculated by a multiple-source version of the PDEPTH program [*Cordell et al.*, 1992] based on the Werner deconvolution method [*Hansen and Simmonds*, 1993]. It estimates depths to magnetic sources approximated by simple models: magnetic contact between two differently magnetised bodies; or a magnetised thin dike. The contact model was chosen as the basic one after test calculations. Initially, the magnetic anomaly profiles in the Nansen Basin were filtered by a six-point running average filter with 3 km window length to remove high frequency noise. Input parameters for the calculations, including number of points in the running window, radius of cluster (a group of solutions around the "real" solution, generated by the program), number of solutions in cluster, etc., were defined on the basis of test estimations within the swath of the geotransect "De Long Islands–North Pole" [*Likhachev,* 1999]. This swath is covered by 5-km-spaced aeromagnetic profiles. The basement relief here is known from seismic data [*Sorokin et al.*, 1999]. Parameters that gave the best fit between the real and estimated depths were chosen as optimal.

Mass depth to magnetic sources estimations were carried out and these formed the initial database for further analysis. Next, detailed analysis and sorting of all estimations were performed to define those estimations belonging to magnetic basement. The editing procedure included several steps:

- Single solutions were regarded least reliable and were removed from the initial database; solutions in clusters were averaged (Figure A-5). Only averaged solutions (AS) were accepted for further analysis and sorting.

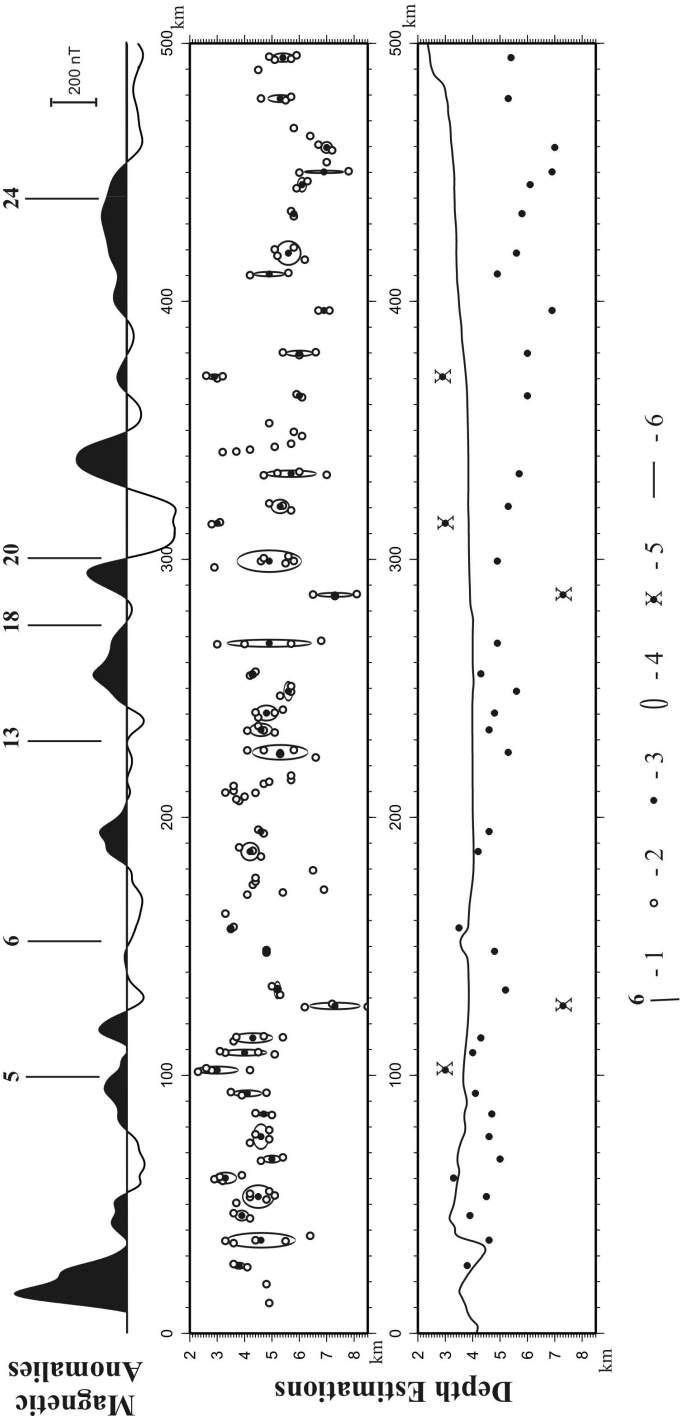

Figure A-5. Analysis and sorting of depth estimations along an aeromagnetic trackline of NRL 1999. Magnetic anomalies and their numbers (1) are shown at the top. All computed (2) and averaged (3) estimations in clusters (4) are shown in the middle section. In the lower section only averaged solutions (3) are shown. Too shallow and too deep solutions were removed (5) after comparison with the IBCAO grid (6) and fault structures.

- The shallowest AS that fell above the ocean floor known from bathymetry were removed from the database and recorded in a separate file. Analysis of these solutions shows that a part of them is connected with high frequency components of the magnetic field (noise), but another part (especially in the axial zone of the Gakkel Ridge) may be connected with real highs of the sea bottom relief smoothed in the bathymetry grid.
- AS from magnetic anomalies with unusual shapes (i.e., elongated along profile or known to differ significantly from the reference anomaly shape assumed in the Werner deconvolution method) were removed from database.
- AS related to magnetic profiles that are not orthogonal to strike of magnetic anomalies (within limits 0–30^o) were corrected (reduced by cos λ, where λ is the angle between directions of profile and the perpendicular to the magnetic anomaly axis). Solutions were removed from the database if λ exceeded 30^o. The cut-off limit of λ was determined from model calculations.
- All remaining AS are presumably connected with oceanic basement were plotted and compared with seismic information in the test area (Figure A-4b).

It is necessary to note that seismic information was used not only for comparison with the results of depth to magnetic basement estimations, but also for the calibration of results. Thus, the process of mass calculations and editing was iterative. Accordingly, the input parameters for depth calculations chosen at first on the basis of Russian data [*Sorokin et al.*, 1999] were gradually adjusted to the best fit of magnetic estimations with acoustic basement in the test area (Figure A-4b). After the completion of this process the majority of these estimations agreed well with the seismic data collected from the icebreaker *Oden* (2001). The average error was within a few hundred meters. However, some estimations conform to magnetic sources at depths noticeably below acoustic basement. It was supposed that such deep sources could be situated within or close to faults. As a result, it became necessary to map fracture zones and other structures in the study area.

The structural map was developed mainly on the basis of potential field and bathymetry maps constructed under the project. Seismic data and recent publications [*Thiede and the Shipboard Scientific Party*, 2002; *Brozena et al.*, 2003; *Engen et al.*, 2003; *Glebovsky et al.*, 2003] were used as additional information. Main fracture zones were interpreted from displacements of magnetic lineations, and from characteristic features of potential fields and their horizontal gradients compared with bathymetry data.

Deep AS corresponding to linear lows in the bottom relief and located near faults were removed from the database. Further analysis made it clear that these solutions may be identified also by statistical analysis along each profile. The deep AS is generally more than two standard deviations away from the average AS of the same magnetic profile.

Since the results of estimations in the test area were encouraging, the mass depth to magnetic sources estimations and further sorting were carried out in the wider region at 80–86°N, 11–35°E (Figure A-4). All finally selected AS presumably related to the top of basement (Figure A-6) were transformed to a grid with cell size 10×10 km using the Kriging method [*Cressie*, 1990]. This method allows grids to be calculated from widely spaced and irregularly distributed point observations. Later,

this grid was used to estimate both the sediment distribution in the study area and the uncertainty of the MSW method.

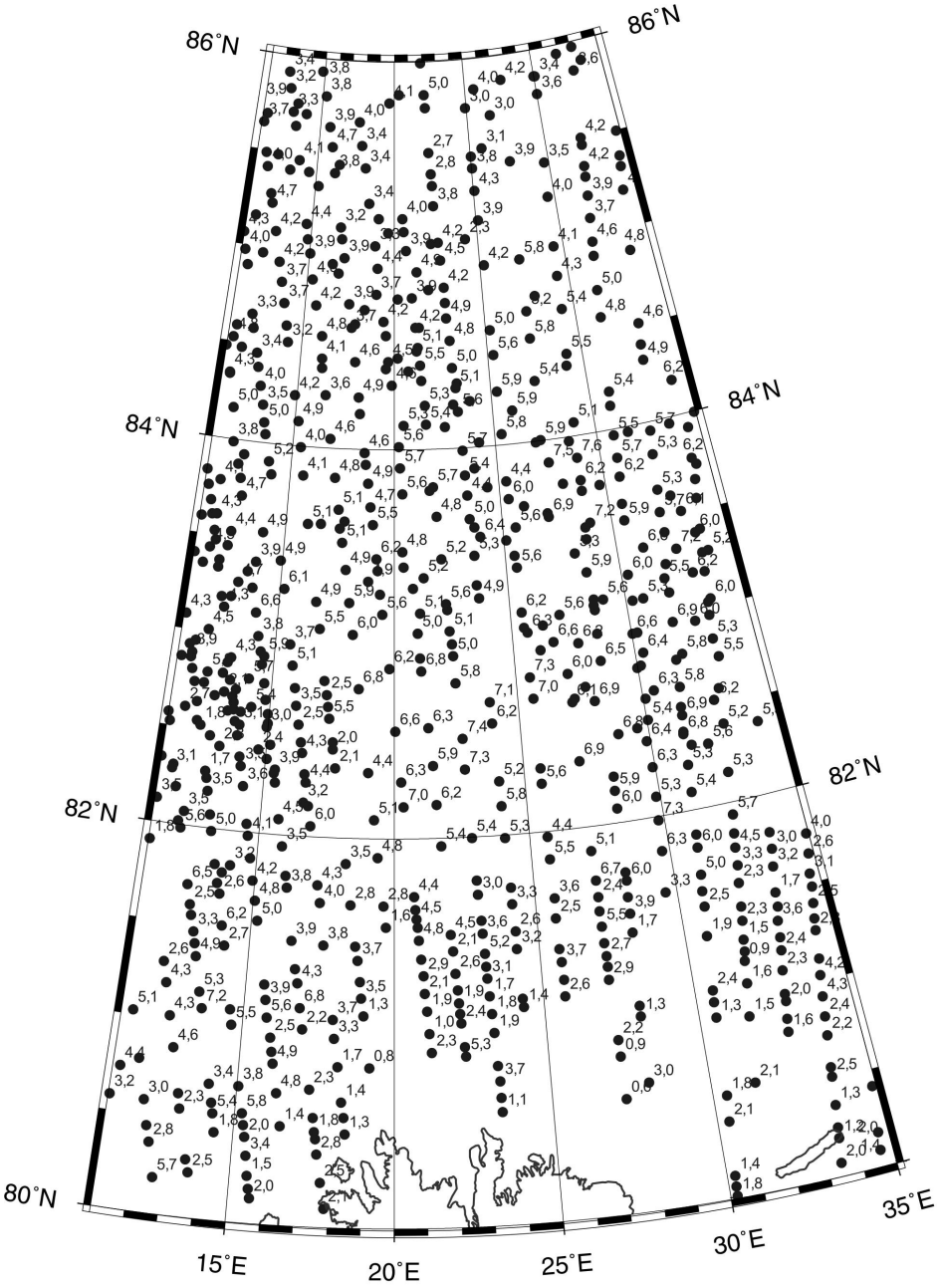

Figure A-6. Points of final depth estimates from magnetic data presumably connected with basement. Depths to basement are annotated in km below sea level.

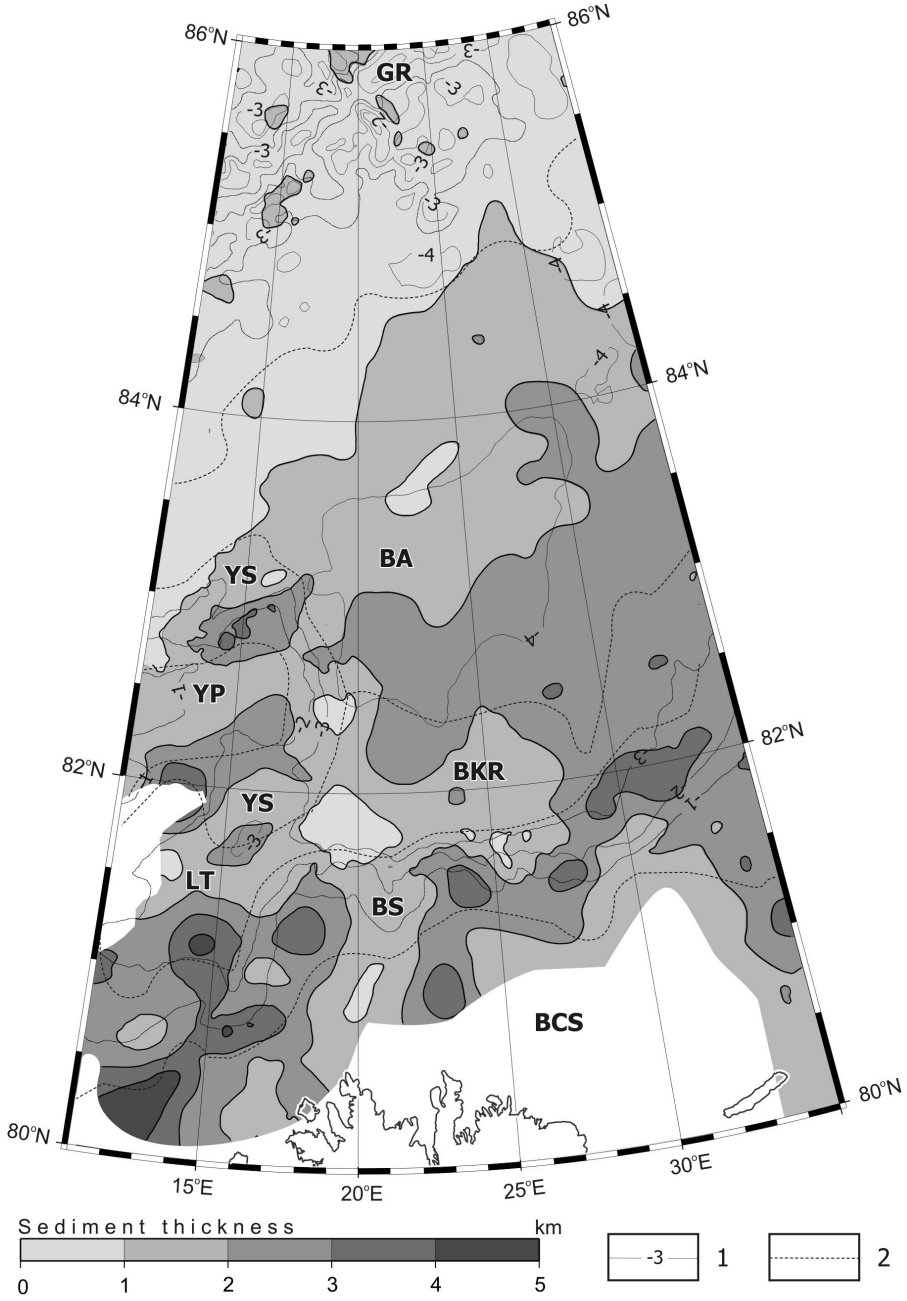

Figure A-7. Sediment thickness from magnetic data (grid 10×10 km). Bathymetry isobaths (1) and physiographic provinces (2) according to *Jakobsson et al.* [2003]. *GR*, Gakkel Ridge; *BA*, Barents Abyssal Plain; *BKR*, Barents–Kara Continental Rise; *BS*, Barents Continental Slope; *BCS*, Barents Continental Shelf; *YP*, Yermak Plateau; *YS*, Yermak Slope; *LT*, Litke Trough.

Analysis of the bathymetry information shows that there are essential differences between different data sets, especially in the axial zone of the Gakkel Ridge. At the same time, it revealed that the IBCAO grid seems to be the most reliable bathymetry model available at present. The final sediment thickness grid and map (Figure A-7) were constructed by subtracting the IBCAO grid [*Jakobsson et al.*, 2000] from the above-mentioned grid of estimated depth to basement.

Uncertainty of the Method

The uncertainty of the method was estimated by comparison of results of depth to magnetic basement calculations with depth sections based on seismic data collected in 2001 from the icebreakers *Oden* and *Polarstern* [*Jokat and Micksch*, 2004; *Engen et al.*, 2005, this volume]. While data from the *Oden* was used to calibrate depth estimations, data from the *Polarstern* was only used to estimate uncertainty of the method. Results of the comparison are presented in Figure A-8. Both final point depths to magnetic basement, projected on seismic profiles within swaths of different width (0–3, 3–6, and 6–10 km), and the difference between seismic basement and magnetic basement extracted from final grid are shown.

The correlation factor (R) and the standard deviation (σ) between seismic and magnetic basement depths were calculated for statistical estimations of uncertainty of the method (Figure A-9). Both point estimations (A) and those extracted from the depth to magnetic basement grid within a 10 km swath (B) were analysed. An integrated analysis of the results presented in Figures A-8 and A-9 allows for several conclusions:

- A high coefficient of correlation between magnetic and acoustic basement depths as well as a small standard deviation testifies to relatively high accuracy of estimations from magnetic data. The average error is less than 20% of depth to basement and usually about 10 %.
- Errors of point estimations are presumably related to two main effects: non-uniqueness inherent in the method of depth to magnetic sources estimation and natural differences between magnetic and acoustic basements.
- In spite of the relatively high resolution of the method, the final grids constructed under the project determine only regional fluctuations of the basement surface and the distribution of sediments. This may be explained by the fact that the density of magnetic profiles in the study area is too low to map basement elevations and lows visible on seismic profiles. Aeromagnetic trackline spacing is about 10–18 km. The majority of basement lows and highs are not more than 10–15 km wide.
- A total amount of 732 final point estimations remained in the data base after analysis and sorting within the 218,810 km^2 study area; only 66 of these were located within 10-km-wide swaths around seismic profiles and were used to estimate the uncertainty of the method.
- Presumably, the effects of non-uniqueness of the method might be reduced if the spacing between magnetic profiles is reduced to about 5 km.

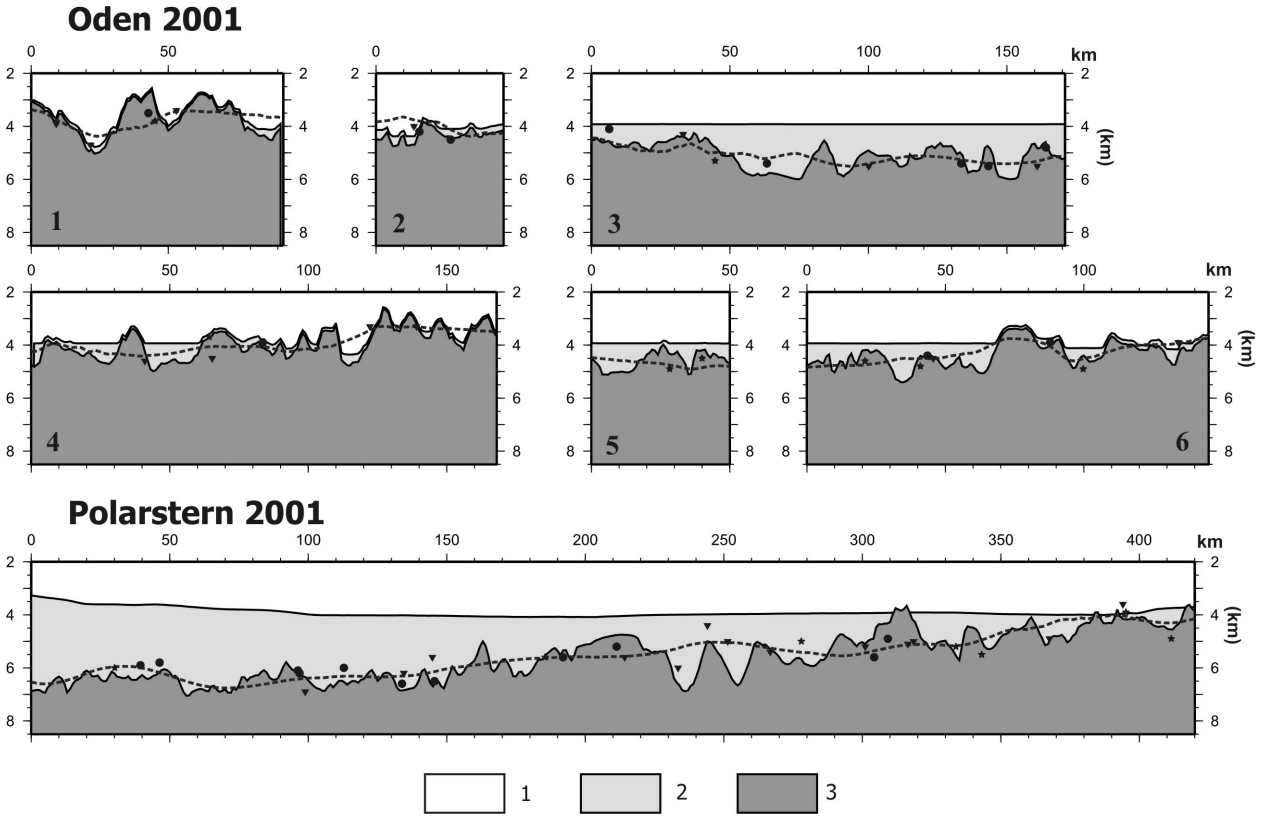

Figure A-8. Comparison of magnetic depth estimates and acoustic basement along *Oden* and *Polarstern* (2001) lines. Position and number on lines correspond to those in Figure A-4a. Water (1), sediments (2) and basement (3) are shown by different grey shades. Depth estimates projected onto seismic profiles from different distances are shown by: black circles (0–3 km), stars (3–6 km) and triangles (6–10 km). Dotted line is the basement relief as extracted from the depth to basement grid (10×10 km) used to construct the map in Figure A-7.

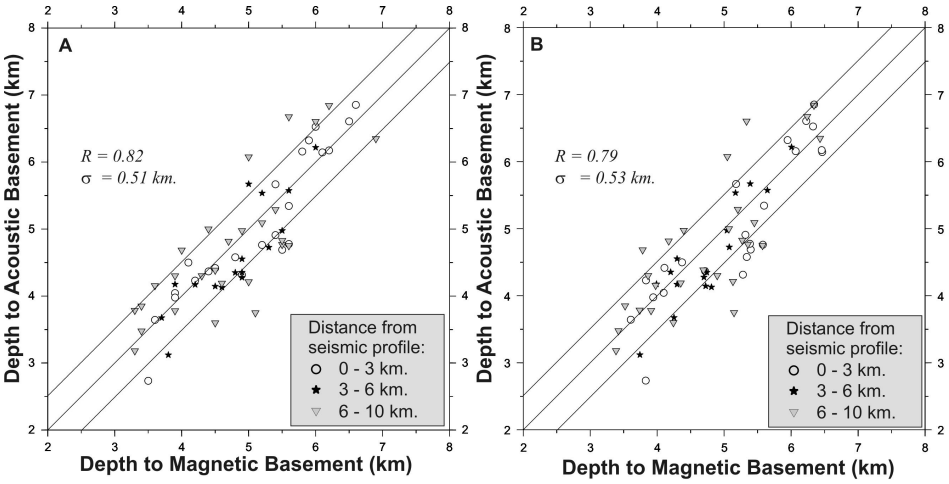

Figure A-9. Statistical estimations of the uncertainty of the method. Correlation between depth to acoustic basement from seismic data and two types of magnetic depth estimates is shown. **(A)** Depth estimates extracted from the database (Figure A-6) and projected onto seismic profiles from different distances. **(B)** The same points extracted from the depth to basement grid and projected onto the lines. R and σ are the computed correlation factor and standard deviation (km), respectively.

Summary and Conclusions

1. Depth to magnetic source calculations by the MSW deconvolution method may support seismic investigations for the estimation of the regional sediment distribution in the Arctic Ocean. The crucial prerequisites to get positive results are the following:
   - High quality of observations and correct direction of magnetic anomaly profiles; any artefacts of magnetic anomaly shape result in incorrect fitting of input parameters for MSW calculations and finally in depth estimation errors. The direction of profiles must not differ noticeably from the orthogonal to the strike of magnetic anomalies in order to avoid sizeable corrections.
   - The tectonic and structural maps constructed on the basis of all available potential field and bathymetry data have to be considered as additional information in the formalised procedure of depth to basement estimation sorting and selection.
2. It is established that, in spite of relatively high resolution of the MSW method, the final maps of the basement surface and sediment distribution maps represent only regional variations in these two features.
3. Despite its regional character, the final sediment thickness map (Figure A-7) looks more detailed than earlier published maps [*Gramberg and Puscharovsky*, 1989; *Jackson and Oakey*, 1990; *Gramberg et al.*, 1999] and shows the principal features of sediment distribution in the study area. In accordance with the physiographic

classification of *Jakobsson et al.* [2003], this area includes a few first-order provinces: Gakkel Ridge; Barents Abyssal Plain, Continental Rise, Slope, and Continental Shelf; and Yermak Plateau and Continental Slope.

4. In general, the thickness of sediments within the whole study area decreases from the Barents Continental Shelf towards the Gakkel Ridge. The least thickness of sediments (less than 0.5 km) is observed in the axial zone of the Gakkel Ridge. The rift valley has practically no sediments. Large accumulations of sediments (3–4 km) are identified within both the Barents Continental Slope and the Yermak Continental Slope north and south of the Plateau. Even larger accumulations of sediments (4–5 km) are found within two small areas confined to the Barents Shelf and Continental Rise and located in the very southwest part of the study area in the Litke Through [*HDNO-VNIIOkeangeologia*, 1999]. The thickness of sedimentary cover both in the central and eastern parts of the Barents Continental Rise and Abyssal Plain varies from 2 to 3 km and gradually decreases towards the Gakkel Ridge. The thickness of sediments within the Yermak Plateau varies from 1 to 2 km.
5. The sediment thickness map (Figure A-7) also indicates that the predominantly buried relief of the basement follows the two main tectonic trends of the area, i.e. an ENE–WSW trend (the trend of the Gakkel Ridge, Eastern Yermak Plateau and the Barents Continental Slope) and a NNW–SSE trend (parallel to the fracture zones of the Gakkel Ridge). Applying the MSW method over larger parts of the basin eastwards may confirm whether this is a systematic feature of the sediment thickness distribution of the Nansen Basin.

It is proposed to use the new sediment thickness grid and map under the international project "Map of the Arctic Sediment Thickness" (MAST).

Acknowledgments. We would like to thank Wilfried Jokat for seismic information required for uncertainty estimation of the approach developed, and for constructive comments to our study. We sincerely thank Robert Scott for improvements on the manuscript and Olav Eldholm for fruitful discussions and collaboration.

References

Brozena, J.M., V.A. Childers, L.A. Lawver, L.M. Gahagan, R. Forsberg, J.I. Faleide, and O. Eldholm (2003), New aerogeophysical study of the Eurasia Basin and Lomonosov Ridge: Implications for basin development, *Geology, 31* (9), 825-828.

Cordell, L., J.D. Phillips, and R.H. Godson (1992), U.S. Geological Survey potential-field geophysical software version 2.0, Open-File Report 93-18, 18 pp., U.S. Geological Survey, Menlo Park, CA.

Cressie, N.A. (1990): The origin of Kriging, *Mathematical Geology, 22*, 239–252.

Engen Ø., J.I. Faleide, A.J. Brevik, F. Tsikalas, A.M. Myhre, and O. Eldholm (2003), Structure of the west and north Svalbard margins in a plate tectonic setting, 4th International Conference on Arctic Margins (ICAM IV), 30 Sept.–3 Oct. 2003, Dartmouth, Nova Scotia, Canada, Program/Abstracts, P-40.

Engen, Ø., J.A. Gjengedal, J.I. Faleide, Y. Kristoffersen, and O. Eldholm (2005), Seismic stratigraphy and basement structure of the Nansen Basin, Arctic Ocean, *Geophysical Journal International*, submitted. This volume, p. 57.

Gjengedal, J.A. (2004), Prosessering og tolkning av seismiske data frå Nansenbassenget og Yermakplatået, Cand. scient. thesis, University of Bergen, Norway (in Norwegian).

Glebovsky, V., N. Gurevich, A. Likhachev, A. Minakov, J.M. Brozena, V.A. Childers, and S. Merkouriev (2003), Geochronology and kinematics of spreading in the western Eurasia Basin, 4th International Conference on Arctic Margins (ICAM IV), 30 Sept.–3 Oct. 2003, Dartmouth, Nova Scotia, Canada, Program/Abstracts, p. 59–60.

Gramberg, I.S., and Yu.M. Puscharovsky (1989), Map of relief of different age and heterogeneous basement in the Arctic and neighbouring areas, scale 1:10,000,000, USSR Academy of Science and Ministry of Geology (in Russian).

Gramberg, I.S., V.V. Verba, M.L. Verba, and M.K. Kos'ko (1999), Sedimentary cover thickness map – sedimentary basins in the Arctic, *Polarforschung*, *69*, 243–250 (published 2001).

Hansen, R.O., and M. Simmonds (1993), Multiple-source Werner deconvolution, *Geophysics, 58* (12), 1792–1800.

HDNO-VNIIOkeangeologia (1999), Bottom relief of the Arctic Ocean, scale 1:5,000,000, St. Petersburg.

Jackson, H.R., and G.H. Oakey (1990), Sedimentary thickness map of the Arctic Ocean, in *The Arctic Ocean Region*, *The Geology of North America*, vol. L, edited by A. Grantz et al., Plate 5, Geological Society of America, Boulder, CO.

Jakobsson, M., N. Cherkis, J. Woodward, R. Macnab, and B. Coakley (2000), New grid of Arctic bathymetry aids scientists and mapmakers, *Eos, Transactions, American Geophysical Union*, *81* (9), 89, 93, 96.

Jakobsson, M., A. Grantz, Y. Kristoffersen, and R. Macnab (2003), Physiographic provinces of the Arctic Ocean seafloor, *Geological Society of America Bulletin*, *115* (12), 1443–1455.

Jokat, W., and U. Micksch (2004), Sedimentary structure of the Nansen and Amundsen basins, Arctic Ocean, *Geophysical Research Letters*, *31*, L02603, doi:10.1029/2003GL018352.

Laxon S., and D. McAdoo (1998), Satellites provide new insights into polar geophysics, *Eos, Transactions, American Geophysical Union, 79* (6) 69, 72–73.

Likhachev, A., (1999), A comparison of automated methods of depth to magnetic sources estimations by the example of the aeromagnetic data from geotransect "De Long Islands – Makarov Basin" interpretation, in *The New in the Arctic and World Ocean Geology*, pp. 36–40, VNIIOkeangeologia, St. Petersburg (in Russian).

Nabighian, M.N. (1974): Additional comments on the analytic signal of two-dimensional magnetic bodies with polygonal cross-section, *Geophysics, 39*, 85–92.

Sorokin, M.Yu., Yu.Ya. Zamansky, A.Ye. Langinen, H.R. Jackson, and R. Macnab (1999), Crustal structure of the Makarov Basin, Arctic Ocean determined by seismic refraction, *Earth and Planetary Science Letters 168*, 187–199.

Thiede, J., and the Shipboard Scientific Party (2002), *POLARSTERN ARKTIS XVII/2 Cruise Report: AMORE 2001 (Arctic Mid-Ocean Ridge Expedition)*, *Reports on Polar Research*, vol. 421, 397 pp., Alfred Wegener Institute for Polar and Marine Research, Bremerhaven, Germany.

Werner S. (1953), Interpretation of magnetic anomalies at sheet-like bodies, *Årsbok 43,* Series C.C., vol. 6, Sveriges Geologiska Undersökning, Uppsala.

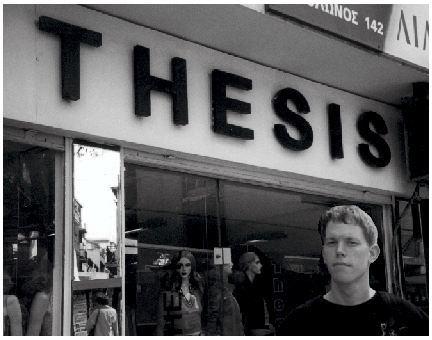
THESIS